Mechanical and Aerospace Engineering

mechanical engineering, aerospace engineering, energy systems engineering, engineering science

A Near-Wall Reynolds-Stress Closure Without Wall Normals

S. P. Yuan and R. M. C. So

Final Report

submitted to

July 15, 1997

College of Engineering and Applied Sciences

Arizona State University

Tempe, Arizona 85287-6106

Table of Contents

iii

Summary

Turbulent wall-bounded complex flows are commonly encountered in engineering practice and are of considerable interests in a variety of industrial applications. The presence of a wall significantly affects turbulence characteristics. In addition to the wall effects, turbulent wall-bounded flows become more complicated by the presence of additional body forces (e.g. centrifugal force and Coriolis force) and complex geometry. Most near-wall Reynolds stress models are developed from a high-Reynolds-number model which assumes turbulence is homogenous (or quasi-homogenous). Near-wall modifications are proposed to include wall effects in near-wall regions. In this process, wall normals are introduced. Good predictions could be obtained by Reynolds stress models with wall normals. However, ambiguity arises when the models are applied in flows with multiple walls.

Many models have been proposed to model turbulent flows. Among them, Reynolds stress models, in which turbulent stresses are obtained by solving the Reynolds stress transport equations, have been proved to be the most successful ones. To apply the Reynolds stress models to wall-bounded flows, near-wall corrections accounting for the wall effects are needed, and the resulting models are called near-wall Reynolds stress models. In most of the existing near-wall models, the near-wall corrections invoke wall normals. These wall-dependent near-wall models are difficult to implement for turbulent flows with complex geometry and may give inaccurate predictions due to the ambiguity of wall normals at corners connecting multiple walls.

The objective of this study is to develop a more general and flexible near-wall Reynolds stress model without using any wall-dependent variable for wall-bounded turbulent flows. With the aid of near-wall asymptotic analysis and results of direct numerical simulation, a new near-wall Reynolds stress model (NNWRS) is formulated based on Speziale et al.'s high-Reynolds-stress model with wall-independent near-wall corrections. Moreover, only one damping function is used for flows with a wide range of Reynolds numbers to ensure that the near-wall modifications diminish away from the walls.

Various simple and complex turbulent wall-bounded flows are used to validate the NNWRS model. Model predictions agree reasonably well with available data from experiments, direct numerical simulation, or large eddy simulation. Complex flow features caused by the centrifugal force and Coriolis force as in swirling pipe flow, axially rotating pipe flow and channel flow with spanwise rotation are essentially captured by the model. The model is able to reproduce complicated flow phenomena induced by complex geometry, such as flow recirculation, reattachment and boundary-layer redevelopment in backward-facing step flow and secondary flow in three-dimensional square duct flow. In simple flows, including fully developed channel/pipe flow, Couette flow and boundary-layer flow, the wall effects are dominant, and the NNWRS model predicts less degree of turbulent anisotropy in the near-wall region compared with the wall-dependent near-wall Reynolds stress model (NWRS) developed by So et al.. However, in complex flows where other effects become more important, the NNWRS model performs almost as well as the NWRS model, and the advantages of the wall-independent model become more evident. The comparison of the predictions given by the two models also rectifies the misconception that the overshooting of skin friction coefficient in backward-facing step flow prevalent in those near-wall models with wall normals is caused by the use of wall normals.

1 INTRODUCTION

1.1 Background

Turbulence closure modeling to solve the mean-averaged Navier-Stokes equations has been pursued for nearly a century. In the last several decades, with the great advances in computer science, numerous turbulence models have been developed to simulate and predict more and more complex turbulent flows. In most engineering problems, flow fields are bounded by walls. The presence of a wall affects significantly the turbulence characteristics: it reduces the length scale of the momentum fluctuations and increases the dissipation rate; it reflects the pressure fluctuation, thereby inhibiting the transfer of turbulence energy into fluctuations normal to the wall; it enforces a no-slip boundary condition, thus ensuring that within a wall-adjacent sublayer, however thin, turbulent stress is negligible and viscous effect on transport processes becomes vitally important (Launder 1989).

In general, there are two types of turbulence models: eddy-viscosity models and second-order closure models (Reynolds stress models). In the eddy-viscosity models, the Reynolds stress tensor is assumed to be the product of an eddy viscosity and the mean strain-rate tensor. In the second-order closure models, turbulent Reynolds stresses are obtained by solving the Reynolds stress transport equations and no relation is presumed between the Reynolds stresses and the mean strain rates. As a result, the second-order closure models are more general and can be used to simulate turbulence anisotropy and the turbulent stress redistribution process in the near-wall region. Furthermore, other important factors such as streamline curvature, centrifugal and Coriolis forces could be properly accounted for in the Reynolds stress models, whereas they are rather difficult to be included in the eddy-viscosity models.

Practically all turbulence closure models invoke the large Reynolds number assumption, thus allowing the viscous effect to be neglected as a first approximation. Consequently, the high-Reynolds-number models cannot be applied to the near-wall region where viscous effect is dominant. To remedy this drawback, wall-functions have been used to bridge the gap between the

1

wall and the location beyond which the high-Reynolds-number models are applicable. The wall-functions are derived under the assumptions of equilibrium turbulence and constant shear stress near a wall, which are less likely to be valid for complex turbulent shear flows. Therefore, many attempts have been made to develop near-wall second-order closure models.

As a wall is approached, the local Reynolds number decreases and the intensity of the anisotropy of the turbulence field increases due to the reflection of the fluctuating pressure by the wall (Kim 1989). This effect is commonly known as wall blocking (wall-reflection or pressure-echo) effects. Although the influence of the viscous effect and wall blocking effect on the turbulent motion are very different by nature, these effects have been frequently modeled together in near-wall turbulence modeling. All the existing near-wall Reynolds-stress models are developed based on the high-Reynolds-number models. To account for wall effects, in principle, near-wall modifications for the turbulent diffusion, velocity-pressure-gradient correlation, and dissipation rate tensor are needed so that these terms have the correct asymptotic behavior near the wall. Asymptotic analysis shows that the turbulent diffusion term is three orders of magnitude smaller than the velocity-pressure-gradient correlation and the dissipation rate tensor in the near-wall region. Therefore, no near-wall modification is actually required for the turbulent diffusion term. On the other hand, the velocity-pressure-gradient correlation and dissipation rate tensor are order one quantities in the near-wall region, and near-wall modifications for these terms are necessary for the models to be applicable in the near-wall region. To ensure that the near-wall modifications diminish away from the wall, a damping function analogous to that proposed by Van Driest (1956) is introduced so that the high-Reynolds-number models are recovered in the region far away from the wall.

The velocity-pressure-gradient correlation and dissipation rate tensor play crucial roles in near-wall turbulence and represent different physical processes. The velocity-pressure-gradient correlation is usually partitioned into a pressure-strain part and a pressure diffusion part. Few models have explicitly considered the pressure diffusion effect (e.g. Lumley 1978).

2

Pressure diffusion is assumed to be either included into the modeling of the turbulent diffusion term, or insignificant in near-wall turbulence as it is treated when the Reynolds number is large. On the other hand, the contribution of the pressure-strain correlation is significant because it redistributes energy among different turbulent stress components. The pressure-strain correlation is a linear function of the pressure fluctuation, and according to the structure of the solution to the Poisson equation for the pressure fluctuation, it consists of a 'return' term, a 'rapid' term and a Stokes term representing the pressure reflection caused by the wall (Mansour et al. 1988). Due to the difficulty to include the Stokes part in the model if local homogeneous turbulence is assumed, the Stokes term is neglected in most of the high-Reynolds-number models (e.g. Launder et al. 1975). When these models are extended to the near-wall region, an additional term proposed to simulate the Stokes term is added back to the pressure-strain correlation (Prud'homme and Elghobashi 1983; Kebede et al. 1984; Shima 1988; Shih and Mansour 1990; Lai and So 1990). Another approach is to modify the coefficients of the return and rapid terms to justify the neglect of the Stokes term (Launder and Shima 1989). In some models, the Stokes term is absorbed into either the return part or the rapid part (Speziale et al. 1991; Launder and Tselepidakis 1993; Launder and Li 1994). To ensure that the near-wall corrections decay exponentially away from the wall, a function depending on the wall normal distance is usually introduced, and the resulting models are no longer coordinate-frame invariant.

The dissipation rate tensor ε_{ij} in the Reynolds-stress equation is formulated as the combination of an isotropic solenoidal part and an anisotropic part according to Hanjalic and Launder (1976). The isotropic part is obtained by solving a transport equation for the dissipation rate ε of the kinetic energy. Hanjalic and Launder (1976) proposed the first ε-equation compatible with their Reynolds-stress model. In spite of its oversimplified form compared with the exact governing equation for dissipation rate, it performs reasonably well and becomes a prototype for later modifications. Modifications have been made mainly to reproduce the near-wall behavior of dissipation rate predicted by direct numerical simulation: a maximum value of ε

is expected to occur at the wall. To reproduce such behavior, near-wall corrections are introduced to the dissipation rate equation and wall dependent variables (wall normals) are used in damping functions (Shima 1988) or transformed dissipation terms (Lai and So 1990). The anisotropic correction part is constructed to satisfy the following two requirements: (i) the contraction of the dissipation rate tensor should be equal to two times the dissipation rate of the kinetic energy, i.e. $\sum \varepsilon_{ii} = 2\varepsilon$; (ii) the components of the dissipation rate tensor should satisfy the kinematic constraints proposed by Launder and Reynolds (1983). Several models have been proposed to improve the dissipation rate tensor in the near-wall region (e.g. Prud'homme and Elghobashi 1983; Kebede et al. 1984; So and Yoo 1986; Lai and So 1990). Among them, Lai and So's (1990) model satisfies the kinematic constraints and contraction requirement with the introduction of the wall unit vectors. Most recently, Shima (1995) proposed a three-term dissipation rate model. This model also satisfies both requirements but eliminates all wall normal unit vectors.

In view of the above discussion, it can be concluded that most of the existing near-wall Reynolds-stress models explicitly invoke wall-dependent variables such as wall normal unit vector and wall normal distance to account for the viscous and wall effects. The influence of each wall in this wall-dependent model is also assumed to act independently. For turbulence flows with complex geometry, which are commonly encountered in most engineering problems, the use of wall normals at corners connecting multiple walls becomes ambiguous. Therefore, in this situation, these models are difficult to implement and may introduce inaccuracy in the prediction of complex turbulent flow field. The present study is aimed to improve the existing near-wall Reynolds-stress models for complex flows caused by complex geometry, as well as streamline curvature and additional body forces such as centrifugal and Coriolis forces in flows with swirl and rotation.

1.2 Present Objectives

The present research is to develop a near-wall Reynolds-stress model for complex turbulent flows without introducing any wall-dependent variables (wall normals). Several near-wall second-

4

order closure models have been proposed at Arizona State University (ASU) in the last decade. They are So and Yoo (1987), Lai and So (1990), So et al. (1991) and So et al. (1994). With the aid of asymptotic analysis, the near-wall modifications in these models were developed based on the high-Reynolds-number model of Launder et al. (1975) except that of So et al's (1994), which was based on the model of Speziale et al. (1991). This latest model (hereafter we will call it NWRS model) has been validated against various applications ranging from incompressible fully developed channel flow to high Mach number compressible boundary-layer flow in a wide range of Reynolds number. Although these models developed by the ASU group are asymptotically consistent to a certain extent in the near-wall region, all of them are dependent on wall variables in one way or another. The present study is part of the on-going near-wall second-order closure model development project. An attempt to develop a near-wall Reynolds-stress model without wall dependence has been carried out by Launder and Li (1994) with partial success. The wall normals were removed from the pressure-strain correlation in their Reynolds-stress model, but remain in the dissipation rate tensor. Therefore, the model developed in this study is expected to be the first near-wall Reynolds-stress model with no wall dependence. The challenge of near-wall modeling lies on the lack of thorough understanding of wall effects on turbulence. A near-wall second-order closure model without wall-dependent variables poses more difficulties because of the limited number of solvable variables and suitable formulations. Guided by the results of direct numerical simulation, we will develop an asymptotically correct near-wall model without wall normals in this study. The new model is a modification of NWRS which can accommodate flow complexities such as streamline curvature and additional body forces related to fluid rotation. The new model, designated as NNWRS, is expected to perform as well as the wall-dependent NWRS model in a wide range of complex flow conditions.

1.3 Report Outline

In Section 2, a new near-wall Reynolds-stress (NNWRS) model without wall normals is developed based on the pressure-strain model of Speziale et al. (1991). Asymptotic analysis and

5

results from direct numerical simulation are used to guide the near-wall modifications for the pressure-strain correlation, dissipation rate tensor, and dissipation rate equation. For comparison, the formulation for the near-wall Reynolds stress (NWRS) model with wall normals proposed by So et al. (1994) is also presented, and its predictions will be compared with those given by the NNWRS model in Sections 3, 4 and 5, together with available data from experiments, direct numerical simulation and large eddy simulation.

In Section 3, simple internal and external flows with a wide range of Reynolds numbers are first used to validate the new proposed model. These flows include fully-developed channel/pipe flow, Couette flow, and boundary-layer flow with zero pressure gradient. In addition to assessing its performance on the mean and turbulence fields, the model's ability to replicate Reynolds number effects on the mean flow and second-order statistics is also examined.

In Section 4, the NNWRS model is applied to swirling pipe flow, axially rotating pipe flow, and a channel flow with spanwise rotation to demonstrate its ability to reproduce complicated flow phenomena caused by streamline curvature, centrifugal force, and Coriolis force in a wide range of Reynolds numbers, swirl numbers, and rotation numbers.

In Section 5, two flows with multiple walls, a two-dimensional backward-facing step flow and a three-dimensional square duct flow, are used to test the model's ability to replicate flow phenomena resulting from complex geometry, such as flow recirculation, reattachment, and boundary-layer redevelopment in backward-facing step flow, and the secondary flow induced by turbulence in square duct flow. The advantages of the NNWRS model for flows with complex geometry are demonstrated.

Section 6 summarizes the performance of the proposed near-wall Reynolds-stress model without wall normals and presents the conclusions drawn.

2. NEAR-WALL REYNOLDS-STRESS MODELING

2.1 Mean Flow Equations

The present study considers turbulent flows of a viscous, incompressible fluid. The fluid motion with the presence of rotation is described by the Navier-Stokes equations, which can be written in Cartesian form or notation as:

$$\frac{\partial \tilde{u}_i}{\partial x_i} = 0 \quad , \tag{2-1}$$

$$\frac{\partial \tilde{u}_i}{\partial t} + \tilde{u}_j \frac{\partial \tilde{u}_i}{\partial x_j} = -\frac{1}{\rho} \frac{\partial \tilde{p}}{\partial x_i} + \upsilon \frac{\partial^2 \tilde{u}_i}{\partial x_j \partial x_j} - 2e_{ijk}\Omega_j \tilde{u}_k \quad , \tag{2-2}$$

where $\tilde{u}_i$ is the instantaneous velocity vector, $\tilde{p}$ is the modified pressure including the centrifugal force potential, Ω_j is the angular velocity, e_{ijk} is the permutation tensor, and ρ and υ are the fluid density and viscosity, respectively. Equations (2-1) and (2-2) express conservation of mass and momentum per unit mass, respectively.

The N-S equations (1) and (2) are fundamental governing equations and can be applied to both laminar and turbulent flows. With specified boundary and initial conditions, in principle, (1) and (2) can be solved numerically. However, for turbulent flows, the resolution of the small scale turbulent fluctuations requires very fine grids; as a result, direct numerical simulations (DNS) of turbulent flows at high Reynolds number are extremely difficult, if not impossible. An alternative approach is to study the mean flow field with the consideration of the influence of turbulence. The mean flow field can be obtained through time, spatial or ensemble averaging. Time averaging has been widely used in engineering since stationary turbulent flows are most frequently encountered. This method is also adopted in this study. By time averaging, the velocity and pressure fields are decomposed into a mean and a fluctuating part:

$$\tilde{u}_i = U_i + u_i \quad , \qquad \tilde{p} = P + p \quad , \tag{2-3}$$

where capital letters denote the time-averaged mean quantities and small case symbols represent the fluctuating quantities.

Substituting (2-3) into (2-1) and (2-2) and taking the time averaging of the resulting equations, we obtain the governing equations for the mean flow field, or

$$\frac{\partial U_i}{\partial x_i} = 0 \quad , \tag{2-4}$$

$$U_j \frac{\partial U_i}{\partial x_j} = -\frac{1}{\rho}\frac{\partial P}{\partial x_i} + \upsilon \frac{\partial^2 U_i}{\partial x_j \partial x_j} - \frac{\partial \overline{u_i u_j}}{\partial x_j} - 2e_{ijk}\Omega_j U_k \quad . \tag{2-5}$$

Note that the effect of turbulence on the mean flow is represented by the Reynolds stress term $\overline{u_i u_j}$ (i.e. correlations between different fluctuating velocity components) on the right hand side of (2-5). Equations (2-4) and (2-5) are called the Reynolds equations for the mean flow field.

To solve the Reynolds equations, one must relate the Reynolds stress term to the mean velocity to close the equations. In the following section we derive the transport equations for the Reynolds stresses and for the dissipation rate.

2.2 Time-Averaged Turbulence Transport Equations

The transport equations for the Reynolds stresses and the dissipation rate can be derived from equations (2-1) and (2-2). Defining a Navier-Stokes operator

$$N(\tilde{u}_i) = \frac{\partial \tilde{u}_i}{\partial t} + \tilde{u}_j \frac{\partial \tilde{u}_i}{\partial x_j} + \frac{1}{\rho}\frac{\partial \tilde{p}}{\partial x_i} - \upsilon \frac{\partial^2 \tilde{u}_i}{\partial x_j \partial x_j} + 2e_{ijk}\Omega_j \tilde{u}_k \quad , \tag{2-6}$$

and carrying out the following time averaging

$$\overline{u_i N(\tilde{u}_j) + u_j N(\tilde{u}_i)} = 0 \quad , \tag{2-7}$$

we obtain the Reynolds-stress transport equations:

$$U_k \frac{\partial \overline{u_i u_j}}{\partial x_k} = \frac{\partial}{\partial x_k}\left(\upsilon \frac{\partial \overline{u_i u_j}}{\partial x_k} \right) - \frac{\partial \overline{u_i u_j u_k}}{\partial x_k} + \left[-\overline{u_i u_k}\frac{\partial U_j}{\partial x_k} - \overline{u_j u_k}\frac{\partial U_i}{\partial x_k} \right]$$

$$- 2\Omega_k\left(\overline{u_j u_m}e_{ikm} + \overline{u_i u_m}e_{jkm} \right) + \overline{p\left(\frac{\partial u_i}{\partial x_j} + \frac{\partial u_j}{\partial x_i} \right)}$$

$$- \frac{\partial}{\partial x_k}\left(\overline{pu_i}\delta_{jk} + \overline{pu_j}\delta_{ik} \right) - 2\upsilon \overline{\frac{\partial u_i}{\partial x_k}\frac{\partial u_j}{\partial x_k}} \quad . \tag{2-8}$$

8

The left-hand side is the convection term and the terms on the right-hand side of (2-8) are viscous diffusion, turbulent diffusion, production due to mean velocity strain, production due to rotation, pressure-strain correlation, pressure diffusion and viscous dissipation. Similarly, the equation for the dissipation rate ε, defined as

$$\varepsilon = \upsilon \overline{\frac{\partial u_i}{\partial x_k} \frac{\partial u_i}{\partial x_k}} \quad , \tag{2-9a}$$

can be derived from

$$2\upsilon \overline{\frac{\partial u_i}{\partial x_j} \frac{\partial}{\partial x_j} [N(u_i)]} = 0 \quad , \tag{2-9b}$$

where $N(u_i)$ is the Navier-Stokes operator defined in (2-6) with $\tilde{u}_i \to u_i$, $\tilde{p} \to p$. After tedious algebraic manipulation, the following equation for ε is obtained

$$U_k \frac{\partial \varepsilon}{\partial x_k} = \frac{\partial}{\partial x_k} \left(\upsilon \frac{\partial \varepsilon}{\partial x_k} \right) + \frac{\partial}{\partial x_k} \left(-\overline{\upsilon u_k \frac{\partial u_i}{\partial x_m} \frac{\partial u_i}{\partial x_m}} \right) - 2\upsilon \overline{\frac{\partial u_i}{\partial x_k} \frac{\partial u_j}{\partial x_k}} \frac{\partial U_i}{\partial x_j}$$

$$- 2\upsilon \overline{\frac{\partial u_k}{\partial x_i} \frac{\partial u_k}{\partial x_j}} \frac{\partial U_i}{\partial x_j} - 2\upsilon \overline{\left[u_k \frac{\partial u_i}{\partial x_j} \right] \frac{\partial^2 U_i}{\partial x_k \partial x_j}} - 2\upsilon \overline{\frac{\partial u_i}{\partial x_k} \frac{\partial u_i}{\partial x_m} \frac{\partial u_k}{\partial x_m}}$$

$$- 2\frac{\upsilon}{\rho} \frac{\partial}{\partial x_j} \left(\overline{\frac{\partial p}{\partial x_m} \frac{\partial u_j}{\partial x_m}} \right) - 2\upsilon^2 \overline{\frac{\partial^2 u_i}{\partial x_k \partial x_m} \frac{\partial^2 u_i}{\partial x_k \partial x_m}} . \tag{2-10}$$

The terms on the right-hand side of (2-10) are generally regarded as viscous diffusion, turbulent diffusion, mixed production, production by mean velocity gradient, gradient production, turbulence production, pressure diffusion and turbulent destruction of the dissipation.

To facilitate the discussions on each term in the Reynolds-stress and dissipation rate transport equations, we recast (2-8) and (2-10) in the following symbolic forms:

$$C_{ij} = D_{ij}^V + D_{ij}^T + P_{ij} + R_{ij} + \Pi_{ij}^* - \varepsilon_{ij} \quad , \tag{2-11}$$

$$C_\varepsilon = D_\varepsilon^V + D_\varepsilon^T + P_\varepsilon^1 + P_\varepsilon^2 + P_\varepsilon^3 + P_\varepsilon^4 + D_\varepsilon^p - \gamma \quad , \tag{2-12}$$

respectively, where each symbol represents each position-corresponding term on the right-hand side of the respective full equations. Note that in (2-11) the turbulent diffusion term is

9

$$D_{ij}^T = \frac{\partial \overline{u_i u_j u_k}}{\partial x_k} \quad . \tag{2-13a}$$

the velocity-pressure-gradient correlation Π_{ij}^* consists of two parts:

$$\Pi_{ij}^* = \Pi_{ij} + D_{ij}^p \quad , \tag{2-13b}$$

where

$$\Pi_{ij} = \overline{p\left(\frac{\partial u_i}{\partial x_j} + \frac{\partial u_j}{\partial x_i}\right)} \quad , \tag{2-13c}$$

$$D_{ij}^p = -\frac{\partial}{\partial x_k}\left(\overline{p u_i}\delta_{jk} + \overline{p u_j}\delta_{ik}\right) \quad , \tag{2-13d}$$

and the dissipation rate tensor is written as

$$\varepsilon_{ij} = 2\upsilon \overline{\frac{\partial u_i}{\partial x_k} \frac{\partial u_j}{\partial x_k}} \quad . \tag{2-13e}$$

All the right-hand side terms in (2-12) except

$$D_\varepsilon^\upsilon = \frac{\partial}{\partial x_k}\left(\upsilon \frac{\partial \varepsilon}{\partial x_k}\right) \quad , \tag{2-14}$$

need modeling if the Reynolds equations for the mean flow field are to be closed.

2.3 High-Reynolds-Number Modeling

In this section, we discuss how the turbulent diffusion D_{ij}^T, velocity-pressure-gradient correlation Π_{ij}^* and dissipation rate tensor ε_{ij} in (2-11) are modeled under the assumption of high Reynolds number (the resulting models are called the high-Reynolds-number models). For high Reynolds number flows, the viscous effect can be neglected. Irrespective of the analytical arguments employed for modeling, all known high-Reynolds-number models use the Reynolds stress gradients to express the turbulent diffusion term (some models also employ the gradient of the turbulence scale or the gradient of the scale-supplying variable, such as the dissipation rate ε). Five formulations have been proposed for the turbulent diffusion term and they are given by Daly

10

and Harlow (1970), Shir (1973), Hanjalic and Launder (1972), Mellor and Herring (1973) and Lumley (1978). The invariant form of turbulent diffusion by Hanjalic and Launder (1972)

$$D_{ij}^T = \frac{\partial}{\partial x_k}\left[C_s \frac{k}{\varepsilon}\left(\overline{u_i u_l} \frac{\partial \overline{u_j u_k}}{\partial x_l} + \overline{u_j u_l} \frac{\partial \overline{u_k u_i}}{\partial x_l} + \overline{u_k u_l} \frac{\partial \overline{u_i u_j}}{\partial x_l} \right) \right] \quad ,$$

(2-15)

is adopted for the present model development, where $k = 1/2\overline{u_i u_i}$ is the turbulence kinetic energy and C_s is a constant. This formula is not only tensorily consistent with the exact expression but also found to perform better in several types of turbulent flows.

Velocity-pressure-gradient correlation Π_{ij}^* is traditionally partitioned into a pressure-strain term Π_{ij} and a pressure diffusion term D_{ij}^p (2-13b). The contribution from D_{ij}^p is usually neglected for high-Reynolds-number flows or is argued to be included in turbulent diffusion model (2-15). In either case, the velocity-pressure-gradient term Π_{ij}^* is considered to be the same as the pressure-strain term Π_{ij} in high-Reynolds-number modeling.

For incompressible flows, the pressure fluctuation is governed by the following Poisson equation

$$\frac{1}{\rho}\nabla^2 p = -2\frac{\partial U_i}{\partial x_j}\frac{\partial u_j}{\partial x_i} - \frac{\partial^2}{\partial x_i \partial x_j}\left(u_i u_j - \overline{u_i u_j} \right) \quad ,$$

(2-16)

with boundary condition

$$\frac{\partial p}{\partial y} = \frac{\partial^2 v}{\partial y^2} \quad ,$$

(2-17)

where v is the velocity fluctuation in the wall normal direction (y direction). The Poisson equation and its boundary condition (2-17) are linear with respect to the fluctuating pressure p. Therefore, its solution can be splitted into three parts, a 'return' part, a 'rapid' part and a 'Stokes' part (Mansour et al. 1988). The return pressure, p_1, is defined as the solution of the following problem

$$\frac{1}{\rho}\nabla^2 p_1 = -\frac{\partial^2}{\partial x_i \partial x_j}\left(u_i u_j - \overline{u_i u_j} \right) \quad ,$$

(2-18a)

with the boundary condition at the wall given by

11

$$\frac{\partial p_1}{\partial y} = 0 \quad . \tag{2-18b}$$

The rapid pressure, p_2, is defined as the solution to

$$\frac{1}{\rho}\nabla^2 p_2 = -2\frac{\partial U_i}{\partial x_j}\frac{\partial u_j}{\partial x_i} \quad , \tag{2-19a}$$

with the boundary condition at the wall given by

$$\frac{\partial p_2}{\partial y} = 0 \quad . \tag{2-19b}$$

Finally, the Stokes pressure, p_s, is defined as the solution to

$$\frac{1}{\rho}\nabla^2 p_s = 0 \quad , \tag{2-20a}$$

with the boundary condition at the walls specified as

$$\frac{\partial p_s}{\partial y} = \frac{\partial^2 v}{\partial y^2} \quad . \tag{2-20b}$$

This split resolves the question of whether to add the inhomogeneous boundary condition to the return part of the pressure or to the rapid part. It does not affect the wall effect on the pressure fluctuations. The pressure-strain term is linear in p (2-13c) and accordingly the Stokes pressure-strain statistics can be added to either the rapid pressure-strain term or the return pressure-strain term without affecting the wall effect on the pressure-strain correlation. However, the Stokes pressure-strain term (representing the wall effect) is neglected in most models due to the mathematical difficulty and the lack of understanding of the wall effect on turbulent flow field. Launder et al.'s (1975) pressure-strain correlation (hereafter denoted as the LRR model) has been widely accepted for most Reynolds-stress models because of its good performance. In the LRR model, a wall reflection term was introduced to simulate the Stokes pressure-strain term and to compensate for the stress anisotropy due to the presence of the wall. The inclusion of the wall reflection term has been regarded as indispensable to simulate the wall effects. However, it causes a major drawback since this term involves the distance from the wall and is not coordinate frame

invariant. On the other hand, the SSG model (Speziale et al. 1991) incorporated the Stokes term into the return and rapid parts, and no additional wall reflection term is proposed.

The recent trend for pressure-strain correlation modeling is to include additional nonlinear terms to the conventional linear terms. The inclusion of nonlinear terms brings more flexibility to satisfy certain kinematic constraints (e.g. realizability). Among the nonlinear models, the SSG model retains the linear parts in the LRR model, but with some coefficients depending on the turbulent stress invariants and turbulence production (hence, it is a quasi-linear model). Other models contain the quadratic and cubic terms in the rapid part and therefore are much more complicated to use in engineering applications (Choi and Lumley 1984; Shih and Lumley 1985; Craft and Launder 1991; Launder and Tselepidikis 1993).

With appropriate rearrangement and transformation (Appendix A), the SSG model can be rewritten in the following form:

$$\Pi_{ij} = -(C_1\varepsilon + C_1^*\tilde{P})b_{ij} + C_2\varepsilon(b_{ik}b_{kj} - \frac{1}{3}\Pi\delta_{ij}) + C_5k(b_{jm}e_{ikm} + b_{im}e_{jkm})\Omega_k$$

$$- \alpha_1(P_{ij} - \frac{2}{3}\tilde{P}\delta_{ij}) - \beta_1(D_{ij} - \frac{2}{3}\tilde{P}\delta_{ij}) - 2(\gamma_1 + \frac{C_3^*}{2}\Pi^{1/2})kS_{ij}, \qquad (2\text{-}21)$$

where C_1, C_1^*, C_2, C_3^*, C_5, α_1, β_1 and γ_1 are constant coefficients, and the expressions for $\tilde{P}$, b_{ij}, Π, P_{ij}, D_{ij} and S_{ij} are given in Appendix A. By rewriting the SSG model in this form, the LRR model is readily recovered by setting $C_1^* = C_2 = C_3^* = C_5 = 0$, and the meaning of each individual term in (2-21) can be easily identified. The first two terms on the right-hand side of (2-21) (C_1^* and C_2 terms) are the nonlinear return part, the third term (C_5 term) is to account for rotation effect, and the rest (α_1, β_1 and γ_1 terms) are similar to the rapid part in the LRR model. The SSG model gives better predictions than the LRR model does for flows with streamline curvature and rotation (Speziale et al. 1992). In view of the above discussion, the SSG model is selected as the base for the development of near-wall second-order closure models in this study.

In high-Reynolds-number turbulence, the dissipation rate tensor is assumed to be isotropic and the form proposed by Kolmogorov (1941) is often adopted, which is

13

$$\varepsilon_{ij} = \frac{2}{3}\varepsilon\delta_{ij} \quad ,$$

(2-22)

where the isotropic dissipation rate ε is obtained by solving the following modeled transport equation,

$$U_k\frac{\partial\varepsilon}{\partial x_k} = \frac{\partial}{\partial x_k}\left(\upsilon\frac{\partial\varepsilon}{\partial x_k}\right) + \frac{\partial}{\partial x_k}\left(C_\varepsilon\frac{k}{\varepsilon}\overline{u_i u_k}\frac{\partial\varepsilon}{\partial x_i}\right) + C_{\varepsilon1}f_1\frac{\varepsilon}{k}\tilde{P} - C_{\varepsilon2}f_2\frac{\varepsilon^2}{k} \quad ,$$

(2-23)

and C_ε, $C_{\varepsilon1}$ and $C_{\varepsilon2}$ are constant coefficients, f_1 and f_2 are the damping functions.

2.4 Near-Wall Reynolds-Stress Modeling Based on the SSG Model

The presence of a wall affects significantly the turbulence behaviors in many aspects. Near-wall turbulence modeling is to simulate the wall effects (including viscous and blocking effects) on turbulent flows. In this section, the high-Reynolds-number models discussed in the previous section are extended to the near-wall region by incorporating asymptotically correct near-wall terms to the model of the pressure-strain correlation, the dissipation rate transport equation and the model of the dissipation rate tensor. The derived near-wall modifications are ensured to vanish away from the wall through the use of damping functions. Two near-wall Reynolds-stress models will be presented in this section, one is wall-dependent (hereafter referred to as NWRS), the other is wall-independent (hereafter referred to as New NWRS or NNWRS). The wall-dependent model has been reported in So et al.(1994), in which the author is one of the co-authors.

Following Lai and So (1991), we expand the fluctuating velocity components, which satisfy the no-slip boundary conditions at the wall, into Taylor series in the near-wall region as

$$u = a_1y + a_2y^2 + a_3y^3 + \dots \quad ,$$

(2-24a)

$$v = b_1y + b_2y^2 + b_3y^3 + \dots \quad ,$$

(2-24b)

$$w = c_1y + c_2y^2 + c_3y^3 + \dots \quad ,$$

(2-24c)

where $u_i = (u,v,w)$, $x_i = (x,y,z)$, and the y-axis is taken to be normal to the wall, the x-axis is in the stream direction and the z-axis is normal to the (x, y)-plane. The coefficients a_i, b_i, c_i are random functions of time, x, and z, but not y. For incompressible flows, $b_1 = 0$ is required to

14

satisfy the continuity equation. The near-wall behavior of each term in the Reynolds stress equation (2-11) can therefore be analyzed by the substitution of (2-24), except the behavior of the velocity-pressure-gradient term, which can be obtained by rearranging (2-11) as $\Pi_{ij}^* = C_{ij} - D_{ij}^T - D_{ij}^V - P_{ij} - R_{ij} + \varepsilon_{ij}$. Table 2.1 shows the near-wall behavior of each term in (2-11). Note that the R_{ij} term has a varying near-wall behavior depending on the orientation of the rotating axis, but its lowest order is $O(y^2)$. Therefore, this term does not contribute to Π_{ij}^* in Table 2.1, which only shows terms to $O(y)$ explicitly.

From Table 2.1, one can see that ε_{ij}, D_{ij}^V and Π_{ij}^* are the leading order terms in the near-wall region and $\varepsilon_{ij} - \Pi_{ij}^*$ is in balance with D_{ij}^V up to $O(y)$. To extend the high-Reynolds-number models to the near-wall region, appropriate expressions for Π_{ij}^* and ε_{ij} are required so that they have the correct asymptotic behavior (Table 2.1) in the near-wall region. Furthermore, according to Launder and Reynolds (1983), in the vicinity of the wall, the behavior of $\varepsilon_{ij} / \overline{u_i u_j}$ has to satisfy the following kinematic relations

$$\varepsilon_{11} / \overline{u_1^2} = \varepsilon_{33} / \overline{u_3^2} = \varepsilon_{13} / \overline{u_1 u_3} = \varepsilon / k \quad , \tag{2-25a}$$

$$\varepsilon_{12} / \overline{u_1 u_2} = \varepsilon_{23} / \overline{u_2 u_3} = 2\varepsilon / k \quad , \tag{2-25b}$$

$$\varepsilon_{22} / \overline{u_2^2} = 4\varepsilon / k \quad . \tag{2-25c}$$

These kinematic constraints are highly anisotropic, and they further indicate the difficulty of near-wall Reynolds-stress modeling, particularly for the 22 component. Another constraint for ε_{ij} is that its high-Reynolds-number model plus whatever near-wall corrections proposed should contract to 2ε.

A similar analysis carried out for (2-12) reveals that to $O(y^0)$, D_ε^V, D_ε^P and γ are the leading-order terms near the wall. Traditionally, D_ε^P is neglected in the ad hoc modeling of the ε-equation. The argument is that its effect can be accounted for in the model proposed for $P_\varepsilon^1 + P_\varepsilon^2 + P_\varepsilon^4 - \gamma$ in (2-12), i.e. the terms $C_{\varepsilon 1} f_1 \tilde{P} \varepsilon / k - C_{\varepsilon 2} f_2 \varepsilon^2 / k$ in (2-23). This reasoning is acceptable for high-Reynolds-number flows; but it is too restrictive for near-wall turbulence. The negligence of D_ε^P is tantamount to the neglect of the pressure diffusion effect in the ε-equation,

15

which becomes very important in the near-wall region. Since the dissipation rate ε influences the Reynolds stress $\overline{u_i u_j}$ behavior in the computations through the interactions between ε_{ij} and $\overline{u_i u_j}$, the importance of having a consistent near-wall model for the ε-equation cannot be over emphasized. In view of this, near-wall modifications for the ε-equation are necessary if proper near-wall modeling of $\overline{u_i u_j}$ is to be accomplished.

Like other pressure-strain models invoking the high-Reynolds-number assumption, the SSG model is not asymptotically correct in the near-wall region. The $O(y^0)$ term in the SSG model comes from the return term (Table 2.2) and is one order of magnitude larger than the exact term, which should be $O(y^1)$ (Table 1.1). Therefore, near-wall corrections are needed for the SSG model in order to make it applicable in the near-wall region. So are the dissipation rate tensor ε_{ij} (2-22) and the dissipation rate equation developed for the high-Reynolds-number flows (2-23). In what follows, two near-wall Reynolds-stress models (NWRS and NNWRS) are presented in a parallel manner to highlight the difference between them.

2.4.1 NWRS Model   With the above guideline, the NWRS model based on the SSG model was first developed by So et al. (1994). The pressure-strain correlation in the NWRS model can be written as

$$
\Pi_{ij} = -(C_1 \varepsilon + C_1^* \tilde{P}) b_{ij} + C_2 \varepsilon (b_{ik} b_{kj} - \frac{1}{3}\Pi\delta_{ij}) + C_5 k (b_{jm} e_{ikm} + b_{im} e_{jkm})\Omega_k
$$
$$
- \alpha_1 (P_{ij} - \frac{2}{3}\tilde{P}\delta_{ij}) - \beta_1 (D_{ij} - \frac{2}{3}\tilde{P}\delta_{ij}) - 2(\gamma_1 + \frac{C_3^*}{2}\Pi^{1/2})k S_{ij} + f_{w,1}\Pi_{ij}^w + \Pi_{ij}^p. \quad (2-26)
$$

The last two terms are the near-wall corrections to the high-Reynolds-number SSG model (cf (2-26) to (2-21)). The Π_{ij}^w term,

$$
\Pi_{ij}^w = (C_1 \varepsilon + C_1^* \tilde{P}) b_{ij} - C_2 \varepsilon (b_{ik} b_{kj} - \frac{1}{3}\Pi\delta_{ij}) + \alpha^* (P_{ij} - \frac{2}{3}\tilde{P}\delta_{ij}) + 2\gamma^* k S_{ij} \quad , \quad (2-27)
$$

where α^* and γ^* are two new coefficients, is proposed to remove the $O(y^0)$ terms in the SSG model (the C_1 and C_2 terms in Table 2.2) and compensate for the insufficient anisotropy as a wall is approached. This term is multiplied by a damping function $f_{w,1}$ to ensure that the near-wall correction diminishes away from the wall. The Π_{ij}^p term, which is given by

16

$$\Pi_{ij}^{p} = -\frac{1}{3}\left[\frac{\partial}{\partial x_l}\left(\upsilon \frac{\partial \overline{u_i u_k}}{\partial x_l} \right) n_k n_j + \frac{\partial}{\partial x_l}\left(\upsilon \frac{\partial \overline{u_j u_k}}{\partial x_l} \right) n_k n_i \right] + \frac{1}{3}\frac{\partial}{\partial x_m}\left(\upsilon \frac{\partial \overline{u_k u_l}}{\partial x_m} \right) n_k n_l n_i n_j \quad , \qquad (2\text{-}28)$$

where $n_i = (0, 1, 0)$ is the wall unit vector, is included to improve the model predictions for the $\overline{vv}$, $\overline{uv}$ and $\overline{vw}$ Reynolds-stress components in the near-wall region. In the course of validating the NWRS model, two different expressions for the damping function $f_{w,1}$ are needed to predict correctly different types of flows with a wide range of Reynolds numbers. These expressions are

$$f_{w,1} = \exp\left[-\left(\frac{\text{Re}_t}{200} \right)^2 \right] \quad , \qquad (2\text{-}29a)$$

$$f_{w,1} = \exp\left[-\left(\frac{A\,\text{Re}_t}{60} \right)^3 \right] \quad , \qquad (2\text{-}29b)$$

where $\text{Re}_t = k^2 / (\upsilon \varepsilon)$ is the local turbulent Reynolds number and $A = 1 - (9/2)\left(b_{ij} b_{ij} - 2 b_{ij} b_{jk} b_{ki} \right)$ is the anisotropy invariant. The choice of either (2-29a) or (2-29b) for the damping function depends on the flow Reynolds number and the type of flows considered. For example, when the model is applied to channel flow with $\text{Re}_\tau = 395$, where $\text{Re}_\tau = u_\tau h / \upsilon$ is the Reynolds number based on the friction velocity u_τ and the channel half width h, (2-29a) gives better results. On the other hand, when Re_τ is reduced to 180, (2-29b) gives better predictions. Overall, (2-29a) is suitable for most of the flows considered, except two cases of very low-Reynolds-number channel and pipe flows. The values of two additional near-wall constants α^* and γ^* in (2-27) are specified to be $\alpha^* = -0.29$ and $\gamma^* = 0.065$ to give the best predictions (compared with the DNS data of Kim et al. 1987 and Kim 1991) of the near-wall turbulence behavior for fully-developed channel flow at $\text{Re}_\tau = 180$ and 395.

A similar approach is used to derive the near-wall correction function ζ for the ε-equation (2-23). The improved ε-equation becomes

$$U_k \frac{\partial \varepsilon}{\partial x_k} = \frac{\partial}{\partial x_k}\left(\upsilon \frac{\partial \varepsilon}{\partial x_k} \right) + \frac{\partial}{\partial x_k}\left[C_s \frac{k}{\varepsilon} \overline{u_k u_i} \frac{\partial \varepsilon}{\partial x_i} \right] + C_{\varepsilon 1} \frac{\varepsilon}{k} \tilde{P} - C_{\varepsilon 2} \frac{\varepsilon \tilde{\varepsilon}}{k} + \zeta \quad , \qquad (2\text{-}30)$$

with

$$\zeta = f_{w,2}\left(-L\frac{\varepsilon}{k}\tilde{P} + M\frac{\bar{\varepsilon}^2}{k} - N\frac{\varepsilon\tilde{\varepsilon}}{k}\right) \quad , \tag{2-30a}$$

$$\bar{\varepsilon} = \varepsilon - 2\upsilon k / y^2 \quad , \tag{2-30b}$$

$$\tilde{\varepsilon} = \varepsilon - 2\upsilon\left(\partial\sqrt{k} / \partial y\right)^2 \quad , \tag{2-30c}$$

where $f_{w,2} = \exp\left[-(\mathrm{Re}_t/40)^2\right]$ is a damping function proposed to influence the decay of ζ away from the wall, and L, M, and N are model constants. Subsequent computations show that $L = 2.25$, $M = 0.5$ and $N = 0.57$ should be used. The modified dissipation rates $\bar{\varepsilon}$ and $\tilde{\varepsilon}$ are introduced to ensure that the leading order terms in (2-30) have correct asymptotic behavior near a wall.

The simple relation between the dissipation rate tensor ε_{ij} and the dissipation rate ε for isotropic turbulence, (2-22), is no longer valid in the near-wall region. Further correction for (2-22) is required to account for turbulence anisotropy caused by the presence of the wall. Here, the relation given by Lai and So (1990), which satisfies the constraints (2-25) and contracts correctly to 2ε, is adopted:

$$\varepsilon_{ij} = \frac{2}{3}\varepsilon\delta_{ij}\left(1 - f_{w,1}\right) + f_{w,1}\frac{\varepsilon}{k}\frac{\overline{u_iu_j} + \overline{u_iu_k}n_kn_j + \overline{u_ju_k}n_kn_i + n_in_j\overline{u_ku_l}n_kn_l}{1 + 3\overline{u_ku_l}n_kn_l / 2k} \quad . \tag{2-31}$$

This relation consists of the isotropic part and the anisotropic correction part. The damping function $f_{w,1}$ is used to recover the Kolmogorov isotropic relation (2-22) at large Reynolds number. The near-wall asymptotic behavior of ε_{ij} given by (2-31) can be found in Table 2.3, which shows that (2-31) is only asymptotically correct to $O(y^0)$ in the near-wall region. But each component has the correct leading order asymptotic behavior.

2.4.2 NNWRS Model   In the NWRS model presented in the previous section, all the near-wall corrections invoke wall dependent variables, such as found in (2-28), (2-30) and (2-31). As a result, the model is rather difficult to implement and may give incorrect predictions for flows with complex geometry. In this section, we develop a new near-wall Reynolds-stress (NNWRS) model with no wall normal dependence.

18

The pressure-strain term in the NNWRS model is modeled similarly as that in the NWRS model:

$$\Pi_{ij} = -(C_1 \varepsilon + C_1^* \tilde{P}) b_{ij} + C_2 \varepsilon (b_{ik} b_{kj} - \frac{1}{3} \Pi \delta_{ij}) + C_5 k (b_{jm} e_{ikm} + b_{im} e_{jkm}) \Omega_k$$

$$- \alpha_1 (P_{ij} - \frac{2}{3} \tilde{P} \delta_{ij}) - \beta_1 (D_{ij} - \frac{2}{3} \tilde{P} \delta_{ij}) - 2(\gamma_1 + \frac{C_3^*}{2} \Pi^{1/2}) k S_{ij} + f_{w,1} \Pi_{ij}^w, \qquad (2\text{-}32a)$$

where Π_{ij}^w is again proposed to remove the incorrect lowest order $O(y^0)$ terms in the SSG model and compensate for the insufficient anisotropy in the near-wall region, which is given by

$$\Pi_{ij}^w = (C_1 \varepsilon + C_1^* \tilde{P}) b_{ij} - C_2 \varepsilon (b_{ik} b_{kj} - \frac{1}{3} \Pi \delta_{ij}) + \alpha^* (P_{ij} - \frac{2}{3} \tilde{P} \delta_{ij}) + 2\gamma^* k S_{ij} \quad, \qquad (2\text{-}32b)$$

and the damping function $f_{w,1}$ is used to make Π_{ij}^w diminish in the high-Reynolds-number flow region. The damping function is proposed to have the following form,

$$f_{w,1} = \exp\left[-(\text{Re}_t / 150)^2\right] \quad, \qquad (2\text{-}33)$$

by arguing that the near-wall modifications are due to the viscous effect and are needed when the local turbulence Reynolds number Re_t is less than 150. This damping function is used for all types of flows. The new constants in (2-32) are chosen to be $\alpha^* = -0.36$ and $\gamma^* = 0.072$ to give good agreements with DNS data of fully developed channel flows at $\text{Re}_\tau = 180$ and 395 (Kim et al. 1987; Kim 1991). Note that the wall-dependent near-wall correction term Π_{ij}^p (2-28) for the pressure-strain term in the NWRS model is not included in Π_{ij} in the NNWRS model (cf (2-32) with (2-26)).

In the NWRS model, the modified dissipation rate $\bar{\varepsilon}$ and $\tilde{\varepsilon}$ in the ε-equation depend on local normal wall distance y (2-30). To remove the wall dependence in the ε-equation requires a complete re-examination of the derivation of the equation. Most recently, a new dissipation rate equation without wall dependence has been proposed by So et al. (1997) for two-equation model to account for wall effects. We re-examined the derivation of this equation thoroughly and decided to adopt it with an additional anisotropic coefficient in the turbulent diffusion term as the ε-equation in the NNWRS model. The final form for the ε-equation in the NNWRS model is

$$U_k \frac{\partial \varepsilon}{\partial x_k} = \frac{\partial}{\partial x_k}\left(v\frac{\partial \varepsilon}{\partial x_k}\right) + \frac{\partial}{\partial x_k}(C_\varepsilon \frac{k}{\varepsilon}\overline{u_i u_k}\frac{\partial \varepsilon}{\partial x_i}) + C_{\varepsilon 1}\frac{\varepsilon}{k}\tilde{P} - C_{\varepsilon 2}f_\varepsilon \frac{\varepsilon^2}{k}$$

$$+ C_{\varepsilon 3}v\frac{\varepsilon}{k}\left(\frac{\partial\sqrt{k}}{\partial x_k}\right)^2 , \tag{2-34}$$

where $f_\varepsilon = 1 - 0.22\exp\left[-(\mathrm{Re}_t/6)^2\right]$ and $f_{w,2} = \exp\left[-(\mathrm{Re}_t/40)^2\right]$ are the damping functions, and $C_\varepsilon = 0.12$, $C_{\varepsilon 1} = 1.5$, $C_{\varepsilon 2} = 1.9$ and $C_{\varepsilon 3} = 2.95$ are model coefficients.

Finally, the relation for the dissipation rate tensor given by Shima (1995) is adopted in the NNWRS model, which is

$$\varepsilon_{ij} = \frac{2}{3}\delta_{ij}\varepsilon(1 - f_{w,1}) + f_{w,1}\varepsilon_{ij}^w + \varepsilon_{ij}^* , \tag{2-35a}$$

where

$$\varepsilon_{ij}^w = \frac{\varepsilon}{k}\overline{u_i u_j} , \tag{2-35b}$$

$$\varepsilon_{ij}^* = \frac{1}{2}\left[\frac{\partial}{\partial x_k}(v\frac{\partial\overline{u_i u_j}}{\partial x_k}) - \frac{\overline{u_i u_j}}{k}\frac{\partial}{\partial x_k}(v\frac{\partial k}{\partial x_k})\right] . \tag{2-35c}$$

The first term in (2-35a) is the isotropic part which recovers (2-22) when Reynolds number is large, the second term is the anisotropic correction in the near-wall region, and the last term is an additional near-wall correction which redistributes the dissipation rate among different Reynolds stress components. It can be shown that ε_{ij} given by (2-35) contracts to 2ε and satisfies kinematic constraints (2-25) except the 22 component. The near-wall behavior of this dissipation rate tensor has been analyzed by applying (2-24) and is summarized in Table 2.3 in comparison with the corresponding components in the NWRS model (2-31). Table 2.3 shows that the asymptotic behavior of the dissipation rate tensor given by (2-35) matches the exact asymptotic behavior up to $O(y^1)$, whereas the one given by (2-31) in the NWRS model only up to $O(y^0)$. The near-wall variations of different dissipation rate components given by (2-31) and (2-35) are compared with the DNS data (Kim et al. 1987), and the results are shown in Figs. 2.1a - 2.1d. In these figures, $\varepsilon_{ij}^+ = v\varepsilon_{ij}/u_\tau^4$ are the non-dimensional dissipation rate components, and $y^+ = yu_\tau/v$ is the non-

dimensional wall distance, where u_τ is the friction velocity . These figures show that for the normal stresses, $\overline{uu}$, $\overline{vv}$, $\overline{ww}$, the dissipation rate tensor relation in the NNWRS model gives better agreement with the DNS data than that in the NWRS model, but for the shear stress $\overline{uv}$, both relations give about the same results.

An alternative proposal has been put forward by Cho et al. (1995), where the dissipation rate tensor was assumed to be given by

$$\varepsilon_{ij} = \frac{2}{3}\delta_{ij}\varepsilon(1 - f_{w,1}) + f_{w,1}\varepsilon_{ij}^{w} \quad , \tag{2-36a}$$

with

$$\varepsilon_{ij}^{w} = \left[\frac{\overline{u_i u_j}}{k}\varepsilon + \frac{\overline{u_m u_n}}{k}\tilde{\varepsilon}_{nm}\delta_{ij} + \frac{\overline{u_m u_i}}{k}\tilde{\varepsilon}_{jm} + \frac{\overline{u_m u_j}}{k}\tilde{\varepsilon}_{im} \right] / \left[1 + \frac{5}{2}\frac{\tilde{\varepsilon}_{pq}}{\varepsilon}\frac{\overline{u_p u_q}}{k} \right] \quad , \tag{2-36b}$$

$$\tilde{\varepsilon}_{mn} = 2\nu\frac{\partial\sqrt{k}}{\partial x_m}\frac{\partial\sqrt{k}}{\partial x_n} \quad . \tag{2-36c}$$

The asymptotic behavior of each component of this dissipation rate tensor and the corresponding overall behavior of the Reynolds-stress equations is given in Table 2.3 and 2.4 together with the NWRS and NNWRS models, respectively. According to these tables, this model (2-36) is only better than the NNWRS model in the 22 component. If (2-36) is used to replaced (2-35) in the NNWRS model, the resultant calculations yield better predictions in the near-wall region for the two channel flows considered. However, the results are not as good as those given by the NWRS model (Figs. 2.1 and 2.2). The improvement shows the importance of the 22 component in wall-bounded flows, thus the better performance of the NWRS model over the NNWRS model. Essentially, there is no difference in the overall predictions of the channel flows (Figs 2.2a - 2.2d) when (2-35) and (2-36) are used. Therefore, the dissipation rate tensor (2-35) is adopted in the NNWRS model.

2.5 Concluding Remarks

In this section, we have presented two near-wall Reynolds-stress models, NWRS model and NNWRS model. The first one involves wall-dependent variables and the second one does not.

These near-wall models are developed from the high-Reynolds-number model by incorporating the near-wall modifications into the expression for the pressure-strain correlation, into the relation for the dissipation rate tensor in the Reynolds-stress equations, and into the modeled dissipation rate equation. Damping functions are used to ensure that the near-wall modifications will not affect the flow field in the region far away from the wall. The overall behavior of the Reynolds-stress equation in the near-wall region is determined by $\varepsilon_{ij} - \Pi_{ij}^*$ and is presented in Table 2.4 for both NNWRS and NWRS models. It shows that the modeled Reynolds-stress equations in both models match the exact equation to $O(y^0)$. For those Reynolds-stress components (the 11, 33 and 13) that are not correlated with the wall normal direction, they are better predicted by the NNWRS model than by the NWRS model. In contrast, the NWRS model, with additional near-wall correction term Π_{ij}^p (see (2-28)), gives better prediction for those components (22, 12 and 23) correlated with the wall normal direction. With no wall dependent variable in the model and only one expression for the damping function used in the pressure-strain formula, the NNWRS model is more general and flexible for flows with complex geometry than the NWRS model. The complete set of modeled equations and constants used in both models are given in Appendix B. The validations of the new developed near-wall Reynolds-stress model for different flow conditions will be presented in the following sections.

Table 2.1 Near-wall asymptotic behavior of each term in Reynolds stress transport equation.

ij	C_{ij}	D_{ij}^T	D_{ij}^ν	P_{ij}	ε_{ij}	Π_{ij}^*
11	$O(y^3)$	$O(y^3)$	$2\nu\overline{a_1^2} + 12\nu\overline{a_1 a_2}y$ $+ O(y^2)$	$O(y^3)$	$2\nu\overline{a_1^2} + 8\nu\overline{a_1 a_2}y$ $+ O(y^2)$	$-4\nu\overline{a_1 a_2}y$ $+O(y^2)$
22	$O(y^5)$	$O(y^5)$	$12\nu\overline{b_2^2}y^2$ $+O(y^3)$	$O(y^5)$	$8\nu\overline{b_2^2}y^2$ $+O(y^3)$	$-4\nu\overline{b_2^2}y^2$ $+O(y^3)$
33	$O(y^3)$	$O(y^3)$	$2\nu\overline{c_1^2} + 12\nu\overline{c_1 c_2}y$ $+ O(y^2)$	$O(y^3)$	$2\nu\overline{c_1^2} + 8\nu\overline{c_1 c_2}y$ $+ O(y^2)$	$-4\nu\overline{c_1 c_2}y$ $+O(y^2)$
12	$O(y^4)$	$O(y^4)$	$6\nu\overline{a_1 b_2}y$ $+O(y^2)$	$O(y^4)$	$4\nu\overline{a_1 b_2}y$ $+O(y^2)$	$-2\nu\overline{a_1 b_2}y$ $+O(y^2)$
23	$O(y^4)$	$O(y^4)$	$6\nu\overline{b_2 c_1}y$ $+O(y^2)$	$O(y^4)$	$4\nu\overline{b_2 c_1}y$ $+O(y^2)$	$-2\nu\overline{b_2 c_1}y$ $+O(y^2)$
13	$O(y^3)$	$O(y^3)$	$6\nu(\overline{a_1 c_2} + \overline{a_2 c_1})y$ $+ O(y^2)$	$O(y^3)$	$2\nu\overline{a_1 c_1}$ $+4\nu(\overline{a_1 c_2} + \overline{a_2 c_1})y$ $+ O(y^2)$	$-2\nu(\overline{a_1 c_2} + \overline{a_2 c_1})y$ $+ O(y^2)$

Table 2.2   Near-wall asymptotic behavior of each term in the SSG model for pressure-strain correlation Π_{ij}.

ij	C_1 term	C_2 term	α term	β term	γ term	C_3 term
11	$-\dfrac{1}{3}\nu C_1(2\overline{a_1^2}-\overline{c_1^2})$ $+O(y)$	$\nu C_2\dfrac{2\left(\overline{a_1^2}\right)^2+3\left(\overline{a_1c_1}\right)^2-2\overline{a_1^2}\,\overline{c_1^2}-\left(\overline{c_1^2}\right)^2}{9\left(\overline{a_1^2}+\overline{c_1^2}\right)}$ $+O(y)$	$O(y^3)$	$O(y^3)$	$O(y^3)$	$O(y^2)$
22	$\dfrac{1}{3}\nu C_1(\overline{a_1^2}+\overline{c_1^2})$ $+O(y)$	$-\nu C_2\dfrac{\left(\overline{a_1^2}\right)^2+6\left(\overline{a_1c_1}\right)^2-4\overline{a_1^2}\,\overline{c_1^2}+\left(\overline{c_1^2}\right)^2}{9\left(\overline{a_1^2}+\overline{c_1^2}\right)}$ $+O(y)$	$O(y^5)$	$O(y^5)$	$O(y^2)$	$O(y^3)$
33	$-\dfrac{1}{3}\nu C_1(2\overline{c_1^2}-\overline{a_1^2})$ $+O(y)$	$-\nu C_2\dfrac{\left(\overline{a_1^2}\right)^2-3\left(\overline{a_1c_1}\right)^2+2\overline{a_1^2}\,\overline{c_1^2}-2\left(\overline{c_1^2}\right)^2}{9\left(\overline{a_1^2}+\overline{c_1^2}\right)}$ $+O(y)$	$O(y^3)$	$O(y^3)$	$O(y^3)$	$O(y^2)$
12	$O(y)$	$O(y)$	$O(y^4)$	$O(y^4)$	$O(y^2)$	$O(y^2)$
23	$O(y)$	$O(y)$	$O(y^4)$	$O(y^4)$	$O(y^3)$	$O(y^2)$
13	$-\nu C_1\overline{a_1c_1}$ $+O(y)$	$\nu C_2\dfrac{1}{3}\overline{a_1c_1}$ $+O(y)$	$O(y^3)$	$O(y^3)$	$O(y^2)$	$O(y^2)$

Table 2.3 Near-wall asymptotic behavior of each component in the dissipation rate tensor ε_{ij}.

ij	ε_{ij} (exact)	NWRS	NNWRS	Cho et al. (1995)
11	$2v\overline{a_1^2} + 8v\overline{a_1 a_2}\,y$ $+ O(y^2)$	$2v\overline{a_1^2} + 4v\overline{a_1 a_2}\,y$ $+ O(y^2)$	$2v\overline{a_1^2} + 8v\overline{a_1 a_2}\,y$ $+ O(y^2)$	$2v\overline{a_1^2} + 4v\overline{a_1 a_2}\,y$ $+ O(y^2)$
22	$8v\overline{b_2^2}\,y^2$ $+O(y^3)$	$8v\overline{b_2^2}\,y^2$ $+O(y^3)$	$7v\overline{b_2^2}\,y^2$ $+O(y^3)$	$8v\overline{b_2^2}\,y^2$ $+O(y^3)$
33	$2v\overline{c_1^2} + 8v\overline{c_1 c_2}\,y$ $+ O(y^2)$	$2v\overline{c_1^2} + 4v\overline{c_1 c_2}\,y$ $+ O(y^2)$	$2v\overline{c_1^2} + 8v\overline{c_1 c_2}\,y$ $+ O(y^2)$	$2v\overline{c_1^2} + 4v\overline{c_1 c_2}\,y$ $+ O(y^2)$
12	$4v\overline{a_1 b_2}\,y$ $+O(y^2)$	$4v\overline{a_1 b_2}\,y$ $+O(y^2)$	$4v\overline{a_1 b_2}\,y$ $+O(y^2)$	$2v\overline{a_1 b_2}\,y$ $+O(y^2)$
23	$4v\overline{b_2 c_1}\,y$ $+O(y^2)$	$4v\overline{b_2 c_1}\,y$ $+O(y^2)$	$4v\overline{b_2 c_1}\,y$ $+O(y^2)$	$2v\overline{b_2 c_1}\,y$ $+O(y^2)$
13	$2v\overline{a_1 c_1}$ $+4v(\overline{a_1 c_2} + \overline{a_2 c_1})y$ $+ O(y^2)$	$2v\overline{a_1 c_1}$ $+2v(\overline{a_1 c_2} + \overline{a_2 c_1})y$ $+ O(y^2)$	$2v\overline{a_1 c_1}$ $+4v(\overline{a_1 c_2} + \overline{a_2 c_1})y$ $+ O(y^2)$	$2v\overline{a_1 c_1}$ $+2v(\overline{a_1 c_2} + \overline{a_2 c_1})y$ $+ O(y^2)$

Table 2.4 Near-wall asymptotic behavior of ε_{ij}-Π_{ij}^* (representing the overall behavior of the Reynolds-stress equation in the near-wall region).

ij	$\varepsilon_{ij} - \Pi_{ij}^*$ (exact)	NWRS	NNWRS	Cho et al. (1995)
11	$2v\overline{a_1^2} + 12v\overline{a_1 a_2}y$ $+ O(y^2)$	$2v\overline{a_1^2} + 4v\overline{a_1 a_2}y$ $+ O(y^2)$	$2v\overline{a_1^2} + 8v\overline{a_1 a_2}y$ $+ O(y^2)$	$2v\overline{a_1^2} + 4v\overline{a_1 a_2}y$ $+ O(y^2)$
22	$12v\overline{b_2^2}y^2$ $+O(y^3)$	$12v\overline{b_2^2}y^2$ $+O(y^3)$	$7v\overline{b_2^2}y^2$ $+O(y^3)$	$8v\overline{b_2^2}y^2$ $+O(y^3)$
33	$2v\overline{c_1^2} + 12v\overline{c_1 c_2}y$ $+ O(y^2)$	$2v\overline{c_1^2} + 4v\overline{c_1 c_2}y$ $+ O(y^2)$	$2v\overline{c_1^2} + 8v\overline{c_1 c_2}y$ $+ O(y^2)$	$2v\overline{c_1^2} + 4v\overline{c_1 c_2}y$ $+ O(y^2)$
12	$6v\overline{a_1 b_2}y$ $+O(y^2)$	$6v\overline{a_1 b_2}y$ $+O(y^2)$	$4v\overline{a_1 b_2}y$ $+O(y^2)$	$2v\overline{a_1 b_2}y$ $+O(y^2)$
23	$6v\overline{b_2 c_1}y$ $+O(y^2)$	$6v\overline{b_2 c_1}y$ $+O(y^2)$	$4v\overline{b_2 c_1}y$ $+O(y^2)$	$2v\overline{b_2 c_1}y$ $+O(y^2)$
13	$2v\overline{a_1 c_1}$ $+6v(\overline{a_1 c_2} + \overline{a_2 c_1})y$ $+ O(y^2)$	$2v\overline{a_1 c_1}$ $+2v(\overline{a_1 c_2} + \overline{a_2 c_1})y$ $+ O(y^2)$	$2v\overline{a_1 c_1}$ $+4v(\overline{a_1 c_2} + \overline{a_2 c_1})y$ $+ O(y^2)$	$2v\overline{a_1 c_1}$ $+2v(\overline{a_1 c_2} + \overline{a_2 c_1})y$ $+ O(y^2)$

(a)

(b)

27
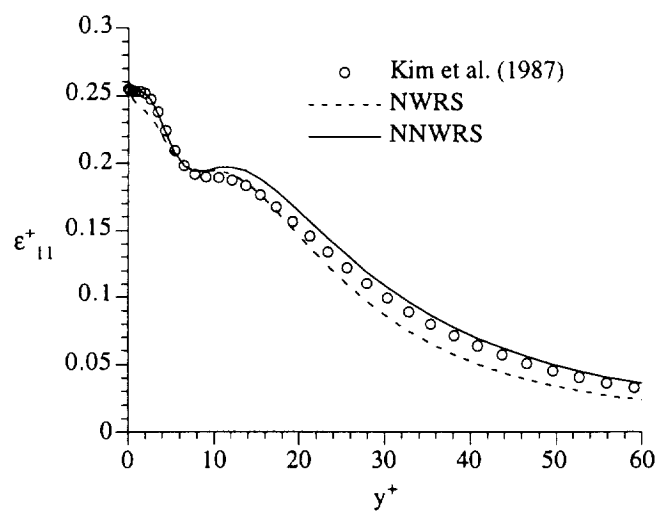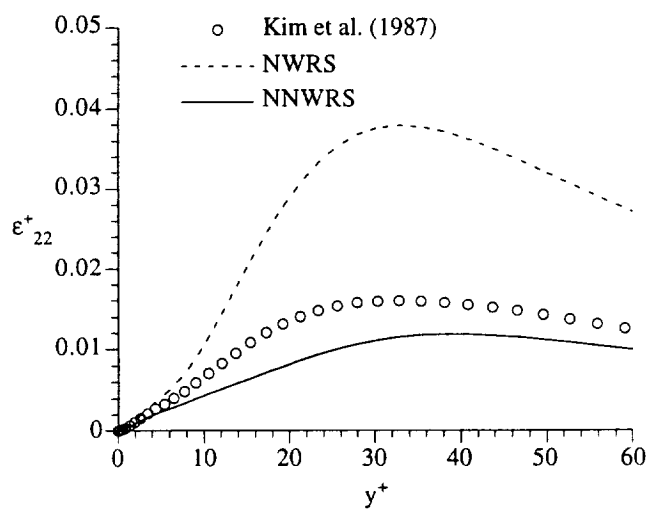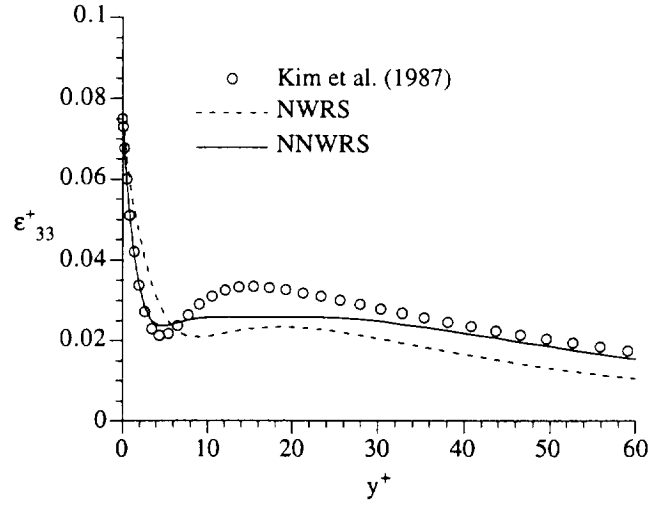
(c)
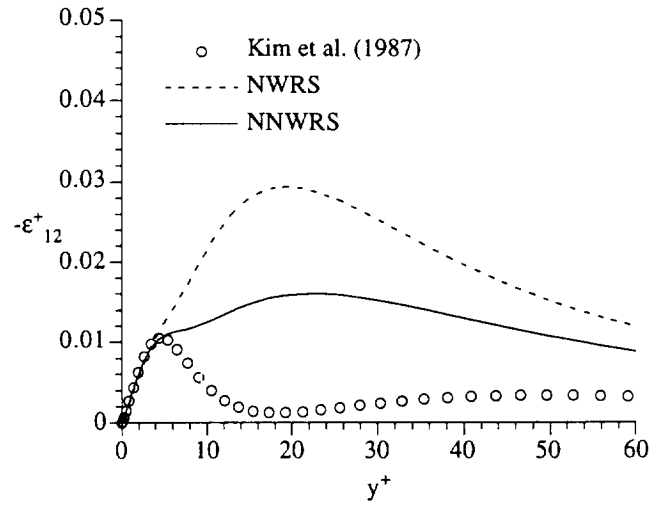
(d)

Fig. 2.1 Near-wall behavior of dissipation rate tensor ε_{ij}^+ compiled from DNS data for fully developed channel flow at $\text{Re}_\tau = 180$: (a) ε_{11}^+, (b) ε_{22}^+ (c) ε_{33}^+, and (d) ε_{12}^+.

28

(a)

(b)

(c)

(d)

30

$$Re_\tau = 180$$
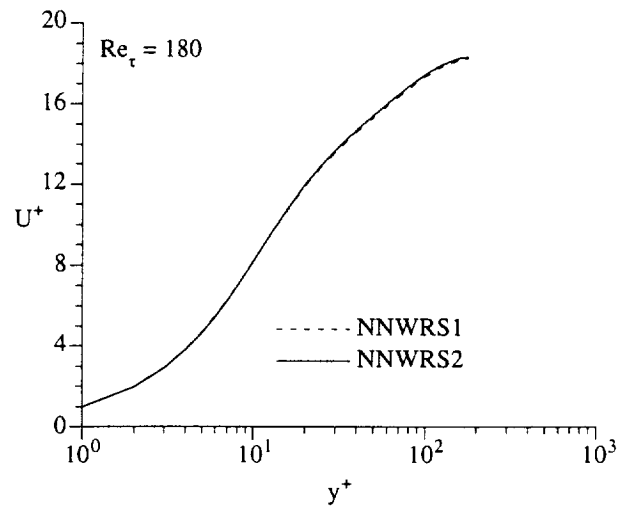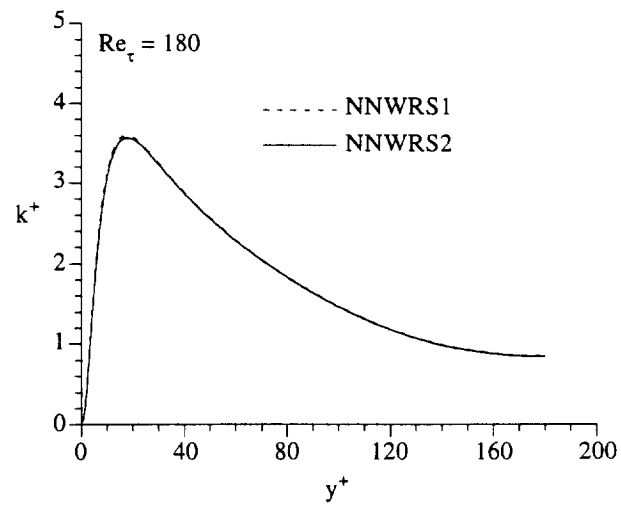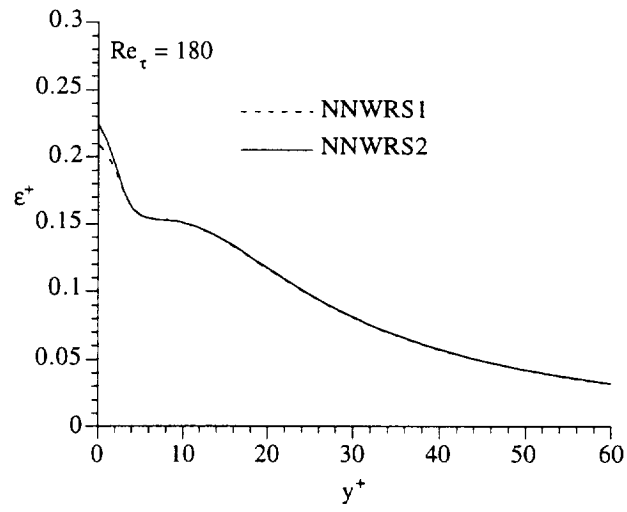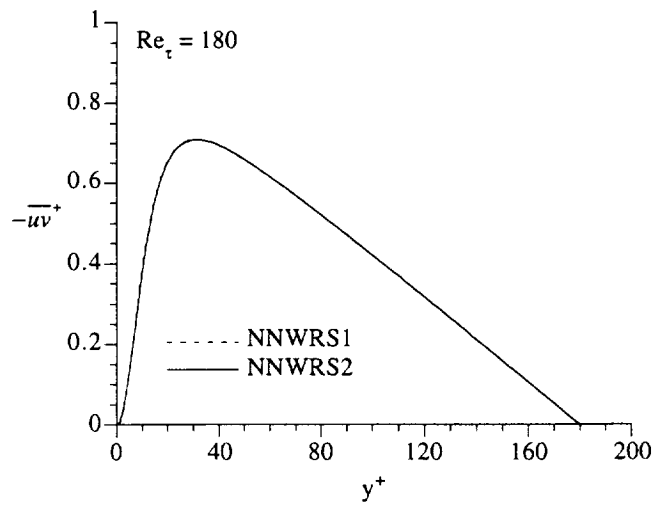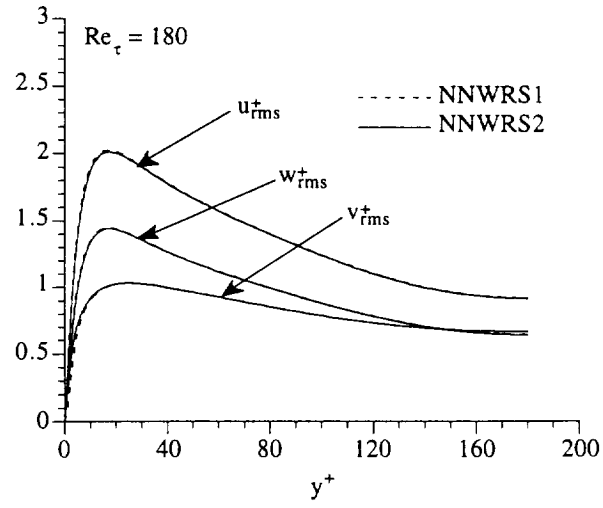
(e)

Fig. 2.2 Comparison of present (NNWRS2) model with its modified version (NNWRS1) using dissipation rate tensor given by Cho et al. (1995): (a) U^+, (b) k^+, (c) ε^+, (d) $\overline{uv}^+$, and (e) u^+_{rms}, v^+_{rms}, and w^+_{rms}.

3   Validation Against Simple Wall-Bounded Turbulent Flows

3.1 Introduction

In this section, the newly developed near-wall Reynolds stress (NNWRS) model is verified by comparing the model predictions with the DNS results and laboratory measurements for fully developed channel flow, pipe flow, and plane Couette flow, and for zero pressure gradient boundary layer flow over a flat plate. Further verification of the model predictions for complex turbulent flows are carried out in the following sections. For comparison, the corresponding predictions from the NWRS model are also presented in this section. The DNS experiments at low Reynolds numbers provide valuable data to validate turbulence models, especially in the near-wall region where measurement inaccuracy often arises. The simple flows considered in this section can be classified as internal and external flows. Channel flow, pipe flow and Couette flow are internal flows, whereas flat plate boundary-layer flow is an external flow.

In a fully developed channel flow, the mean velocity is governed by

$$\frac{1}{\rho}\frac{dP}{dx} = \frac{\partial}{\partial y}\left(\upsilon \frac{\partial U}{\partial y} - \overline{uv} \right) \quad , \tag{3-1}$$

which shows that the constant pressure gradient balances the gradient of the total shear stress (including the viscous and turbulent stress), and acts as the driving force of the flow. The mean flow equation governing fully developed pipe flow is the same as (3-1) but written in cylindrical coordinate. The momentum equation for a fully developed Couette flow is governed by

$$0 = \frac{\partial}{\partial y}\left(\upsilon \frac{\partial U}{\partial y} - \overline{uv} \right) \quad , \tag{3-2}$$

where the pressure gradient is zero, and the flow is driven by the moving wall. Consequently, the total shear stress in a Couette flow is constant in the entire flow domain. The pressure gradient in a boundary-layer flow over a flat plate is also zero, and equation (3-2) applies to the near-wall region. Away from the wall, the inertial force becomes important, and the momentum equation has the form

$$U\frac{\partial U}{\partial x} + V\frac{\partial U}{\partial y} = \frac{\partial}{\partial y}\left(\upsilon\frac{\partial U}{\partial y} - \overline{uv}\right) \quad . \tag{3-3}$$

In wall-bounded flows, two regions can be identified; the inner layer and the outer layer (or the defect layer). The overlap of these two layers gives arise to the logarithmic layer where the log law of the wall applies (Fig. 3.1). Thus, the mean velocity in the log layer can be expressed as

$$U^+ = K^{-1}\ln y^+ + B \quad , \tag{3-4}$$

where $U^+ = U/u_\tau$, $y^+ = yu_\tau/\upsilon$ are the non-dimensional mean velocity and wall normal distance, respectively; K is the von Karman constant, and B is another constant, with $K \sim 0.4$ and $5 \le B \le 5.5$ depending on the type of flows. It is essential for a turbulence model to predict correctly the log-law region for both internal and external wall-bounded flows. Very close to the wall ($y^+ \le 5$) is the viscous sublayer, where viscosity dominates and velocity varies linearly with the wall normal distance. In the outer layer (or defect layer), far away from the wall, the flow field is entirely turbulent, and fully developed channel, pipe and Couette flows show little wake characteristic compared with boundary layer flow with zero pressure gradient.

In addition to the comparisons of the predicted mean and turbulent flow fields with existing data, the NNWRS model is also tested by examining its ability to reproduce Reynolds number effects on simple flows. Both the mean and the turbulent flow fields are influenced by the flow Reynolds number. So et al. (1996) demonstrated that the NWRS model is capable of assessing Reynolds number effects on internal and external flows. Following So et al. (1996), we shall also examine the ability of the NNWRS model to replicate Reynolds number effects in simple flows. The Reynolds number range considered varies from $\mathrm{Re}_\tau = 180$ to $\mathrm{Re}_\tau = 8758$ for fully-developed channel/pipe flows and from $\mathrm{Re}_\theta = 1410$ to $\mathrm{Re}_\theta = 2420$ for flat plate boundary layers, where $\mathrm{Re}_\tau = u_\tau h/\upsilon$, $\mathrm{Re}_\theta = U_\infty\theta/\upsilon$, h is the half-width of the channel or pipe radius, θ is the momentum thickness and U_∞ is the freestream mean velocity.

33

3.2 Fully-Developed Channel/Pipe and Couette Flows

For fully developed channel/pipe and Couette flows, the modeled equations in NNWRS and NWRS models reduce to ordinary differential equations (see appendix C.1-C.3). Therefore, they are relatively easy to solve. Here an iterative scheme is used to solve the governing equations with the following convergence condition,

$$\left| \frac{\Phi_j^{n+1} - \Phi_j^n}{\Phi_j^n} \right| \le 10^{-5} \quad , \tag{3-6}$$

where Φ_j^n denotes a dependent variable at the jth grid point in the nth iteration. Only the lower half flow domain is considered in fully developed channel/pipe flows because the flow fields are symmetric about the centerline. The grid points are clustered close to the wall and stretched out away from the wall. For Couette flow, the entire flow domain is computed with specified mean velocity at the moving wall. The grid points are distributed symmetrically about the centerline with more points near the walls. The number of grid points used in channel/pine flow computations varies from 180 to 250 depending on the flow Reynolds number, and about twice the number of grid points are used in Couette flow computations. The first grid point away from the wall is located at $y^+ = y u_\tau / \upsilon = 1$, where y is the wall distance.

The no-slip boundary conditions are used to specify the mean velocity and turbulent stresses at a moving ($U_m > 0$) or stationary ($U_m = 0$) wall,

$$U = U_m, \ \overline{uu} = \overline{vv} = \overline{ww} = \overline{uv} = 0 \quad , \tag{3-7a}$$

and the following expression,

$$\varepsilon_w = 2\upsilon \left(\partial \sqrt{k} / \partial y \right)_w^2 \quad , \tag{3-7b}$$

is used to specify the dissipation rate ε at the wall. In fully developed channel/pipe flows, the boundary conditions at the centerline can be given as

$$\frac{\partial U}{\partial y} = \frac{\partial \overline{u^2}}{\partial y} = \frac{\partial \overline{v^2}}{\partial y} = \frac{\partial \overline{w^2}}{\partial y} = \frac{\partial \varepsilon}{\partial y} = \overline{uv} = 0 \quad , \tag{3-7c}$$

34

due to the symmetry of the flow field (in case of pipe flow, cylindrical polar coordinates are used and (3-7c) with $y^+ = \mathrm{Re}_\tau - r^+$, where r^+ is the radial coordinate, gives the corresponding boundary conditions at the centerline of the pipe ($r^+ = 0$).

3.2.1 Fully-developed channel flows   For fully developed channel flow, two DNS cases studied by Kim et al. (1987) at $\mathrm{Re}_\tau = 180$ and Kim (1991) at $\mathrm{Re}_\tau = 395$ are used to test the models. Two damping functions, (2-29a) for $\mathrm{Re}_\tau = 395$ and (2-29b) for $\mathrm{Re}_\tau = 180$, are required for the NWRS model to give a reasonable agreement with the DNS results. On the other hand, only one damping function, (2-33), is used in the NNWRS model for both $\mathrm{Re}_\tau = 180$ and 395.

The model predictions of the mean velocity profiles over the half channel width at $\mathrm{Re}_\tau = 180$ and 395 are plotted in Figs. 3.2a - 3.2b. Both the NNWRS and NWRS model results agree very well with the DNS results (Kim et al. 1987; Kim 1991). Near the centerline, the velocity profiles predicted by the NNWRS model slightly deviate from those given by the DNS data. In the log layer, the von Karman constant (3-4) is determined with the procedure outlined by So et al. (1994). The NNWRS (NWRS) model gives $K = 0.38$ ($K = 0.40$) at $\mathrm{Re}_\tau = 180$ and $K = 0.40$ ($K = 0.39$) at $\mathrm{Re}_\tau = 395$. Compared to $K = 0.40$ given by the DNS for both cases, the NNWRS slightly underpredicts the K value at $\mathrm{Re}_\tau = 180$, but gives same K value at $\mathrm{Re}_\tau = 395$. In contrast, the NWRS model underpredicts the K value at $\mathrm{Re}_\tau = 395$, but replicates the same DNS result at $\mathrm{Re}_\tau = 180$. Overall, the mean velocity profiles in fully developed channel flow given by both models, including the log-law behavior, are in good agreement with the DNS results.

The comparisons between the model predictions for turbulence quantities in fully developed channel flow at $\mathrm{Re}_\tau = 180$ and $\mathrm{Re}_\tau = 395$ and the DNS results are presented in Figs. 3.3 - 3.6. Figs. 3.3a-3.3b show the turbulent kinetic energy profiles over the entire computational domain, i.e., half the channel width. The agreement between the NWRS model predictions and the DNS results is very good for both Reynolds numbers. The agreement between the NNWRS model results and the DNS results is reasonable, although the peak values of k^+ are underpredicted by the NNWRS model in both cases. Away from the wall, the NNWRS model gives slightly higher turbulent kinetic energy k^+ at $\mathrm{Re}_\tau = 180$, but slightly lower k^+ at $\mathrm{Re}_\tau = 395$. Figs. 3.4a-3.4b

plot the dissipation rate profiles for $\mathrm{Re}_\tau = 180$ and $\mathrm{Re}_\tau = 395$ in the near-wall region, respectively. Both models essentially capture the variations of the dissipation rate predicted by DNS, e.g., a maximum value at the wall, a small plateau in a region close to the wall, and gradual attenuation away from the wall. The NNWRS and NWRS models overpredict the dissipation rate in the near-wall region, but agree well with the DNS away from the near-wall region. Figs. 3.5a-3.5b show the comparison of the predicted turbulent shear stress profiles with the DNS data. The shear stress $\overline{uv}^+$ appears in the equation for mean flow (3-1), and therefore it is crucial for the correct prediction of the mean velocity. These figures show that the agreement between model predictions of the turbulent shear stress and the DNS results is excellent in both cases. Finally, Figs. 3.6a-3.6b plot the root-mean-square of the turbulent fluctuations (square root of the turbulent normal stresses) in the streamwise, wall normal and transverse directions, u_{rms}^+, v_{rms}^+, w_{rms}^+, respectively. Compared to the DNS results, in the near-wall region, both models underpredict u_{rms}^+, but overpredict v_{rms}^+ and w_{rms}^+. The NWRS model predictions of the turbulent fluctuations are in better agreement with the DNS data than those from the NNWRS model. Consequently, the NWRS model predicts more accurately the anisotropy of the near-wall turbulence than the NNWRS model. Away from the wall, turbulence becomes more isotropic, and both models give almost the same results.

According to asymptotic expansions (2-24), we have $k^+ / \varepsilon^+ = 0.5y^{+2} + O(y^{+3})$ in the near-wall region. To further examine the performance of the models in the near-wall region, we plot model predictions of k^+ / ε^+ versus y^{+2} in Fig. 3.7 to see if $k^+ / (\varepsilon^+ y^{+2}) = 1/2$ is true in the near-wall region. Fig. 3.7 shows that $k^+ / (\varepsilon^+ y^{+2}) = 1/2$ is indeed true in the near-wall region for both models.

3.2.2 Fully-developed pipe flows

Fully developed pipe flow also has a constant pressure gradient in the streamwise direction. It is marginally more complicated than fully developed channel flow because of the cylindrical geometry. Four experimental data sets with a large range of Reynolds number are selected to test the models: they are the measurements of Durst et al. (1993) with $\mathrm{Re}_\tau = 250$, Schildknecht et al. (1979) with $\mathrm{Re}_\tau = 489$, and Laufer (1954) with

$\mathrm{Re}_\tau = 1052$ and 8758. In terms of bulk Reynolds number $\mathrm{Re} = U_m D / v$, it ranges from 7,500 to 500,000 in these four cases. Thus, the Reynolds number considered is quite high compared to many test cases investigated by other researchers. The number of grid points required for grid independent results are found be 108. In the NWRS model, damping function (2-29b) is used for the lowest Reynolds number case $\mathrm{Re}_\tau = 250$, and (2-29a) is used for the other three high Reynolds number cases.

Figs. 3.8a - 3.8d show the comparison between the predicted and measured mean velocity profiles for the four cases considered. The NNWRS model gives an excellent prediction of U^+ in the near-wall region for all cases and in the entire flow region for $\mathrm{Re}_\tau = 250$ case, but it slightly underpredicts the velocity in the region close to the centerline as the Reynolds number increases. Even with the use of damping function (2-29b) for the low Reynolds number flow, the NWRS model still underpredicts the mean velocity in the log-law region for the $\mathrm{Re}_\tau = 250$ case. For the other three higher Reynolds number cases, the NWRS model also underpredicts the mean velocities in the region close the centerline, although its predictions are slightly better than those obtained from the NNWRS model. The predicted and measured von Karman constants for these four cases are presented in Table 3.1. Overall, both models reproduce well the mean velocity profiles including the log-law behavior in fully developed pipe flow.

Figs. 3.9 - 3.12 compare the predicted turbulence quantities with available experimental data. In each figure, four panels are presented for the four different Reynolds number cases. In Figs. 3.9a - 3.9d, the peak value of the turbulent kinetic energy k^+ is underestimated by the NNWRS model except for the $\mathrm{Re}_\tau = 250$ case, whereas it is well predicted by the NWRS model in all cases. Away from the wall, both models give almost the same results, which agree with the measurements reasonably well. Both models give almost the same predictions of the dissipation rate (see Figs. 3.10a - 3.10d), except in the near-wall region where the dissipation rate predicted by the NWRS model has a more noticeable plateau. The predicted dissipation rate has a maximum value at the wall (Figs. 3.10a - 3.10d), which disagrees with the experimental data in the near-wall region (Figs. 3.10b - 3.10c). Away from the wall, the agreement between the model predictions

and measurements is very good. Figs. 3.11a - 3.11d show the excellent agreement between the model predictions of the turbulent shear stress and the measurements whenever the measured data are available. As in channel flow, model predictions underestimate the turbulence fluctuation in the streamwise direction u_{rms}^+ in the near-wall region, whereas overestimate the turbulence fluctuations in the wall normal and transverse directions v_{rms}^+ and w_{rms}^+ (Figs. 3.12a - 3.12d). The exception is the highest Reynolds number case $Re_\tau = 8758$ in which the w_{rms}^+ is underpredicted by both models (Fig. 3.12d). Fig. 3.13 plots k^+ / ε^+ as a function of y^{+2} for the four cases with Re_τ ranging from 250 to 8758. As in channel flow, the predicted k^+ / ε^+ in pipe flow follows the line representing $k^+ / (\varepsilon^+ y^{+2}) = 1 / 2$ in the near-wall region.

3.2.3 Fully-developed plane Couette flows

In plane Couette flows, one wall is stationary and the other is moving. A fully developed state is reached when the moving wall is dragged with a constant speed. The moving wall provides the energy to drive the flow. In the fully developed state, the total shear stress (viscous plus turbulent) is constant everywhere. Despite the seemingly simplicity of the flow, fully developed Couette flow is rather difficult to realize in laboratory, because of the difficulty in setting up the moving wall. But, it is a simple case for DNS (Lee and Kim 1991; Kristoffersen et al. 1993). The DNS data revealed some distinct features in Couette flow. For example, large scale eddies can be identified in the core region; flow in this region is quasi-homogeneous with turbulence production equal to dissipation rate but highly anisotropic. These features are quite different from those in Poiseuille flow driven by pressure gradient.

Calculations are carried out for Couette flow with Reynolds number (based on half channel width) $Re_\tau = 170$ and $Re_\tau = 625$, and the results are compared with the DNS data given by Lee and Kim (1991) for the $Re_\tau = 170$ case and the experimental data given by El Telbany and Reynolds (1980) for the $Re_\tau = 625$ case. The damping function (2-29a) is found to be suitable for both cases, although the Reynolds number in Lee and Kim's (1991) case is rather low ($Re_\tau = 170$). This indicates that plane Couette flow is less dependent on Re_τ than Poiseuille flow, which becomes more transparent by comparing the mean flow equations given in Appendix C. A term proportional to $1 / Re_\tau$ appears in the non-dimensional mean flow equations for channel

(C-1) and pipe flows (C-14). However, no such term appears in the mean flow equation for Couette flow (C-27).

Since all the turbulent quantities in Couette flow are symmetric about the centerline and $(U / U_m - 1 / 2)$ is anti-symmetric about the centerline (U_m is the speed of the moving wall), we first present the model results in the lower half of the flow domain for both cases, and then show the results for the second case ($\text{Re}_\tau = 625$) in the entire domain. Figs. 3.14a-3.14b compare the model predictions of the mean velocity profiles with the DNS results for $\text{Re}_\tau = 170$ and the experimental data for $\text{Re}_\tau = 625$. Model predictions agree well with the data, although the NNWRS model slightly underpredicts the mean velocity in the core region. The predicted von Karman constant is very close to the K values from DNS and measurements (Table 3.2).

In the near-wall region, the behavior of turbulent quantities is similar to their counterparts in Poiseuille flow (channel/pipe flows) (Figs. 3.15-3.18). Away from the near wall region, all the turbulent quantities rapidly becoming constant, and the turbulent flow field becomes homogeneous but remains isotropic (see Fig. 3.18). Again, the predicted k^+ / ε^+ by both models in the near-wall region follow $k^+ / (\varepsilon^+ y^{+2}) = 1 / 2$ (Fig. 3.19). Fig. 3.20 compares the predicted U / U_m, k^+, ε^+, $\overline{uv}^+$, u_{rms}^+, v_{rms}^+, w_{rms}^+ with the measurements for the $\text{Re}_\tau = 625$ case over the entire flow domain. The mean velocity and the turbulent shear stress are accurately reproduced by both models. In the core region, both models underestimate the turbulent kinetic energy k^+ and the turbulent fluctuation in the wall normal direction v_{rms}^+. The turbulent fluctuation in the other two directions u_{rms}^+ and w_{rms}^+ are predicted quite accurately.

3.3 Plane Boundary-Layer Flows with Zero Pressure Gradient

For two dimensional boundary-layer flow, the governing equations of the models become parabolic (Appendix C.4). Wilcox's (1993) implicit, two-dimensional code developed for two-equation turbulence models is modified for the NNWRS and NWRS models. His code incorporates the compressible form of Levy-Lees transformation (Appendix C.5), which removes the singularity near the leading edge of the plate. In this transformation, dimensionless parameters

39

are introduced to represent the compressible effects. These parameters are set to zero and one for incompressible and isothermal flows, respectively. Thus, we still can use the same transformation to remove the singularity near the leading edge of the plate for incompressible turbulent boundary-layer flow.

Computations are carried out by marching in the downstream (x) direction with iterations in the wall normal (y) direction. The step size in the downstream direction is adjusted according to how well the solution is converged at the previous cross-section location. In each cross-section, the distribution of the grid points follows a geometric progression ratio formula. After each iteration, the code checks for sufficient grid width. This is done by checking the difference of the mean velocity values between two successive grid points near the edge of the layer. If the difference is larger than about 10^{-4}, a grid point is added to the domain. This ensures that all the wall normal derivatives will be zero near the boundary layer edge. Convergence is attained if the maximum errors in the mean and turbulence quantities between two successive iterations is less than 10^{-4}.

The turbulence quantities at the edge of the boundary layer, $\overline{uu}_e$, $\overline{vv}_e$, $\overline{ww}_e$, $\overline{uv}_e$ and ε_e, are determined by solving the following ordinary differential equations,

$$U_e \frac{\partial \overline{uu}_e}{\partial x} = -C_1 \varepsilon_e b_{11} + C_2 \varepsilon_e (b_{11}^2 + b_{12}^2 - \frac{1}{3}\Pi) - \frac{2}{3}\varepsilon_e \quad , \tag{3-8a}$$

$$U_e \frac{\partial \overline{vv}_e}{\partial x} = -C_1 \varepsilon_e b_{22} + C_2 \varepsilon_e (b_{22}^2 + b_{12}^2 - \frac{1}{3}\Pi) - \frac{2}{3}\varepsilon_e \quad , \tag{3-8b}$$

$$U_e \frac{\partial \overline{ww}_e}{\partial x} = -C_1 \varepsilon_e b_{33} + C_2 \varepsilon_e (b_{33}^2 - \frac{1}{3}\Pi) - \frac{2}{3}\varepsilon_e \quad , \tag{3-8c}$$

$$U_e \frac{\partial \overline{uv}_e}{\partial x} = -C_1 \varepsilon_e b_{12} + C_2 \varepsilon_e (b_{11} b_{12} + b_{12} b_{22}) \quad , \tag{3-8d}$$

$$U_e \frac{\partial \varepsilon_e}{\partial x} = -C_{\varepsilon 2} \frac{\varepsilon_e^2}{k_e} \quad . \tag{3-8e}$$

which are reduced from the Reynolds stress equations in the models (Appendix C.4) under the assumption that all the wall normal derivatives vanish in the free stream. Therefore,

$\overline{uu}_e$, $\overline{vv}_e$, $\overline{ww}_e$, $\overline{uv}_e$, and ε_e given by (3-8) automatically satisfy the zero normal gradient conditions.

At the initial marching location, a total of 150 grid points are used to cover the computational domain. As the boundary layer grows in the downstream, the number of grid points increases. In the numerical computations, the grids are distributed so that at least 15 points are located within $y^+ \leq 5$, and more than 40 points are placed in the region $5 < y^+ < 65$. Furthermore, the distribution ensures that the first grid away from the wall is placed within $y^+ < 1$.

Two boundary-layer flow cases are selected to test the models' ability to replicate simple external flows. Model results are compared with the DNS data given by Spalart (1988) at $Re_\theta = 1,410$ and the detailed measurements of Karlsson and Johansson (1988) at $Re_\theta = 2,420$ (Figs. 3.21 - 3.25). The predicted mean velocity profiles, which show the existence of a wake region in the outer layer, agree well with the DNS data and measurements (Figs. 3.21a - 3.21b). The agreement between the predicted turbulent quantities k^+, ε^+, $\overline{uv}^+$, u_{rms}^+, v_{rms}^+, and w_{rms}^+ and the available data for both cases is reasonable (Figs. 3.22 - 3.25). At $Re_\theta = 1,410$, the turbulent quantities k^+, $\overline{uv}^+$, u_{rms}^+, v_{rms}^+, and w_{rms}^+ are first presented in the near-wall region and cross the boundary layer. In general, the NWRS model gives more satisfying predictions of the turbulence field in the near-wall region. The variations of the predicted turbulence quantities in the near-wall region are similar to those of the internal flows, with the exception that the maximum dissipation rate predicted by the NNWRS model is at a location very close to the wall, instead of the wall itself (Figs. 3.23a - 3.23b). As expected, all the turbulence quantities approach zero close to the edge of the boundary layer and match the freestream condition (Figs. 3.22 - 3.25). Fig. 3.26 shows that predicted ratio k^+ / ε^+ in the near-wall region varies according to y^{+2}, as in the internal flows.

Note that unlike the internal flow computations in which Re_τ is specified, the boundary-layer computations are carried out by providing mean velocity and turbulent quantities at the initial location and free stream. Consequently, the wall shear stress, τ_w, is a predicted result rather than an input. The accuracy of this quantity or the skin friction coefficient $C_f = 2\tau_w / (\rho U_\infty^2)$ can be taken as an indication of the models' ability to predict external flows. Thus, in addition to

41

comparing the von Karman constant K, the calculated and measured C_f are also compared (see Table 3.1). From Table 3.1, one can see that the predicted K and C_f agree well with the known results for both cases.

3.4 Reynolds-Number Effects on Simple Turbulent Flows

Using dimensional analysis, Millikan (1939) argued that Reynolds number effects could not be present in the mean velocity in wall-bounded turbulent flows. His argument is correct only in the near-wall region. Mellor and Gibson (1966) showed that Reynolds number has influence on the mean velocity in the outer region. Purtell et al (1981) pointed out that as Reynolds number decreases, the logarithmic region slowly disappears, while the viscous region remains unaffected by the decreasing Reynolds number.

When local similarity arguments are applied to the higher-order turbulent statistics, they imply that, at least in the inner layer, individual second-order statistics at different Reynolds numbers would collapse into a single curve if they are nondimensionalized by using inner-layer scalings. Recently, direct numerical simulations, together with experimental measurements and analysis, have shown that Reynolds number effects on wall-bounded turbulent flows are evident, not only in the mean flow but also in the second-order statistics of the turbulence field. A most convincing demonstration of the Reynolds number effects on second-order statistics was given by Bandyopadhyay and Gad-el-Hak (1994), who showed that the location of the peak value of the turbulent shear stress, normalized by υ / u_τ, increases with Reynolds number. So et al. (1996) have demonstrated that the NWRS model can predict the Reynolds number effects on mean and turbulence flow fields in simple flows with a wide range of Reynolds numbers. In what follows, we examine the ability of the NNWRS model to replicate the Reynolds number effects in wall-bounded simple turbulent flows.

3.4.1 Reynolds-number effects on mean flow   To show the Reynolds number effects on the mean flow, the predicted normalized mean velocity by the NNWRS model for internal (channel and pipe) and external (boundary layer) flows with different Reynolds numbers are plotted together

in Figs. 3.27a and 3.27b, respectively. Note that Couette flow is excluded in this section because it is less dependent on Reynolds number compared with the other internal flows. For comparison, the available DNS and experimental data are also plotted in Fig. 3.27. For channel/pipe flow, model predictions and the available data show little wake component, and the log layer extends all the way to the centerline (Fig. 3.27a). The extent of the log layer increases as Reynolds number increases. In the viscous layer, the data and model results are all very well correlated by a single curve $U^+ = y^+$. On the other hand, for boundary layer flow, the model results and the available data show a wake component in the defect layer and a reduction of the log-law region as Reynolds number decreases (Fig. 3.27b). However, the mean velocity in the viscous layer is unaffected by Reynolds number and again is well approximated by $U^+ = y^+$.

In the log layer, the velocity profile varies according to (3-4). The von Karman constant K obtained by following the procedure outlined in So et al. (1994) for each individual case has been given in Table 3.1. From Table 3.1, one can see that Reynolds number has no influence on the von Karman constant in wall-bounded flows. In fact, the velocity profiles for different Reynolds numbers in the log layer can be well correlated by (3-4) with $K = 0.40$ and $B = 5.2$ for channel/pipe flow (Fig. 3.27a), except for the $Re_\tau = 8758$ case where the mean velocity is underpredicted by the NNWRS model, and with $K = 0.41$ and $B = 5.2$ for boundary layer flow (Fig 3.27b). Both models do a fair job of reproducing the universal inner-layer behavior and the prediction of K is within the error margin of its determination from experiments. In general, a value of 0.40 is obtained and this is in agreement with experimental and DNS data.

For boundary-layer flow, the effects of Reynolds number on the shape factor $H = \delta^* / \theta$ (where δ^* and θ are the displacement and momentum thickness of the boundary layer, respectively) and skin friction coefficient $C_f = 2\tau_w / \rho U_\infty^2$ are also examined. The predicted and measured H and C_f are reported in Table 3.1. The DNS and experimental data show that H and C_f decrease as Reynolds number increases, which is also predicted by the models. Both models predict the shape factor well. But the NWRS model gives a more accurate prediction of the skin

43

friction coefficient than the NNWRS model. Overall, Reynolds number effects on the mean flow are fairly well reproduced by the NNWRS model, as well as by the NWRS model.

3.4.2 Reynolds-number effects on turbulence statistics   Momentum transport in two-dimensional wall-bounded turbulent flows is mainly carried out by the Reynolds shear stress. Therefore, it is of paramount importance to model the shear stress behavior correctly. In fully developed channel/pipe flows, the normalized shear stress can be expressed as

$$-\overline{uv}^{+} = (1 - y^{+} / \mathrm{Re}_{\tau}) - dU^{+} / dy^{+} \quad . \tag{3-9}$$

Assuming a universal velocity profile, it can be seen from (3-9) that the Reynolds number dependence of the shear stress in the inner layer is rather strong at low Reynolds number. Wei and Willmarth (1989) examined channel/pipe flows and found that the normalized shear stress at different Reynolds numbers does not collapse in the outer layer and the separation of the different profiles is still discernible in the inner layer. The calculated shear stress profiles for different Reynolds numbers are plotted together in Figs. 3.28a and 3.28b for channel/pipe and boundary-layer flows, respectively. Whenever the DNS and experimental data are available, they are also plotted in the figures for comparison. Fig 3.28 shows that in the logarithmic and outer regions, the shear stress profiles spread out as Reynolds number increases. In the viscous layer, the shear stress profiles at different Reynolds number in channel/pipe flow do not quite collapse into a single curve, whereas they do collapse into a single curve in boundary-layer flow. Thus, the influence of Reynolds number on the shear stress is more pronounced in channel/pipe flow than in boundary-layer flow.

Another test of the ability of the NNWRS model to reproduce Reynolds number effects is to plot the location of the peak shear stress versus Re_{τ}; for boundary layer flow, the reduced Reynolds number defined as $\mathrm{Re}_{\tau}^{*} = u_{\tau} \delta / \upsilon$ is used instead (Bandyopadhyay and Gad-el-Hak 1994). The location of the peak shear stress, denoted by y_{p}^{+}, can be determined from the shear stress profiles shown in Fig. 3.28. A log-log plot of y_{p}^{+} versus Re_{τ} is shown in Fig. 3.29 for all the flows examined. According to Sreenivasan (1988), a linear relation should exist between $\ln y_{p}^{+}$

44

and $\ln \text{Re}_\tau$. Bandyopadhyay and Gad-el-Hak (1994) showed that the straight line $y_p^+ = 2(\text{Re}_\tau)^{1/2}$ correlates well with the experimental data they examined in a log-log plot. Fig. 3.29 shows that the calculated results by the NNWRS model also correlate well with the same straight line.

The normalized production of kinetic energy, $\tilde{P}^+ = -\overline{uv}^+(dU^+ / dy^+)$, is shown to be relatively independent of Reynolds number in the outer region of channel flow but not so in the inner region (Wei and Willmarth 1989). Furthermore, the location of the peak value of $\tilde{P}^+$ is also relatively independent of Reynolds number (Bandyopadhyay and Gad-el-Hak 1994), although the location of the peak shear stress varies with Re_τ (see Fig. 3.29). These conclusions can also be deduced from (3-9) and the definition of $\tilde{P}^+$. As $\text{Re}_\tau \to \infty$, $\tilde{P}^+$ reaches its maximum 1/4. The calculations and measurements of $\tilde{P}^+$ plotted versus $\ln y^+$ are shown in Figs. 3.30a - 3.30b. As expected, there are no Reynolds number effects on the calculated $\tilde{P}^+$ in the outer layer for channel/pipe flow and boundary-layer flow. In the inner layer, the dependence of $\tilde{P}^+$ on Reynolds number in internal and external flows is different (cf. Fig. 3.30a with 3.30b). In channel/pipe flow, $\tilde{P}^+$, particularly its peak value, distinctly depends on Re_τ. Although the calculated location of the peak shear stress $\overline{uv}^+$ varies with Re_τ (Fig. 3.29), there is little variation in the location of the peak value of the predicted $\tilde{P}^+$. In both channel/pipe flow and boundary-layer flow, $\tilde{P}^+$ peaks at about $y^+ = 10$, which is consistent with $y^+ = 12$ given by Bandyopadhyay and Gad-el-Hak (1994) who examined different sets of data with a different Reynolds number range. The peak value of the calculated $\tilde{P}^+$ is close to 1/4 and approaching 1/4 only at high Reynolds number. The Reynolds number also has more effects on the peak value of the shear stress than the peak value of the production of kinetic energy (cf. Fig. 3.30 with 3.28). The ability of the NNWRS model to predict these important features of wall-bounded flows is another indication of the validity of the model.

The predicted turbulent dissipation rate ε^+ and the viscous diffusion of turbulent kinetic energy, $D_v^+ = d^2 k^+ / dy^{+2}$, are compared with DNS data and measurements in Figs. 3.31a - 3.31b. Very near the wall, the dissipation rate is approximately balanced by the viscous diffusion.

According to the asymptotic analysis in Section 2, this suggests that the pressure diffusion is much weaker than the viscous diffusion and the dissipation rate in the viscous layer. The predicted viscous diffusion is not sensitive to the variation of Reynolds number, neither is the dissipation rate except at very low Reynolds numbers.

3.5 Concluding Remarks

In this section, the NNWRS model has been verified by comparing model predictions with the DNS data and measurements for fully-developed wall-bounded simple flows: channel flow, pipe flow, and Couette flow, and for boundary-layer flow. The results show that the NNWRS model predicts the mean and turbulent flow fields of internal and external flows reasonably well. The model is also able to capture the log-law region with a correct von Karman constant and replicate the Reynolds number effects on the mean flow and second-order statistics. The main deficiency in the model is that it predicts less degree of turbulence anisotropy in the near-wall region compared to the NWRS model. This may be attributed to the more general formulation in the NNWRS model, i.e., no wall normal has been used in the model. In the next section, we shall apply the NNWRS to study wall-bounded complex turbulent flows.

Table 3.1 Comparison of the predicted K, H, and C_f with data in channel/pipe and boundary layer flows.

Data Source	Flow Type	Re_τ	Re_θ (Re_τ^*)	H	$C_f \times 10^3$	H	$C_f \times 10^3$	NNWRS	NWRS	Data
Kim et al. (1987) (DNS)	Channel	180	-	-	-	-	-	0.38	0.40	0.40
Durst et al. (1993) (EXP)	Pipe	250	-	-	-	-	-	0.40	0.39	0.40
Kim (1991) (DNS)	Channel	395	-	-	-	-	-	0.40	0.39	0.41
Schildknecht et al. (1979) (EXP)	Pipe	489	-	-	-	-	-	0.40	0.41	0.40
Laufer (1954) (EXP)	Pipe	1052	-	-	-	-	-	0.39	0.40	0.40
Laufer (1954) (EXP)	Pipe	8758	-	-	-	-	-	0.40	0.40	0.40
Spalart (1988) (DNS)	Boundary Layer	-	1410 (538)	1.41 (1.42)	3.76 (4.10)	1.42 (1.42)	4.04 (4.10)	0.39	0.40	0.41
Karsson & Johansson (1988) (EXP)	Boundary Layer	-	2420 (813)	1.38 (1.39)	3.42 (3.54)	1.38 (1.39)	3.65 (3.54)	0.39	0.40	0.41

Table 3.2 Comparison of the predicted K with data in Couette flow.

Data Source	Re_τ	Data	NNWRS	NWRS
Lee and Kim (1991) (DNS)	170	0.40	0.40	0.39
El Telbany and Reynolds (1980) (EXP)	625	0.39	0.40	0.40
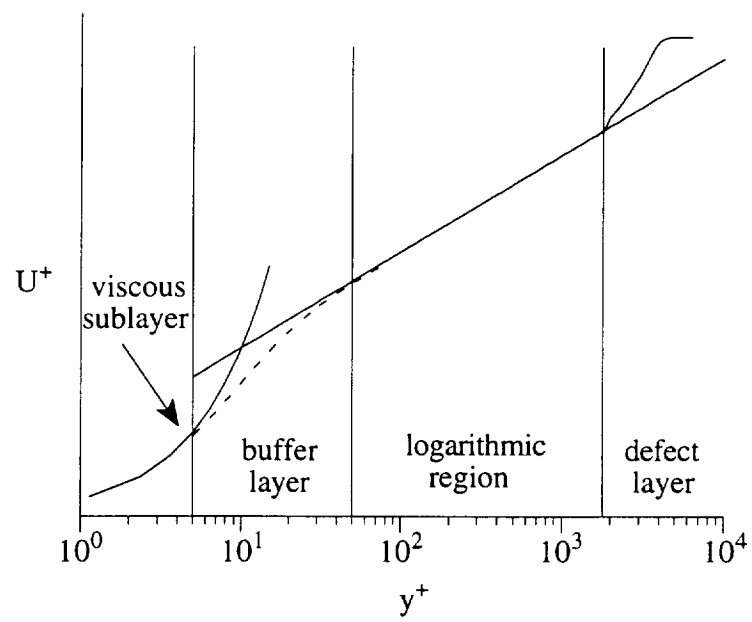
Fig. 3.1 Sketch of different flow regions in a wall-bounded turbulent flow.
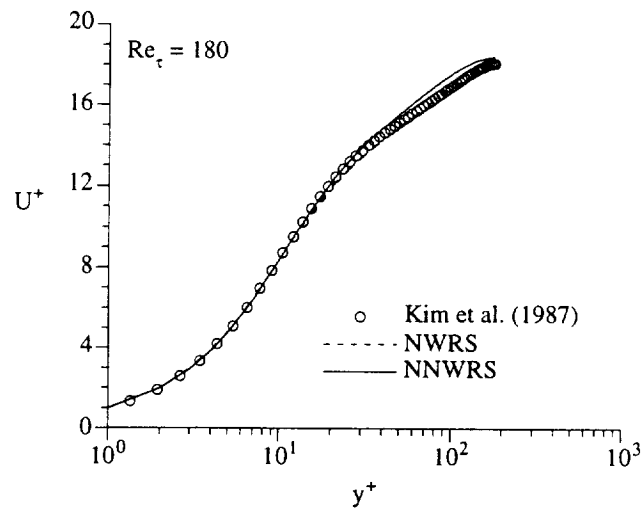
Fig. 3.2a Comparison between the predicted and DNS mean velocity profiles in the fully developed channel flow at $\mathrm{Re}_\tau = 180$.
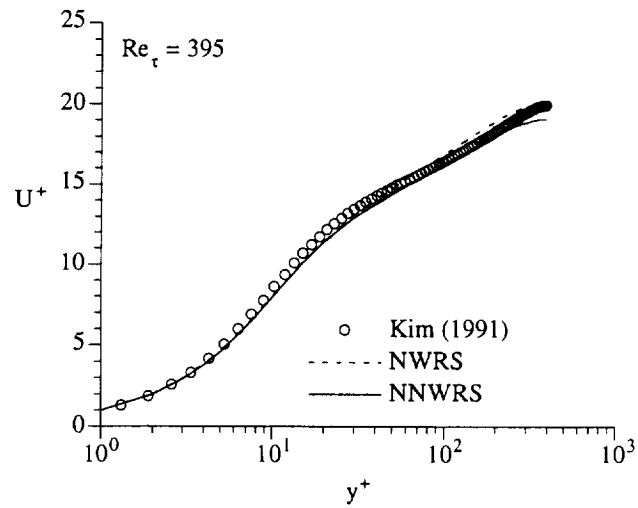
Fig. 3.2b Comparison between the predicted and DNS mean velocity profiles in the fully developed channel flow at $\mathrm{Re}_\tau = 395$.
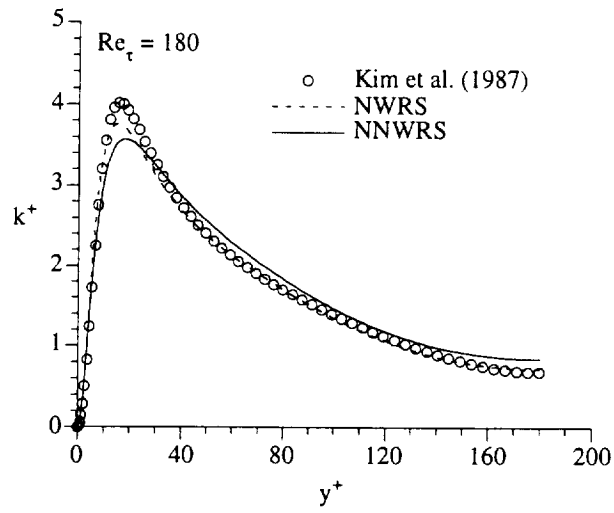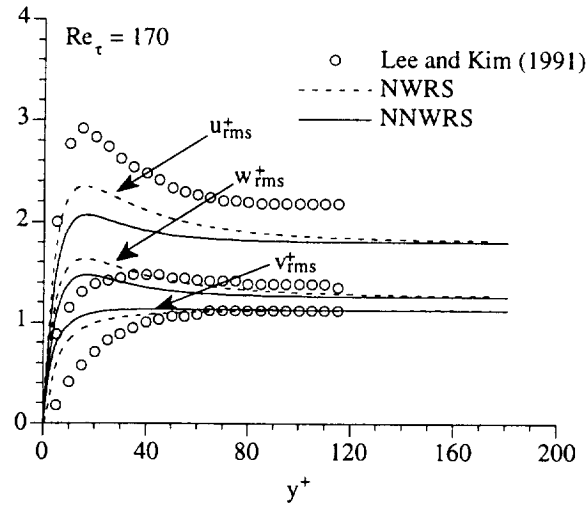
Fig. 3.3a Comparison between the predicted and DNS turbulent kinetic energy in the fully developed channel flow at $Re_\tau = 180$.
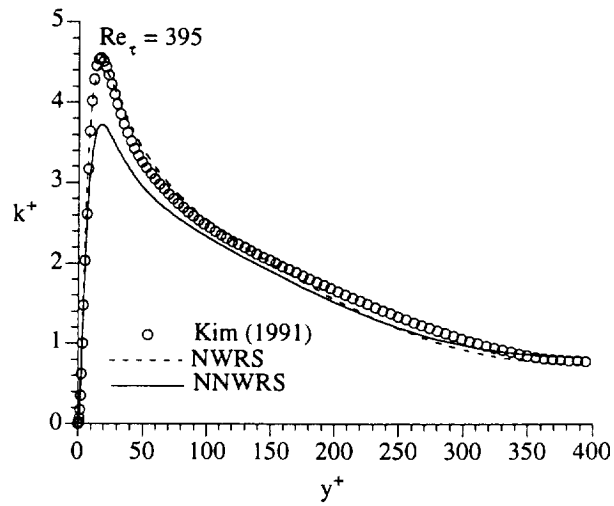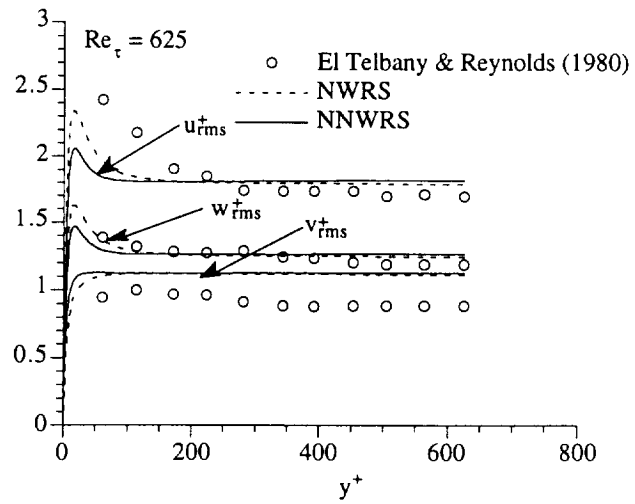

Fig. 3.3b Comparison between the predicted and DNS turbulent kinetic energy in the fully developed channel flow at $Re_\tau = 395$.

51
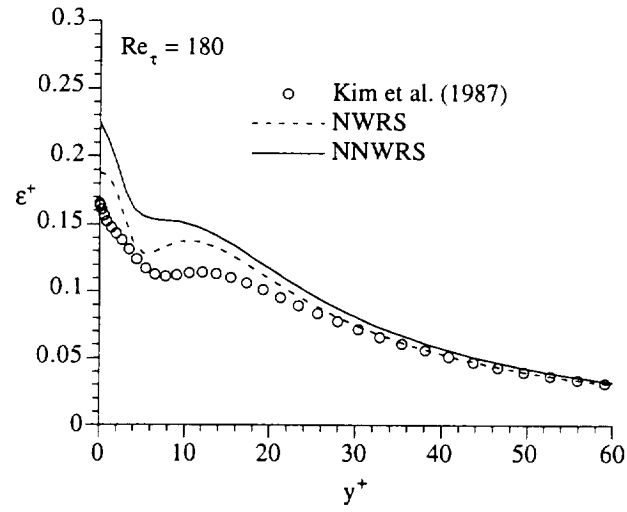
Fig. 3.4a Comparison between the predicted and DNS dissipation rate in the near-wall region of fully developed channel flow at $Re_\tau = 180$.
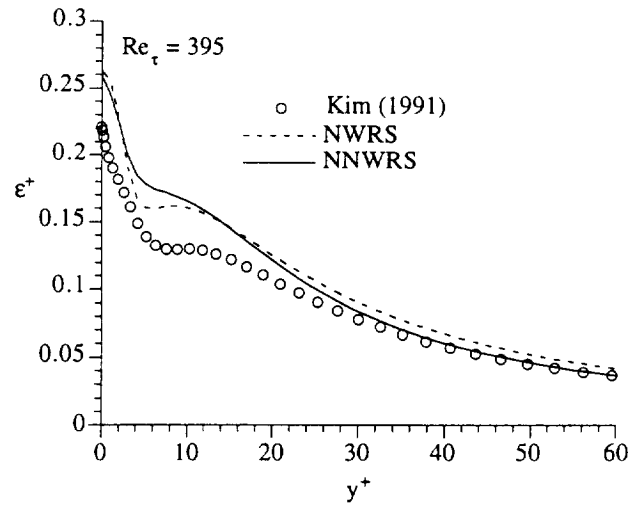
Fig. 3.4b Comparison between the predicted and DNS dissipation rate in the near-wall region of fully developed channel flow at $Re_\tau = 395$.
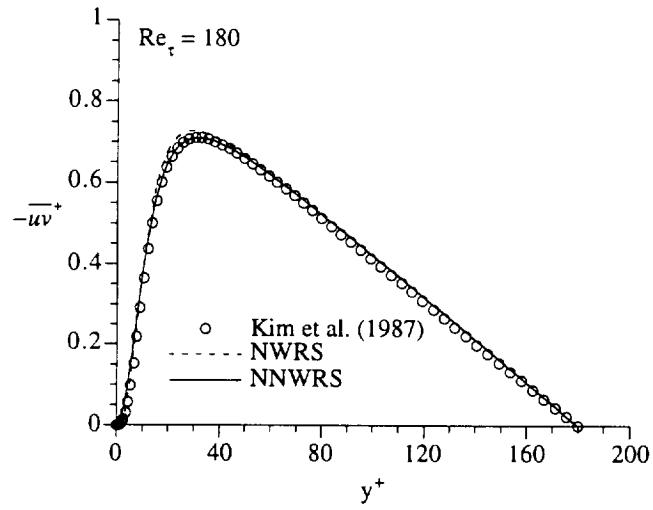
Fig. 3.5a Comparison between the predicted and DNS turbulent shear stress in the fully developed channel flow at $Re_\tau = 180$.
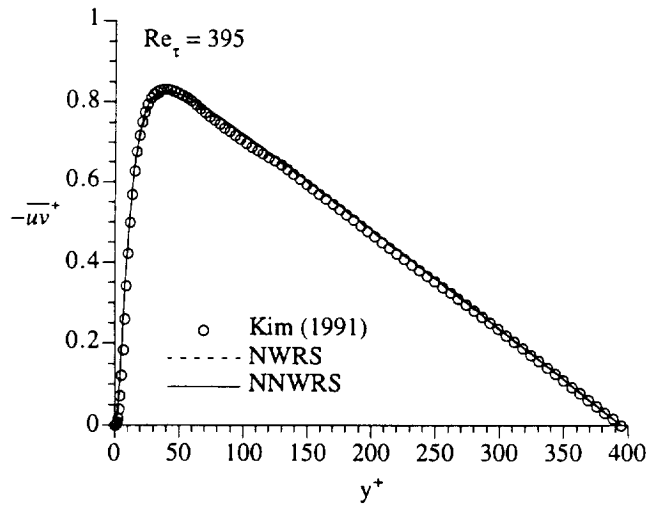
Fig. 3.5b Comparison between the predicted and DNS turbulent shear stress in the fully developed channel flow at $Re_\tau = 395$.

53
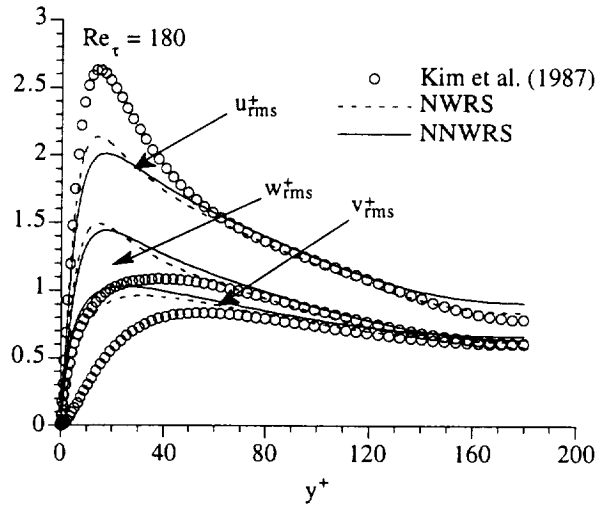
Fig. 3.6a Comparison between the predicted and DNS turbulent fluctuations in the fully developed channel flow at $Re_\tau = 180$.
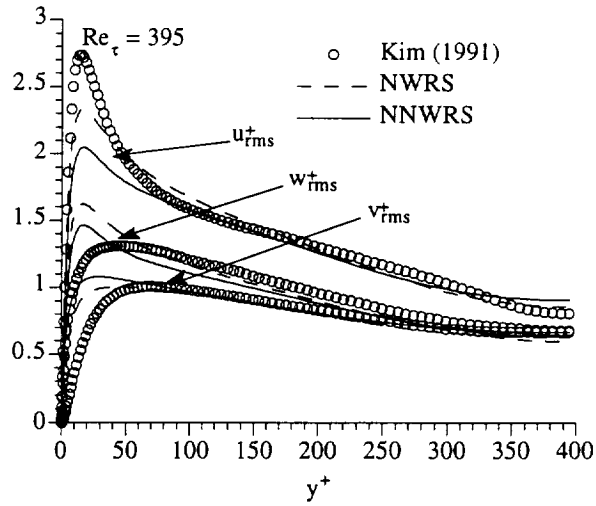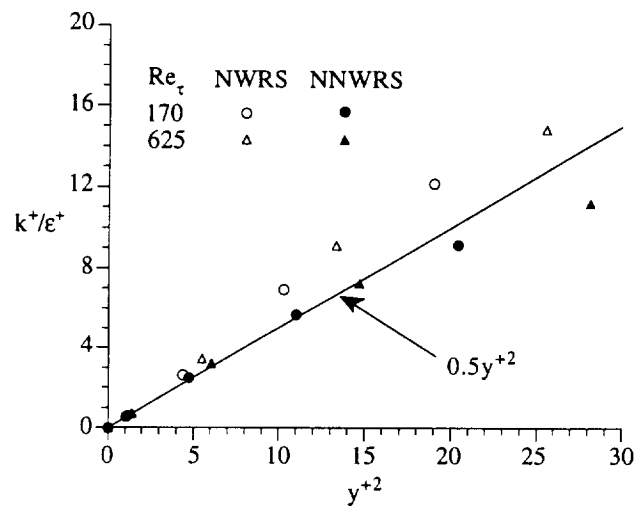

Fig. 3.6b Comparison between the predicted and DNS turbulent fluctuations in the fully developed channel flow at $Re_\tau = 395$.
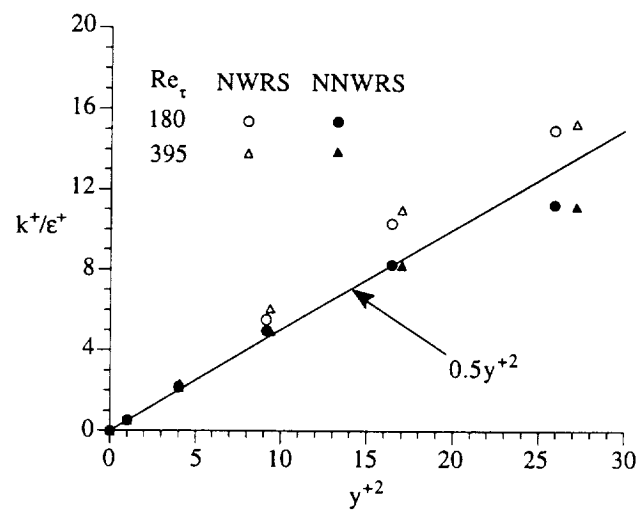
Fig. 3.7 Predicted k^+ / ε^+ vs y^{+2} in the near-wall region for fully developed channel flows.
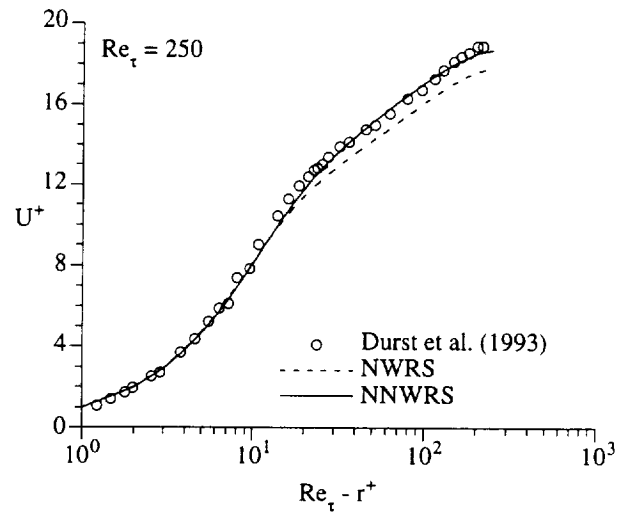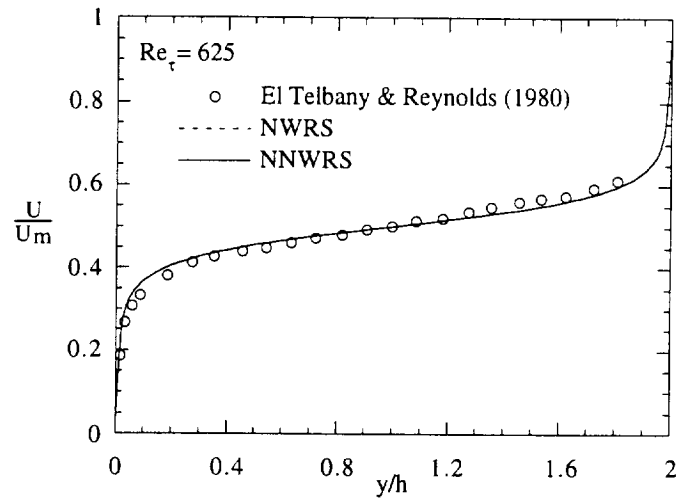
Fig. 3.8a Comparison between the predicted and measured mean velocity profiles in the fully developed pipe flow at $Re_\tau = 250$.
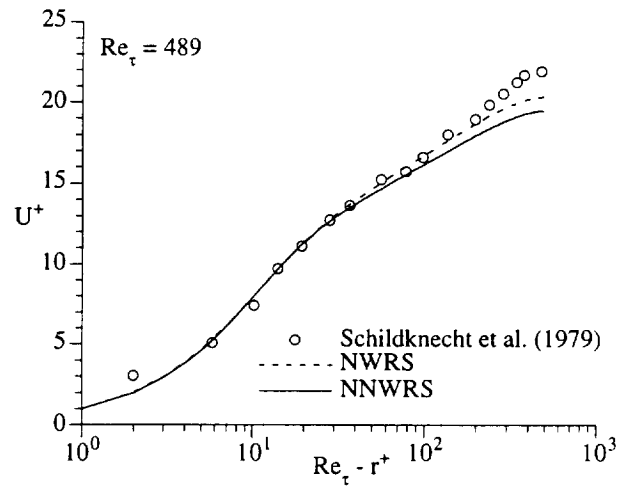
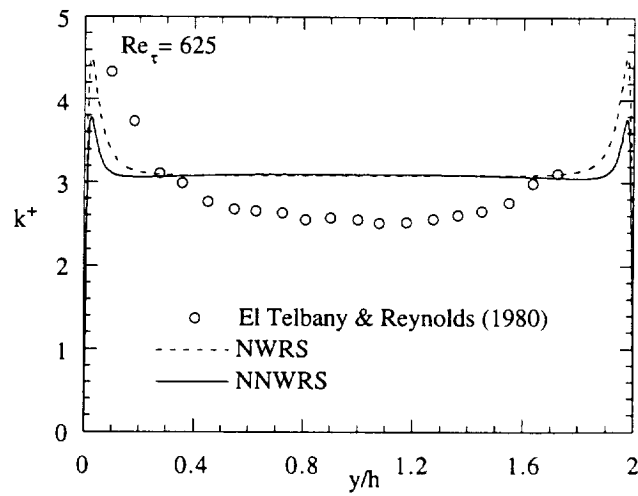Fig. 3.8b Comparison between the predicted and measured mean velocity profiles in the fully developed pipe flow at $Re_\tau = 489$.
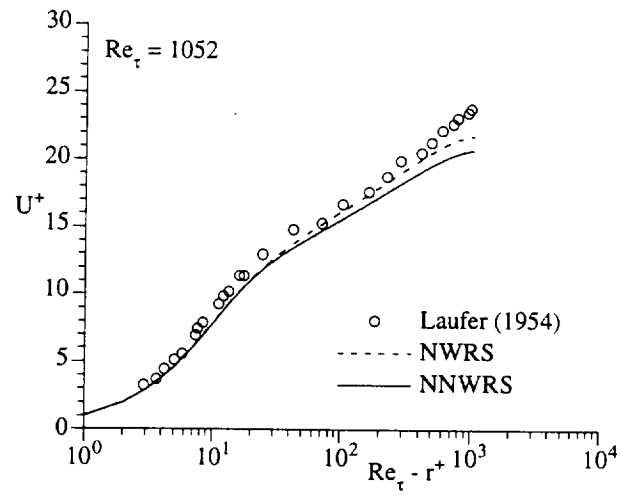
Fig. 3.8c Comparison between the predicted and measured mean velocity profiles in the fully developed pipe flow at $\mathrm{Re}_\tau = 1052$.
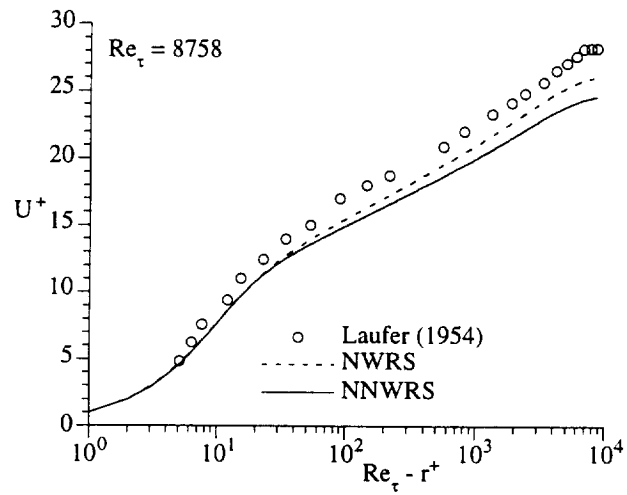
Fig. 3.8d Comparison between the predicted and measured mean velocity profiles in the fully developed pipe flow at $\mathrm{Re}_\tau = 8758$.
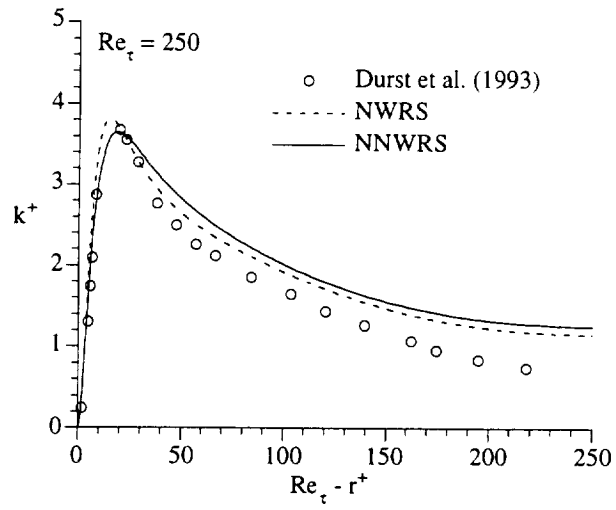
Fig. 3.9a Comparison between the predicted and measured turbulent kinetic energy in the fully developed pipe flow at $Re_\tau = 250$.
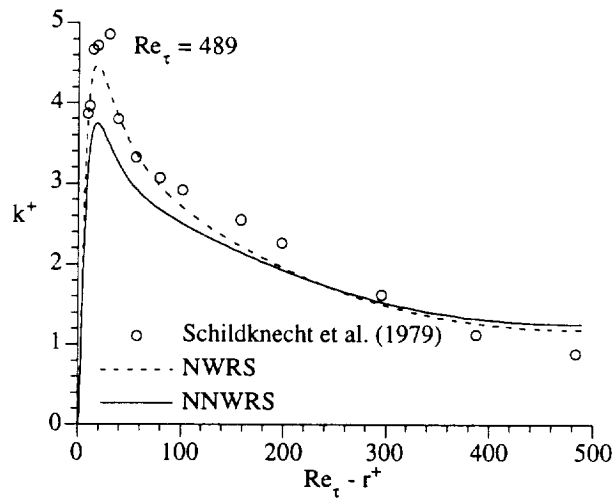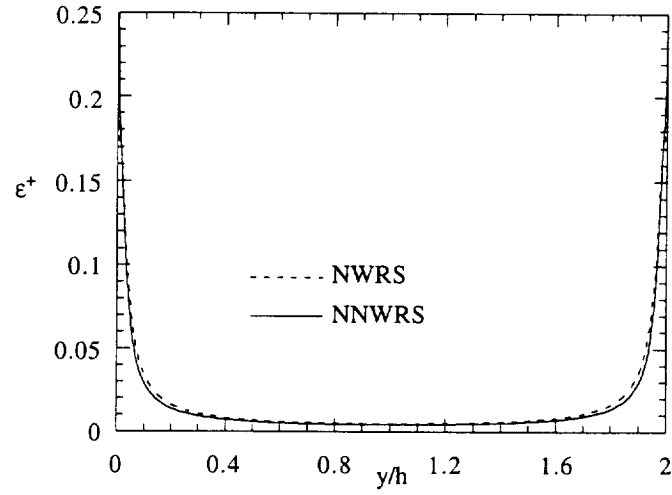

Fig. 3.9b Comparison between the predicted and measured turbulent kinetic energy in the fully developed pipe flow at $Re_\tau = 489$.
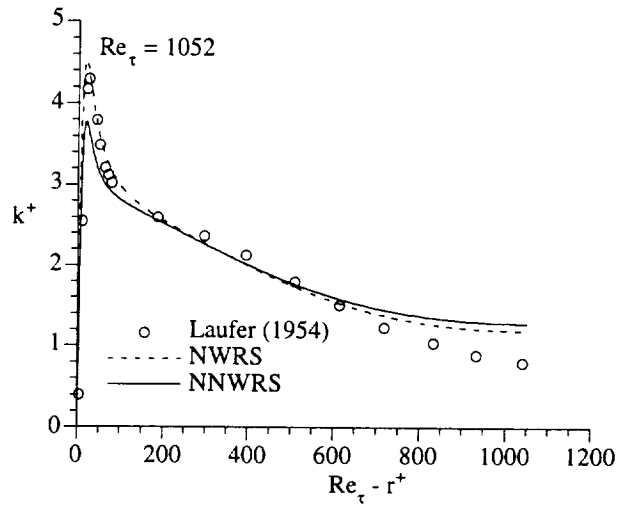
Fig. 3.9c Comparison between the predicted and measured turbulent kinetic energy in the fully developed pipe flow at $Re_\tau = 1052$.
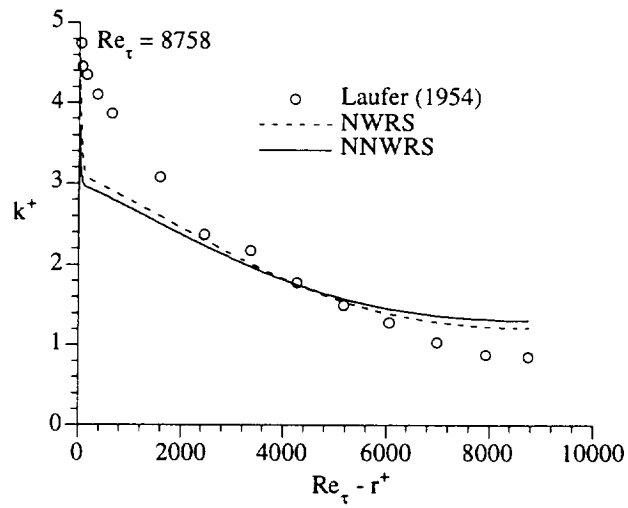
Fig. 3.9d Comparison between the predicted and measured turbulent kinetic energy in the fully developed pipe flow at $Re_\tau = 8758$.

59
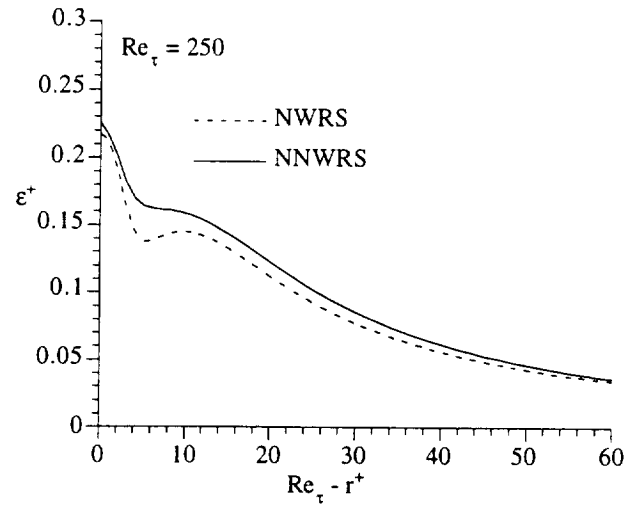
Fig. 3.10a Comparison of the predicted dissipation rate in the near-wall region of fully developed pipe flow at $\mathrm{Re}_\tau = 250$.
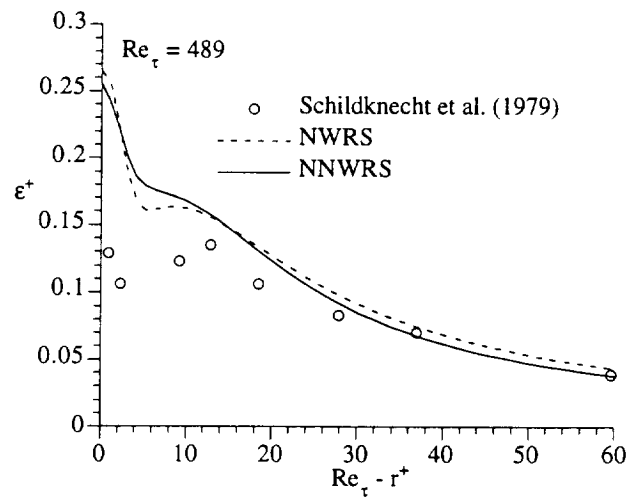
Fig. 3.10b Comparison between the predicted and measured dissipation rate in the near-wall region of fully developed pipe flow at $\mathrm{Re}_\tau = 489$.
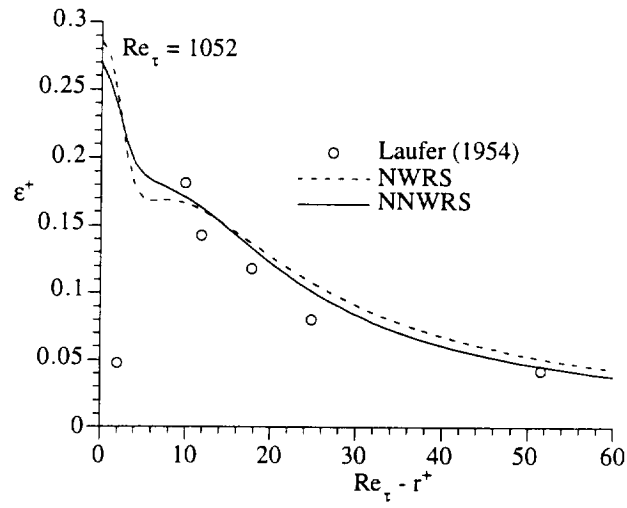
Fig. 3.10c Comparison between the predicted and measured dissipation rate in the near-wall region of fully developed pipe flow at $Re_\tau = 1052$.
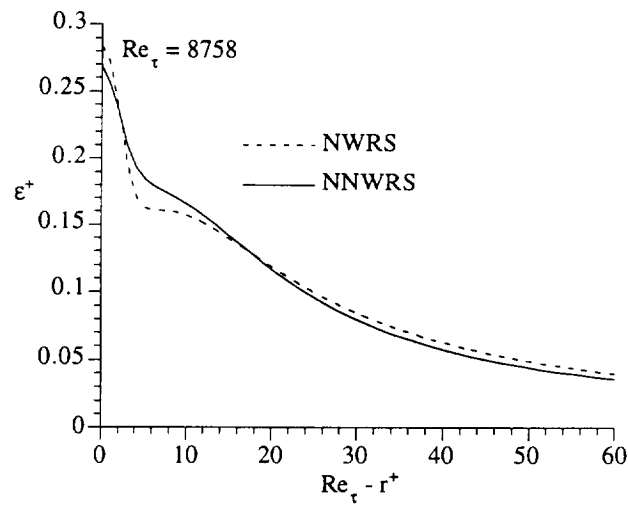
Fig. 3.10d Comparison of the predicted dissipation rate in the near-wall region of fully developed pipe flow at $Re_\tau = 8758$.

61
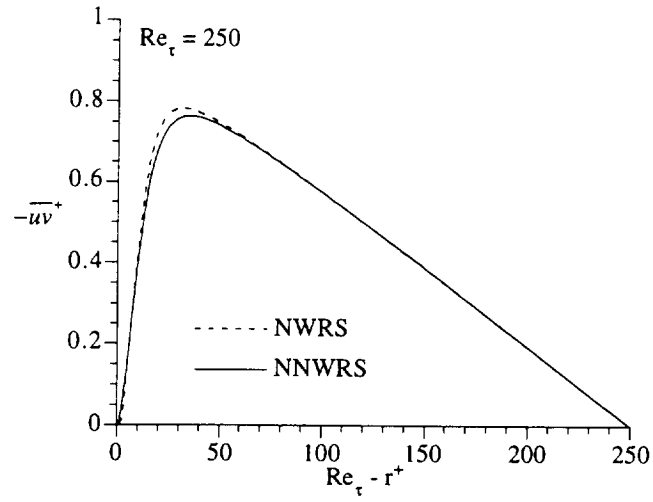
Fig. 3.11a Comparison of the predicted turbulent shear stress in the fully developed pipe flow at $\mathrm{Re}_\tau = 250$.
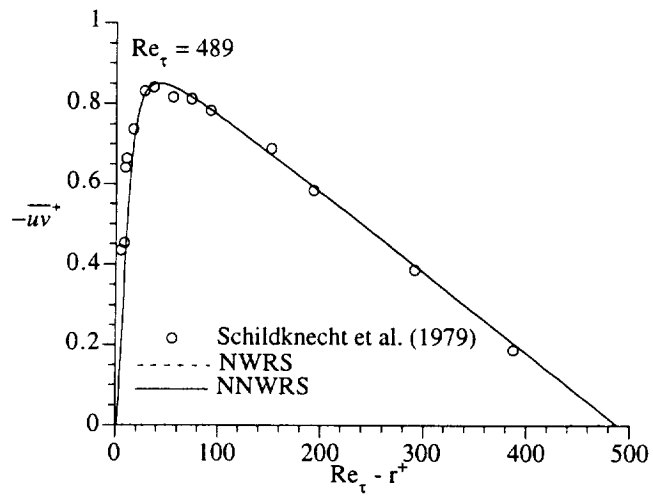
Fig. 3.11b Comparison between the predicted and measured turbulent shear stress in the fully developed pipe flow at $\mathrm{Re}_\tau = 489$.
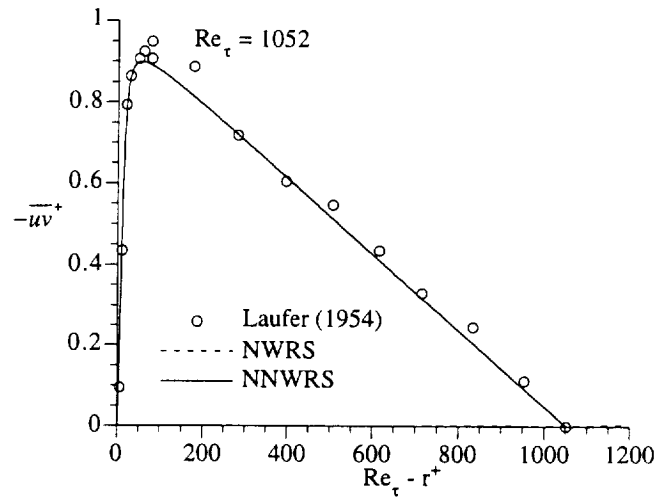
Fig. 3.11c Comparison between the predicted and measured turbulent shear stress in the fully developed pipe flow at $Re_\tau = 1052$.
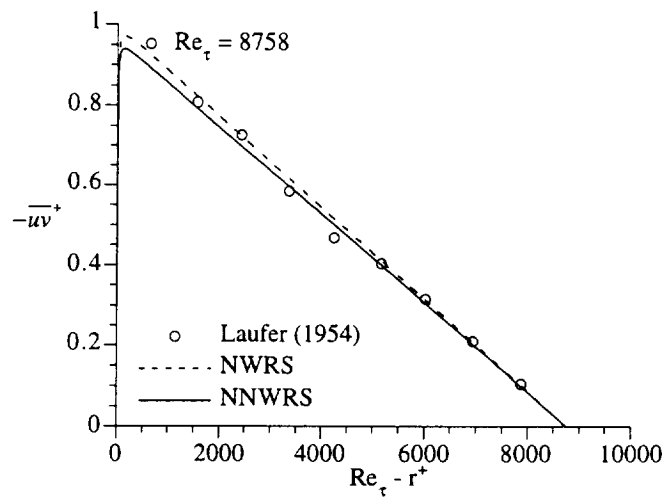
Fig. 3.11d Comparison between the predicted and measured turbulent shear stress in the fully developed pipe flow at $Re_\tau = 8758$.
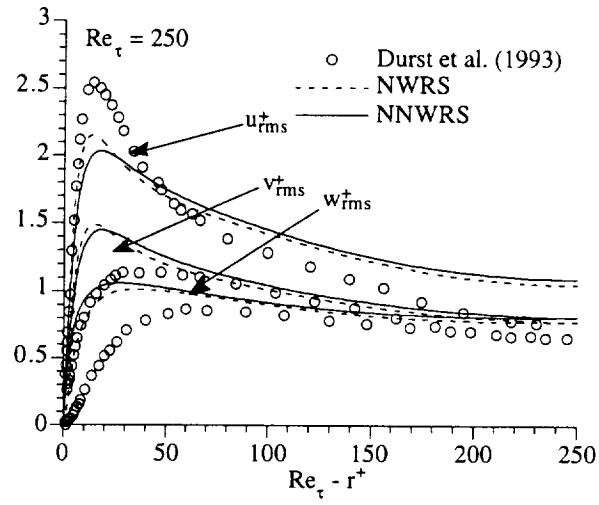
Fig. 3.12a Comparison between the predicted and measured turbulent fluctuations in the fully developed pipe flow at $Re_\tau = 250$.
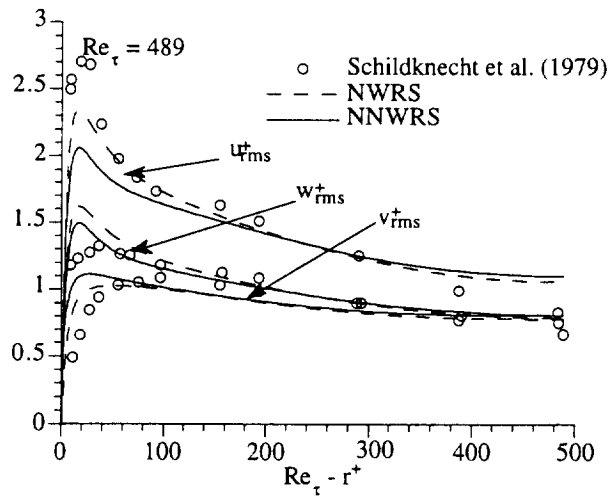
Fig. 3.12b Comparison between the predicted and measured turbulent fluctuations in the fully developed pipe flow at $Re_\tau = 489$.
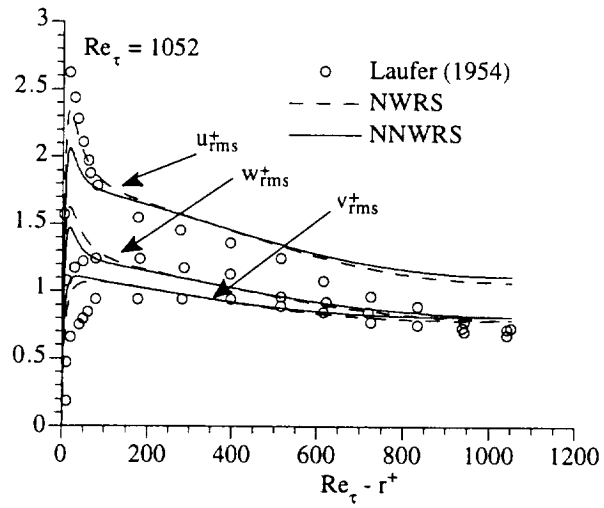
Fig. 3.12c Comparison between the predicted and measured turbulent fluctuations in the fully developed pipe flow at $Re_\tau = 1052$.
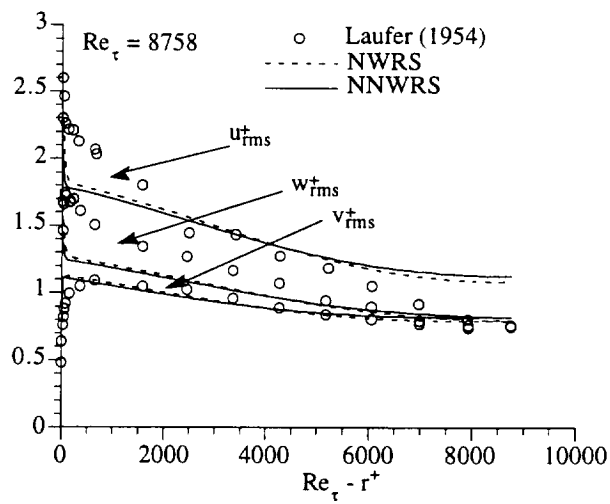
Fig. 3.12d Comparison between the predicted and measured turbulent fluctuations in the fully developed pipe flow at $Re_\tau = 8758$.
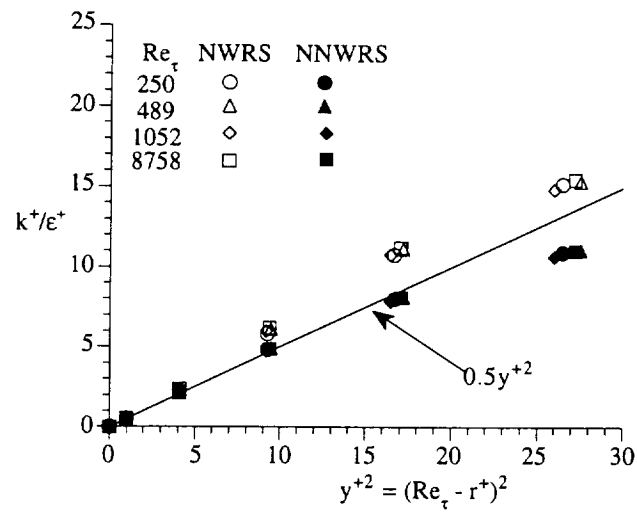
Fig. 3.13 Predicted k^+ / ε^+ vs. $y^{+2} = (\mathrm{Re}_\tau - r^+)^2$ in the near-wall region for fully developed pipe flow.
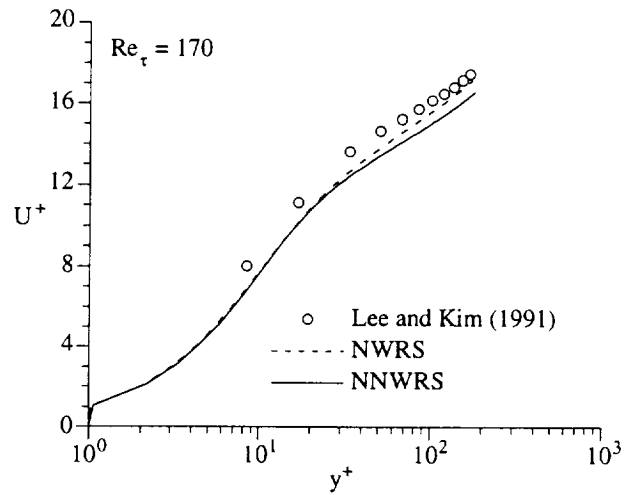
Fig. 3.14a Comparison between the predicted and DNS mean velocity profiles in the fully developed Couette flow at $Re_\tau = 170$.
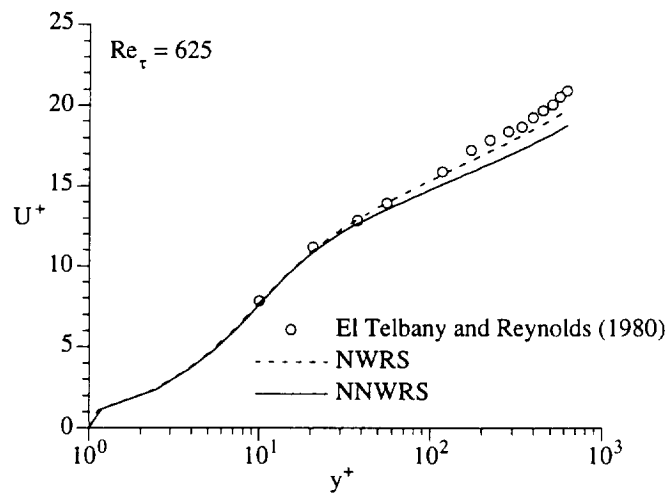
Fig. 3.14b Comparison between the predicted and measured mean velocity profiles in the fully developed Couette flow at $Re_\tau = 625$.

67
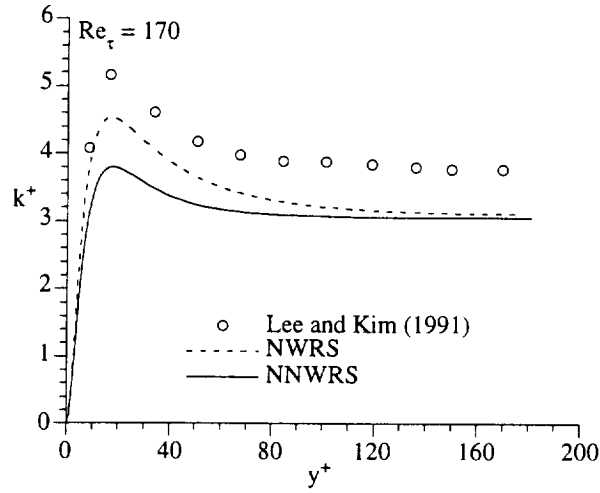
Fig. 3.15a Comparison between the predicted and DNS turbulent kinetic energy in the fully developed Couette flow at $Re_\tau = 170$.
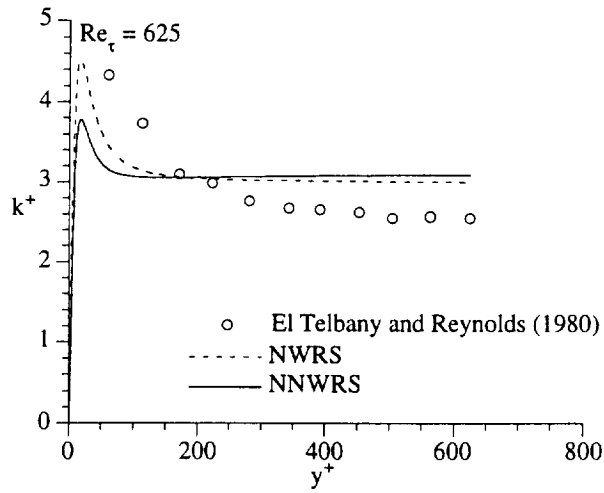
Fig. 3.15b Comparison between the predicted and measured turbulent kinetic energy in the fully developed Couette flow at $Re_\tau = 625$.

68
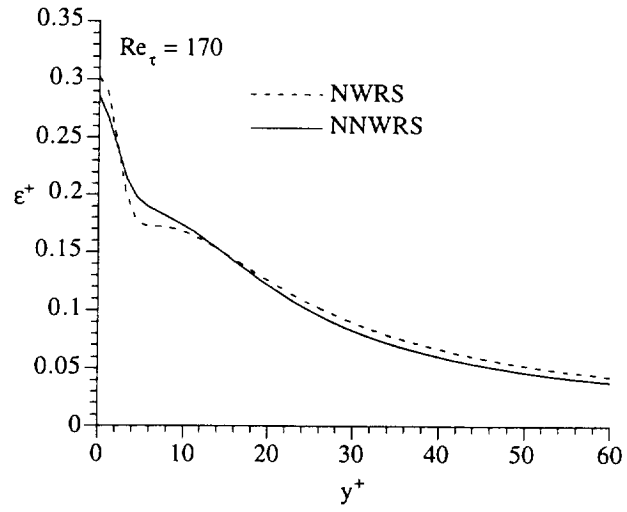
Fig. 3.16a Comparison of the predicted dissipation rate in the near-wall region of fully developed Couette flow at $Re_\tau = 170$.
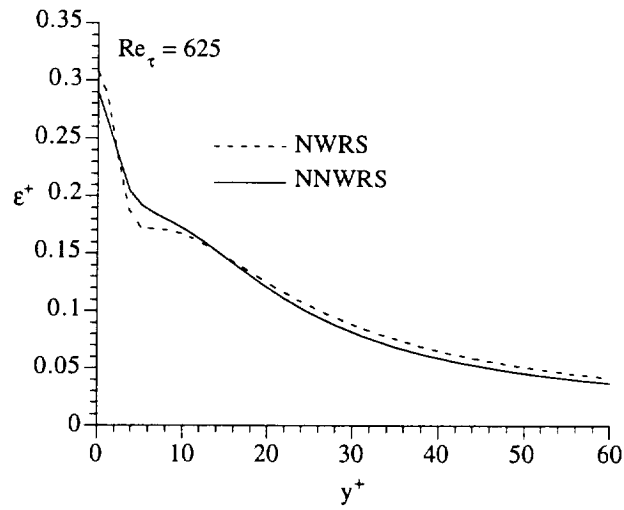
Fig. 3.16b Comparison of the predicted dissipation rate in the near-wall region of fully developed Couette flow at $Re_\tau = 625$.
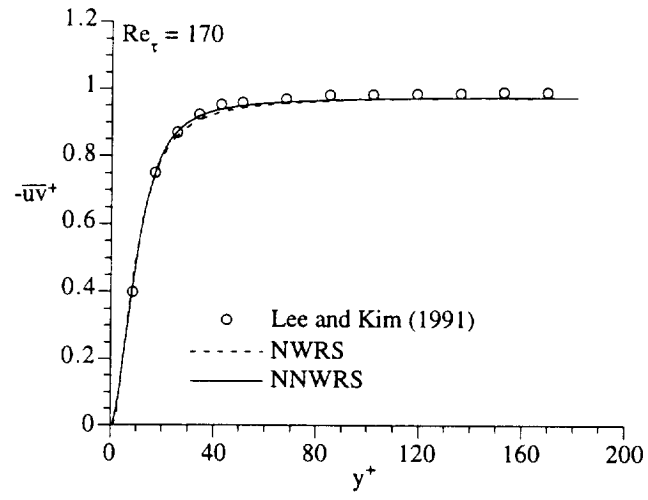
Fig. 3.17a Comparison between the predicted and DNS turbulent shear stress in the fully developed Couette flow at $Re_\tau = 170$.
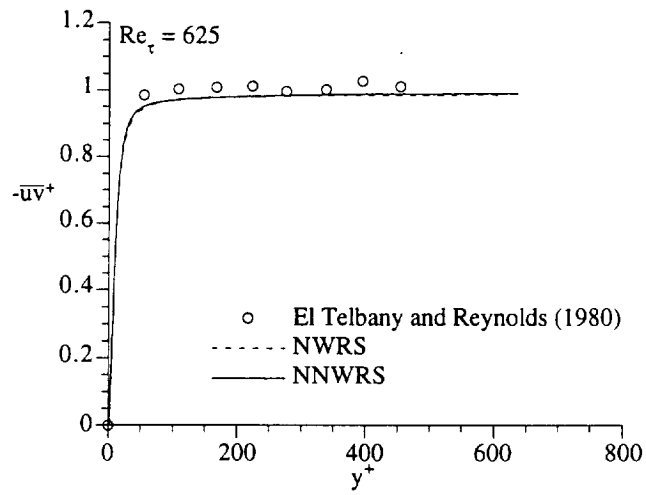
Fig. 3.17b Comparison between the predicted and measured turbulent shear stress in the fully developed Couette flow at $Re_\tau = 625$.

70

Fig. 3.18a Comparison between the predicted and DNS turbulent fluctuations in the fully developed Couette flow at $\mathrm{Re}_\tau = 170$.

Fig. 3.18b Comparison between the predicted and measured turbulent fluctuations in the fully developed Couette flow at $\mathrm{Re}_\tau = 625$.

71

Fig. 19 Predicted k^+ / ε^+ vs. y^{+2} in the near-wall region for fully developed Couette flows.

Fig. 3.20a Comparison between the predicted and measured mean velocity profiles over the entire fully developed Couette flow region at $Re_\tau = 625$.

Fig. 3.20b Comparison between the predicted and measured turbulent kinetic energy over the entire fully developed Couette flow region at $Re_\tau = 625$.

73

Fig. 3.20c Comparison of the predicted dissipation rate over the entire fully developed Couette flow region at $\mathrm{Re}_\tau = 625$.
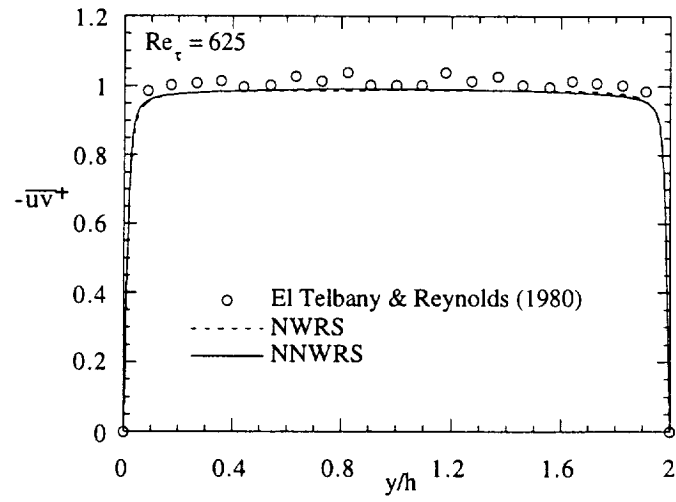
Fig.3.20d Comparison between the predicted and measured shear stress over the entire fully developed Couette flow region at $\mathrm{Re}_\tau = 625$.

74
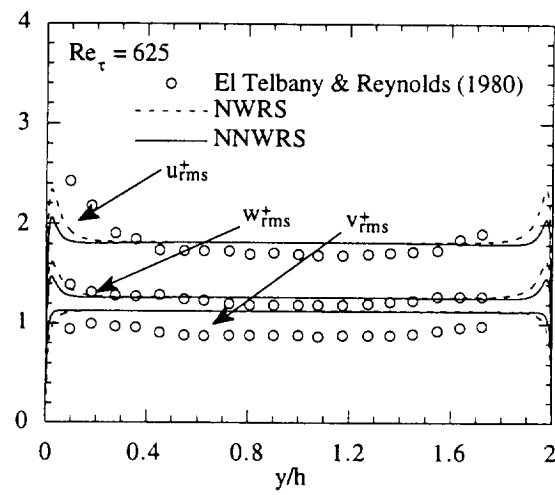
Fig. 3.20e Comparison between the predicted and measured turbulent fluctuations over the entire fully developed Couette flow region at $Re_\tau = 625$.
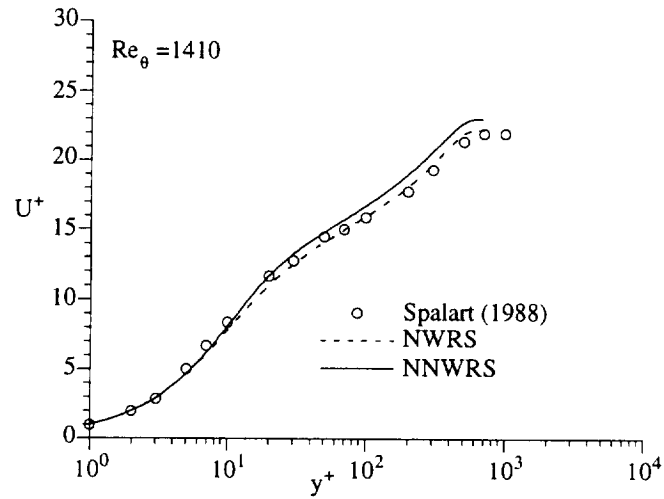
Fig. 3.21a Comparison between the predicted and DNS mean velocity profiles of boundary-layer flow at $Re_\theta = 1410$.
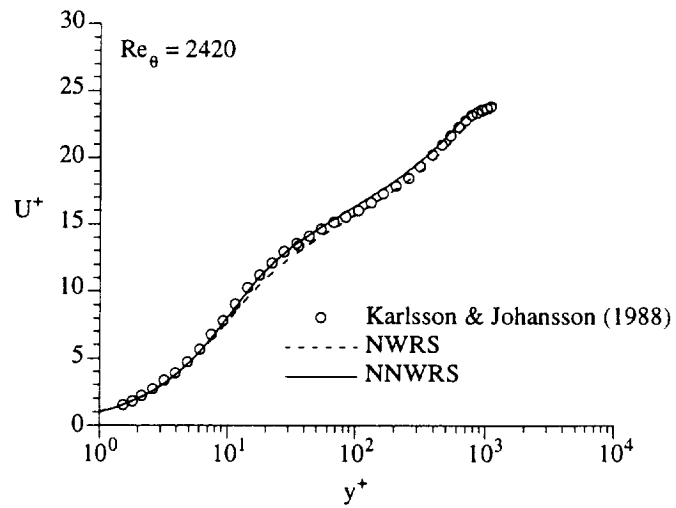
Fig. 3.21b Comparison between the predicted and measured mean velocity profiles of boundary-layer flow at $Re_\theta = 2420$.
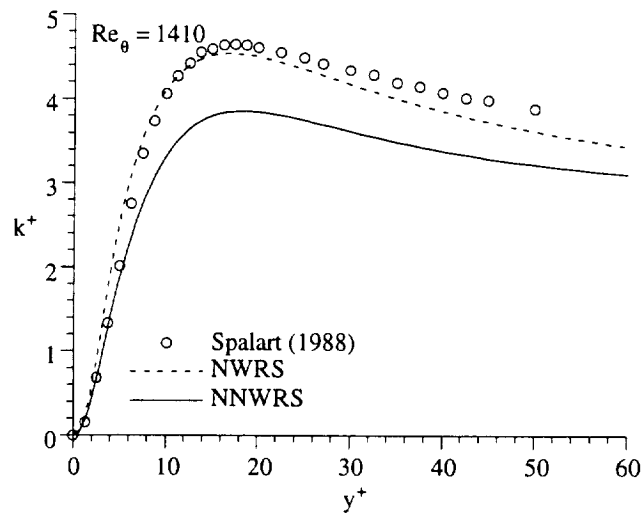
Fig. 3.22a Comparison between the predicted and DNS turbulent kinetic energy in the near-wall region of boundary-layer flow at $Re_\theta = 1410$.
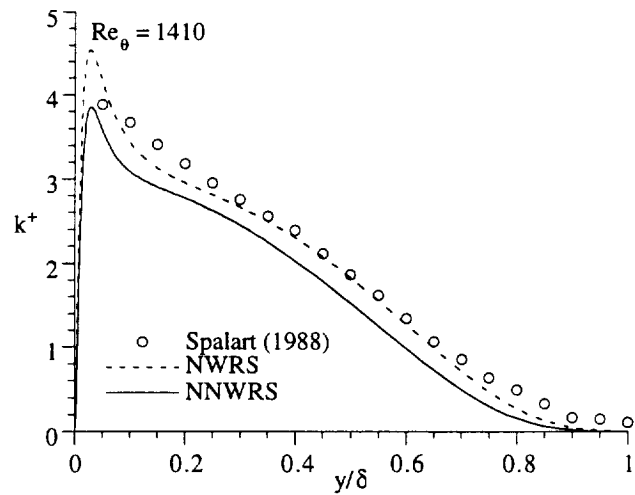
Fig. 3.22b Comparison between the predicted and DNS turbulent kinetic energy cross the boundary layer at $Re_\theta = 1410$.

77
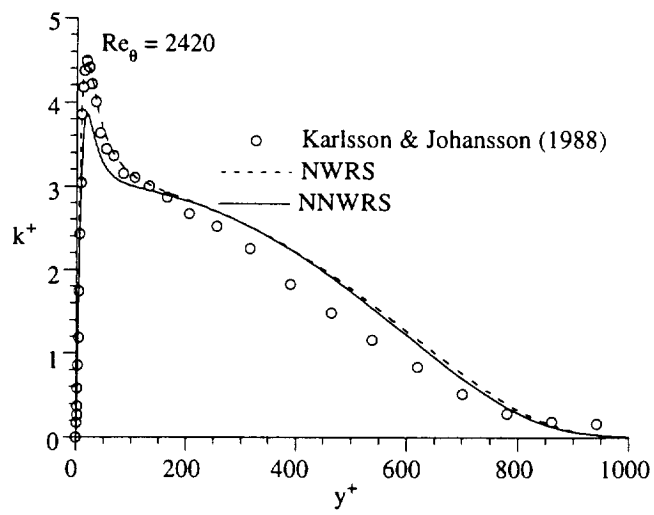
Fig. 3.23 Comparison between the predicted and measured turbulent kinetic energy cross the
boundary layer at $Re_\theta = 2420$.
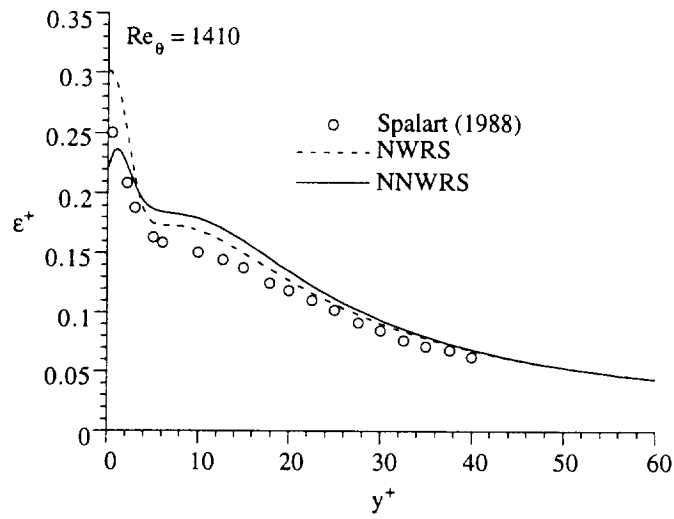
Fig. 3.24a Comparison between the predicted and DNS dissipation rate in the near-wall region of boundary-layer flow at $Re_\theta = 1410$.
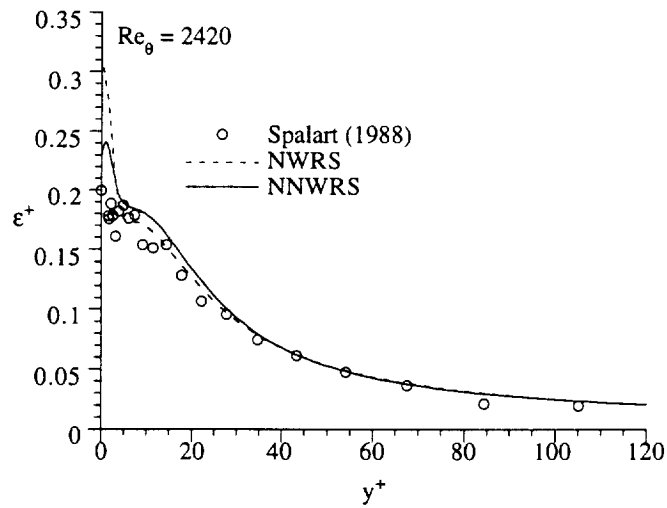
Fig. 3.24b Comparison between the predicted and measured dissipation rate in the near-wall region of boundary-layer flow at $Re_\theta = 2420$.
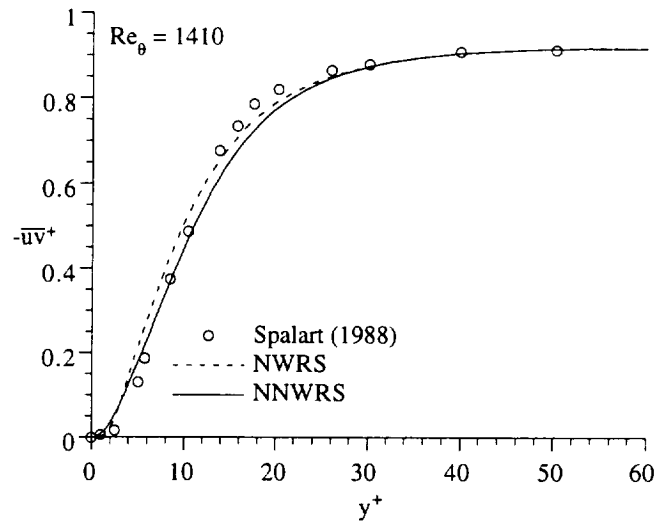
Fig. 3.25a Comparison between the predicted and DNS turbulent shear stress in in the near-wall region of boundary-layer flow at $Re_\theta = 1410$.
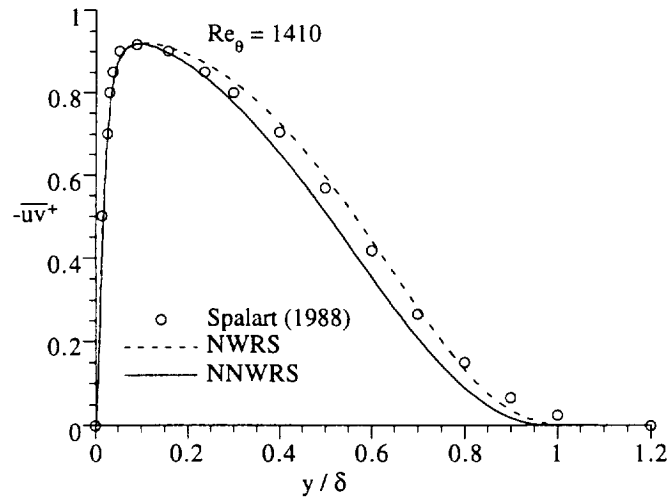
Fig. 3.25b Comparison between the predicted and DNS turbulent shear stress cross boundary layer at $Re_\theta = 1410$.
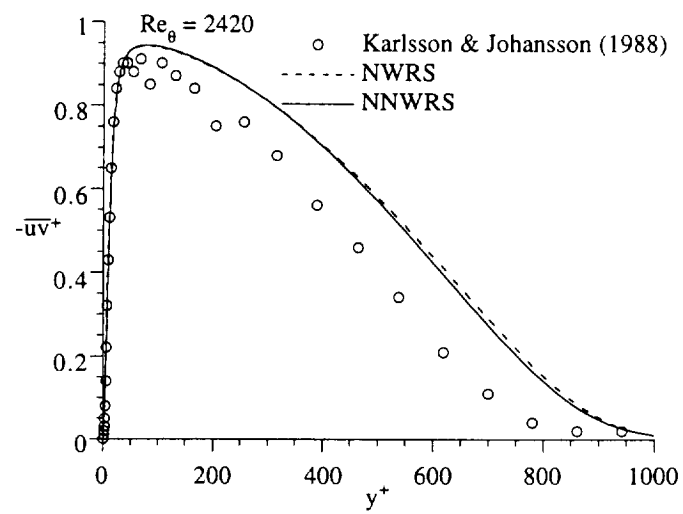
Fig. 3.26 Comparison between the predicted and measured turbulent shear stress cross boundary layer at $Re_\theta = 2420$.
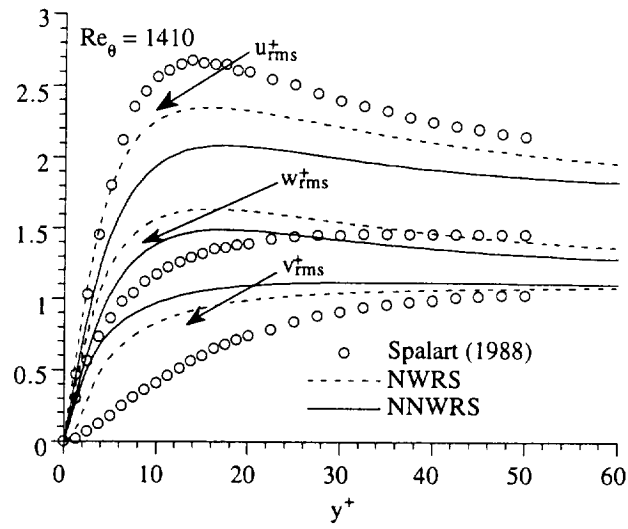
Fig. 3.27a Comparison between the predicted and DNS turbulent fluctuations in the near-wall region of boundary layer flow at $Re_\theta = 1410$.
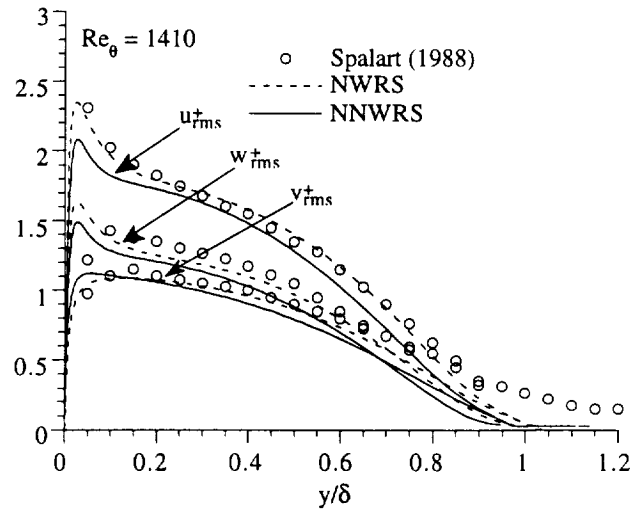
Fig. 3.27b Comparison between the predicted and DNS turbulent fluctuations cross boundary layer at $Re_\theta = 1410$.

82
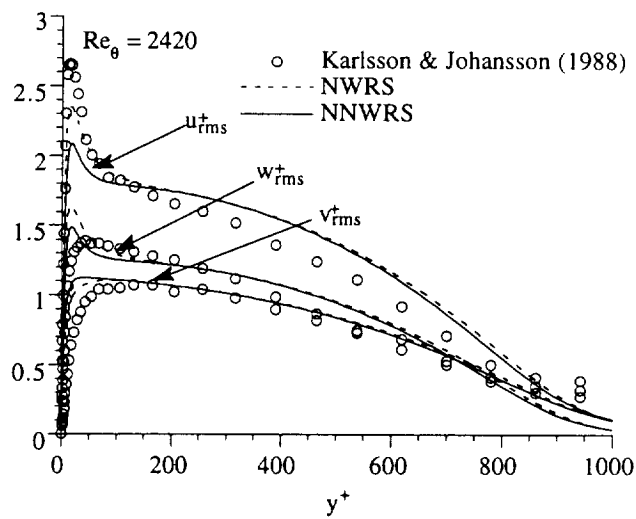
Fig. 3.28 Comparison between the predicted and measured turbulent fluctuations cross boundary layer at $\mathrm{Re}_\theta = 2420$.
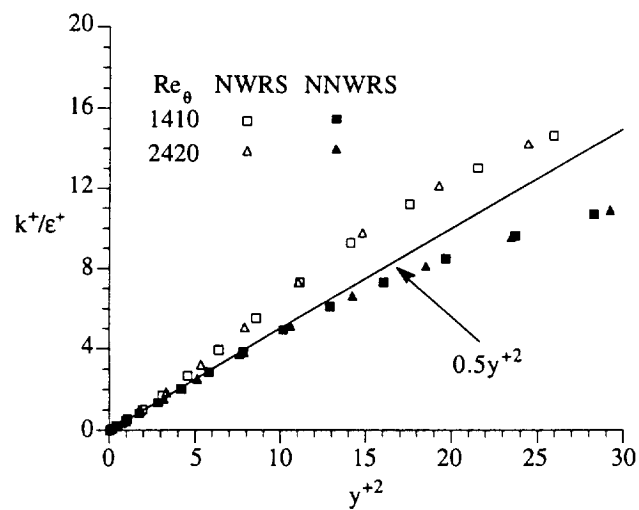
Fig. 3.29 Predicted k^+ / ε^+ vs. y^{+2} in the near-wall region for boundary layer flows.
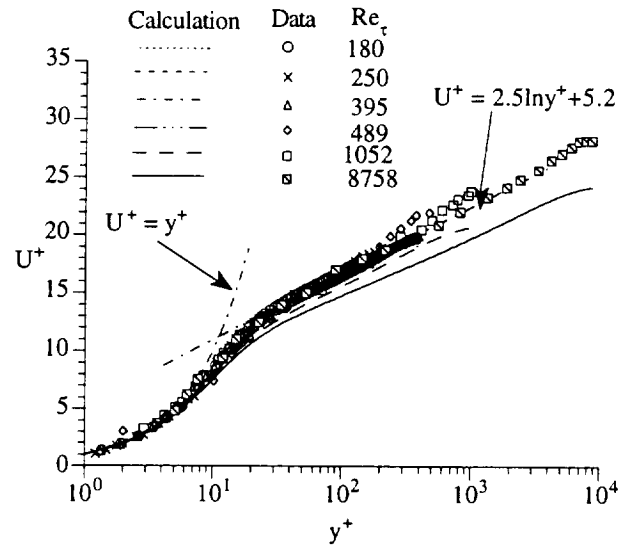
Fig. 3.30a Comparison of calculated mean velocity plotted in inner-layer variables to show Reynolds number effects in channel and pipe flows.
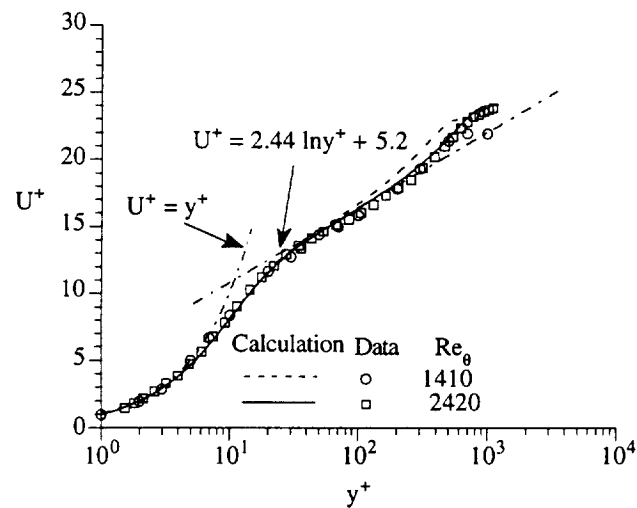
Fig. 3.30b Comparison of calculated mean velocity plotted in inner-layer variables to show Reynolds number effects in boundary layer flows.

Calculation   Data   Re$_\tau$

$\cdots\cdots$ o   180

$\cdots\;\cdots$ 250

$-\cdot-\cdot$ △   395

$-\cdots$ ◊   489

$--\;-\;\cdot$ □   1052

$-\!-\!-\!-$ 8758

$-\overline{uv}+$

y$^+$
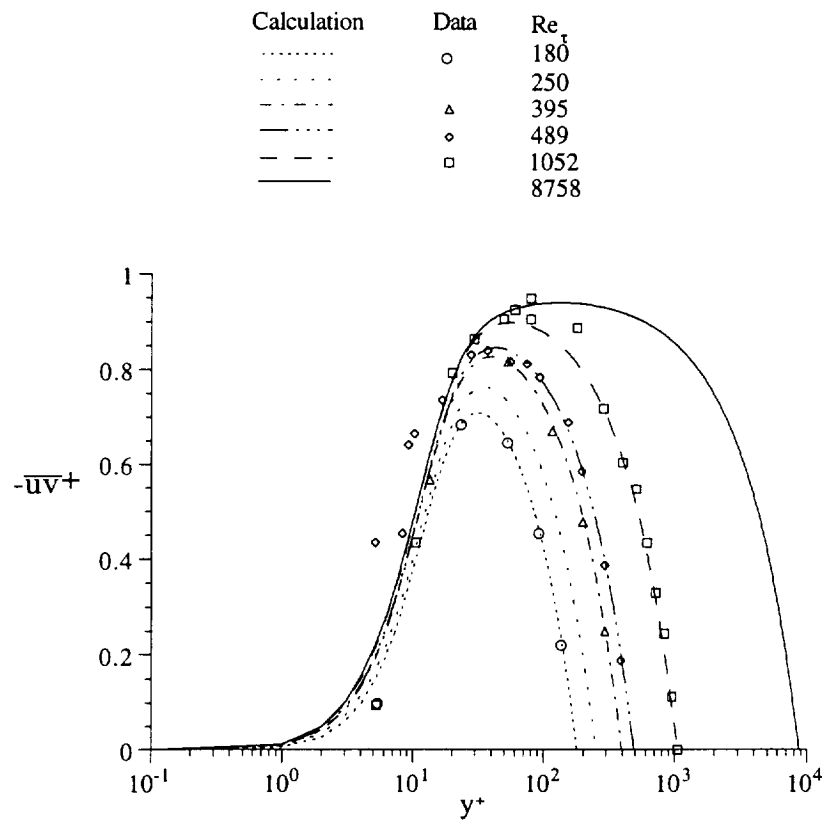
Fig. 3.31a Comparison of calculated turbulent shear stress $\overline{uv}^+$ with data to show Reynolds number effects in channel and pipe flows.

85
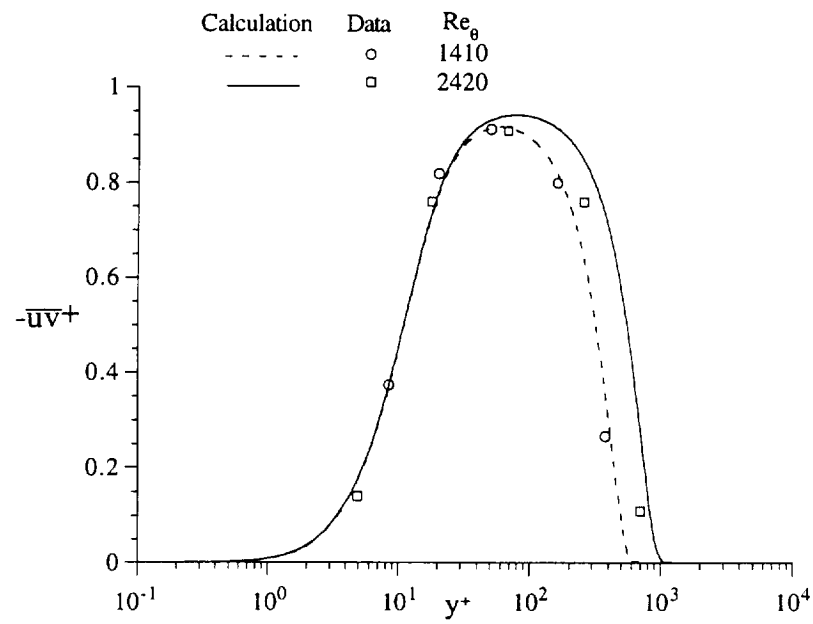
Fig. 3.31b Comparison of calculated turbulent shear stress $\overline{uv}^+$ with data to show Reynolds number effects in boundary-layer flows.
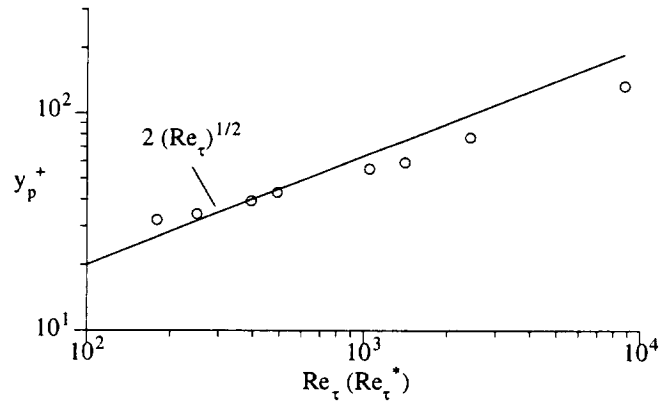
Fig. 3.32 Variation of the shear stress peak location y_p^+ wtih Re_τ.

Calculation	Data	Re_τ
··········	o	180
· · · · ·		250
— · — · ·	Δ	395
—·····	◦	489
— — ·	□	1052
—————		8758
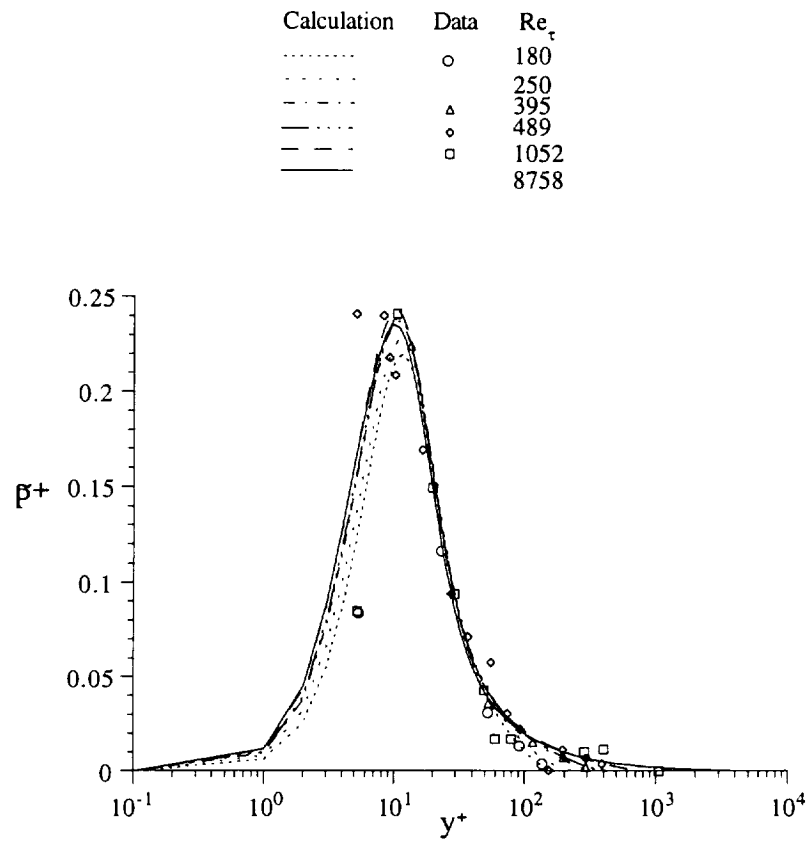
Fig. 3.33a Comparison of the calculated production of turbulent kinetic energy $\tilde{P}^+$ with data to show Reynolds number effects in channel and pipe flows.
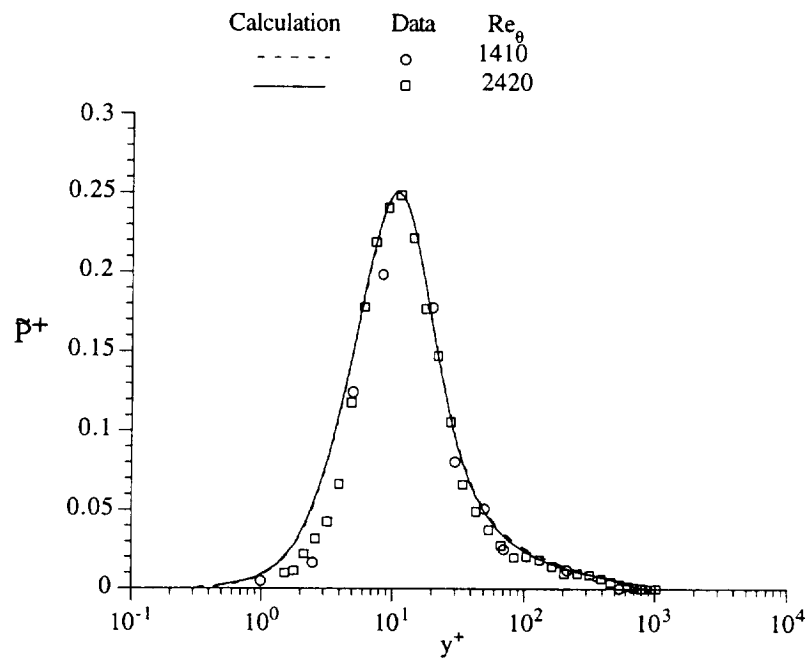
Fig. 3.33b Comparison of the calculated production of turbulent kinetic energy $\tilde{P}^+$ with data to show Reynolds number effects in boundary layer flows.
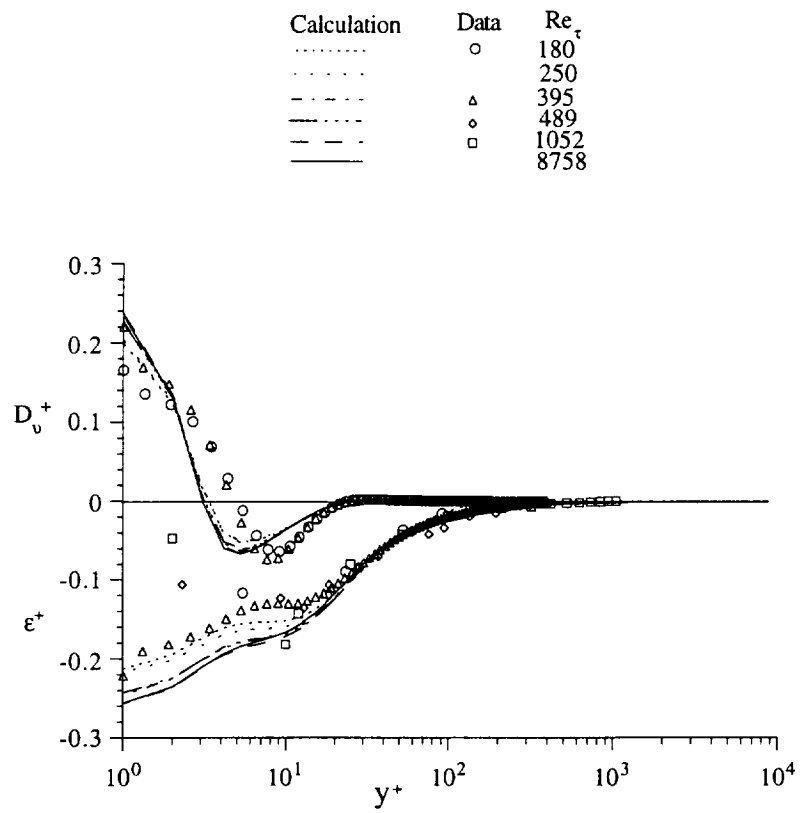
Fig. 3.34b Comparison of the calculated turbulent dissipation rate ε^+ and diffusion D_v^+ of turbulent kinetic energy with data to show Reynolds number effects in boundary-layer flows.

4 VALIDATION AGAINST TURBULENT FLOWS WITH SWIRL AND SYSTEM ROTATION

4.1 Introduction

Swirling and rotating turbulent flows are often encountered in engineering applications. In swirling flows, the induced swirl velocity component changes the paths of fluid particles from parallel to spiral. The flow pattern is affected by the centrifugal force associated with local streamline curvature. Recirculation may appear in the central region of the pipe close to the inlet. In rotating flows, the rotation effect on flow patterns depends on the orientation of the rotating axis to the mean flow plane, i.e. the relative importance of the centrifugal force to the Coriolis force. Flow in a rotating pipe is mainly subject to the centrifugal force because the rotating axis is parallel to the mean flow direction. On the other hand, only Coriolis force is dynamically important to fully developed channel flow with rotating axis perpendicular to the mean flow plane. Therefore, with the presence of swirl and rotation, the flows become much more complicated than those discussed in Section 3. Although the present wall-independent near-wall Reynolds stress (NNWRS) model is developed for flows with complex geometry, the model is also expected to perform well for swirling and rotating flows. In this section, its ability to replicate such complex flows is tested and compared with that of the NWRS model.

4.2 Turbulent Swirling Flows in a Straight Pipe

4.2.1 Background Earlier studies on swirling flows were mainly concerned with the mean flow and pressure drop measurements and the decay of swirl along the pipe (Kreith and Sonju 1965; Backshall and Landis 1969; Yajnik and Subbaiah 1973; Murakami et al. 1976; Padmanabhan and Janek 1980; Ito et al. 1980; Kito 1984; Kito and Kato 1984). Little attention was paid to the decay of the turbulence field. Measurements on the evolution of the turbulence field were carried out only recently (Algifri et al.1987; Kitoh 1991; Parchen et al. 1993).

Swirling flows in a straight pipe can be generated by rotating an inlet section of the pipe (Weske and Sturov 1974) or by a vane swirler installed at the entrance of the pipe (Kitoh 1991).

92

The swirl intensity can be measured by the swirl number S defined as the ratio of the angular momentum to the axial momentum. For axisymmetric flows, swirl number can be expressed as (Kitoh, 1991)

$$S = \frac{2\int_0^{r_0} UWr^2 dr}{r_0^3 U_m^2} \quad ,$$

(4-1)

where U and W are the mean velocity components in the axial and azimuthal, respectively; U_m is the bulk mean axial velocity; r and r_0 are the radial position and the pipe radius.

Fig. 4.1 shows a typical azimuthal velocity profile W in axisymmetric swirling pipe flows. In the so called forced-vortex region, the velocity profile resembles that associated with rigid-body rotation, i.e., the velocity linearly increases with increasing distance from the centerline. The mean vorticity in the axial direction is a constant in this region. Outside the forced-vortex region, the velocity starts decreasing and matches the wall boundary condition through the boundary layer. The region between the boundary layer and the forced-vortex region is called the free-vortex region because the axial vorticity strength is almost zero there. Table 4.1 summaries the characteristics of swirling flows in forced- and free-vortex region. In forced vortex region, the rotational strain associated with swirl $(\partial W / \partial r - W / r) / 2$ is zero and swirl does not provide additional turbulent production. On the other hand, in the free-vortex region, the rotational strain is not zero and swirl provides extra production. Turbulence is thus stabilized in the forced-vortex region and destabilized in the free vortex generated by swirl. The extent of the forced- and free-vortex region in swirling flows depends on swirl intensity and the way swirl is generated. For instance, the swirling flows in Weske and Sturov's (1974) experiments, generated by a rotating gird in the inlet section, are forced-vortex-dominated, whereas the swirling flows generated by a vane swirler in Kitoh's (1991) experiments are free-vortex-type.

Flow characteristics near the pipe centerline also depends on the swirl number S. For flows with $S < 1$, a reverse flow region usually is not observed because the pressure depression is not strong enough to create a reverse flow. For flows with $S > 1$, a reverse flow region may appear

depending on whether other conditions, such as Reynolds number, inlet conditions and the way swirl is generated, are favorable to the formation of such region or not. For example, the experiments of Kitoh (1991) showed a reverse flow region existed, whereas the experiments of Weske and Sturov (1974) did not indicate such region existed, although the initial swirl number S_o is greater than one in both cases.

Swirl decays along the pipe as a result of wall friction, and the mean azimuthal velocity profile alters as flow approaches to the fully-developed state downstream. Swirl decay rate was found to be dependent on inlet swirl intensity, Reynolds number, and pipe roughness (Seno and Nagata 1972; Baker 1967; Padmanabhan and Janek 1980). For small swirl number, Kitoh (1991) derived an exponential formula to predict the attenuation of axisymmetric swirling flow along the pipe. For large swirl number, swirl decay rate can be obtained only by experiments or numerical computations.

The unique features of swirling flows have already been made use of in a number of engineering applications. Prominent among them are flames in gas turbines and furnace combustors in which swirl strongly contributes to efficiency of combustion by enhancing mixing, and to flame stability through recirculation. The primary mixing enhancement is attributed to higher levels of turbulence generated by the additional mean shear strain. Table 4.2 compares the mean shear strain components in swirling flows and parallel flows.

Turbulence in swirling flows is anisotropic. The anisotropy results from the uneven weighting of swirl effect on turbulent normal and shear stresses. The degree of anisotropy depends on the swirl intensity and the location in the flow. A rather careful analysis of this anisotropic behavior was carried out by Lilley and Chigier (1971) using the mean flow measurements of the swirling free jet experiment of Lilley and Chigier (1967). They found that depending on swirl number, the ratio $\tau_{rx} / \tau_{r\theta}$ varies from 2 to more than 8, where τ_{rx} and $\tau_{r\theta}$ are the rx and $r\theta$ components of the turbulent shear stress, respectively. Consequently, only

94

those more advanced turbulence models that can replicate stress anisotropic behavior are expected to give satisfactory predictions of swirling flows.

So far, most modeling work on swirling flows have been carried out by using modified versions of two-equation models (Sloan et al. 1986). With the isotropic turbulence assumption, two-equation models need to be modified before they are used to predict anisotropic swirling flows. Great efforts have been put on the improvement of swirl effect in two-equation modeling. The improvement was often marginal and obtained in a single tested case without further validation in others. This necessitates the need of using other turbulence modeling beyond the Boussinesq approximation. In other words, Reynolds stress modeling is needed for a more accurate prediction of swirling flows. A small number of attempts have been made to predict strongly swirling flows (free or confined) by using Reynolds-stress models (Jones and Pascau 1989; Hogg and Leschziner 1989; Fu et al. 1988). The results show clearly the superiority of the Reynolds stress models to the modified two-equation models.

4.2.2 Boundary conditions and numerical implementation   For axisymmetric swirling flows in a straight pipe, the model governing equations are elliptic. To solve the equations in the (x, r)-plane, boundary conditions at the inlet and outlet of the computational domain, along the centerline of the pipe and at the wall are required. The inlet boundary conditions for numerical computations are provided by the available experimental data at the first measured location (with interpolations if necessary). Turbulence kinetic energy k_{in} at the inlet of the computational domain can be specified from the available turbulent normal stresses by

$$k_{in} = \frac{\overline{uu}_{in} + \overline{vv}_{in} + \overline{ww}_{in}}{2} \quad . \tag{4-2}$$

The dissipation rate at the inlet is estimated from the turbulent kinetic energy according to

$$\varepsilon_{in} = \frac{k_{in}^{3/2}}{\lambda l} \quad , \tag{4-3}$$

where l is the characteristic length scale of the case considered (such as the radius of the pipe in a swirling pipe flow), and $\lambda = 0.02$ is a parameter. The turbulent shear stresses at the inlet are

95

specified from the mean shear strain rates through the Boussinesq approximation. At the outlet of the computational domain, negligible diffusion condition in the axial direction is found to be the most appropriate outlet boundary condition. This implies that the second derivatives of the dependent variables can be assumed to be zero for a sufficient long computational domain (100 diameters in the present study).

Along the centerline of the pipe, zero normal gradient is specified for all dependent variables except those that they are zero themselves,

$$\frac{\partial(U, \ W, \ \overline{uu}, \ \overline{vv}, \ \overline{ww}, \ \overline{uw}, \ \varepsilon)}{\partial r} = 0 \ , \text{ and } V = \overline{uv} = \overline{vw} = 0 \quad . \tag{4-4}$$

At the wall, the no-slip conditions are applied, i.e., all the variables are zero except dissipation rate ε, which is given by

$$\varepsilon_w = 2\upsilon \left(\frac{\partial \sqrt{k}}{\partial r} \right)_w^2 \quad . \tag{4-5}$$

The TEACH code for incompressible flows by Gosman and Ideriah (1976) is adopted for the numerical computations. This code uses the finite volume (cell) method to discretize the transport equations and adopts the SIMPLE (Semi-Implicit Method for Pressure-Linked Equations) algorithm of Patankar and Spalding (1972) to solve the discretized system of equations. A detailed account of the finite volume method and SIMPLE algorithm can be found in Patankar (1980), among many other references. Here, a brief description is given to the finite volume method and the solution procedure.

The time-averaged transport equations of mean and turbulence quantities can be rewritten in the following form

$$\nabla \bullet (U\Phi) = \nabla \bullet (\Gamma_\Phi \nabla \Phi) + S_\Phi \quad , \tag{4-6}$$

where Φ is a dependent variable representing U_i, ε, and $\overline{u_i u_j}$; Γ_Φ is the effective diffusion coefficient, and S_Φ represents the rest of terms that cannot be included into convection and diffusion terms. The flow domain is divided into a series of control volumes according to the given grid points. Equation (4-6) is integrated within each control volume and the result is

expressed in terms of the unknown variable at neighboring grid points. In a control volume centered at grid point P (Fig. 4.2), which is surrounded by the neighboring grid points E, W, N and S, the resulting discretized equation for Φ can be written as

$$A_P \Phi_P = A_E \Phi_E + A_W \Phi_W + A_N \Phi_N + A_S \Phi_S + \bar{S} \Delta V \quad , \tag{4-7}$$

where the subscript of Φ indicates the evaluated location; coefficients As involve U_i and Γ_ϕ, and depend on the method used to discretize the integrals corresponding to the convection and diffusion terms in (4-6); $\bar{S}$ is the average of the source term S_Φ in (4-6) over the control volume, and ΔV is the volume of the cell. The averaged source term $\bar{S}$ is expressed formally as a linear function of Φ,

$$\bar{S} = S_C + S_P \Phi_P \quad , \tag{4-8}$$

where S_P is the coefficient of Φ_P, and S_C is the part in $\bar{S}$ that does not depend on Φ_P (formally). For the turbulent transport equations governing the Reynolds stresses and dissipation rate ε, the averaged source term $\bar{S}$ is a strong function of the dependent variable Φ. One can come up with different expressions for S_P and S_C, especially for the complex source terms in the Reynolds-stress equations. It suffices to say that the way $\bar{S}$ is partitioned into S_C and $S_P \Phi_P$ plays a very crucial role in finding the solution. In general, it is desirable to have a negative S_P since a positive S_P could cause divergence.

In the present modeling of axisymmetric swirling flows, the hybrid scheme (a combination of the central difference and upwind schemes) described by Patankar (1980) is used. The control volume shown in Fig. 4.2 is used for all the dependent variables except the mean velocity in the axial and radial directions U and V. The control volumes for U and V are staggered as shown in Fig. 4.3a and Fig. 4.3b, respectively.

Since the system of equations (4-6) are nonlinear with coefficients and source terms as functions of Φ itself and other dependent variables, the final solution is obtained by iteration. Under-relaxation iteration technique (Patankar 1980) is used to solve the system of equations. With the introduction of the under-relaxation parameter α, (4-7) can be rewritten as,

97

$$\frac{A_P}{\alpha} \Phi_P = A_E \Phi_E + A_W \Phi_W + A_N \Phi_N + A_S \Phi_S + \bar{S}\Delta V + \frac{(1-\alpha)A_P \Phi_P^*}{\alpha} \quad , \tag{4-11}$$

where Φ_P^* stands for the value of Φ_P from the previous iteration.

A tridiagonal matrix algorithm is used to solve the system of equations (4-11). A line-by-line iterative approach is adopted in alternating directions within the consecutive stages of the SIMPLE algorithm as described by Patankar (1980). The details of handling the mean velocity and pressure variables and associated difficulties can also be found in Patankar (1980).

The implementation of the above numerical procedure to solve a Reynolds stress model is not a trivial task. For axisymmetric swirling flows, we still have eleven equations for eleven unknowns: three mean velocity components, six Reynolds stresses, one dissipation rate and one mean pressure variable. Obtaining the solutions of these highly nonlinear and coupled transport equations requires a great number of iterations. Intermediate results of a near-wall two-equation model are used to initialize the iterations, which usually lead to the converged solution faster. Converged solutions are obtained when the maximum residuals of the mass and momentum equations in the entire computational domain are less than a small number $\delta = O(10^{-3})$, i.e.,

$$R_{\max} = \max\{R_m, R_U, R_V\} < \delta \quad , \tag{4-12}$$

where R_Φ is the sum of the normalized absolute residuals across all the computational nodes, namely

$$R_\Phi = \frac{\sum \left| \sum_{I=E,W,N,S} (A_I \Phi_I) + \bar{S}\Delta V - A_P \Phi_P \right|}{F_{in} \Phi_{in}} \quad , \tag{4-13}$$

and $\Phi = 1$, U and V for the mass equation, momentum equations in axial and radial directions, respectively. F_{in} is the mass-flow rate at the inlet, and, Φ_{in} takes the inlet axial mean velocity for the momentum equations. Note that the azimuthal velocity W does not appear in the mass conservation equation for axisymmetric flows. Therefore, it is not used in the criteria for convergence (4-12).

4.2.3 Cases studied   Swirling flows with a reverse flow region provide further challenges for turbulence modeling. To rigorously test our turbulent models, the experiments of Weske and Sturov (1974) and Kitoh (1991) are selected for model validations. The reverse flow region observed in Kitoh's (1991) experiments starts near the inlet and has a length about 40 diameters of the pipe. According to the definition of swirl number (4-1), the reference or entrance swirl number S_o is about 1.3 in Weske and Sturov's case and approximately 1 in Kitoh's (1991) case; the Reynolds number (based on the pipe diameter and averaged mean axial velocity) is about 30,000 and 50,000, respectively. As mentioned before, due to different ways of generating swirl, the mean azimuthal velocity at the inlet of the pipe is forced-vortex dominated in the Weske and Sturov's case, whereas it is free-vortex-type in the Kitoh's case. As a result, the azimuthal velocity profiles evolve differently downstream. In Weske and Sturov's case, the dominated forced-vortex region reduces and the free-vortex region grows as swirl decays, with maximum azimuthal velocity shifting to the centerline of the pipe. In Kitoh's case, the free-vortex region is dominated in the reverse flow region, and initial swirl decay is only associated with free vortex motion.

4.2.4 Comparisons with data   The computational domain is one radius in the radial direction and 100 diameters in the axial direction. Two sets of grid points, 102×86 and 51×56 in the axial and radial directions (Figs. 4.4a - 4.4b), are tested. The first grid shown in Fig 4.4a is clustered in the inlet region, near-wall region and core (near centerline) region. The second grid shown in Fig. 4.4b is also clustered in near-wall region, but less dense in the inlet and core regions. For the NNWRS and NWRS models, both grids give almost the same predictions of the mean and turbulence flow fields. Thus, only the results from the grid 51×56 are presented here.

The numerical results are presented first for the Weske and Sturov's (1974) case and then for the Kitoh's (1991) case. Fig. 4.5 shows the streamline defined on the (x, r)-plane given by the NNWRS model. Similar flow pattern given by the NWRS model (no shown) is observed. The predicted flow pattern indicates no reserve flow occur in the flow region, which agrees with the experimental observations. Owing to small radial velocity V, the streamlines on (x, r)-plane are

almost parallel to the centerline. The predicted swirl intensity along the pipe is compared with the data in Fig. 4.6. Both models give about the same swirl decay rate, which gradually decreases along the pipe and approaches to a constant in the downstream. The predicted swirl number agrees very well with the data up to $x/D = 20$, but it is slightly overestimated at $x/D = 50$. Further downstream, no data are available for comparisons.

Figs. 4.7-4.9 compare model predictions of the mean flow and turbulent fields with available data at measured locations $x/D = 5.1$, 20 and 50 (note the first measured location, corresponding to $x = 0$ in the computational domain, is $x/D = 0.35$). Both models give almost the same results. The agreement between the predicted mean axial velocity U and the data is very good (Figs. 4.7a, 4.8a, and 4.9a). The mean axial velocity in the core region increases with increasing axial distance (x), and its profile becomes almost uniform across the entire cross-section (except the near-wall region) in the downstream. The predicted azimuthal velocity W also agree well with the data (Figs. 4.7b, 4.8b, and 4.9b), although it gives a slightly higher vorticity strength in the forced-vortex region and its peak location is shifted a little bit toward to the centerline. The peak value of W decreases due to the decay of swirl along the pipe, and W in the downstream becomes more uniform (cf. Fig. 4.7b with 4.9b). Both models essentially repeat the experimental findings that the forced-vortex region shrinks and the vorticity strength weakens as the distance from the inlet increases, whereas the free-vortex region increases with increasing distance. Predicted flow skewness near the wall at different measured locations is shown in Fig. 4.10 by plotting U as a function of W. Very close to the wall, the ratio U/W is a constant, which becomes larger as x increases.

The agreement between the predicted turbulent quantities (kinetic energy k and root-mean-squared turbulent fluctuations u_{rms}, v_{rms}, and w_{rms}) and the data is not very satisfactory (Figs. 4.7c-f and 4.9c-f; note that no experimental data are available at $x/D = 20$ for k, u_{rms}, v_{rms}, and w_{rms}). Near the inlet, at $x/D = 5.1$, the models predict the trends of these turbulent quantities reasonably well, and the agreement between the model predictions and the data in the core region is

100

acceptable (Figs. 4.7c-f). Further downstream, at $x/D = 50$, the model predictions agree well with the data in the region covering half the radius from the wall, but are underestimated in the core region (Figs. 4.9c-f).

For the Kitoh's case, the models are able to capture the recirculation in the core region near the inlet reported by Kitoh (1991) (Fig. 4.11). However, the length of the reverse flow region predicted by the models is only about 7 diameters, which is much smaller than the observed length. This accounts for the major discrepancies between the predicted and measured flow fields discussed below.

The predicted swirl number along the pipe is compared with the data and the empirical formula given by Kitoh (1991) (Fig. 4.12). The agreement among them is excellent. Swirl attenuates exponentially along the pipe with a constant decay rate. Figs. 4.13 - 4.17 compare the model results with the experimental data at following measured locations, $x/D = 12.3$, 19.0, 25.4, 32.4 and 39.0 (note that the first measured location, corresponding $x = 0$ in the computational domain, is $x/D = 5.7$). At each location, six plots are presented for the mean velocities U and W, turbulence kinetic energy k the root-mean-squares of turbulent fluctuations u_{rms}, v_{rms}, and w_{rms}. Overall, both models give almost the same predictions for mean flow and turbulent field (Figs. 4.13-4.17). Reverse axial velocity ($U < 0$) (predicted by the models) is observed only at $x/D = 12.3$, the closest location to the inlet (cf. lines in Fig. 4.13a with 4.14a-4.17a). This is consistent with the flow pattern shown in Fig. 4.11. At each location, the predicted mean velocities follow the data well in the near-wall region, whereas they depart from the data in the core region of the pipe with U being overpredicted and W being underpredicted. The disagreement becomes worse as the location is further downstream. Fig. 4.18 shows the predicted flow skewness in the near wall region. Again, very close to the wall, U is a linear function of W with a slope increases as the distance from the inlet increases.

For turbulence kinetic energy k and root-mean-squared turbulent fluctuations u_{rms}, v_{rms}, and w_{rms}, good agreement between the model predictions and the data is found in the near-wall region,

101

while discrepancy is observed in the core region of the pipe (Figs. 4.13c-f, 4.14c-f, 4.15c-f, 4.16c-f; 4.17c-f). Both models perform consistently in predicting the mean velocities and in predicting the turbulence variables. Note that in this case the turbulent stresses are quite irregular in the core region due to the recirculation. This case is a real challenge for any turbulence model.

4.3 Turbulent Developing Flow in a Rotating Pipe

4.3.1 Background   Flows in a rotating pipe can be classified as a subset of swirling flow discussed in the previous section because they are also subject to extra shear strain associated with the mean azimuthal velocity component. However, swirl intensity does not decay in rotating pipe flow because angular momentum is continuously imparted into the flow. In the downstream, the flow approaches to an equilibrium state as the profile of the mean azimuthal velocity approaches to a rigid-body-rotation distribution.

The rotation effect on a fully-developed pipe flow was studied by White (1964) and Murakami and Kikuyama (1980). Both studies showed that rotation stabilizes the turbulent flow field and reduces the flow resistance with a rate increasing as the rotation increases. In other words, rotation promotes the relaminization of a fully-developed turbulent flow. Experimental study of the rotation effect on developing turbulent flow in a rotating pipe was carried out by Kikuyama et al. (1983). They found out that when flow enters a rotating pipe with a uniform entrance velocity, it is affected by both destabilizing effect created by a large circumferential shear strain and stabilizing effect due to centrifugal force. Near the entrance, the wall boundary layer is very thin, and the mean azimuthal velocity has to decrease rapidly from the circumferential velocity of the wall to zero outside the boundary layer. The flow near the wall is subject to a very high mean circumferential shear strain, which results in great enhancement of the turbulence production. Therefore, the near-wall flow in the upstream region is destabilized by the dominated destabilizing effect. As flow moves to the downstream, the boundary layer becomes thicker and thicker, and the intensity of the destabilizing effect decreases due to the decrease of the circumferential shear strain. Far downstream, the flow becomes fully developed, and the fluid inside the rotating pipe rotates as

102

a rigid body. Since the rigid-body motion does not give rise to additional turbulence production, the flow is stabilized by the stabilizing effect of centrifugal force. It follows that as the flow develops along the rotating pipe, the destabilizing effect gives away to the stabilizing effect, and the flow will pass through a region where both effects are equally important. Hence, the flow in a rotating pipe is very complicated and provides a severe test for turbulent modeling.

Flow characteristics associated with developing turbulent flows in a rotating pipe are commonly found in the inlet part of fluid machines, heat exchangers, and cooling system of the rotors. Therefore, correct modeling of rotating turbulent flows is very important for the design and development of any rotating machines. Attempts have been made to model developing turbulent flow in a rotating pipe through the streamline curvature modification with partial success. Most recently Yoo et al. (1991) used a near-wall Reynolds stress model based on the LRR pressure-strain model discussed in Section 2 to model the rotating pipe flow. Their model gave fairly good predictions in comparison with Kikuyama et al.'s (1983) data. In this section, the performance of the NNWRS model will be assessed by comparing the model predictions with Kikuyama et al.'s (1983) data and those given by the NWRS model and Yoo et al.'s model.

4.3.2 Numerical considerations   The governing equations for rotating pipe flow are the same as those for swirling flow. At the inlet of the flow domain, the mean axial velocity is determined from the measurement, and the turbulence quantities are estimated from the inlet mean axial velocity U_{in}. More specifically, the turbulent kinetic energy k_{in} and normal stresses $\overline{uu}_{in}$, $\overline{vv}_{in}$, and $\overline{ww}_{in}$ are specified according to the following formula:

$$k_{in} = IU_{in}^2 \quad , \tag{4-14a}$$

$$\overline{uu}_{in} = k_{in} \quad , \tag{4-14b}$$

$$\overline{vv}_{in} = 0.6k_{in} \quad , \tag{4-14c}$$

$$\overline{ww}_{in} = 0.4k_{in} \quad , \tag{4-14d}$$

where I is the measured turbulence intensity at the inlet, the dissipation rate is estimated according to the formula (4-3), and the turbulent shear stresses are approximated by Boussinesq approximation. Negligible diffusion conditions in the axial direction are imposed at the outlet of the computational domain, and axisymmetry condition (4-4) is used at the centerline. No-slip condition requires that at the moving wall W equal to the circumferential velocity of the pipe surface W_o, and other variables, except mean pressure and dissipation rate, be zero. The dissipation rate ε at the moving wall is given by (4-5). Same numerical procedure discussed in section 4.2 is adopted here for the calculation of developing flow in a rotating pipe.

4.3.3 Results and discussion   The developing pipe flow experiments of Kikuyama et al. (1983) are used to validate our models. Three sets of experimental data with rotation number $N = W_o / U_m = 0, 0.5$ and 0.83 are available, where U_m is the averaged mean axial velocity at the inlet. The corresponding swirl number S is 0, 0.25, and 0.415, respectively. The entrance velocity is almost uniform with Reynolds number $\mathrm{Re} = U_m D / \upsilon = 6 \times 10^4$. The turbulence intensity I at the entrance was about 0.3%. Both mean and turbulence flow quantities were measured at several locations.

The computational domain again is $0.5D\ (r) \times 100D\ (x)$ with a 51×56 grid in radial and axial directions. The grid is found to be able to give grid independent results. Numerical computations are carried out for three cases with rotation numbers $N = 0$, 0.5 and 0.83 in Kikuyama's (1983) experiments. The results for the most severe case, namely $N = 0.83$ case is presented below to show the models' ability to predict developing turbulent flow in a fast rotating pipe. For other two smaller rotation number cases, model predictions are in better agreement with the measurement. The rotation effects on the turbulent kinetic energy is shown as N increases from 0 to 0.83.

Model predictions of the mean axial and azimuthal velocity profiles are compared with the data at the first and last measured locations $x / D\ =\ 2.7$ and 28.5 in Fig. 4.19a-4.19b. All three models give good predictions of the mean velocity profiles, and the results given by the NNWRS and NWRS models are very close. For the axial velocity U, the NNWRS and NWRS models

104

give better predictions at the first measured location $x / D = 2.7$ than at the last measured location $x / D = 28.5$. For the azimuthal velocity W, the agreement between the predictions given by the NNWRS and NWRS models and the data is almost the same at these two locations. Our model predictions of U and W follow the trend of the data with a small deviation. Yoo et al.'s (1991) model gives slightly better predictions of U and W in terms of magnitude, but not slope. The measurements in Fig. 4.19 indicate that the boundary layer becomes more developed downstream, and the mean axial velocity profile at $x / D = 28.5$ is close to that in a fully-developed pipe flow. These features are essentially captured by all three models.

The comparisons for Reynolds stress components at $x / D = 2.7$ and $x / D = 28.5$ are presented in Figs. 4.20-4.25. Turbulent fluctuations (or normal stresses) and shear stresses spread out into the core region as the destabilizing effect associated with the circumferential shear strain decreases and the stabilizing effect due to centrifugal force becomes more dominated (cf. panel a to panel b in Figs. 4.20-4.25). In the near-wall region, all the models overpredict the turbulent fluctuations (normal stresses) u_{rms}, v_{rms} and w_{rms}, except u_{rms} at $x / D = 2.7$ where the peak value is predicted well by the models (Figs. 4.20 - 4.22). Yoo et al.'s model much more overpredicts the peak values of the v_{rms} than the NNWRS and NWRS models do (see Fig. 4.21a and 4.21b). Overall, the predicted turbulent fluctuations by the NNWRS and NWRS models agree slightly better with the measurements than those by Yoo et al.'s model do. The components of the shear stresses are generally overpredicted by the NNWRS and NWRS models (Figs. 4.23 - 4.25) except for $\overline{vw}$ at $x / D = 28.5$ and $\overline{uw}$ at $x / D = 2.7$ (Figs 4.24b and 4.25a). The performance of Yoo et al.'s model varies depending on the individual component and the measured location. It gives good predictions of each shear strain component at one location, but either overpredicts or underpredicts the same component at the other location.

To show how the mean velocity profiles evolve along the pipe from the upstream to the downstream, we plot the axial and azimuthal velocity components at four different measured locations: $x / D = 2.7$, 9.7, 15.5 and 28.5 in Figs. 4.26a - 4.26b. Note that only the results of

the NNWRS model and the measurements are compared. Both the axial and azimuthal velocities have similar profiles at these four different locations. As the flow moves to the downstream, the boundary layer thickness increases and the variations of U and W across the boundary layer become less rapid. The NNWRS model follows the trends of the measurements quite well but with a small offset. Distributions of the turbulent kinetic energy k at the same locations are shown in Fig. 4.26c. As expected, the turbulent kinetic energy k spreads out into the core region resulting from the increase of the stabilizing effect and the decrease of the destabilizing effect in the downstream. The NNWRS model replicates this observed phenomenon, but it overestimates the maximum kinetic energy and underestimates the spreading rate.

The effects of rotation number N on the mean axial and azimuthal velocity profiles at the last measured location $x / D = 28.5$ are shown in Figs. 4.27a - 4.27b. The NNWRS model gives better predictions for the moderate rotation number $N = 0.5$ case than for the high rotation number $N = 0.83$ case. Both the measurements and model predictions show that the mean axial and azimuthal velocity components far away from the inlet are not very sensitive to the rotation rate. Finally, the effects of rotation number N on evolution of the turbulent kinetic energy k are shown in Fig. 4.28. At the upstream location $x / D = 2.7$, the NNWRS model shows an increase of k with the rotation rate. This is because more turbulent production associated with the more intense shear strain is generated as rotating rates increases. At $x / D = 15.5$, the total kinetic energy for different rotation numbers are close to each other since the stabilizing and destabilizing effects are well balanced there. The drop in k at the downstream location $x / D = 28.5$ indicates the stabilizing effect there is dominated, resulting in the decrease of the turbulent kinetic energy with increasing rotation rate. These predictions are consistent with the experimental measurements given by Kikuyama et al. (1983).

4.4 Fully-Developed Turbulent Flow in a Rotating Channel

4.4.1 Background For fully developed flow in a spanwise rotating channel with constant angular velocity Ω (Fig. 4.29), the system rotation gives rise to two additional body forces:

Coriolis force and centrifugal force. However, only the Coriolis force is dynamically important because the centrifugal force term can be absorbed in the effective pressure

$$P_{eff} = P - \frac{1}{2}\rho(\Omega r)^2 \quad , \tag{4-15}$$

where P is the stationary pressure and r denotes the distance from the rotating axis. The strength of the Coriolis force can be measured by a rotation number

$$Ro = \frac{2|\Omega|h}{U_m} \quad , \quad \text{or} \quad Ro_\tau = \frac{2|\Omega|h}{u_\tau} \quad , \tag{4-16}$$

which is the relative strength of the Coriolis force to the inertial force. Here U_m is the bulk mean velocity, h is the half the channel width, and u_τ is the global friction velocity.

The flow under consideration is driven by an imposed mean pressure gradient,

$$\frac{dP_{eff}}{dx} = -\frac{\rho u_\tau^2}{h} \quad , \tag{4-17}$$

in the streamwise (x) direction. Thus, the turbulence can be treated as homogeneous in the streamwise (x) and spanwise (z) directions. In other words, the mean properties and turbulence statistics vary only in the transverse (y) direction. With the use of effective pressure, the governing equation for the mean flow is identical to that for non-rotating channel flow, i.e.,

$$\frac{1}{\rho}\frac{dP_{eff}}{dx} = \frac{d}{dy}\left(\upsilon \frac{dU}{dy} - \overline{uv} \right) \quad . \tag{4-18}$$

It follows from (4-17) and (4-18) that

$$u_\tau^2 = \frac{1}{2}\left(u_{\tau s}^2 + u_{\tau p}^2 \right) \quad , \tag{4-19}$$

where $u_{\tau s}$ and $u_{\tau p}$ denote the local friction velocity at the suction side and pressure side, respectively. When $\Omega > 0$ (< 0), $y / h = +1$ is the suction (pressure) side and $y / h = -1$ is the pressure (suction) side. Without system rotation, the mean flow is symmetric with respect to the (x, z)-plane at $y = 0$ and $u_\tau = u_{\tau s} = u_{\tau p}$.

In the transport equations for the individual Reynolds stress components, the production terms associated with mean shear and rotational stress generation are

$$P_{ij} = -\left[\overline{u_i u_k} \frac{\partial U_j}{\partial x_k} + \overline{u_j u_k} \frac{\partial U_i}{\partial x_k} \right] \quad , \tag{4-20a}$$

$$G_{ij} = -2\Omega_k \left[\overline{u_j u_m} e_{ikm} + \overline{u_i u_m} e_{jkm} \right] \quad , \tag{4-20b}$$

respectively. The components of P_{ij} and G_{ij} are given in Table 4.3. Since G_{kk} vanishes, no additional turbulence energy is generated directly through the rotational production term G_{ij}.

Pioneering work on fully developed flow in a channel rotating about a spanwise axis was carried out by Johnston et al. (1972). Their measurements covered a wide range of rotation numbers, Ro, from 0 up to 0.21 with Reynolds number Re ranging from 11500 to 35000. Here the Reynolds number is defined based on the bulk mean velocity U_m and the channel width $2h$ as $\text{Re} = 2U_m h / \upsilon$. The Coriolis force was found to affect both local and global stability of the flow. Three stability-related phenomena caused by the Coriolis force were observed or inferred: (1) it can change the streak bursting rate in the wall-layers; (2) it can suppress the turbulence production near the suction (stabilized) side; (3) it can develop a large-scale roll cell on the pressure (destabilized) side.

Theoretical and experimental studies were performed by Nakabayashi and Kitoh (1996) on low-Reynolds-number, fully developed turbulent flow in a rotating channel. Low-Reynolds-number flow is found to be more strongly affected by the Coriolis force than high-Reynolds-number flow. The Coriolis force affects the logarithmic layer and the core region. By dimensional analysis, they deduced that Reynolds number $\text{Re}_\tau = u_\tau h / \upsilon$ and Ro are the two parameters determining the overall flow structure. The ranges of these two parameters in the experiments they investigated are $28 \le \text{Re}_\tau \le 155$ ($1700 < \text{Re} < 10000$) and $0 < Ro < 0.055$.

Laboratory investigations of turbulence in rotating reference systems are more difficult to accomplish than most other experiments, simply because the flow apparatus has to be mounted on a rotating turntable. While fully developed flows are relatively difficult to realize in the laboratory,

108

especially in a rotating system, such flows have been attractive objects for numerical study in the past two decades. Kim (1983) was the first to perform large-eddy simulations (LES) for rotating channel flow with a moderate rotation number $Ro = 0.068$, which revealed how the Coriolis force introduced by the system rotation can stabilize or destabilize turbulence on different sides of the plates. Miyake and Kajishima (1986) also carried out large-eddy simulations for rotation number up to 0.2. They presented various statistical turbulence quantities and concluded that in the near-wall region, the Coriolis force enhances sweep and ejection on the pressure side, while reduces them on the suction side. However, the rather course grid used made their results less reliable and the conclusions less convincing.

Kristoffersen and Anderson (1993) performed direct numerical simulations (DNS) of fully-developed rotating channel flow for rotation number Ro up to 0.50 at Re = 5800. Their simulation results showed that with increasing rotation the damping and augmentation of turbulence along the suction side and pressure side, respectively, become more significant, resulting in highly asymmetric profiles of mean velocity and turbulent Reynolds stresses. The mean velocity profile exhibits an appreciable region with slope 2Ω, in accordance with the experimental observations of Johnston et al. (1972). At $Ro = 0.50$ the Reynolds stresses vanishes in the vicinity of the suction (stabilized) side. Because the gird they used, $128 \times 128 \times 128$, is find enough to resolve all essential scales of the low-Reynolds-number turbulence, their rather complete data become very useful to verify turbulent models for rotating turbulent flow.

A Reynolds stress model is required to model rotating channel flow because of high anisotropic turbulence caused by the Coriolis force. Second-order turbulence models have been used to predict rotating channel flow recently. Launder et al. (1987) and Shima (1993) obtained good agreement with the experimental results of Johnston et al. (1972) and large-eddy simulations of Kim (1983). Tselepidakis (1991) made an attempt to model the fully developed rotating channel flow studied by Kristoffersen and Anderson (1993). Very good agreement was obtained with low rotation number $Ro = 0.05$. However, no results were reported for higher rotation number due to

numerical stability. He suggested that the problem could be overcome by reconstructing a new dissipation rate tensor ε_{ij}.

4.4.2 Results and discussion   In the present study, the cases studied by Kim (1983) and Kristoffersen and Anderson (1993) are selected to test our near wall models' ability to predict fully developed channel flow with spanwise rotation. In Kim's case, the rotation number is $Ro = 0.068$ ($Ro_\tau = 1.47$) and the Reynolds number is $\mathrm{Re}_c = 2U_c h / \upsilon = 13800$ (where U_c is the centerline mean velocity) ($\mathrm{Re}_\tau = 640$); in Kristoffersen and Anderson's case the rotation number $Ro(Ro_\tau)$ varies from 0 to 0.50 (7.55) at Reynolds number $\mathrm{Re} = 5800$ ($\mathrm{Re}_\tau = 194$). The iterative scheme for the fully developed channel flow in Section 3 is adopted here for the calculations of the fully developed flow in a rotating channel.

The numerical results are presented first for Kim's (1983) case, and then for Kristoffersen and Anderson's (1993) case. Note that the channel in these two cases rotates in opposite directions, i.e. $\Omega > 0$ in Kim's case, whereas $\Omega < 0$ in Kristoffersen and Anderson's case. Accordingly, $y/h = -1$ is the pressure side and $y/h = +1$ is the suction side in Kim's case, whereas $y/h = -1$ is the suction side and $y/h = +1$ is the pressure side in Kristoffersen and Anderson's case. The global wall friction velocity u_τ is used to normalize the flow variables when variations across the entire channel $-1 \leq y/h \leq +1$ are presented, whereas the local friction velocities $u_{\tau p}$ and $u_{\tau s}$ are used in the scaling of computed results whenever the inner coordinate y^+ near the pressure and suction sides, respectively, labels the abscissa. In the computations, two damping functions, (2-29a) for Kim's case and (2-29b) for Kristoffersen and Anderson's case, are used in the NWRS model due to the significant difference in Reynolds numbers, whereas same damping function (2-33) is used in the NNWRS model for both cases.

Figs. 4.30a - 4.30b compare the predicted mean velocity with the LES data given by Kim (1983) in wall coordinates. The LES data show that the normalized mean velocity U^+ lies above and below the semi-logarithmic law $U^+ = 2.5\ln y^+ + 5.5$ in the region near the centerline on the suction side (Fig. 4.30a) and pressure side (Fig. 4.30b), respectively. On the suction side

110

($y / h = +1$), the wake component is increased due to the decrease of local friction velocity $u_{\tau s}$ (i.e. $u_{\tau s} < u_\tau$). On the pressure side ($y / h = -1$), the increased local friction velocity (i.e. $u_{\tau p} > u_\tau$) suppresses the wake component in the velocity profile. Both the NNWRS and NWRS models are basically able to capture these features; the NWRS model is in better agreement with the LES data than the NNWRS model does.

Fig. 4.31a plots the normalized mean velocity U / U_c distribution between the plates. The model results are essentially identical and follow the LES data quite well. The data and the model results show a slight asymmetry in the mean velocity profiles due to the presence of rotation. Both models give about the same shear stress $\overline{uv}$ predictions as shown in Fig. 4.31b. Fig. 4.31c shows that the peak value decreases on the suction side ($y / h = +1$) and increases on the pressure side ($y / h = -1$) in comparison with the non-rotating case (no shown). Note that although the rotational production term G_{ij} does not have a direct contribution to the generation of turbulent kinetic energy, it affects the mean shear production term P_{ij} through changing the turbulent stress distributions and the mean velocity gradient, resulting in the redistribution of the kinetic energy k^+ between the plates. The NWRS model predicts a much higher peak value of k^+ on both sides compared with the NNWRS model. Away from the walls, both models give almost the same predictions, which are slightly overestimated on the suction side and underestimated on the pressure side. In Fig. 4.31d, the LES shows that in the core region, turbulence is more isotropic on the pressure side than on the suction side. Both models also show that turbulent fluctuations are more isotropic (i.e. u_{rms}^+, v_{rms}^+ and w_{rms}^+ are closer to each other) on the pressure side. However, except for u_{rms}^+ on the pressure side, model predictions of turbulent fluctuations do not agree well with the LES data. Overall, the models seem to have the ability to replicate the rotation effect, but they are less responsive to the influence of the rotation. Further verification for the models is needed since in this case the rotation number $Ro = 0.068$ is relatively small compared with its high Reynolds number $Re_c = 13800$.

111

According to Nakabayashi and Kitoh (1996), with the same rotation number, the rotation effect is more influential in low-Reynolds-number flow than in high-Reynolds-number flow. To further examine the rotation effect in the model, computations are carried out for the low-Reynolds-number case of Kristoffersen and Anderson with rotation numbers $Ro = 0$, 0.01, 0.05, 0.10, 0.15, 0.20, and 0.50 (these values correspond to $Ro_\tau = 0$, 0.15, 0.755, 1.51, 2.265, 3.02, and 7.55, respectively). The calculation for rotation number $Ro = 0$ is to test the code and provide a reference to identify the rotation effects (Fig. 4.32-4.33). The NWRS and NNWRS models repeat their performance in fully developed channel flow without rotation. Note that all flow variable profiles are symmetric about the center plane $y = 0$ (Fig 4.33). In the following presentation, the mean velocity profiles are shown in the wall and global coordinates for each rotation number, whereas the turbulence quantities are plotted only in the global coordinate.

Figs. 4.34a - 4.34b plot the mean velocity profiles in the wall coordinates for $Ro = 0.01$. According to the DNS, the effect of the Coriolis force at this low rotation number can be considered as a small perturbation to the non-rotating case, and the velocity profiles in the core region on different sides deviate slightly from the log law $U^+ = 2.5\ln y^+ + 5.5$. The deviation on the pressure side is more noticeable than that on the suction side. Our model predictions agree very well with the DNS data on the suction side (Fig. 4.34a). On the pressure side, the NNWRS model predicts a slight larger mean velocity in the core region compared with the DNS data, whereas the predictions given by the NWRS model are closer to the DNS data. Predicted mean velocity and turbulence quantities are further compared with the DNS data in the global coordinate (Fig. 4.35). The agreement between our model predictions and the DNS data is very close to that in the non-rotating case (cf. Fig. 4.35 with its counterpart Fig. 4.33). The weak rotation in this case only causes a small perturbation from the non-rotating state.

The predicted mean velocity profiles and the DNS data for $Ro = 0.05$ are shown in Fig. 4.36. The DNS data show that the rotation effect becomes more pronounced, namely the wake component is appreciably enhanced on the suction side and is eliminated on the pressure side. This

112

is accompanied by the rather significant decrease and increase of the wall fiction velocity on the suction and pressure sides respectively. The velocity profiles predicted by the NNWRS and NWRS models, however, only slightly deviate from the law of the wall. Compared to their predictions for $Ro = 0.01$ (cf. Fig. 4.36 with Fig 4.34), the models are not sensitive to the increase of rotation. This insensitivity is also observed when mean velocity and turbulence quantities are plotted in the global coordinate (compare the model predictions in Fig. 4.37 with Fig. 4.35). The DNS data show that the rotation already has a significant influence on the turbulent field at this rotation number. The peak of the shear stress $\overline{uv}$ increases on the pressure side but decreases on the suction side (cf. Fig. 4.37b with Figs. 4.33b and 4.35b). This is because the rotational production term G_{ij} (see Table 4.3) in the $\overline{uv}$-transport equation is positive near the wall and therefore tends to reduce the negative value of $\overline{uv}$ on the suction side and increase it on the pressure side. Away from the walls, the viscous effect is negligible, and the shear stress profile becomes linear (see (4-18)). The peak value of the turbulent kinetic energy drops on the suction side ($y / h = -1$) and rises on the pressure side ($y / h = +1$) quite significantly (Fig. 4.37c); the peaks of turbulent fluctuations v_{rms}^{+} and w_{rms}^{+} in the vicinity of the suction side tends to disappear (Fig. 4.37d). The models do not predict such features. The rotation number $Ro = 0.05$ in this case is close to $Ro = 0.068$ in Kim's case. Comparing the LES data in Figs. 4.30-4.31 and the corresponding DNS data in Figs. 4.36 - 4.37, we find that the rotation effect is more influential in this low-Reynolds-number case ($Re_{\tau} = 194$) than in the high-Reynolds-number Kim's case ($Re_{\tau} = 640$), which is in accordance with Nakabayashi and Kitoh (1996).

As the rotation number increases up to $Ro = 0.20$, comparisons between the models' results and the data are qualitatively similar to those for $Ro = 0.05$ with some quantitative differences. The comparisons for mean velocity profiles in the wall coordinates are presented in Figs. 4.38, 4.40, and 4.42 for rotation number $Ro = 0.10$, 0.15 and 0.20, respectively, whereas those for turbulence quantities can be found in Figs. 4.39, 4.41, and 4.43.

At $Ro = 0.50$, the difference in the mean flow and turbulent field on the suction side and pressure side becomes striking. The DNS shows that the mean velocity profile is close to the linear law $U^+ = y^+$ on the suction side, whereas an anomalous behavior is observed on the pressure side: the profile diverges from the linear law at $y^+ \approx 5$. The NNWRS and NWRS models seem to be able to capture these features, although the predicted profiles deviate from the data. Unlike those lower rotation number cases ($Ro < 0.5$) (see Figs. 4.34b, 4.36b, 4.38b, 4.40b, and 4.42b), the difference in the predicted mean velocity profiles is quite large on the pressure side in this case. The NWRS model results are in a better agreement with the data. In the global coordinate (Fig. 4.45a), a linear region in the DNS mean velocity profile is observed. Both models are able to predict this characteristic flow region, though the predicted slope is smaller than the expected 2Ω as indicated by the data. The predicted shear stress $\overline{uv}$ shows a better agreement with the data in this case than in all lower rotation number cases except for $Ro = 0.01$ case (cf. Fig. 4.45b with Figs. 4.37b, 4.39b, 4.41b, and 4.43b). More pronounced rotation effects are also observed in the kinetic energy and turbulence fluctuations at $Ro = 0.50$ (Figs. 4.45c - 4.45d). According to the data, on the suction side, the strong rotation effect has eliminated the peaks of the kinetic energy k^+ and the normal stress in the wall normal direction v_{rms}^+, and tends to eliminate the peaks in the other two normal stresses u_{rms}^+ and w_{rms}^+. In the core region, v_{rms}^+ is dominant among the three normal stress components. The NNWRS and NWRS models have shown a more significant rotation effect at $Ro = 0.50$ in comparison with the lower Ro cases. More asymmetry due to rotation in the predictions is observed at this rotation number. However, the rotation effect predicted by the models are still much weaker than that shown in the DNS. For instance, the peaks in the kinetic energy k^+ and normal stresses u_{rms}^+, v_{rms}^+, and w_{rms}^+ near the suction side still remain.

To show more clearly the variations of the predicted mean velocity as the rotation rate increases, we plot the mean velocity profiles predicted by the NNWRS model for different Ro in the wall coordinates together in Fig. 4.46a and Fig. 4.46b. The mean velocity profiles on the

114

suction side lie above the profile for the non-rotating case in the semi-logarithmic region. The profile for small Ro still exhibits a logarithmic region. As Ro increases, the profile has a more laminar-like shape and approaches the linear law $U^+ = y^+$. Correspondingly, the mean velocity profiles on the pressure side lie below the profile for $Ro = 0$. These profiles still exhibit the characteristic turbulent semi-logarithmic shape, but with a slope that decreases as Ro increases. At the highest rotation rate ($Ro = 0.50$), an anomalous behavior is observed.

Finally, Fig. 4.47 shows the effect of rotation on local wall friction velocities $u_{\tau s}$ and $u_{\tau p}$. The NNWRS and NWRS models follow the trend indicated by the DNS data, namely the wall friction velocity decreases on the suction side and increases on the pressure side as the rotation rate increases. The model results, however, show a weaker rotation effect on the wall friction velocities.

4.5 Concluding Remarks

The performance of the NNWRS model in predicting complex turbulent flow with swirl and rotation is examined in this section. More specifically, we apply the model to swirling pipe flow, developing rotating pipe flow, and fully developed channel flow with spanwise rotation and compare the model results with available experimental and LES/DNS data. The complexity of these flows provides severe tests for our models. In swirling pipe flow, the NNWRS model gives reasonable predictions for flow with no reverse flow region, whereas for flow with a reverse flow region, the model predicts a much smaller reverse flow region than that observed in the experiments. In developing flow along a pipe rotating around its axis, the NNWRS model is able to capture the flow pattern subject to both destabilizing effect resulting from the mean circumferential shear strain and stabilizing effect due to the centrifugal force. In the fully developed channel flow with spanwise rotation, at low rotation rate, the model predictions agree with the LES/DNS data. As the rotation rate increases, the model underestimates the rotation effect, which causes the augmentation and damping of the turbulence along the pressure and suction sides, respectively. The NWRS model behaves similarly as the NNWRS model in all the

115

cases considered. This implies that the near-wall modifications in the turbulence models become less important for complex flows such as swirling and rotating flows. Further improvement on the modeling is needed for a better agreement with the experimental data and the direct numerical/large-eddy simulations, in particular in the reverse flow region of the swirling pipe flow and semi-logarithmic region of the rotating channel flow where the Coriolis force is important. In the next section, the NNWRS model is further examined for turbulent flows with complex geometry.

Table 4.1   Comparison of shear strain rates in swirling and parallel flows

S_{ij}	Swirling flow	Parallel flow
S_{xx}	$\dfrac{\partial U}{\partial x}$	$\dfrac{\partial U}{\partial x}$
S_{rr}	$\dfrac{\partial V}{\partial r}$	$\dfrac{\partial V}{\partial r}$
$S_{\theta\theta}$	$\dfrac{1}{r}\left(\dfrac{\partial W}{\partial \theta}+V\right)$	$\dfrac{V}{r}$
S_{xr}	$\dfrac{1}{2}\left(\dfrac{\partial U}{\partial r}+\dfrac{\partial V}{\partial x}\right)$	$\dfrac{1}{2}\left(\dfrac{\partial U}{\partial r}+\dfrac{\partial V}{\partial x}\right)$
$S_{r\theta}$	$\dfrac{1}{2}\left(\dfrac{1}{r}\dfrac{\partial V}{\partial \theta}+\dfrac{\partial W}{\partial r}-\dfrac{W}{r}\right)$	$\dfrac{1}{2}\left(\dfrac{1}{r}\dfrac{\partial V}{\partial \theta}\right)$
$S_{x\theta}$	$\dfrac{1}{2}\left(\dfrac{1}{r}\dfrac{\partial U}{\partial \theta}+\dfrac{\partial W}{\partial x}\right)$	$\dfrac{1}{2}\left(\dfrac{1}{r}\dfrac{\partial U}{\partial \theta}\right)$

Table 4.2   Swirling flow characteristics

	Tangential velocity	Angular velocity	Vorticity
Forced vortex	$w = c * r$	$\omega = w / r$	2ω
Free Vortex	$w = c / r$	-	0

117

Table 4.3   Production terms in fully developed channel with spanwise rotation

ij	11	22	33	12
P_{ij}	$-2\overline{uv}\partial U / \partial y$	0	0	$-\overline{vv}\partial U / \partial y$
G_{ij}	$4\Omega\overline{uv}$	$-4\Omega\overline{uv}$	0	$-2\Omega(\overline{uu} - \overline{vv})$

Note: P_{ij} and G_{ij} are the production terms due to mean shear and rotation, respectively, and the expressions are:

$$P_{ij} = -\left[\overline{u_iu_k}\frac{\partial U_j}{\partial x_k} + \overline{u_ju_k}\frac{\partial U_i}{\partial x_k}\right],$$

and

$$G_{ij} = -2\Omega_k\left[\overline{u_ju_m}e_{ikm} + \overline{u_iu_m}e_{jkm}\right].$$

118
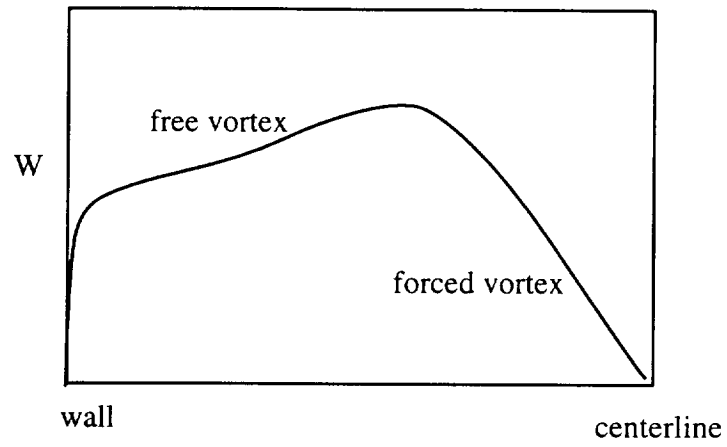
Fig. 4.1 Typical azimuthal velocity profile in a swirling pipe flow.
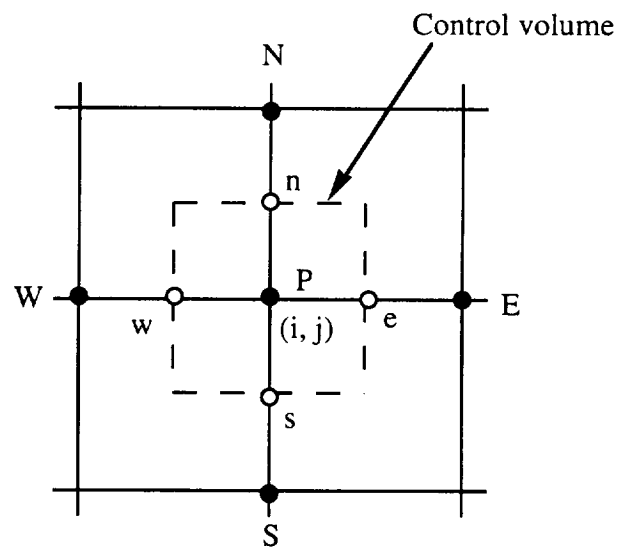
Fig. 4.2 Control volume centered at grid point P.
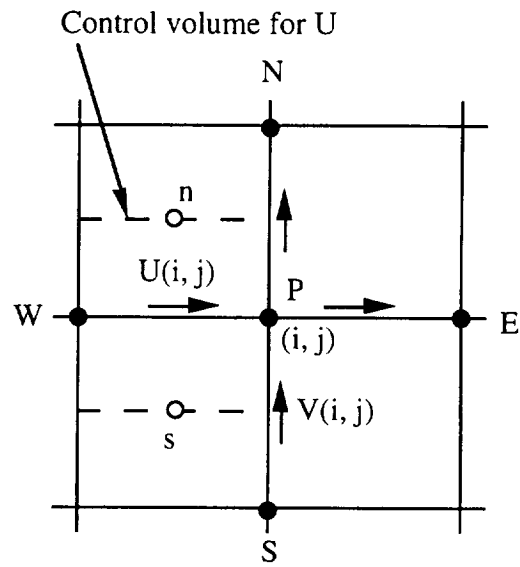
Fig. 4.3a Control volume for mean velocity in the axial direction (U).
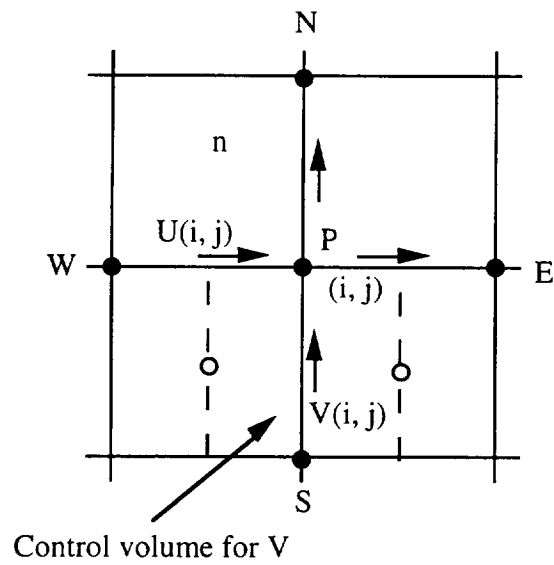
Fig. 4.3b Control volume for mean velocity in the radial direction (V).

120
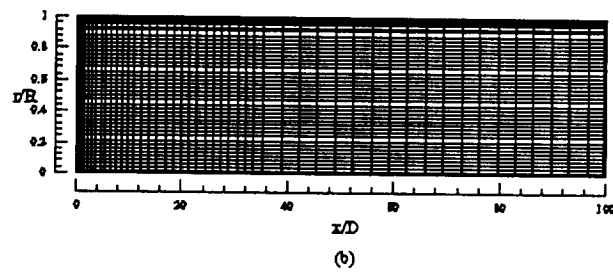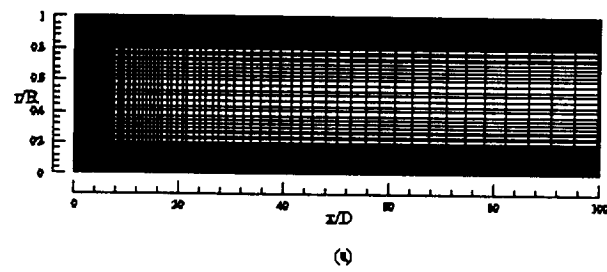
Fig. 4.4 Computational domain with grid distribution: (a) 102x86 and (b) 51x56 in the axial and radial directions.
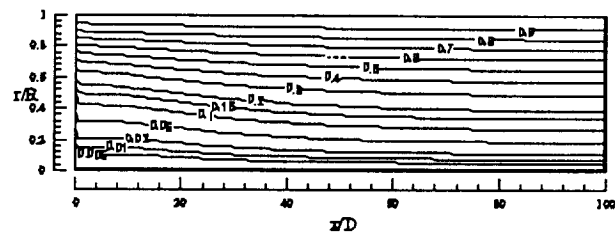
Fig. 4.5 Predicted streamlines in the (x, r) plane by the NNWRS model for Weake and Sturov's (1974) case.
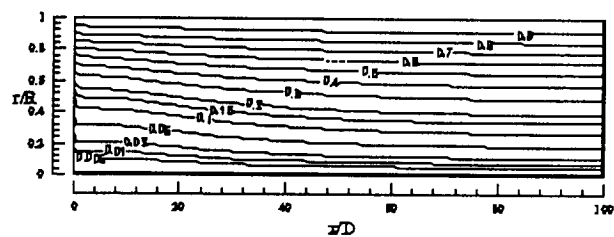
Fig. 4.5 Predicted streamlines in the (x, r) plane by the NNWRS model for Weske and Sturov's (1974) case.
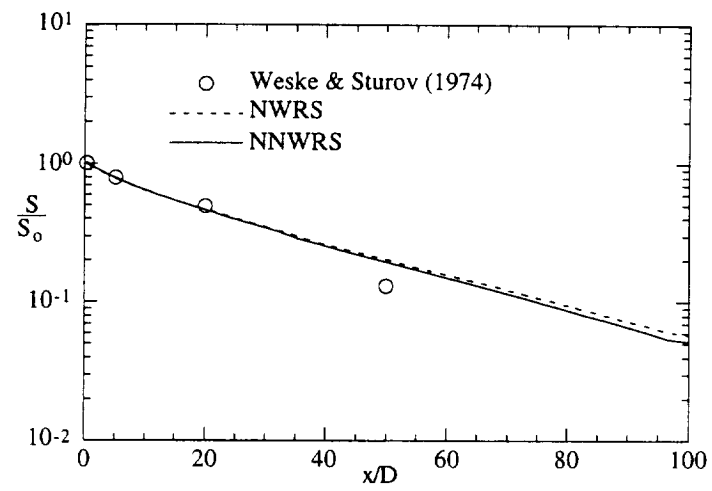
Fig. 4.6 Comparison between the predicted and the measured swirl number for
Weske and Sturov's (1974) case.
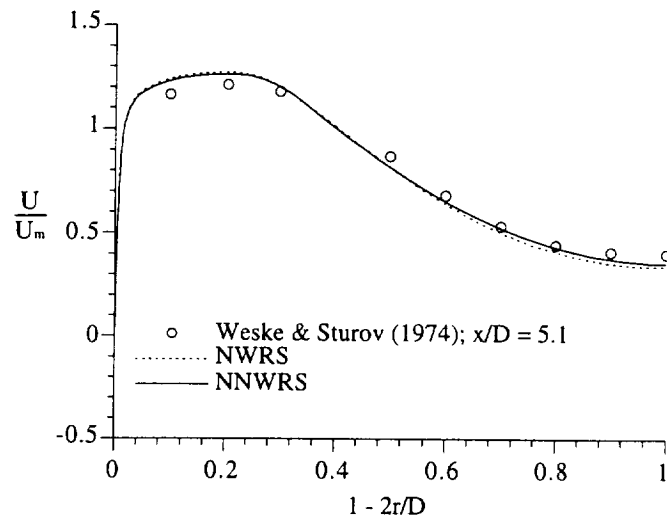
Fig. 4.7a Comparison between the predicted and measured mean axial velocity profiles at measured location $x / D = 5.1$.
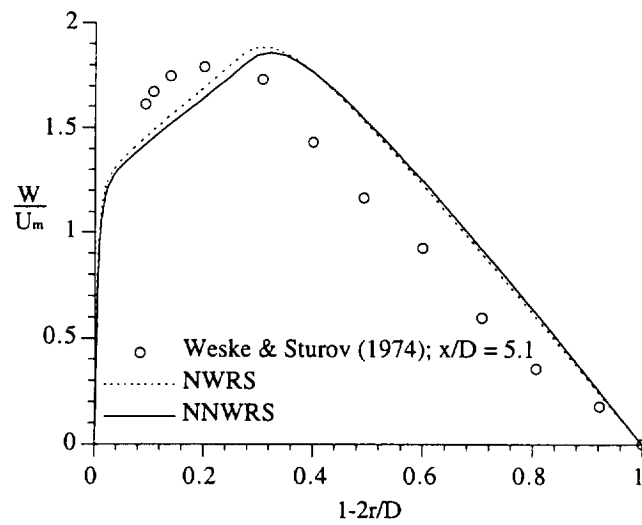
Fig. 4.7b Comparison between the predicted and measured mean azimuthal velocity profiles at measured location $x / D = 5.1$.
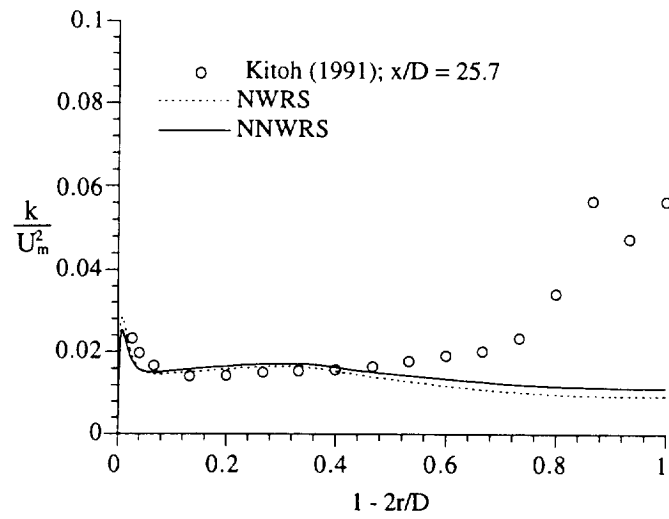
125
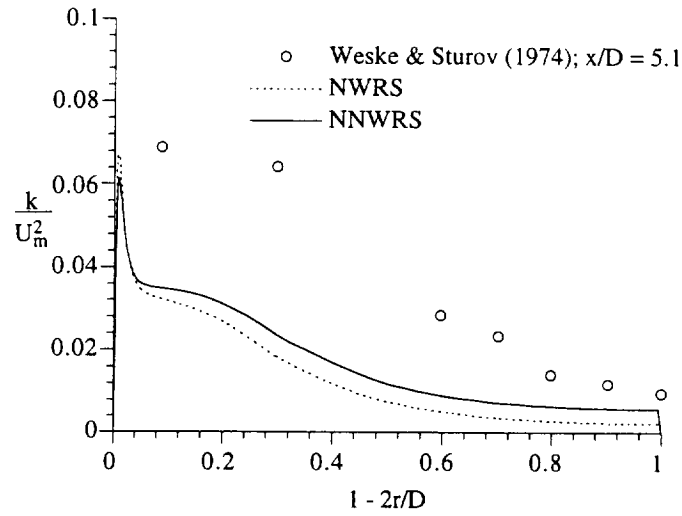
Fig. 4.7c Comparison between the predicted and measured turbulent kinetic energy at measured location $x / D = 5.1$.
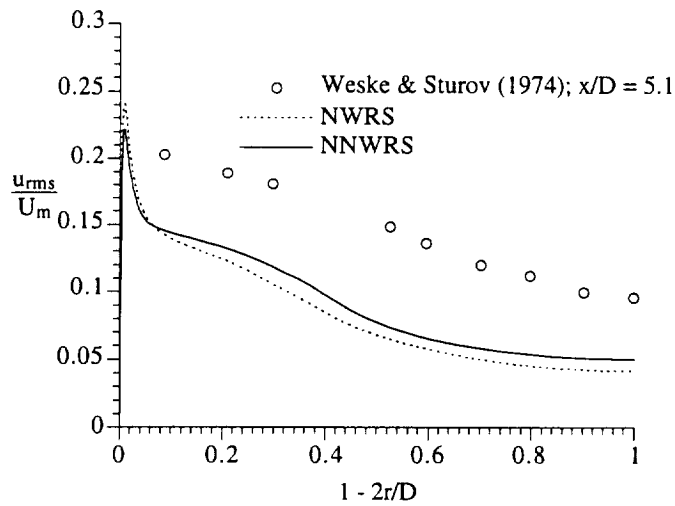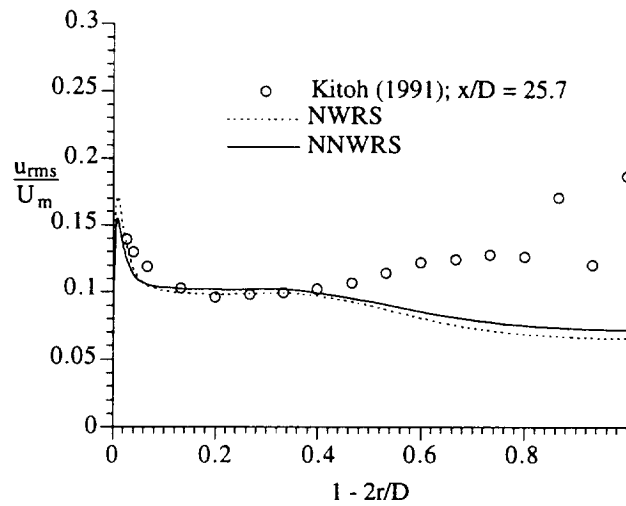

Fig. 4.7d Comparison between the predicted and measured turbulent fluctuation in the axial direction at measured location $x / D = 5.1$.
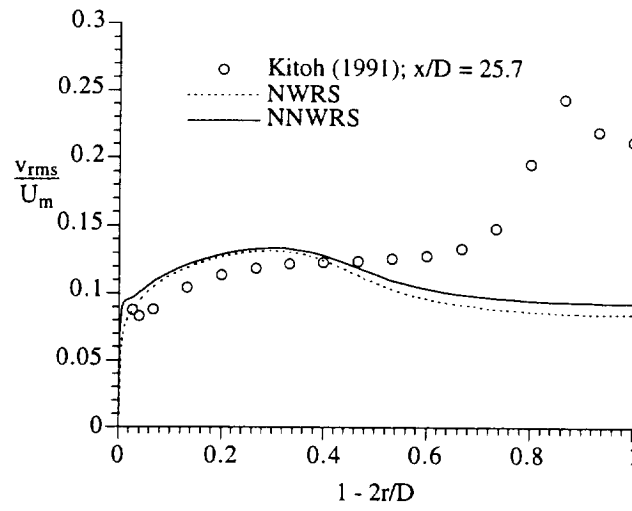
126
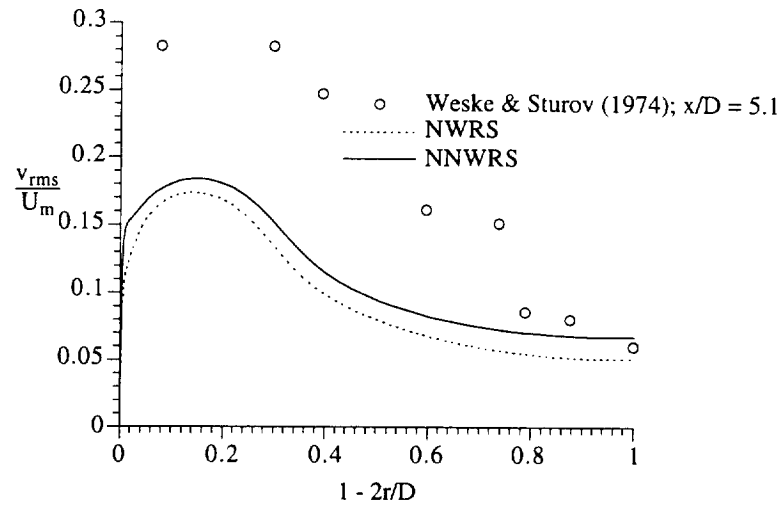
Fig. 4.7e Comparison between the predicted and measured turbulent fluctuation in the radial direction at measured location $x / D = 5.1$.
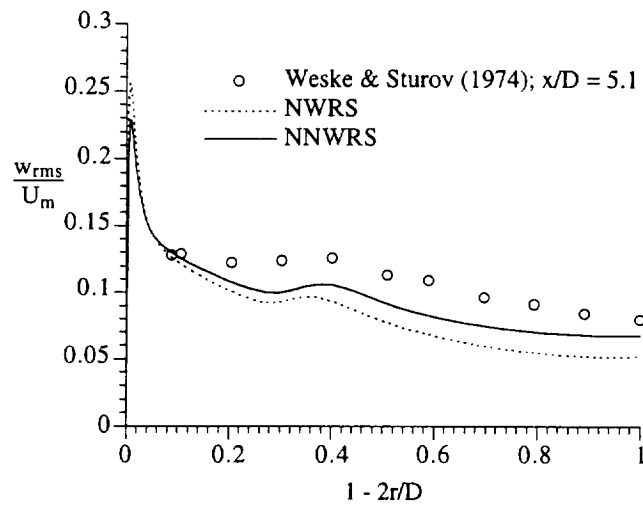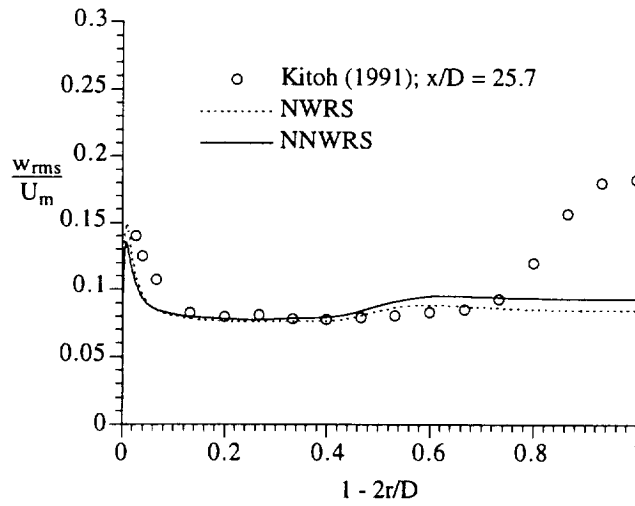

Fig. 4.7f Comparison between the predicted and measured turbulent fluctuation in azimuthal direction at measured location $x / D = 5.1$.
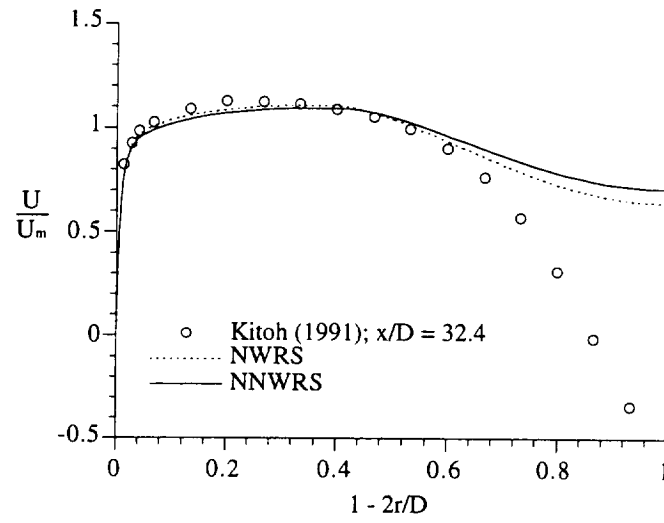
127
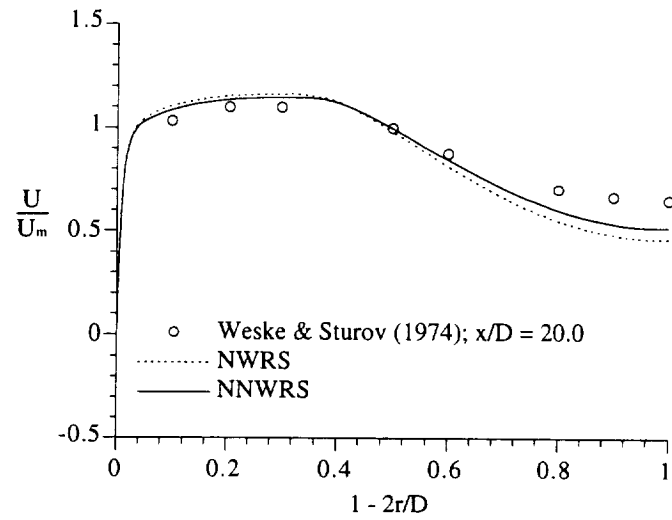
Fig. 4.8a Comparison between the predicted and measured mean axial velocity profiles at measured location $x / D = 20.0$.
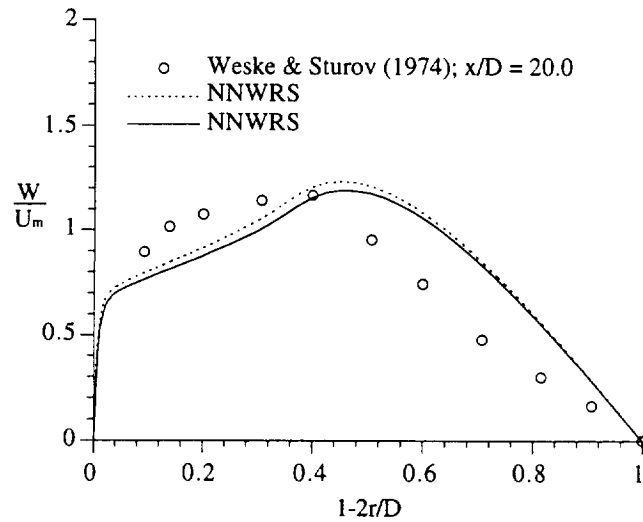
Fig. 4.8b Comparison between the predicted and measured mean azimuthal velocity profiles at measured location $x / D = 20.0$.
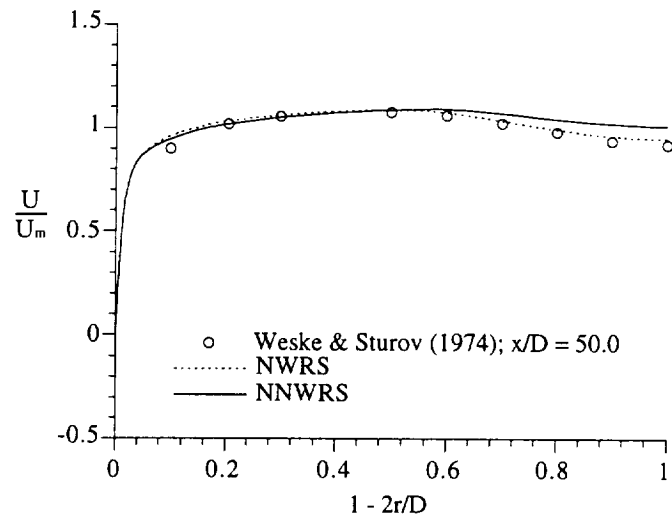
Fig. 4.9a Comparison between the predicted and measured mean axial velocity profiles at measured location $x / D = 50.0$.
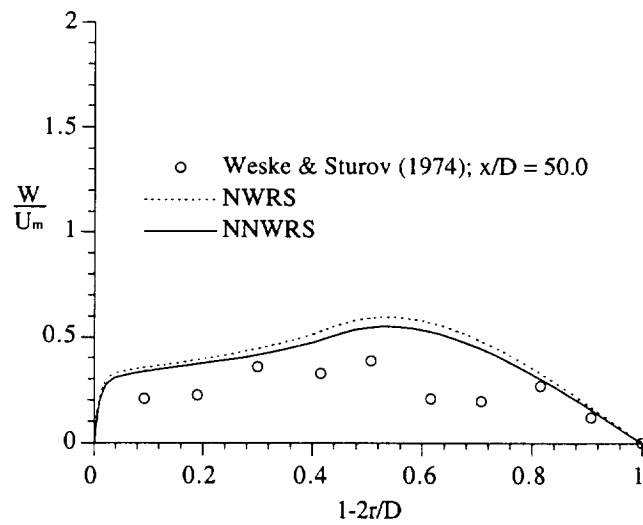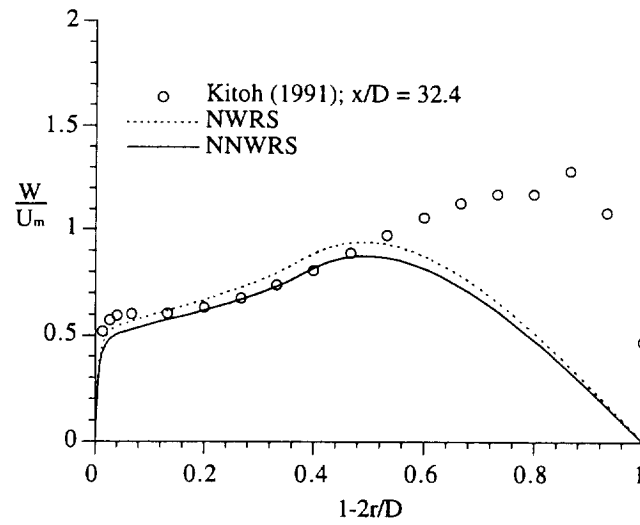

Fig. 4.9b Comparison between the predicted and measured mean azimuthal velocity profiles at measured location $x / D = 50.0$.
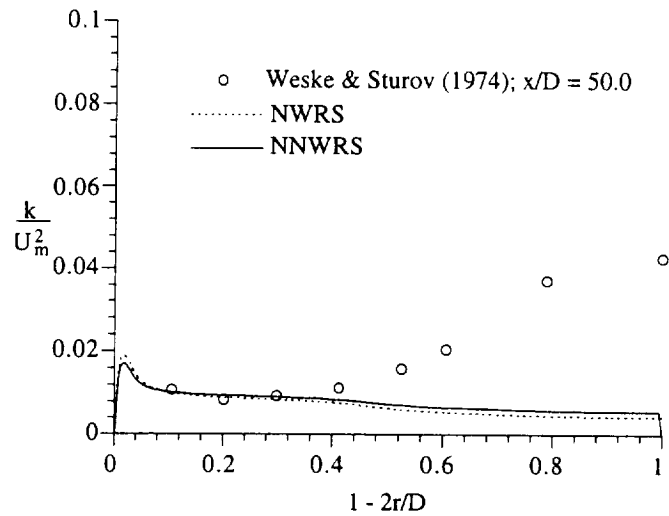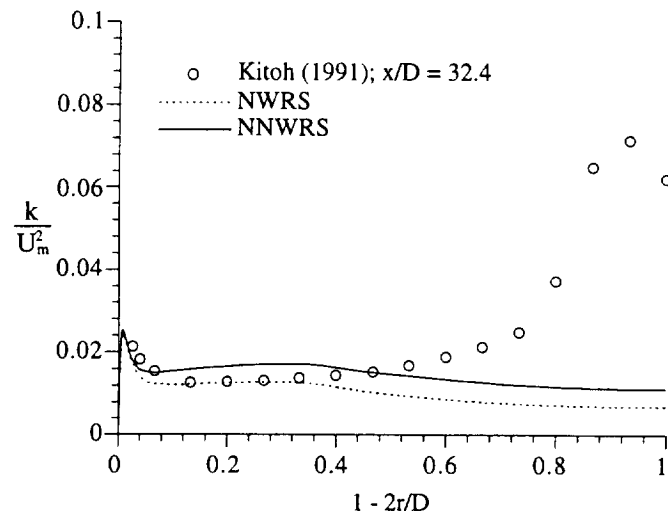
Fig. 4.9c Comparison between the predicted and measured turbulent kinetic energy at measured location $x / D = 50.0$.
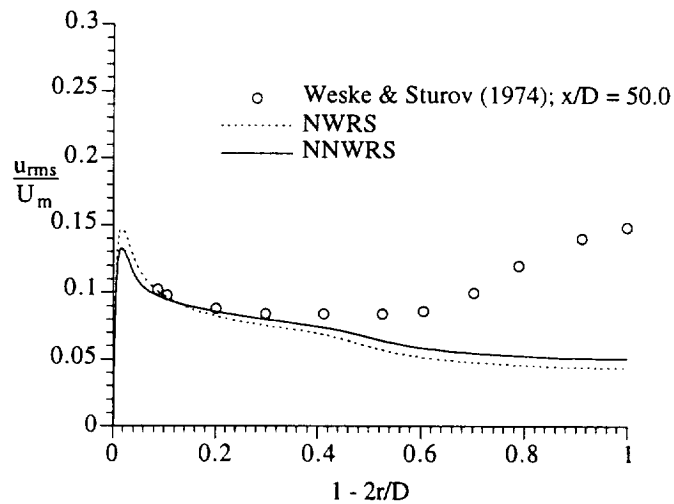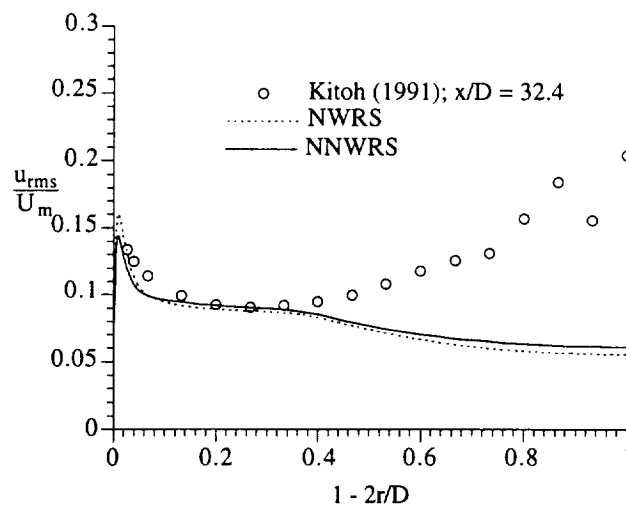

Fig. 4.9d Comparison between the predicted and measured turbulent fluctuation in the axial direction at measured location $x / D = 50.0$.
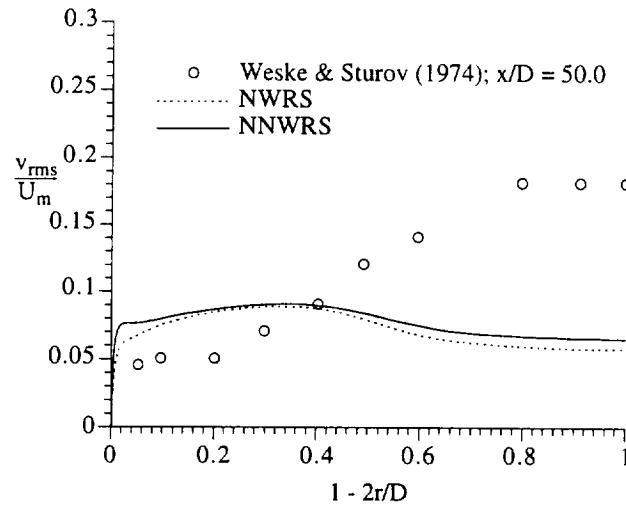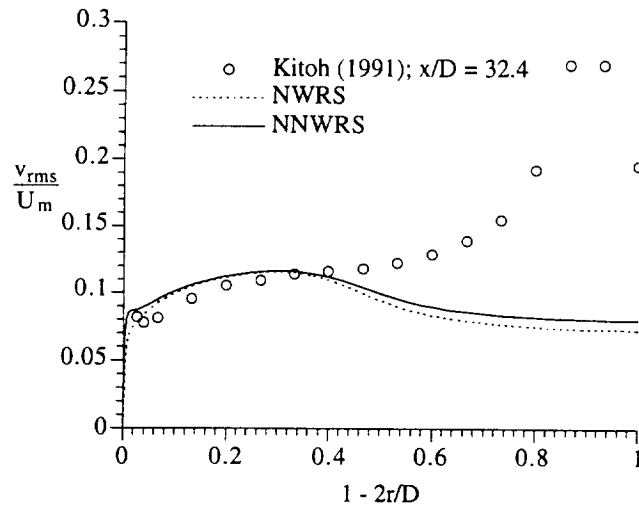
Fig. 4.9e Comparison between the predicted and measured turbulent fluctuation in the radial direction at measured location $x / D = 50.0$.
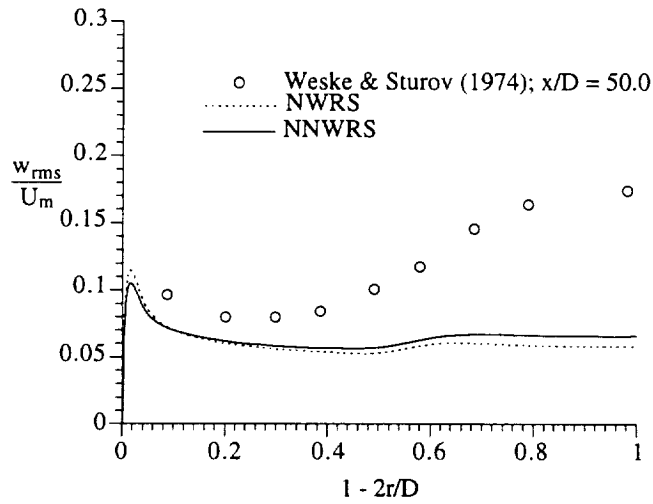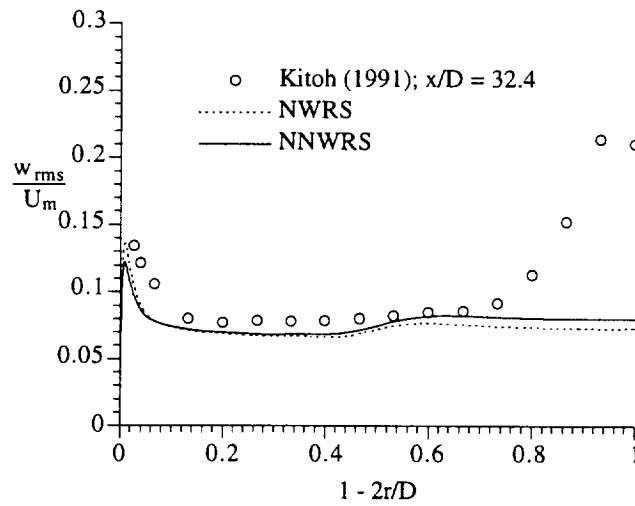

Fig. 4.9f Comparison between the predicted and measured turbulent fluctuation in azimuthal direction at measured location $x / D = 50.0$.

131
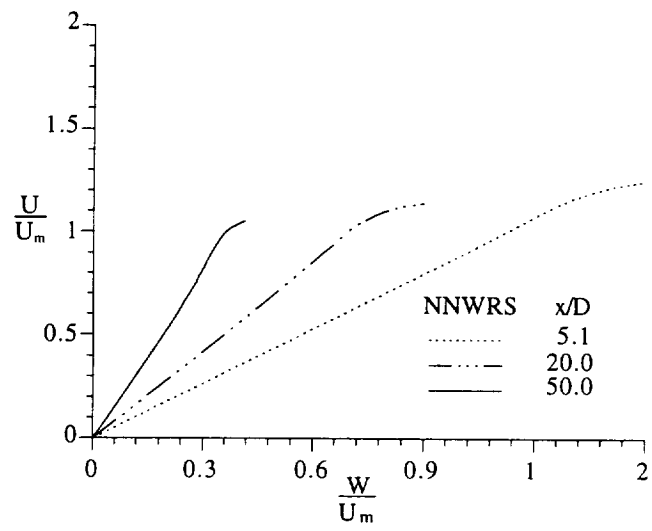
Fig. 4.10 Flow skewness in the near-wall region.

(a)

(b)
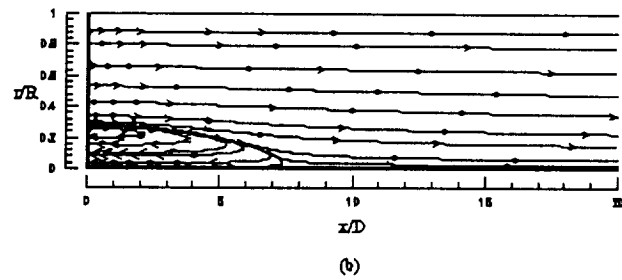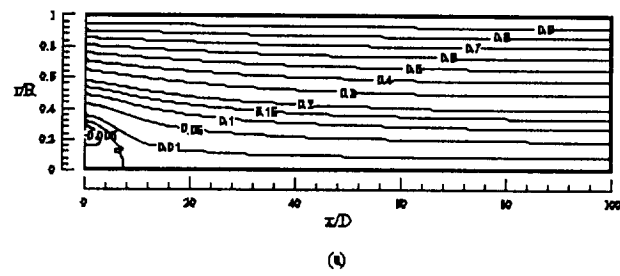
Fig. 4.11 Predicted streamlines in the (x, r) plane by the NNWRS model for Kloh's (1991) case (a) entire computational domain and (b) upstream portion.
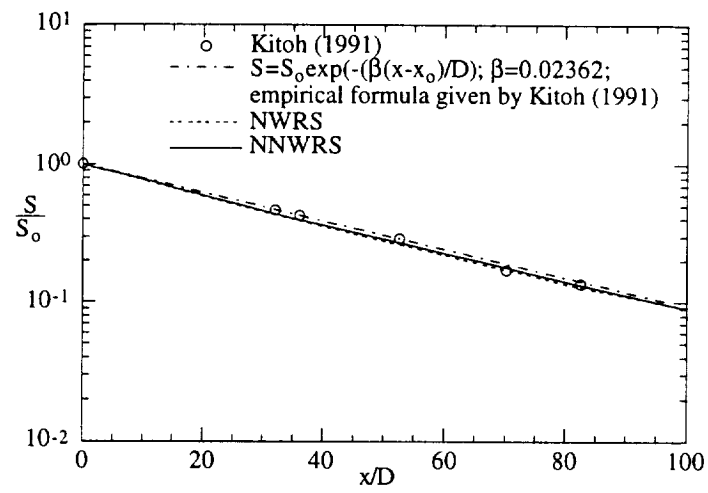
Fig. 4.12 Predicted swirl number for Kitoh's (1991) case and its comparison with the experimental data and the empirical formula given by Kitoh (1991).
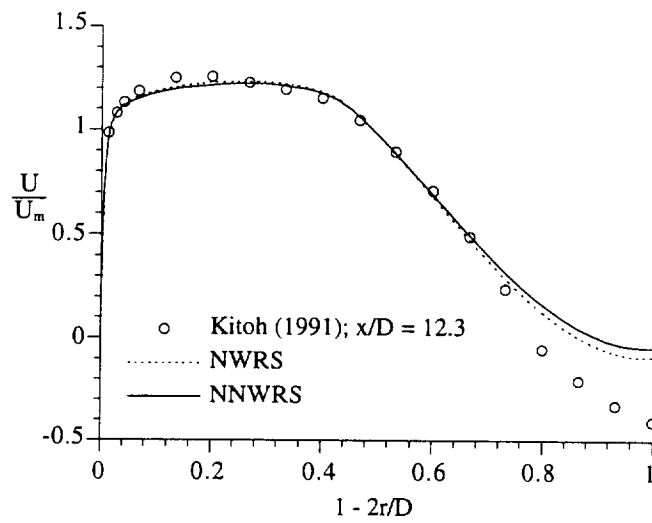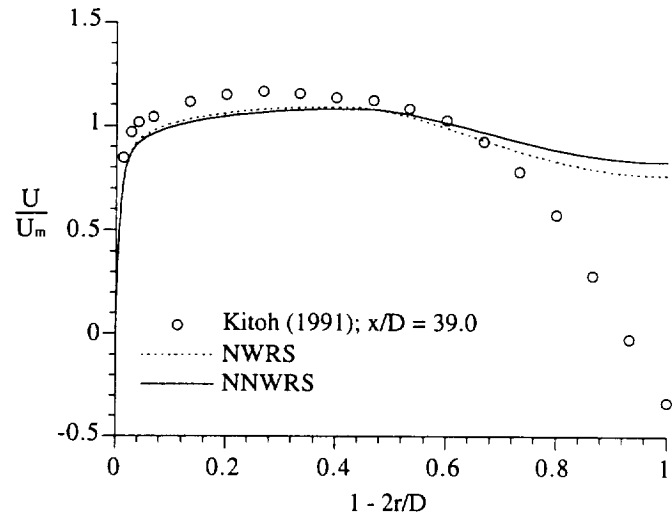
Fig. 4.13a Comparison between the predicted and measured mean axial velocity profiles at measured location $x / D = 12.3$.
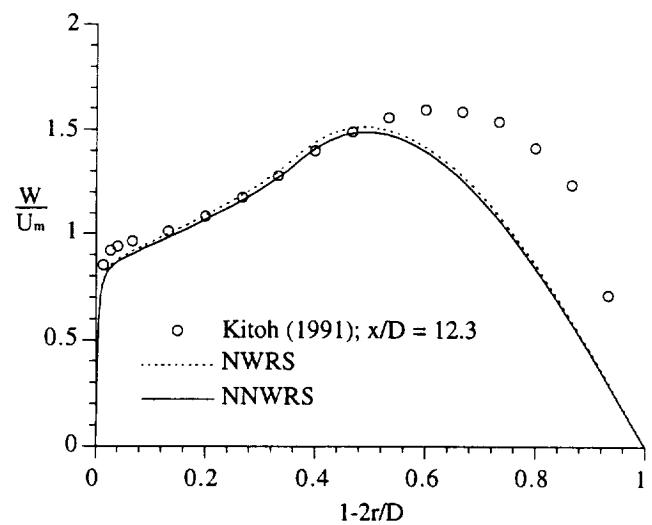
Fig. 4.13b Comparison between the predicted and measured mean azimuthal velocity profiles at measured location at $x / D = 12.3$.

135
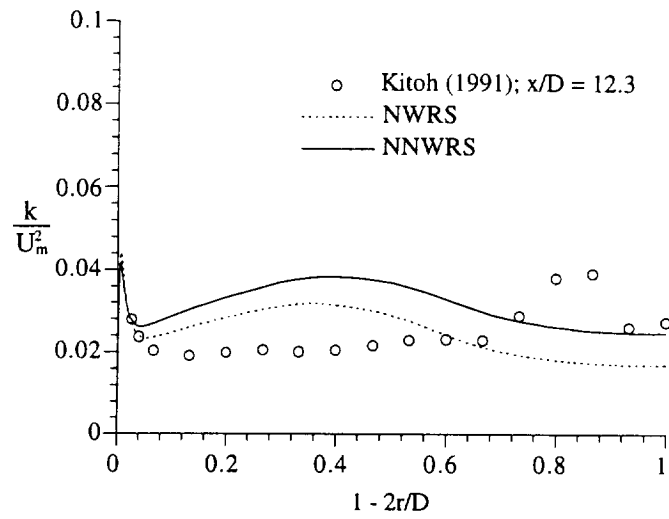
Fig. 4.13c Comparison between the predicted and measured turbulent kinetic energy at measured location $x / D = 12.3$.
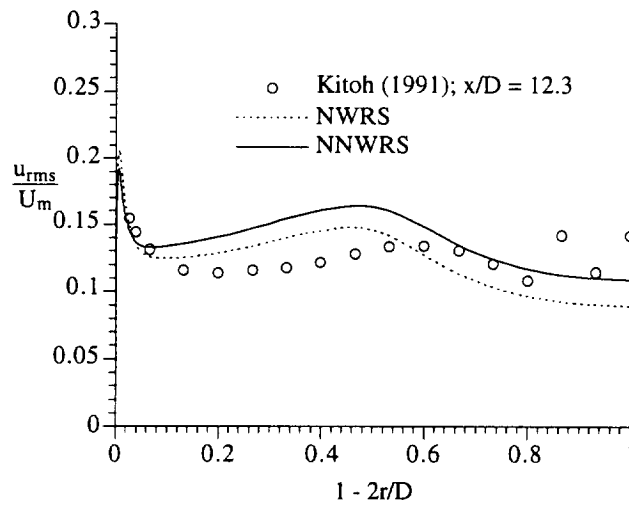
Fig. 4.13d Comparison between the predicted and measured turbulent fluctuation in the axial direction at measured location $x / D = 12.3$.

136
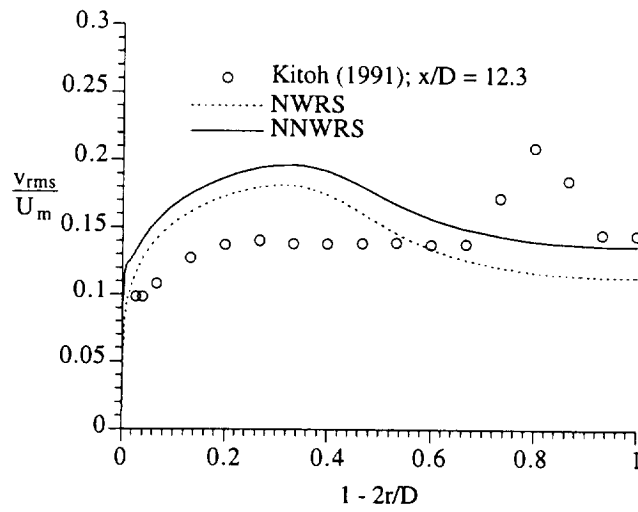
Fig. 4.13e Comparison between the predicted and measured turbulent fluctuation in the radial direction at measured location $x / D = 12.3$.
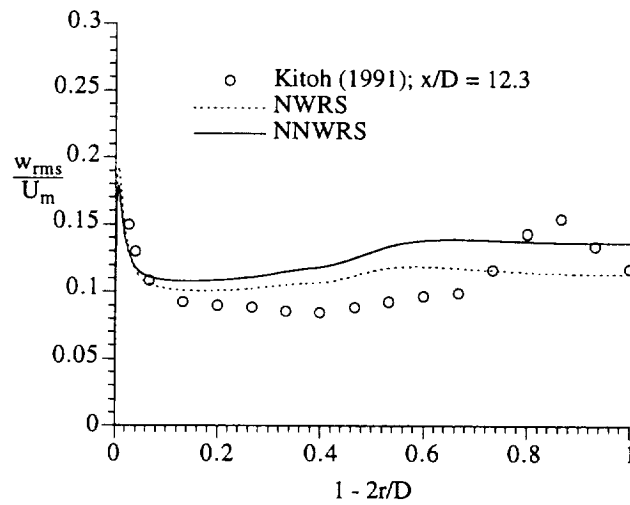
Fig. 4.13f Comparison between the predicted and measured turbulent fluctuation in azimuthal direction at measured location $x / D = 12.3$.
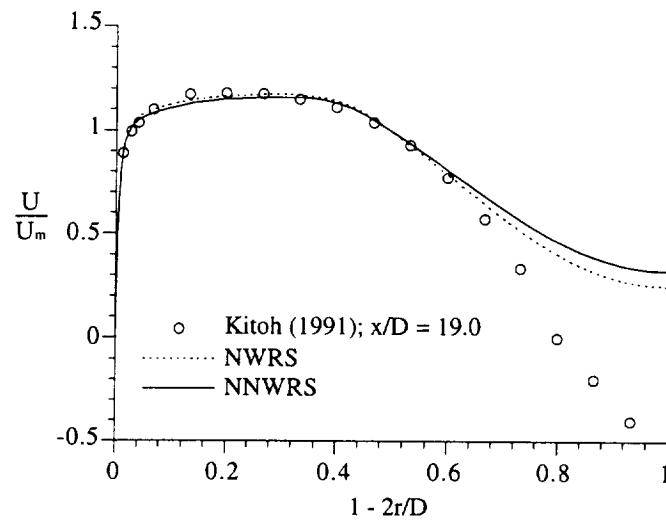
Fig. 4.14a Comparison between the predicted and measured mean axial velocity profiles at measured location $x / D = 19.0$.
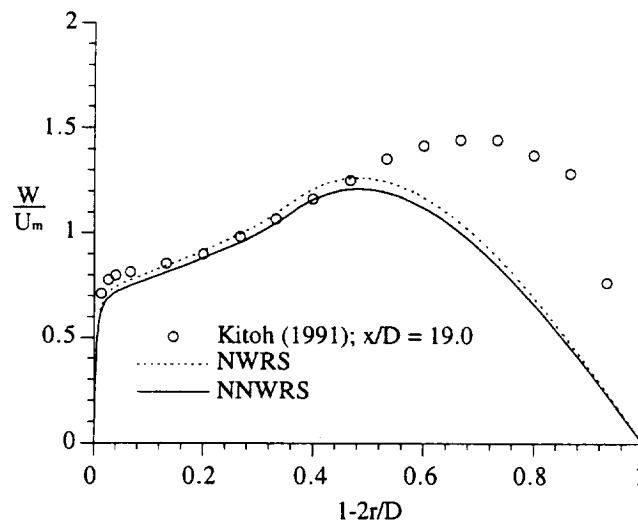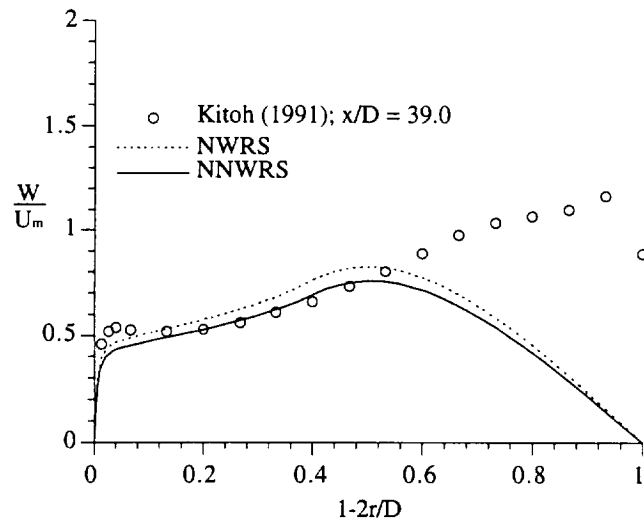

Fig. 4.14b Comparison between the predicted and measured mean azimuthal velocity profiles at measured location $x / D = 19.0$.
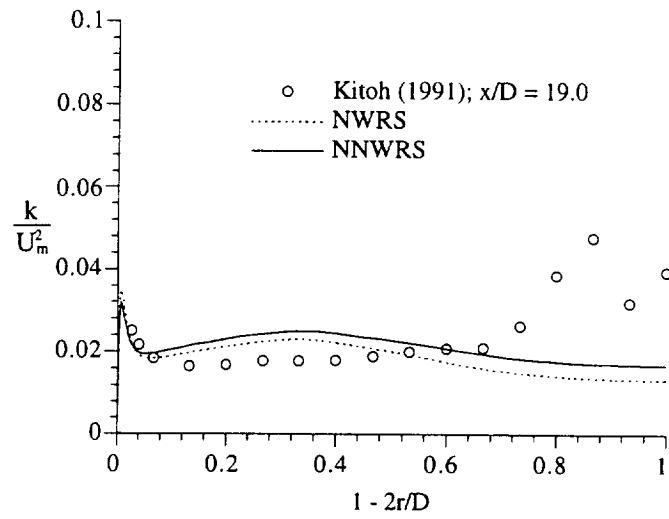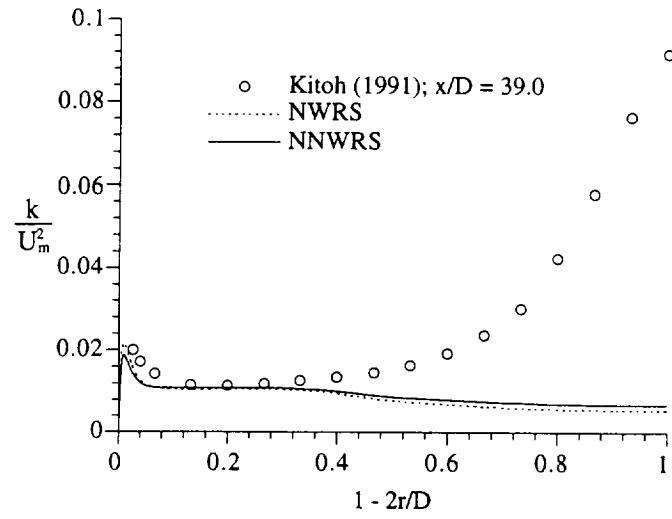
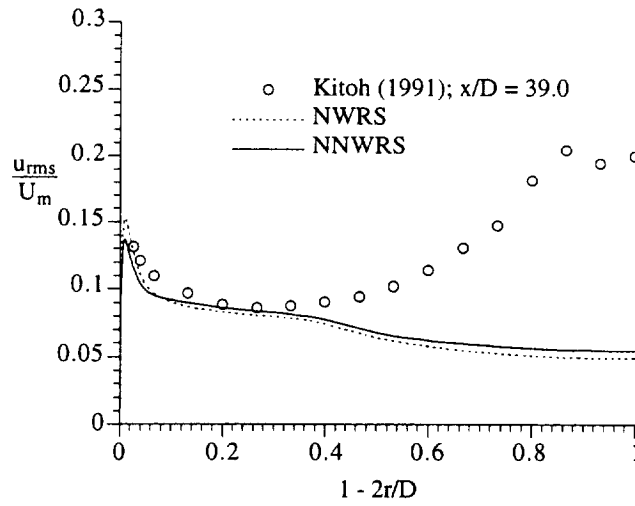Fig. 4.14c Comparison between the predicted and measured turbulent kinetic energy at measured location $x / D = 19.0$.
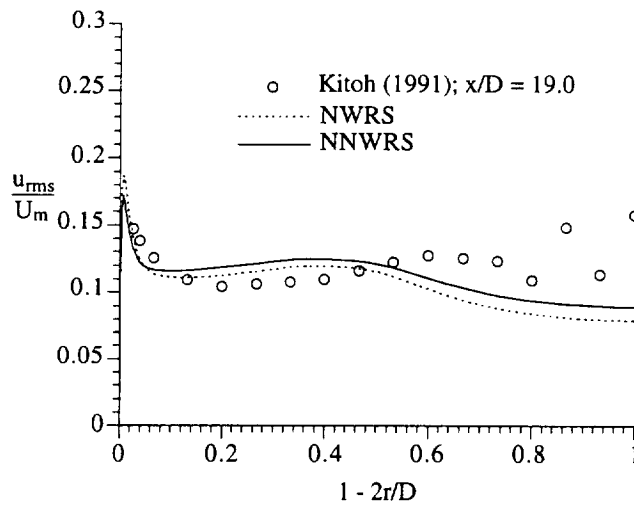
Fig. 4.14dComparison between the predicted and measured turbulent fluctuation in the axial direction at measured location at $x / D = 19.0$.
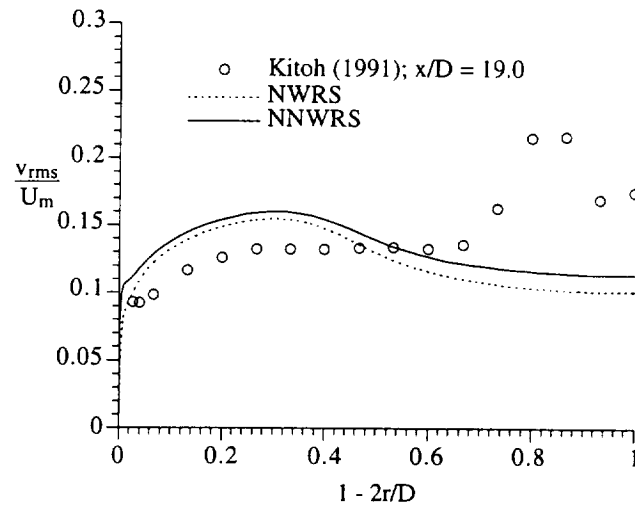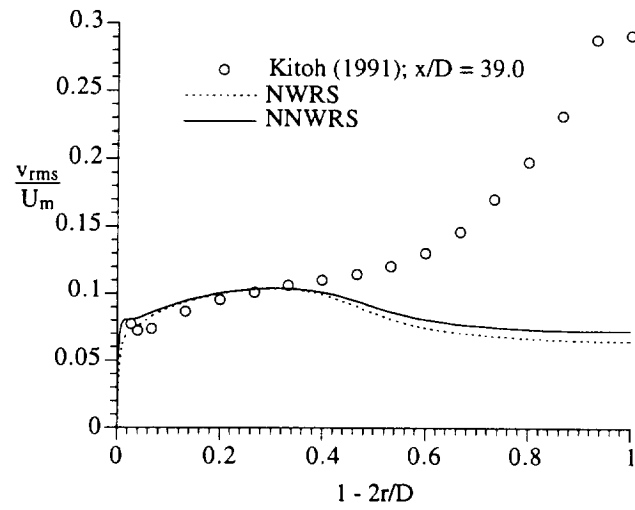
Fig. 4.14e Comparison between the predicted and measured turbulent fluctuation in the radial direction at $x / D = 19.0$.
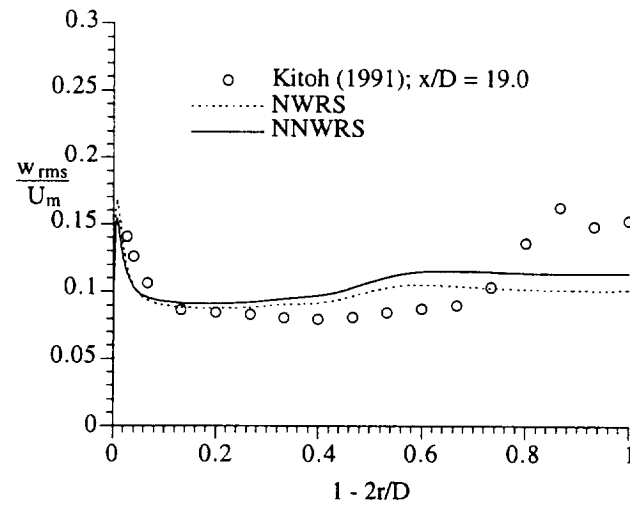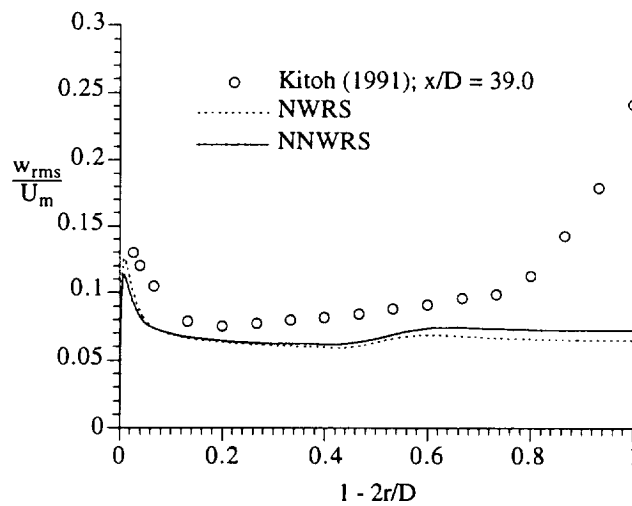

Fig. 4.14f Comparison between the predicted and measured turbulent fluctuation in azimuthal direction at measured location $x / D = 19.0$.

140
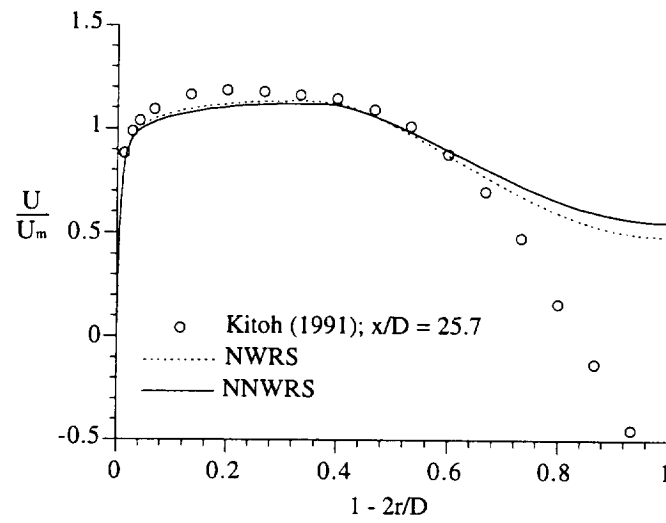
Fig. 4.15a Comparison between the predicted and measured mean axial velocity profiles at measured location $x / D = 25.7$.
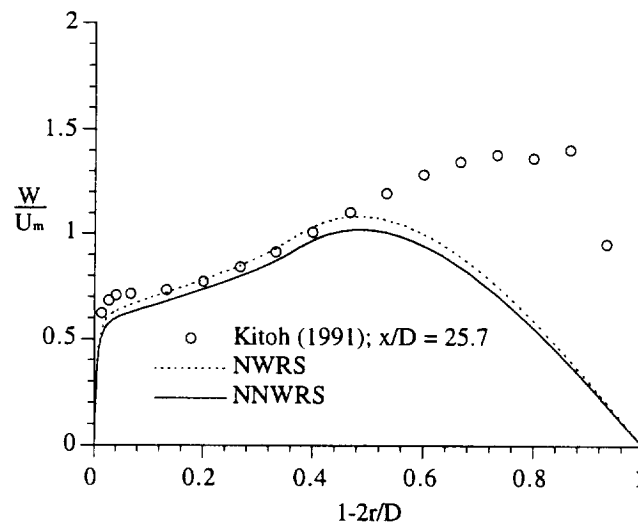
Fig. 4.15b Comparison between the predicted and measured mean azimuthal velocity profiles at measured location $x / D = 25.7$.

141

Fig. 4.15c Comparison between the predicted and measured turbulent kinetic energy at measured location $x / D = 25.7$.

Fig. 4.15d Comparison between the predicted and measured turbulent fluctuation in the axial direction at measured location $x / D = 25.7$.

Fig. 4.15e Comparison between the predicted and measured turbulent fluctuation in the radial direction at measured location $x / D = 25.7$.
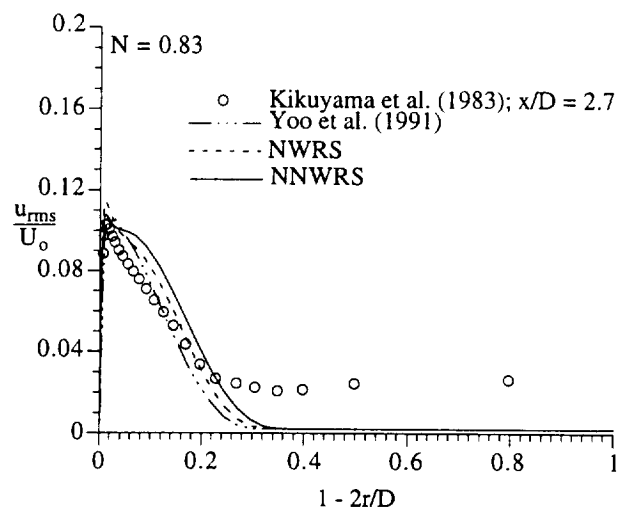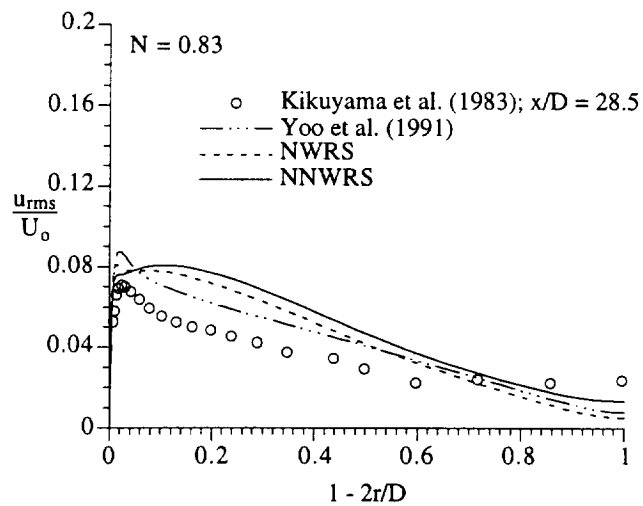

Fig. 4.15f Comparison between the predicted and measured turbulent fluctuation in the azimuthal direction at $x / D = 25.7$.

143

Fig. 4.16a Comparison between the predicted and measured mean axial velocity profiles at measured location $x / D = 32.4$.

Fig. 4.16b Comparison between the predicted and measured mean azimuthal velocity profiles at measured location $x / D = 32.4$.

Fig. 4.16c Comparison between the predicted and measured turbulent kinetic energy at measured location $x / D = 32.4$.

Fig. 4.16d Comparison between the predicted and measured turbulent fluctuation in the axial direction at measured location $x / D = 32.4$.

145

Fig. 4.16e Comparison between the predicted and measured turbulent fluctuation in the radial direction at measured location $x / D = 32.4$.

Fig. 4.16f Comparison between the predicted and measured turbulent fluctuation in azimuthal direction at measured location $x / D = 32.4$.

146

Fig. 4.17a Comparison between the predicted and measured mean axial velocity profiles at measured location $x / D = 39.0$.

Fig. 4.17b Comparison between the predicted and measured mean azimuthal velocity profiles at measured location $x / D = 39.0$.

Fig. 4.17c Comparison between the predicted and measured turbulent kinetic energy at measured location $x / D = 39.0$.

Fig. 4.17d Comparison between the predicted and measured turbulent fluctuation in the axial direction at measured location $x / D = 39.0$.

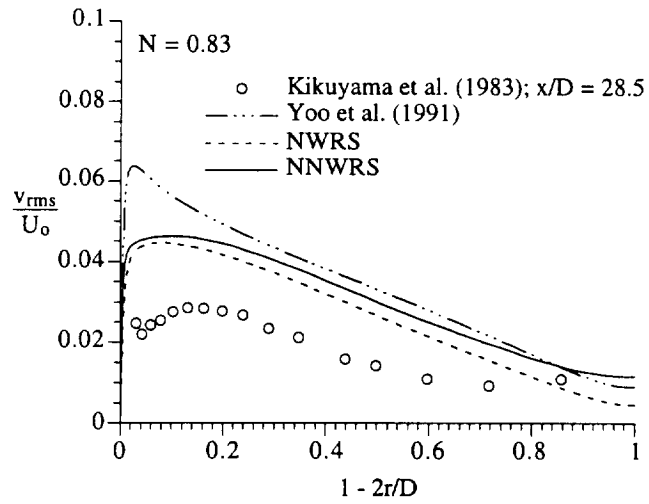Fig. 4.17e Comparison between the predicted and measured turbulent fluctuation in the radial direction at measured location $x / D = 39.0$.

Fig. 4.17f Comparison between the predicted and measured turbulent fluctuation in azimuthal direction at measured location $x / D = 39.0$.

149
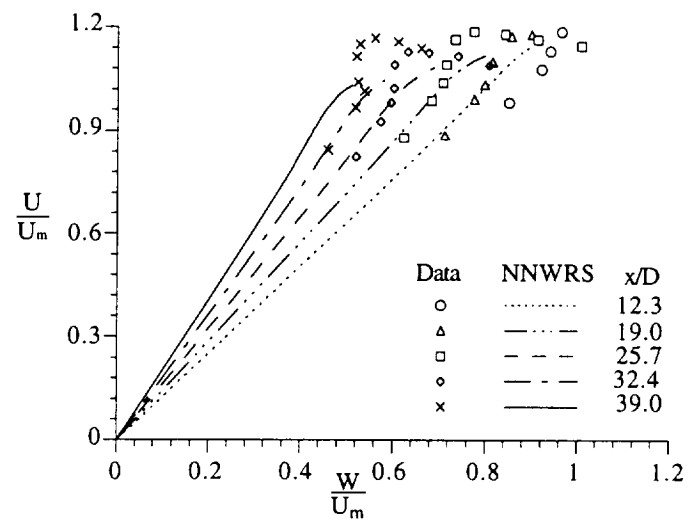
Fig. 4.18 Flow skewness in the near-wall region.
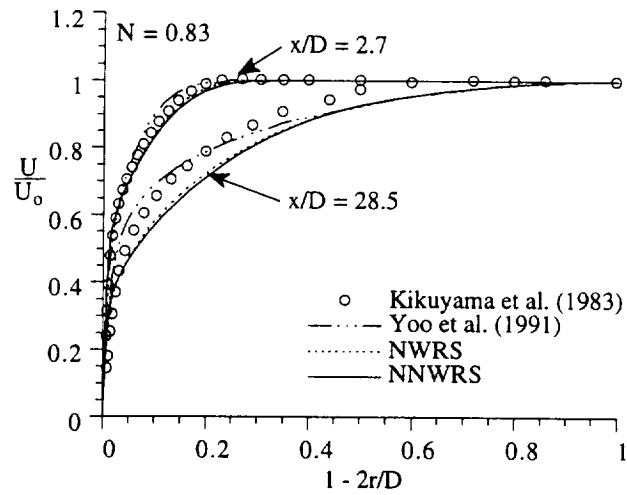
Fig. 4.19a Comparison between predicted and measured axial mean velocity at $x / D = 2.7$ and 28.5 (U_o is the axial mean velocity at the pipe centerline).
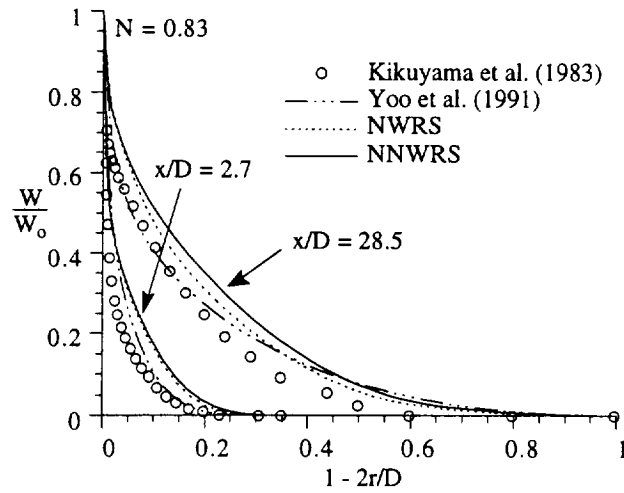
Fig. 4.19b Comparison between predicted and measured azimuthal mean velocity at $x / D = 2.7$ and 28.5 (W_o is the azimuthal mean velocity at the pipe wall).

Fig. 4.20a Comparison between predicted and measured turbulent fluctuation in the axial direction at $x / D = 2.7$.

Fig. 4.20b Comparison between predicted and measured turbulent fluctuation in the axial direction at $x / D = 28.5$.
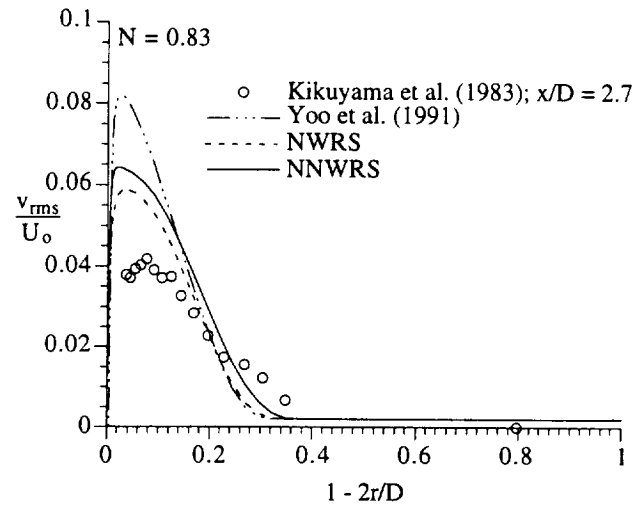
Fig. 4.21a Comparison between predicted and measured turbulent fluctuation in the radial direction at $x / D = 2.7$.

Fig. 4.21b Comparison between predicted and measured turbulent fluctuation in the radial direction at $x / D = 28.5$.
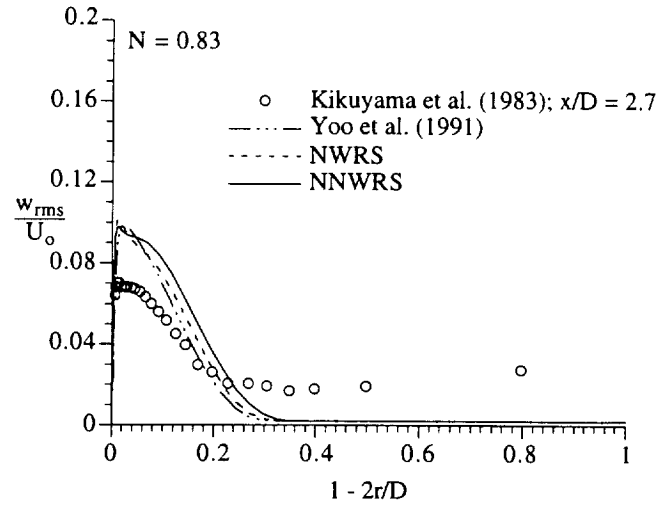
Fig. 4.22a Comparison between predicted and measured turbulent fluctuation in the azimuthal direction at $x / D = 2.7$.
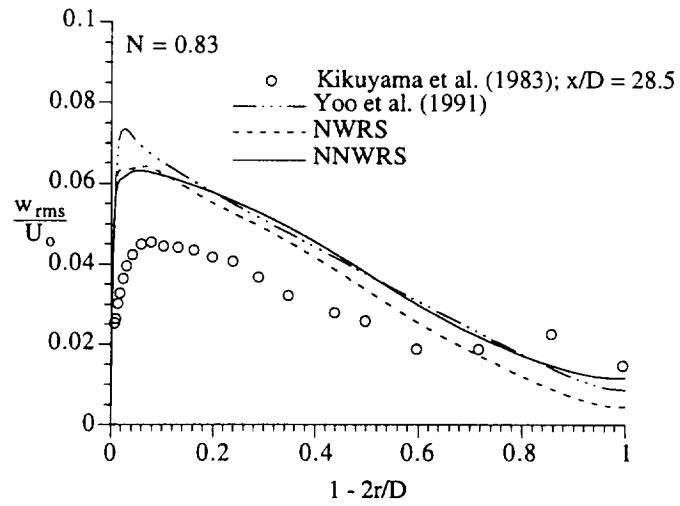
Fig. 4.22b Comparison between predicted and measured turbulent fluctuation in the azimuthal direction at $x / D = 28.5$.
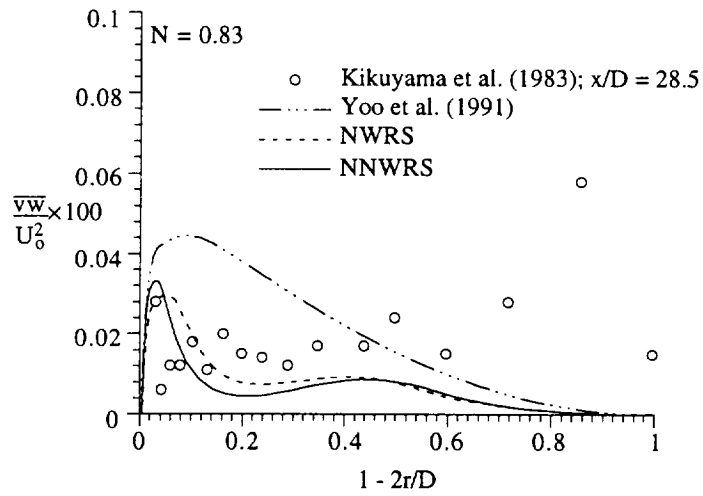
154
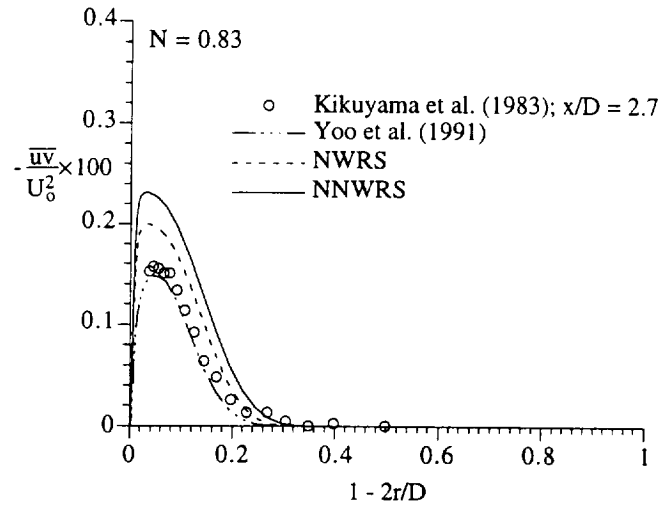
Fig. 4.23a Comparison between predicted and measured turbulent shear stress $\overline{uv}$ at $x \, / \, D = 2.7$.
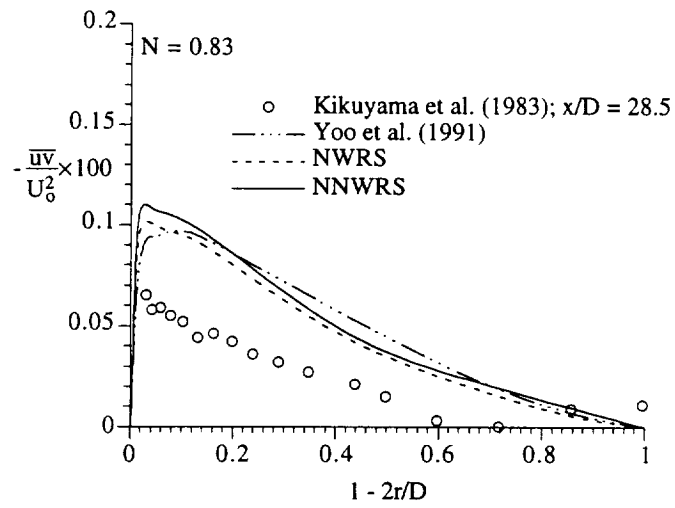
Fig. 4.23b Comparison between predicted and measured turbulent shear stress $\overline{uv}$ at $x \, / \, D = 28.5$.
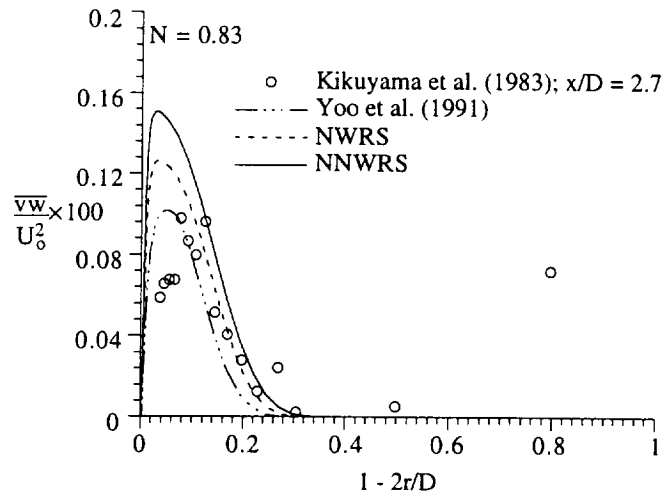
Fig. 4.24a Comparison between predicted and measured turbulent shear stress $\overline{vw}$ at $x / D = 2.7$.

Fig. 4.24b Comparison between predicted and measured turbulent shear stress $\overline{vw}$ at
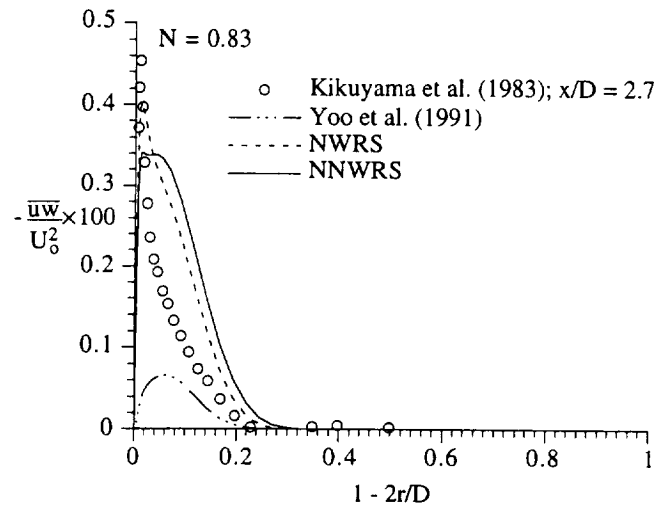$x / D = 28.5$.

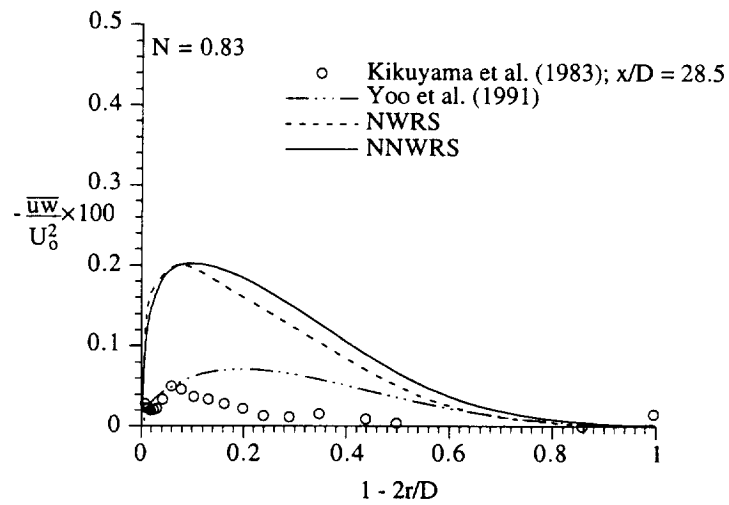Fig. 4.25a Comparison between predicted and measured turbulent shear stress $\overline{uw}$ at $x / D = 2.7$.

Fig. 4.25b Comparison between predicted and measured turbulent shear stress $\overline{uw}$ at $x / D = 28.5$.
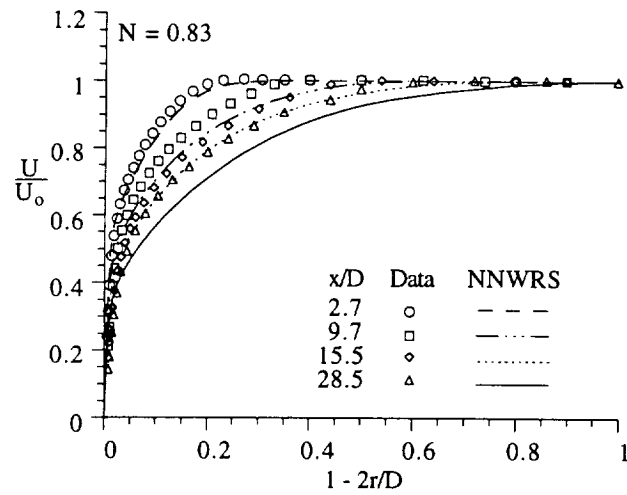
Fig. 4.26a Comparison between the predicted and measured axial mean velocity at four different axial locations.
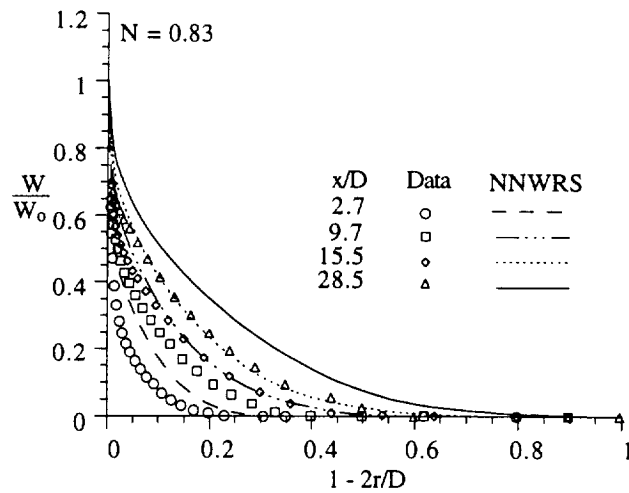

Fig. 4.26b Comparison between the predicted and measured azimuthal mean velocity at four different axial locations.
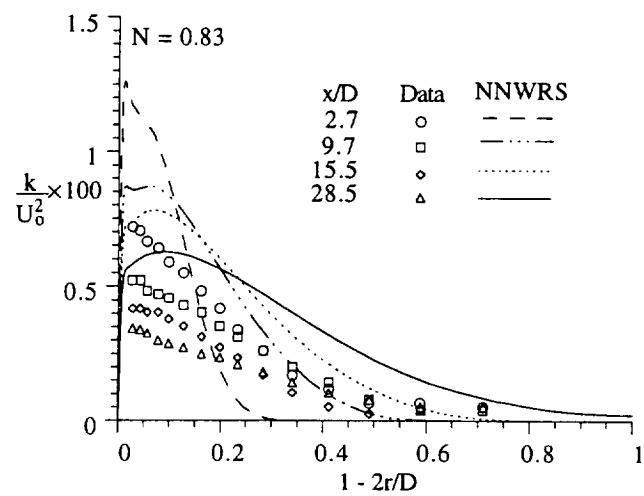
Fig. 4.26c Comparison between the predicted and measured turbulent kinetic energy at four different axial locations.
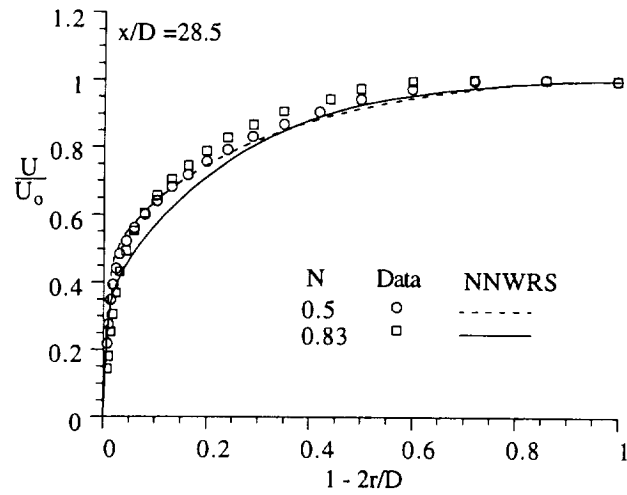
Fig. 4.27a Comparison between the predicted and measured rotation effects on axial mean velocity for different rotation numbers at $x / D = 28.5$.
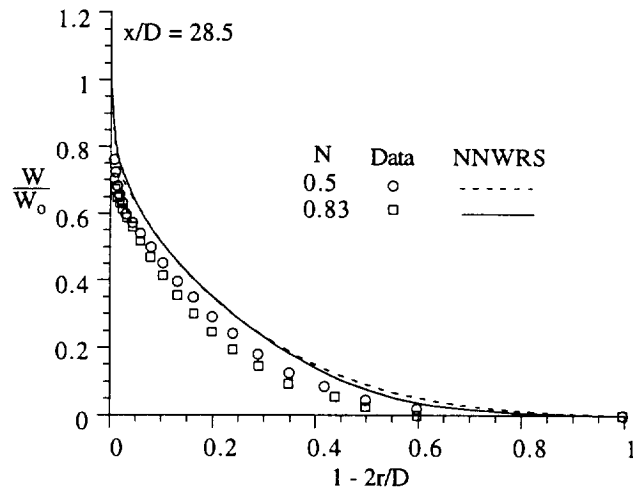

Fig. 4.27b Comparison between the predicted and measured rotation effects on azimuthal mean velocity for different rotation numbers at $x / D = 28.5$.

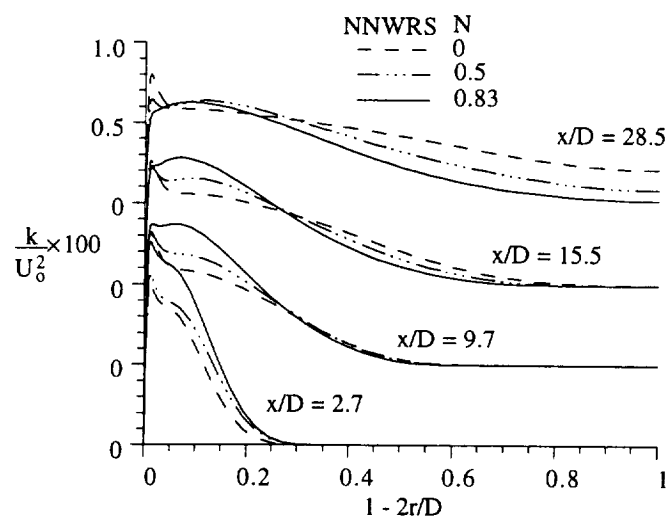160

Fig. 4.28 Comparison of the predicted rotation effects on turbulent kinetic energy at various axial locations.

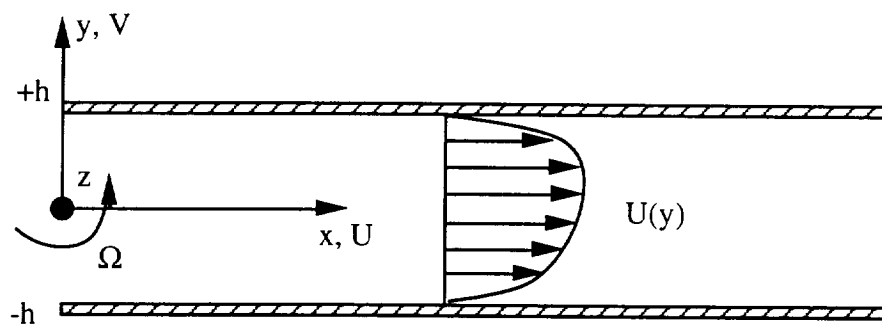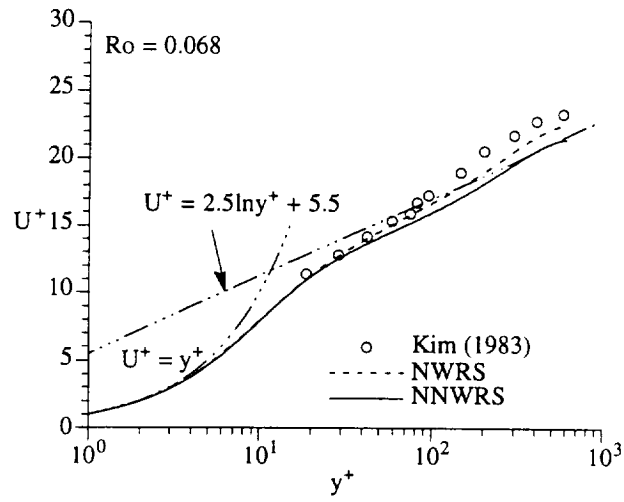Fig. 4.29 Sketch of coordinate system and computational domain for a fully developed flow in a rotating channel.

162

(a)
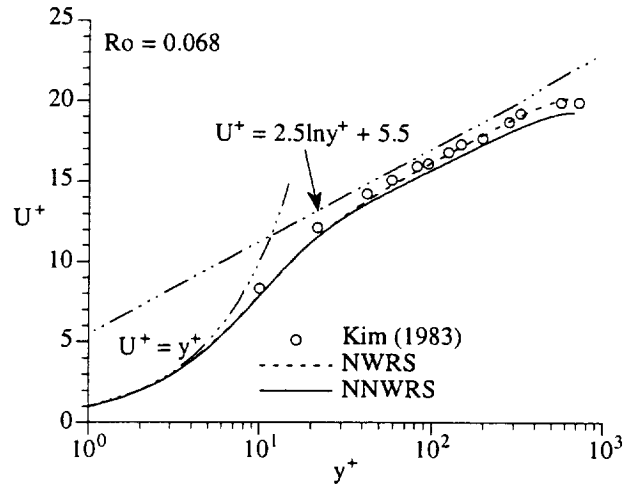
(b)

Fig. 4.30 Comparison between predicted and LES mean velocity profiles in wall coordinates on (a) suction side ($U^+ = U / u_{\tau s}$, $y^+ = (1 - y)u_{\tau s} / \upsilon$) and (b) pressure side ($U^+ = U / u_{\tau p}$, $y^+ = (1 + y)u_{\tau p} / \upsilon$) for $Ro = 0.068$.

163

(a)

(b)

(c)

(d)

Fig. 4.31 Comparison between model predictions and LES data across the channel for (a) mean velocity; (b) turbulent shear stress; (c) turbulent kinetic energy; and (d) turbulent fluctuations.

Fig. 4.32 Comparison between predicted and DNS mean velocity in wall coordinates
$y^+ = (1 \pm y)u_\tau / \upsilon$ for $Ro = 0$.

(a)

(b)

(c)

(d)

Fig. 4.33 Comparison between model predictions and DNS data across the channel for (a) mean velocity; (b) turbulent shear stress; (c) turbulent kinetic energy; and (d) turbulent fluctuations.
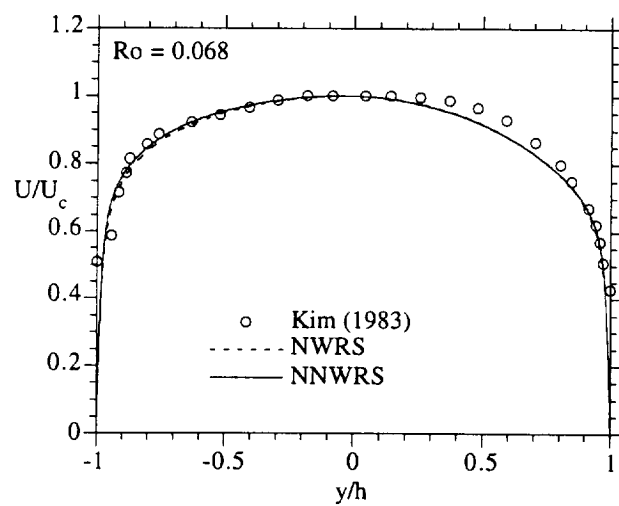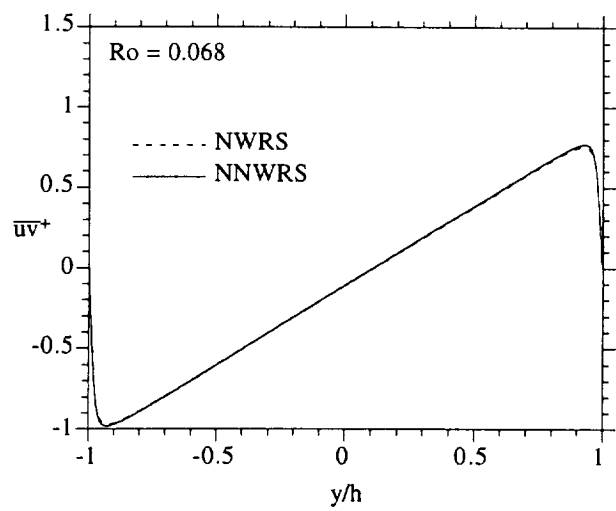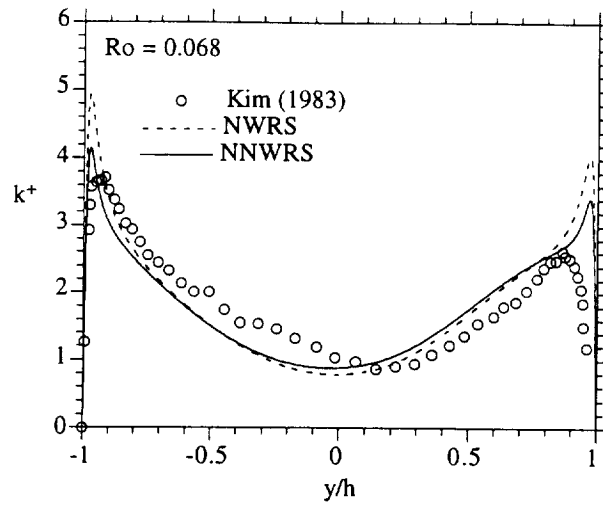
168

(a)

(b)

Fig. 4.34 Comparison between predicted and DNS mean velocity profiles in wall coordinates on (a) suction side ($U^+ = U / u_{\tau s}$, $y^+ = (1+y)u_{\tau s} / v$) and (b) pressure side ($U^+ = U / u_{\tau p}$, $y^+ = (1-y)u_{\tau p} / v$) for $Ro = 0.01$.

(a)

(b)

(c)

(d)

Fig. 4.35 Comparison between model predictions and DNS data across the channel for (a) mean velocity; (b) turbulent shear stress; (c) turbulent kinetic energy; and (d) turbulent fluctuations.
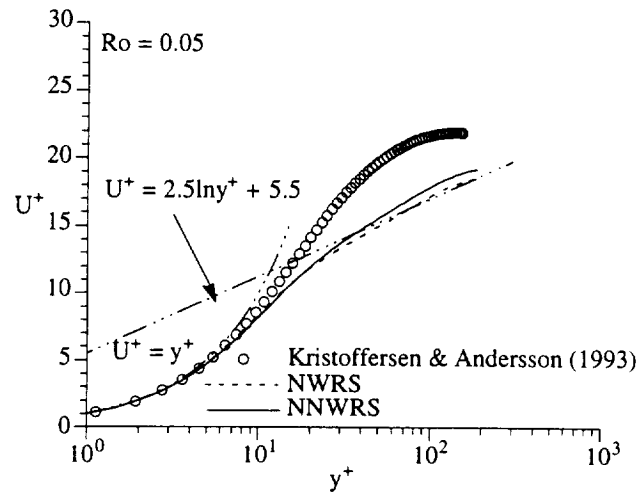
(a)
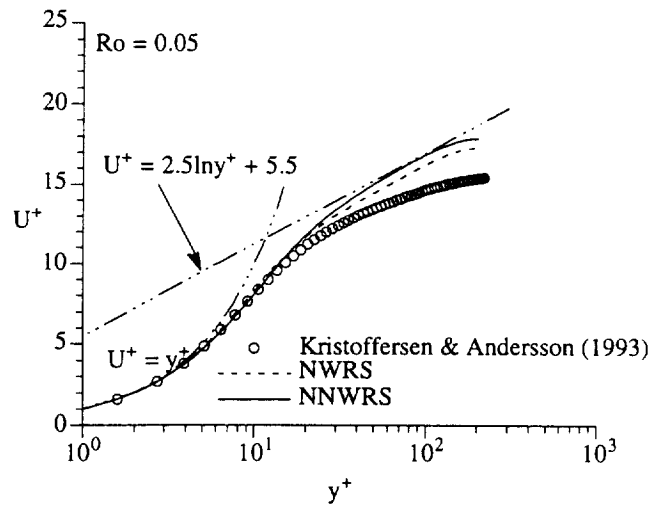
(b)

Fig. 4.36 Comparison between predicted and DNS mean velocity profiles in wall coordinates on (a) suction side and (b) pressure side for $Ro = 0.05$.
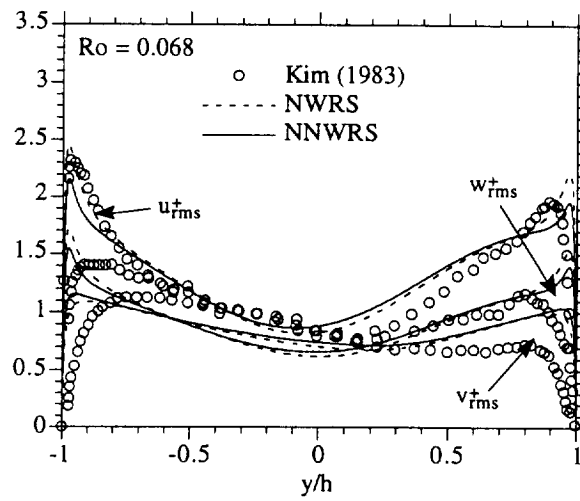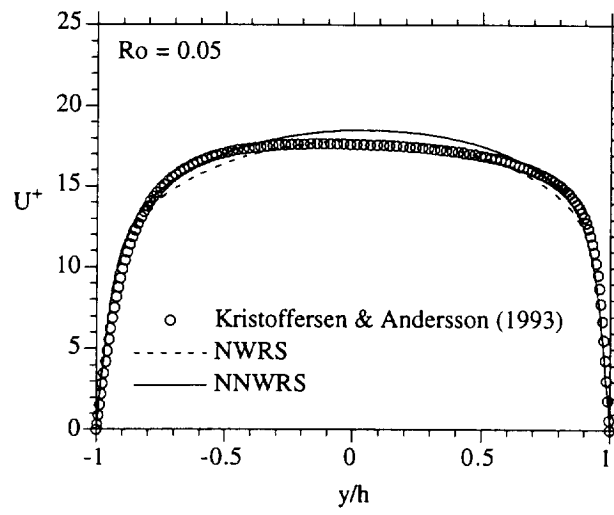
(a)
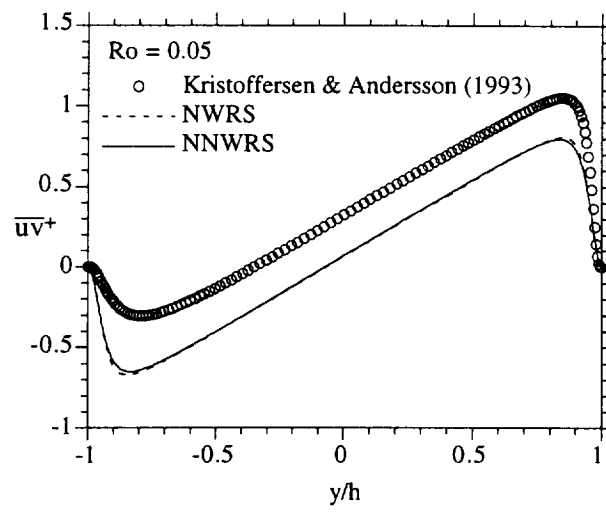
(b)
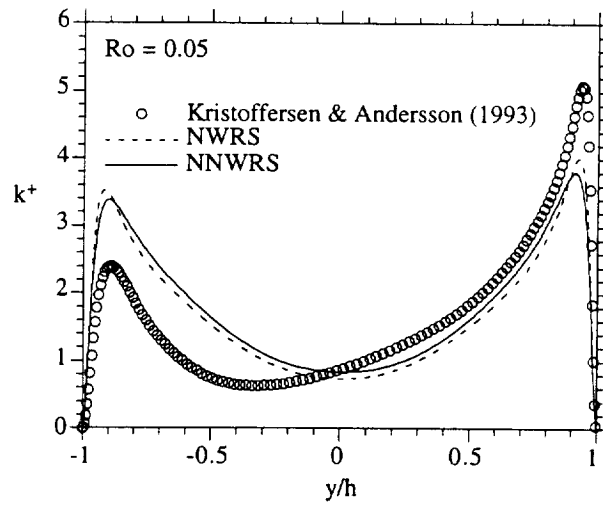
(c)
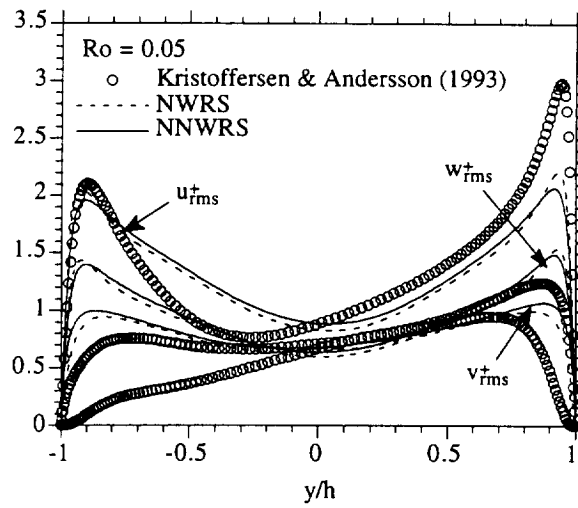
(d)

Fig. 4.37 Comparison between model predictions and DNS data across the channel for (a) mean velocity; (b) turbulent shear stress; (c) turbulent kinetic energy; and (d) turbulent fluctuations.

174
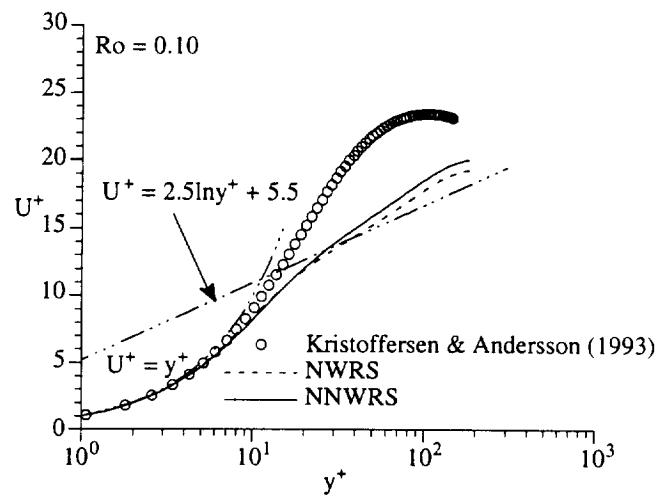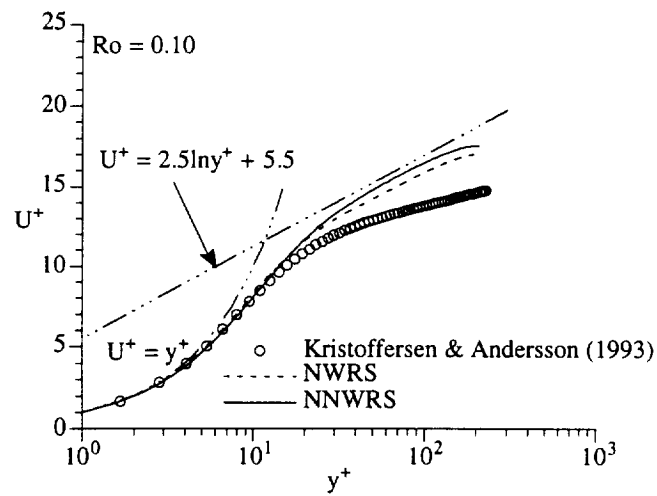
Fig. 4.38 Comparison between predicted and DNS mean velocity profiles in wall coordinates on (a) suction side and (b) pressure side for $Ro = 0.10$.

(a)

(b)

176
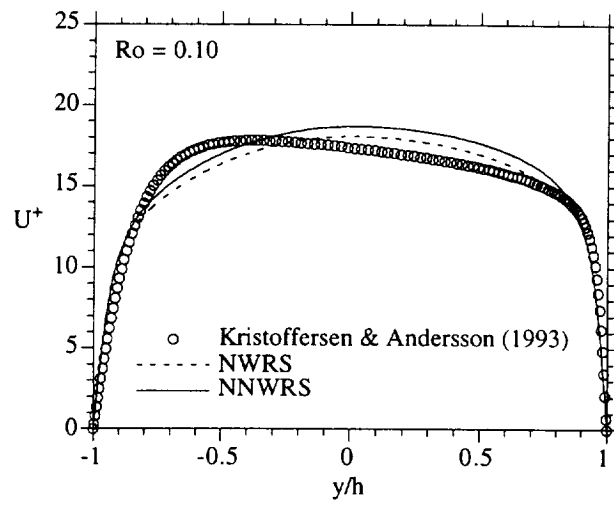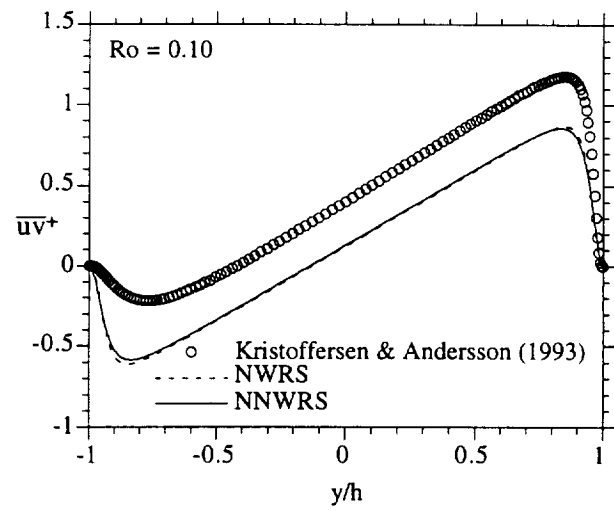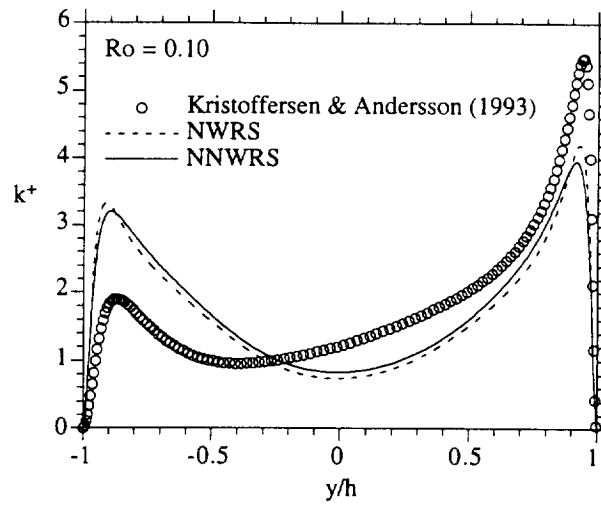
(c)
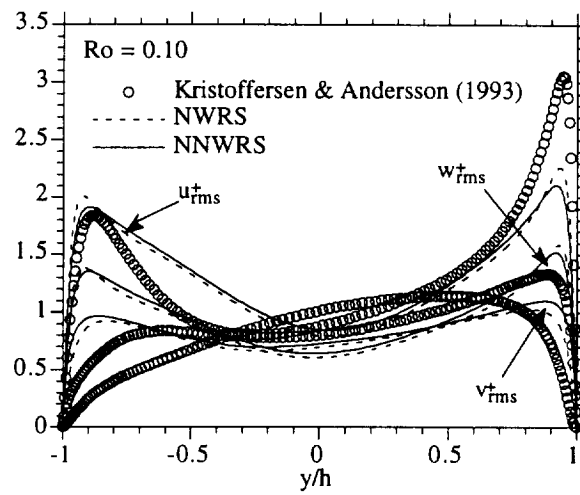
(d)

Fig. 4.39 Comparison between model predictions and DNS data across the channel for (a) mean velocity; (b) turbulent shear stress; (c) turbulent kinetic energy; and (d) turbulent fluctuations
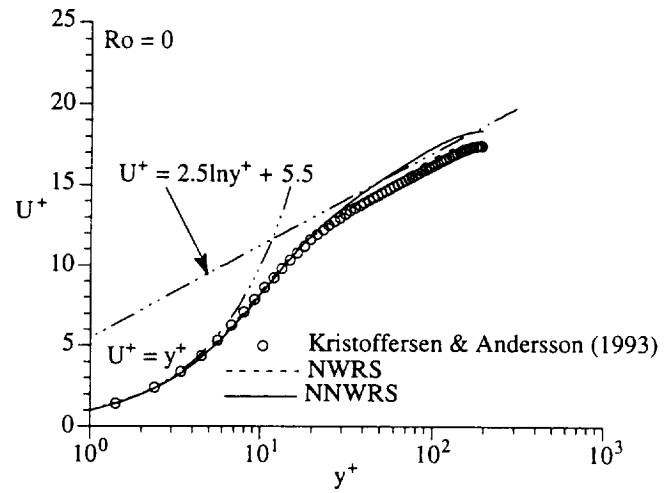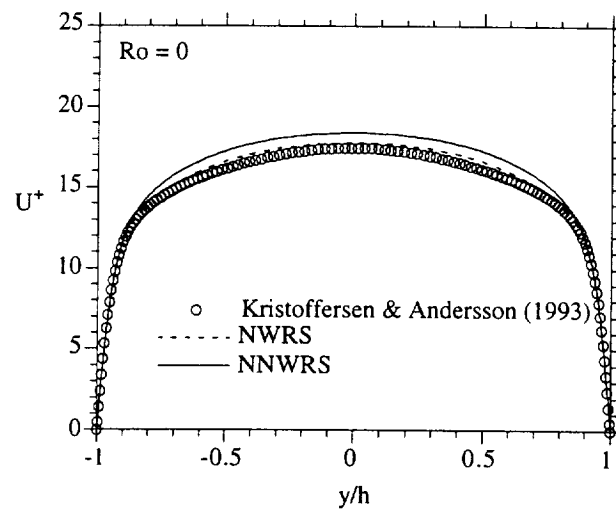
177
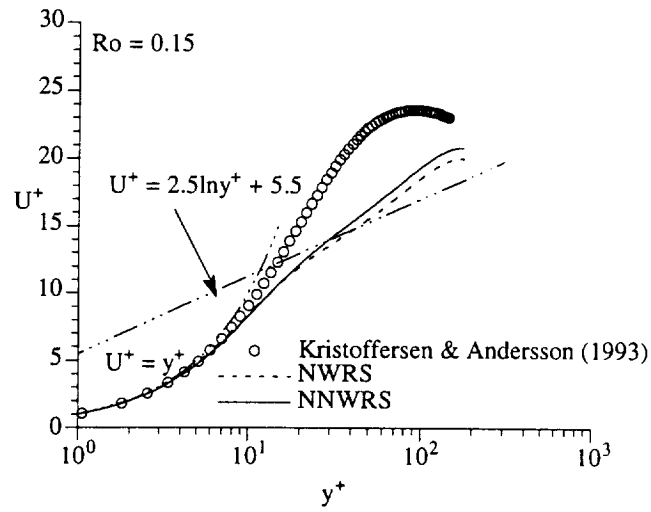
(a)
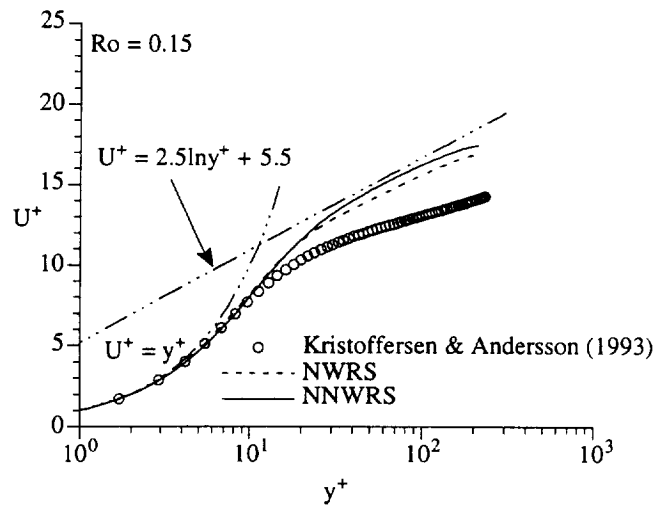
(b)

Fig. 4.40 Comparison between predicted and DNS mean velocity profiles in wall coordinates on (a) suction side and (b) pressure side for $Ro = 0.15$.
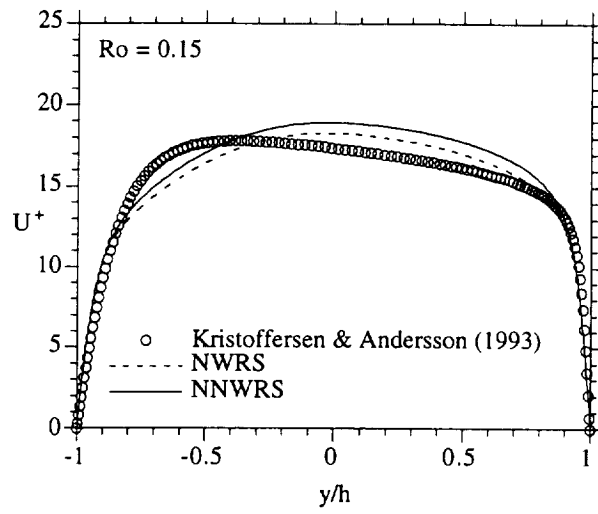
(a)
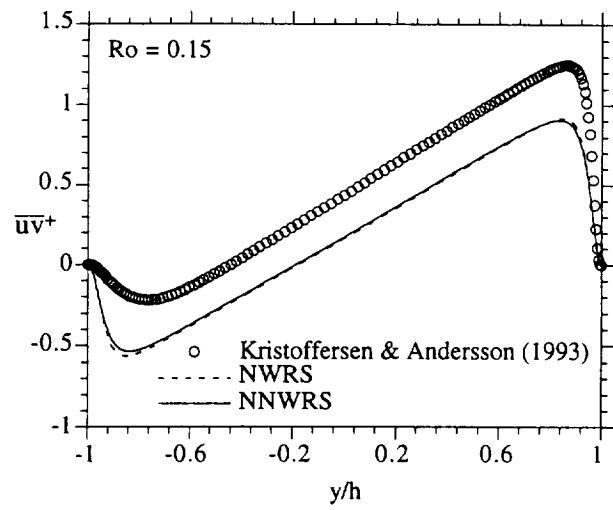
(b)
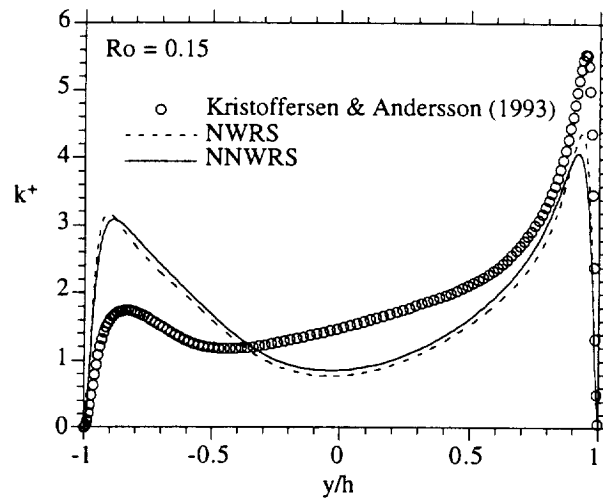
(c)
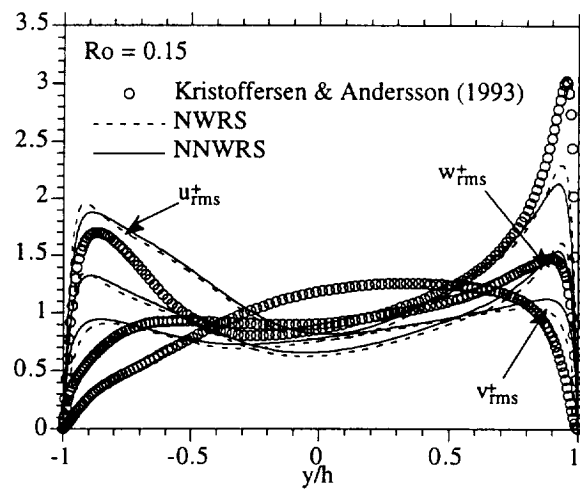
(d)

Fig. 4.41 Comparison between model predictions and DNS data across the channel for (a) mean velocity; (b) turbulent shear stress; (c) turbulent kinetic energy; and (d) turbulent fluctuations.
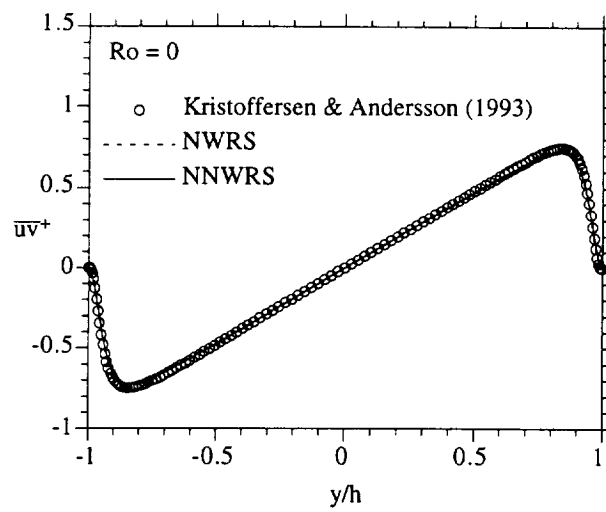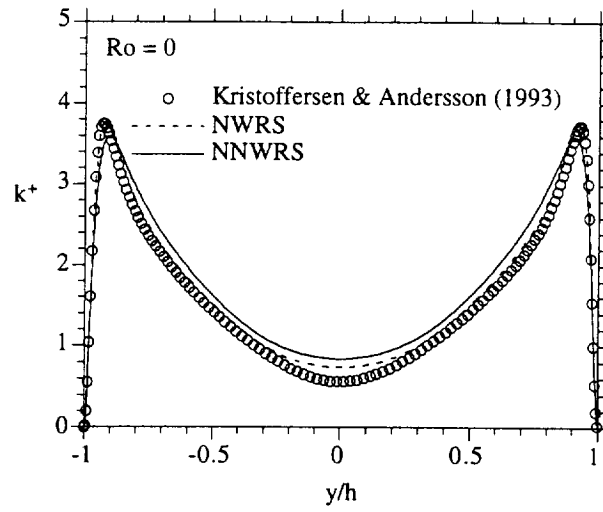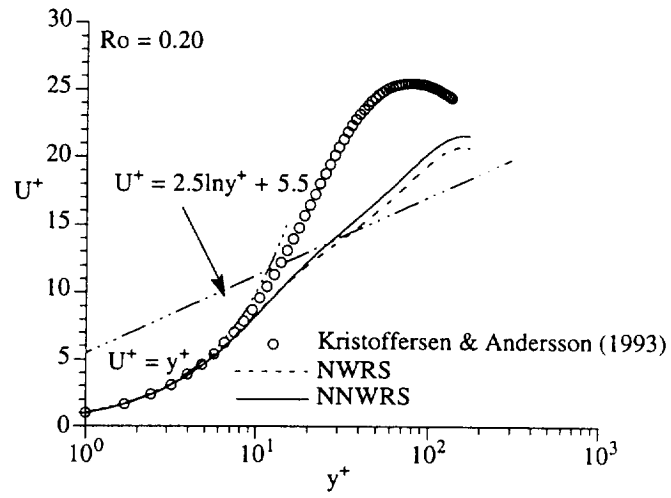
(a)
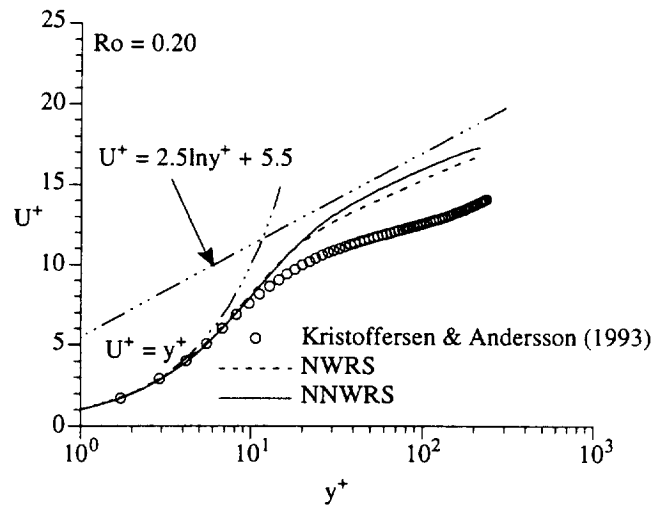
(b)

Fig. 4.42 Comparison between predicted and DNS mean velocity profiles in wall coordinates on (a) suction side and (b) pressure side for $Ro = 0.20$.
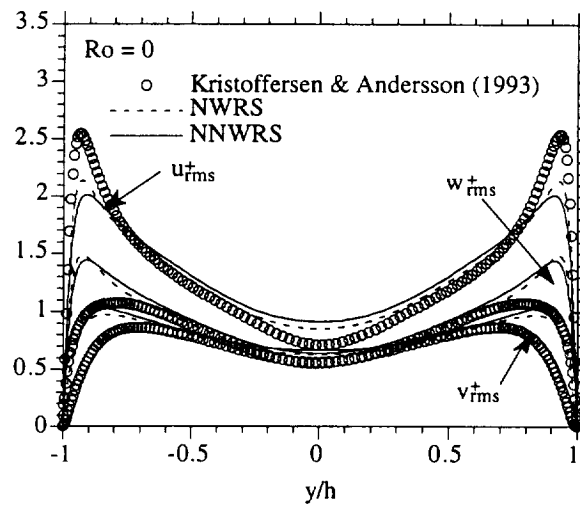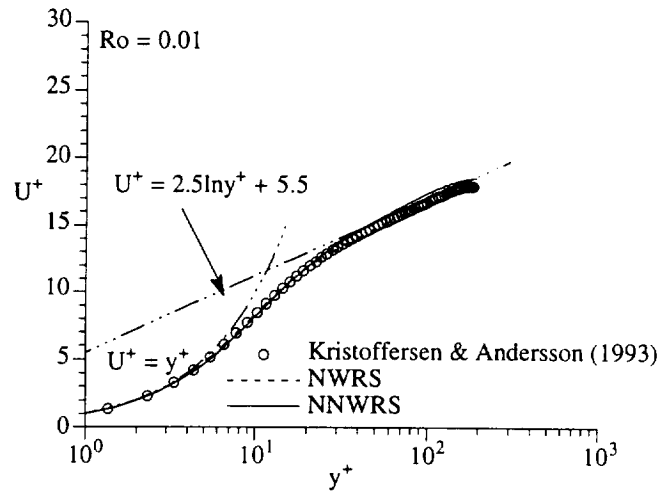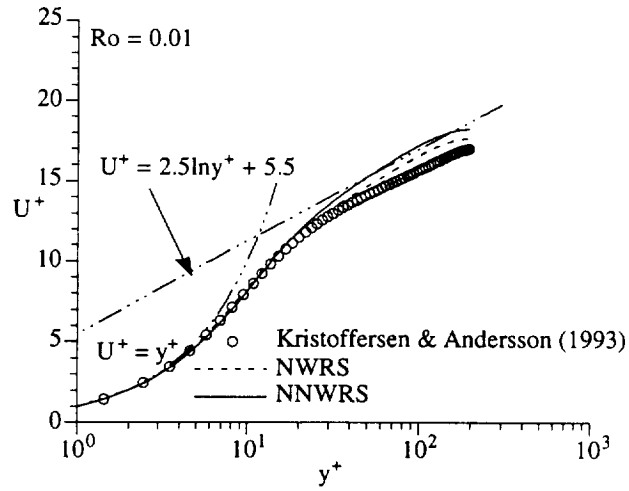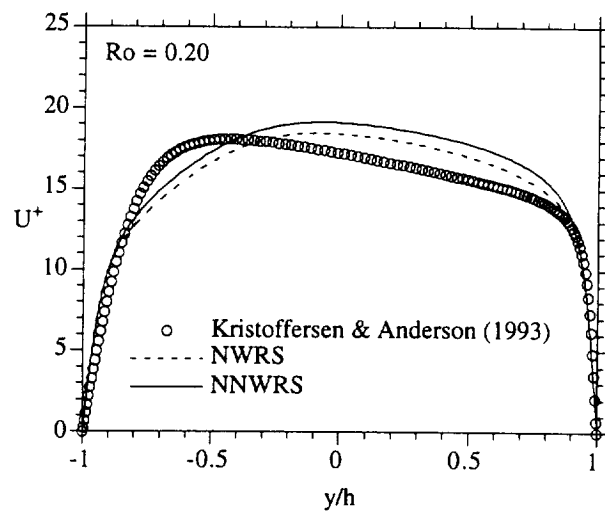
(a)
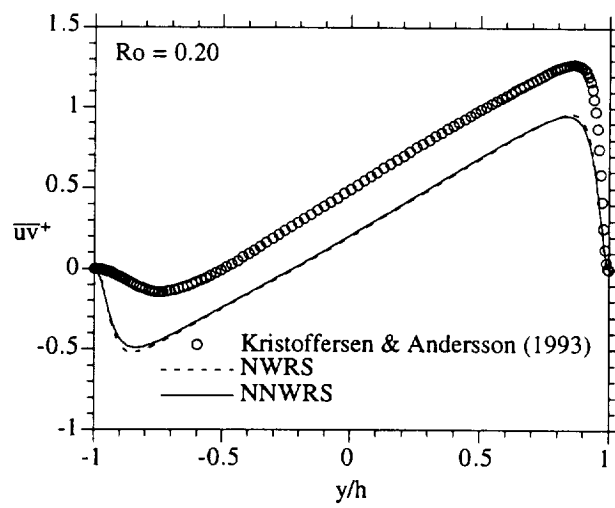
(b)
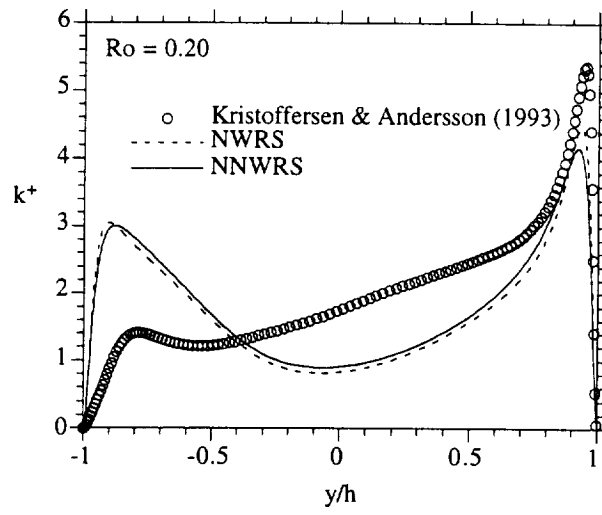
(c)
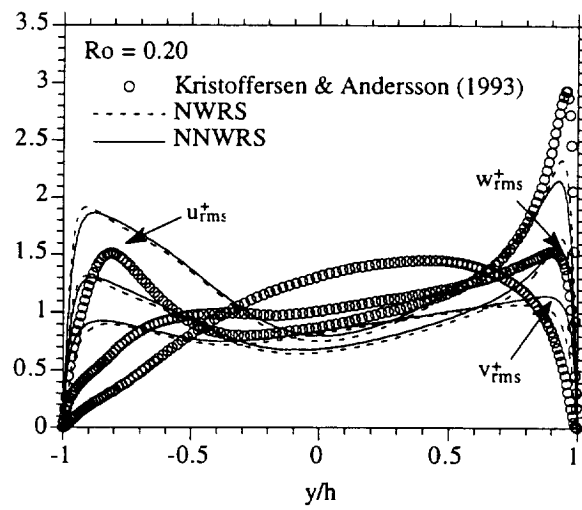
(d)

Fig. 4.43 Comparison between model predictions and DNS data across the channel for (a) mean velocity; (b) turbulent shear stress; (c) turbulent kinetic energy; and (d) turbulent fluctuations.
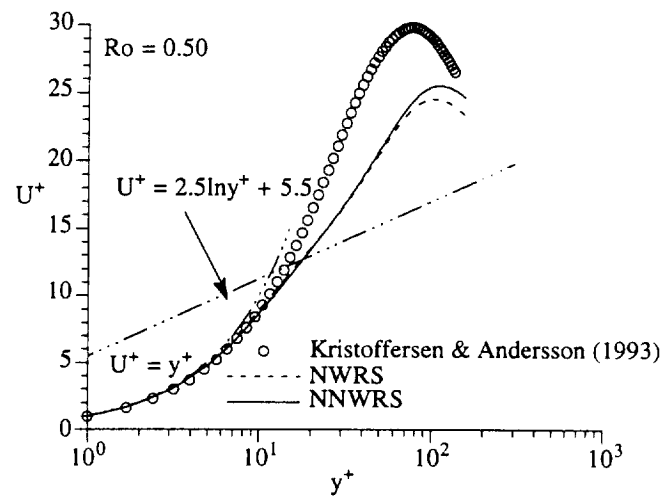
(a)
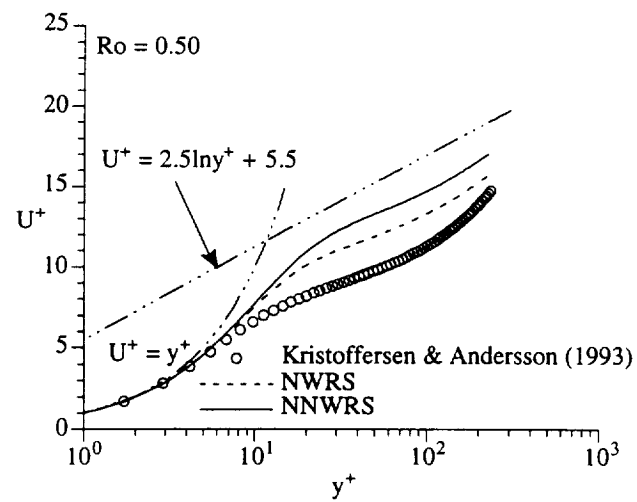
(b)

Fig. 4.44 Comparison between predicted and DNS mean velocity profiles in wall coordinates on (a) suction side and (b) pressure side for $Ro = 0.50$.

184

(a)

(b)

Ro = 0.50

o   Kristoffersen & Andersson (1993)
----- NWRS
——— NNWRS

k^+

-1   -0.5   0   0.5   1
y/h

(c)

Ro = 0.50

o   Kristoffersen & Andersson (1993)
----- NWRS
——— NNWRS

w^+_{rms} u^+_{rms} v^+_{rms}

-1   -0.5   0   0.5   1
y/h
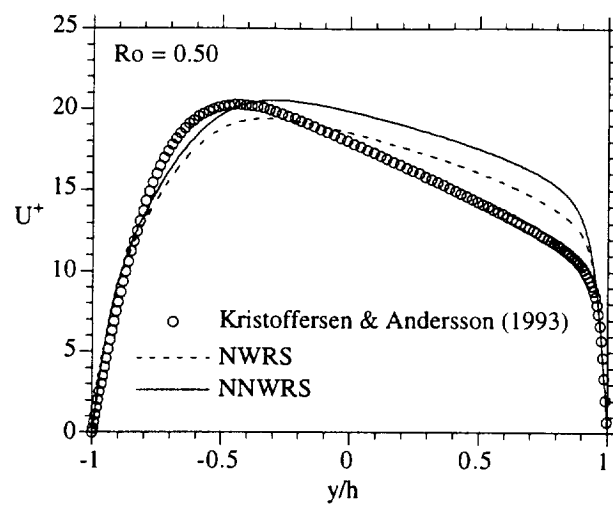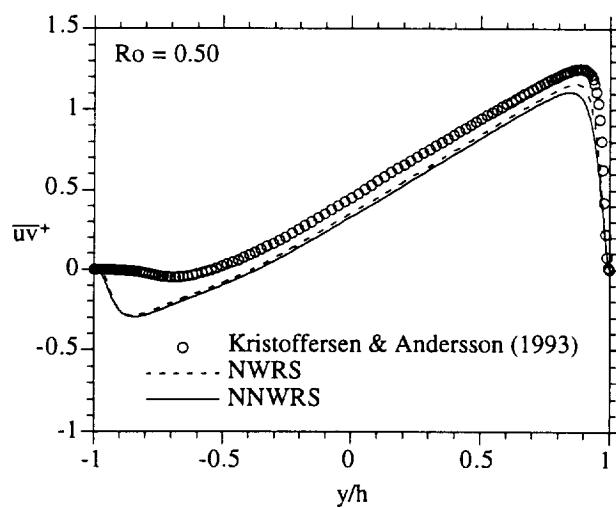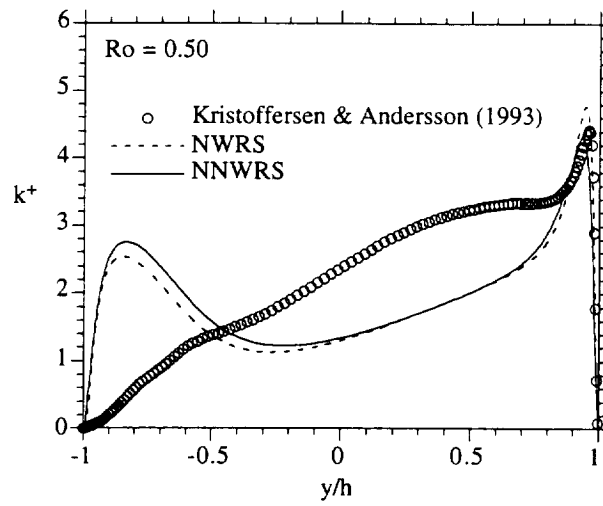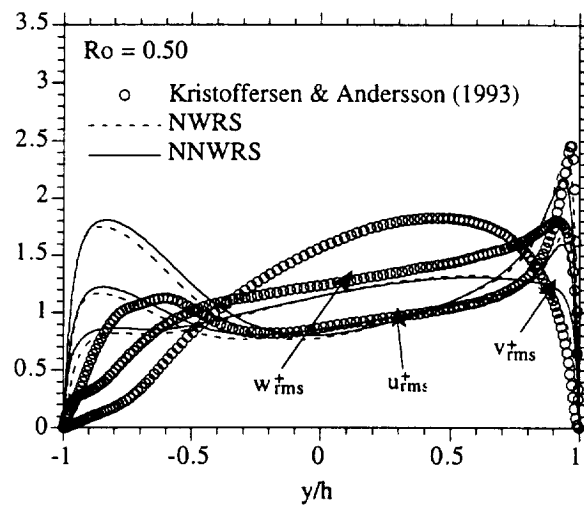
(d)

Fig. 4.45 Comparison between model predictions and DNS data across the channel for (a) mean velocity; (b) turbulent shear stress; (c) turbulent kinetic energy; and (d) turbulent fluctuations.
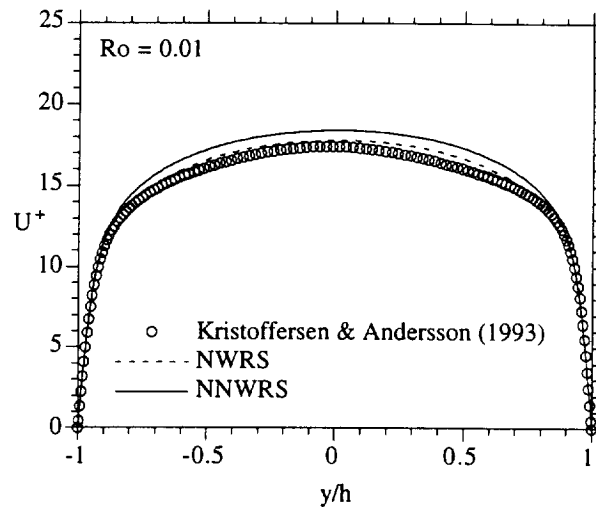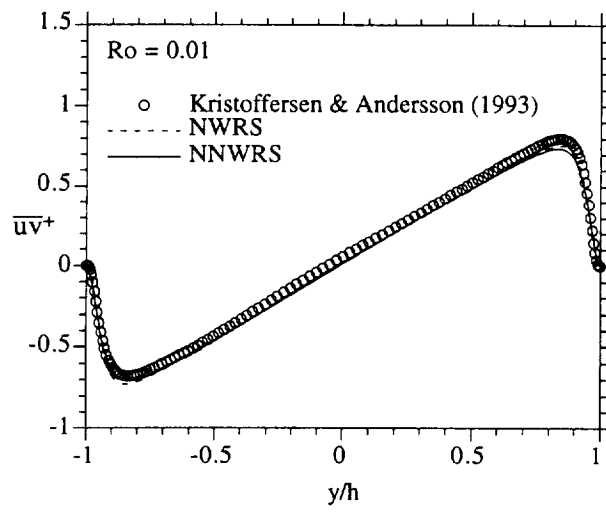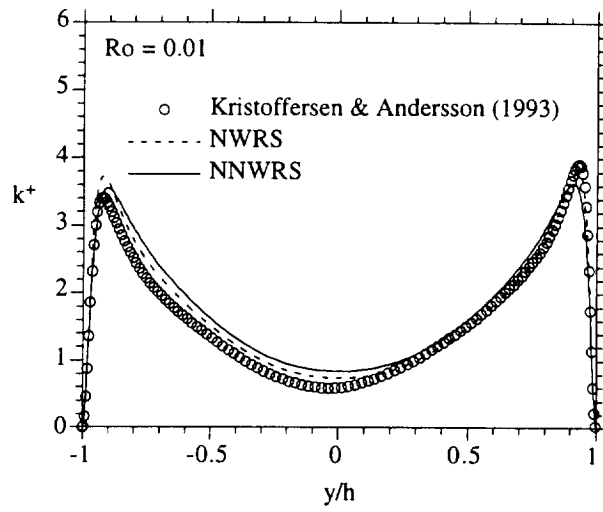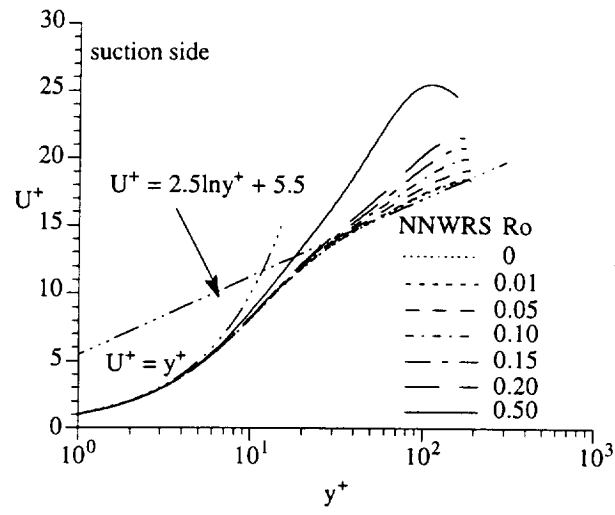
(a)
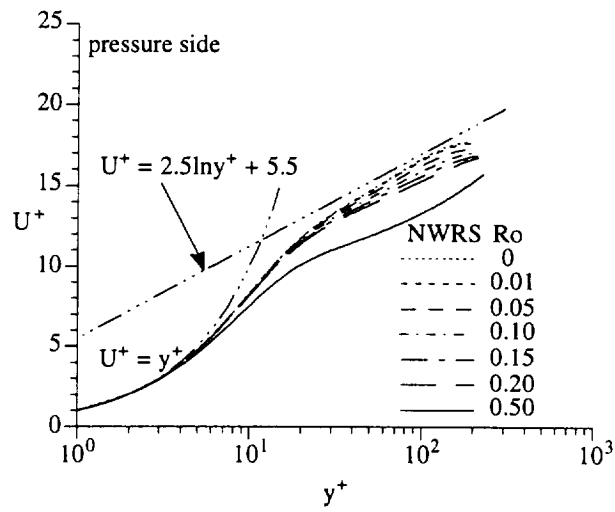
(b)

Fig. 4.46 Predicted mean velocity profiles for different rotation numbers in wall coordinates on (a) suction side and (b) pressure side.

187
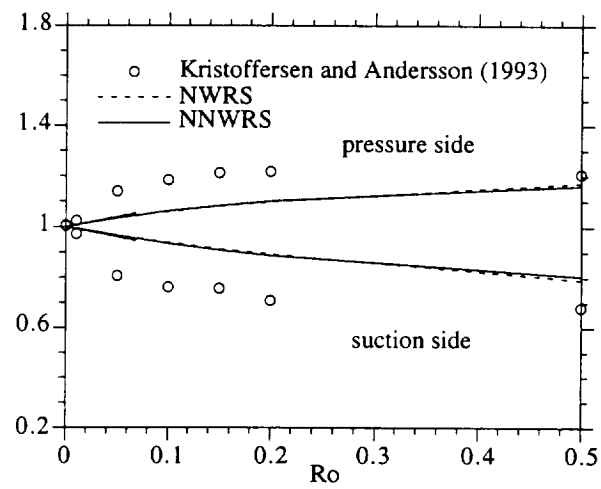
Fig. 4.47 Comparison between predicted and DNS wall friction velocities $u_{\tau p} / u_\tau$ and $u_{\tau s} / u_\tau$ as function of Ro.

5. VALIDATION AGAINST TURBULENT FLOWS WITH COMPLEX GEOMETRIES

5.1 Introduction

The NNWRS model is developed for complex turbulent flows, in particular for flows with complex geometry. Two-dimensional flow over a backward-facing step and three-dimensional flow in a square duct are typical complex flows resulting from the presence of multiple walls. Complex flow phenomena such as recirculation, reattachment, and boundary layer re-development to a fully-developed state are observed in the plane backward-facing step flow (Fig. 5.1). These flow features all result from the existence of the step. In a straight square duct (Fig. 5.10), the local flow structure is dominated by a transverse mean flow commonly known as secondary flow of the second kind induced by the presence of the corners. The mean transverse secondary flow consists of eight streamwise vortices, two counter-rotating in each corner, with the flow toward the corners from the duct center along the corner bisector, and toward the duct center along the bounding wall and wall bisector. In the following sections, two-dimensional backward-facing step flow and three-dimensional flow in a square duct are used as the testing cases to verify the NNWRS model's ability to predict flows with complex geometry.

5.2 Two-Dimensional Flow Over a Backward-Facing Step

5.2.1 Background   Numerous attempts have been made to model two-dimensional backward-facing step flow by using various Reynolds stress models. Errors up to 50% ~ 100% between the model predictions of skin friction coefficient $C_f = 2\tau_w / (\rho U_o^2)$ and available data are often observed (So et al. 1988; Ko and Durbin 1994; Lien and Leschziner 1994). Here, U_o is the bulk mean velocity at the entrance, ρ is fluid density and τ_w is the wall shear stress. One finding in the prediction of C_f by near-wall second-order models employing wall normals in the near-wall corrections is that the models tend to overshoot C_f in the adverse pressure gradient region after the reattachment point. However, no such overshooting is observed in predictions given by those high-Reynolds-number models invoking wall functions to satisfy the boundary conditions (So et

189

al. 1988) and Durbin's Reynolds stress model (1993). In Durbin's model, redistributive terms in the Reynolds stress equations are modeled by an elliptic relaxation equation to represent strongly non-homogeneous effects produced by the presence of walls, and no damping functions are needed (hereafter Durbin's model is referred to as the elliptic-relaxation model). Thus, the overshooting of C_f persisting in the near-wall Reynolds models is speculated to be caused by the use of wall normals in the near-wall correction terms. Since no wall normal is used in the NNWRS model, the comparison between the NNWRS model predictions of C_f and those given by the NWRS model will shed light on whether the use of wall normals is responsible for the overshooting of C_f in the near-wall turbulence modeling.

5.2.2 Numerical implementations and boundary conditions The TEACH code and corresponding numerical procedures discussed in Section 4.2.2 are adopted for the current two-dimensional numerical computations in Cartesian coordinates. Only half of the expanded channel is considered since the flow is symmetric about the centerline. The computations are conducted in a domain $50h \times 6h$ shown in Fig. 5.2 with a grid distribution 91×81 in the streamwise and transverse directions, respectively. The grid is clustered at the inlet and the near-wall regions. Finer grid 131×151 was tested to give essentially identical results. Thus, grid 91×81 is used in the final computations. The convergence criterion is again given by (4-12).

The model equations for two-dimensional backward-facing step flow are elliptic-type equations. To solve these equations in the (x, y)-plane, boundary conditions at the inlet and outlet of the computational domain, along the centerline of the expanded channel and the step walls are required. The mean velocity and the turbulent statistics at the inlet ($x = 0$) are provided by the available DNS data. Negligible diffusion boundary conditions are specified at the outlet ($x = 50h$), i.e.

$$\frac{\partial^2 (U, V, \overline{uu}, \overline{vv}, \overline{ww}, \overline{uv}, \varepsilon)}{\partial x^2} = 0 \quad .$$ (5-1)

Along the step walls all the variables are zero according to the no-slip condition except the dissipation rate, which is given by

$$\varepsilon = 2\upsilon \left(\frac{\partial \sqrt{k}}{\partial x} \right)_w^2 \quad ,$$

(5-2)

along the vertical wall ($x = 0$) and by

$$\varepsilon = 2\upsilon \left(\frac{\partial \sqrt{k}}{\partial y} \right)_w^2 \quad ,$$

(5-3)

along the horizontal wall ($y = 0$). Symmetry conditions are applied at the centerline ($y = 6h$) which yield

$$\frac{\partial (U, \overline{uu}, \overline{vv}, \overline{ww}, \varepsilon)}{\partial y} = 0 \quad , \text{ and } \quad V = \overline{uv} = 0 \quad .$$

(5-4)

5.2.3 Cases studied and comparisons with data   Both numerical and experimental study has been carried out for the same backward-facing step flow (Le et al. 1993; Jovic and Driver 1993) with $Re_h = U_o h / \upsilon = 5,100$ and the expansion ratio $\delta / h = 1.2$, where δ is the boundary layer thickness and h is the step height. Detailed distributions of skin friction coefficient C_f, wall pressure coefficient $C_P = 2(P - P_o) / \rho U_o^2$ (where P is the wall static pressure along the streamwise direction and P_o is the wall static pressure at $x = 0$), mean velocity U, kinetic energy k, and turbulent stresses u_{rms}, v_{rms}, w_{rms}, and $\overline{uv}$ at several downstream locations were given. The same case is used to test our models.

Fig. 5.3 shows the flow pattern predicted by the NNWRS model. As a result of flow separation, immediately after the step, a primary cell and a corner cell rotating in opposite directions are generated. Further downstream, the flow develops into a plate boundary layer flow. The NWRS model predicts a similar flow pattern (no shown). Predicted friction coefficient C_f, DNS results and measurements are compared in Fig. 5.4. The length between two zero crossing points of C_f is the recirculation region in the streamwise direction. The first zero crossing point signifies the beginning of the reverse flow. The corner cell locates between the step corner and the first zero crossing point of C_f. The NWRS model predicts the length of the corner cell is about $2h$, which agrees with the DNS prediction, whereas the NNWRS model gives a slightly smaller

191

length. Durbin's elliptic-relaxation model predicts the smallest corner cell length among the three turbulent models. The second zero crossing point of C_f is the mean reattachment point defined as the location of zero wall shear stress. The DNS and measurements show the flow has a reattachment length of $6h$, which is also predicted by both the NNWRS and NWRS models. The elliptic-relaxation model, however, overpredict the reattachment length, which is $6.6h$. The maximum friction coefficient ($|C_f|$) in the reverse flow region is predicted well by the NNWRS and NWRS models, but it is underpredicted by the elliptic-relaxation model. After the reattachment point, the elliptic-relaxation model follows the DNS data and measurement quite well, although underpredicting C_f slightly. The overshooting of C_f in Reynolds-stress models mentioned by So et al. (1988) is also observed in the NNWRS model. This indicates that wall normals used in the near-wall corrections in the NWRS model are not the culprit for the overshooting. Further investigation is needed to find out the cause for this peculiar overshooting behavior in the Reynolds stress models.

Fig. 5.5 compare the wall pressure coefficient C_P. Model predictions and data all show the wall pressure along the horizontal step wall first slowly decreases from P_o (indicating a favorable pressure gradient), and then rapid increases at some location in the recirculation region (indicate an adverse pressure gradient). It continues to increase and approaches to a constant as the boundary layer redevelops in the downstream. Contrary to their prediction of C_f, the predictions of C_P given by the NNWRS and NWRS models agree very well with both DNS data and measurements, whereas the elliptic-relaxation model underpredicts C_P in adverse pressure gradient region.

Fig. 5.6 shows the comparison of normalized mean velocity $U^+ = U / u_\tau$ in the wall coordinate $y^+ = u_\tau y / \upsilon$ at three downstream locations after the reattachment point: $x / h = 10$, 15, and 19. The log-law and linear law are also included for comparison in the figure. The non-dimensional mean velocity profiles at these locations are predicted well by the elliptic-relaxation model, but underestimated by the NNWRS and NWRS models. This is consistent with the model predictions of the friction coefficient C_f after the reattachment (Fig. 5.4). The DNS data and

measurements show that the log region in the velocity profile at location $x / h = 10$ is very small and the intercept with U^+-axis is also much smaller than 5.4 (Fig. 5.6a). As the flow develops further downstream, the length of log-law region increases and U^+ becomes closer to the log law (cf. Fig. 5.6a with Figs. 5.6b and 5.6c). The deviation of the velocity profile U^+ from the log-law may be due to the strong streamwise adverse pressure gradient (Nagano et al. 1991). It may also result from the non-equilibrium effects persistent after the reattachment. Further downstream, the adverse pressure gradient decreases, and the mean velocity profile U^+ becomes closer to the log-law.

The performance of the models are further examined by comparing the model predictions of the streamwise mean velocity U and turbulent statistics (including kinetic energy k, normal stresses u_{rms}, v_{rms}, w_{rms}, and shear stress $\overline{uv}$) with the DNS data and measurements in the global coordinate at locations $x / h = 4, 6$, and 10 (Figs. 5.7-5.9). Note that the location of the y axis in these figures is shifted for different measured locations. Fig. 5.7 plots the mean velocity profile U / U_o versus y / h at $x / h = 4, 6$, and 10. It shows that U experiences rapid changes in the near-wall region and approaches a constant as $y / h > 2$. Unlike their predictions of U^+ in the wall coordinate y^+, the NNWRS and NWRS models give better predictions of U / U_o in the global coordinate than the elliptic-relaxation model does (cf. Fig. 5.7 with 5.6). In the near-wall region, all three models predict a negative U at $x / h = 4$, which agrees with the data. This confirms that location $x / h = 4$ indeed is inside the reverse flow region determined from the friction coefficient C_f (see Fig. 5.4). At $x / h = 6$, the elliptic-relaxation model predicts a small negative U in the inner layer, whereas the NNWRS and NWRS models predict a small positive U there. This indicates that the reverse flow region ends and reattachment begins near $x / h = 6$. After the reattachment point, at $x / h = 10$, all the models predict a positive U across the expanded channel; the NWRS and NNWRS models follow the data better than the elliptic-relaxation model does.

The predicted turbulent kinetic energy k is compared with the DNS data in Fig. 5.8. Note that Jovic and Driver (1993) did not report the measured normal turbulent fluctuation w_{rms}, so the measured kinetic energy k is not available. The mixing layer type structure in the flow separation

region behind the step significant enhances the turbulent production (Jovic and Driver 1993), resulting in high kinetic energy peak. As flow moves to the downstream, turbulence decays and the peak of the kinetic energy decreases. Compared with the DNS data, the NNWRS and NWRS models give pretty good predictions of k, although the NNWRS model slightly overpredicts the peak of k at $x/h = 6$ and 10, and the NWRS model underestimates the peak at $x/h = 4$. The elliptic-relaxation model underpredicts k at all three locations. The comparisons of turbulent normal stresses u_{rms}, v_{rms}, w_{rms} and shear stress $\overline{uv}$ at the same locations are shown in Fig. 5.9. Overall, the elliptic-relaxation model given better predictions of turbulent stresses in the near wall region than the NNWRS and NWRS models, but the NNWRS and NWRS models outperform the elliptic-relaxation model in the outer region. The peak value of u_{rms} is overestimated by the NNWRS and NWRS models, whereas the peak value of w_{rms} is underpredicted by the elliptic-relaxation model.

5.3 Three-Dimensional Flow in a Square Duct

5.3.1 Background Turbulent flow in a square duct is characterized by the existence of secondary flow of the second kind (as classified by Prandtl) in the plane perpendicular to the streamwise direction. This kind of secondary flow in a non-circular straight duct is created by turbulent motion. Although relatively weak (2-3% of the streamwise bulk velocity), its effects on wall shear stress distribution, heat transfer rates, or transport of passive tracers are quite significant (Demuren 1990). Being of considerable engineering interests, turbulent flow in a straight non-circular duct has been the subject of many experimental and numerical investigations (Demuren and Rodi 1984). Systematic measurements of flow in a non-circular straight duct have been carried out by Gessner's group (Po 1975; Lund 1977; Eppich 1982; Gessner and Emery 1981). The farthest measured location in their experiments away from the entrance is $84\,D_h$, where D_h is the hydraulic diameter of the duct. According to the measurements, flow at this location is already fully developed. Similar experiments were also conducted in a duct with a length shorter than $84\,D_h$ (Melling and Whitelaw 1976; Launder and Ying 1972). Although Brundett and Baines

(1964) carried out measurements as far as $260\,D_h$ from the entrance, where the flow is fully developed, the inaccurate method used to measure the turbulent stresses made their measurements less reliable.

Direct numerical simulation provides an alternative approach to study the fully developed square duct flow at low Reynolds numbers. Recently, Huser and Biringen (1993) and Gavrilakis (1992) carried out direct numerical simulation for square duct flow at Reynolds number $Re_b = U_b D_h / \upsilon = 10{,}320$ (U_b is the bulk velocity in the streamwise direction) and $Re_b = 4{,}410$, respectively. Although the Reynolds numbers in the DNS are much lower than those in the experiments mentioned above, it appears that the mechanisms driving the corner secondary flow at disparate Reynolds numbers are similar. Huser and Biringen (1993) showed that the low-Reynolds-number effects are manifested in the reduction of the distance from the vortex centers to the corner and the reduction of the secondary flow near the wall bisector compared to high-Reynolds-number experiments. Gavrilakis (1992) also found out that viscous effects are quite important in the transportation of mean vorticity in low-Reynolds-number flow, whereas they are important only in the region very close to the corner in high-Reynolds-number flow (Demuren and Rodi 1984).

The origin of the secondary motion can be identified through analyzing the streamwise vorticity development along the duct. The mechanisms which cause streamwise vorticity to develop in turbulent flow along a corner are responsible for the initiation of the secondary flow. Following Prandtl's (1926) original idea on the secondary motion, Einstein and Li (1958) carried out a rigorous analysis to show that the gradients of Reynolds stresses are the actual source of the secondary motion. For a fully developed incompressible flow, the mean streamwise vorticity Ω_x is governed by

$$V\frac{\partial \Omega_x}{\partial y} + W\frac{\partial \Omega_x}{\partial z} = \frac{\partial^2}{\partial y \partial z}\left(\overline{w^2} - \overline{v^2}\right) - \left(\frac{\partial^2}{\partial z^2} - \frac{\partial^2}{\partial y^2}\right)\overline{vw} + \upsilon\left(\frac{\partial^2 \Omega_x}{\partial y^2} + \frac{\partial^2 \Omega_x}{\partial z^2}\right) \quad , \tag{5-5}$$

where

195

$$\Omega_x = \frac{\partial V}{\partial z} - \frac{\partial W}{\partial y} \quad . \tag{5-6}$$

In (5-5), the terms on the left-hand side represent the convection of the streamwise mean vorticity in the transverse plane; the first two terms on the right-hand side express the influence of the turbulent stresses on the production or destruction of the streamwise vorticity; and the last term on the right-hand side is the viscous-damping term. The two turbulent-stress terms are found to be the dominant terms, and it is the difference between these two relatively large terms that drives the weak secondary motion (Demuren and Rodi 1984). This implies that modeling the secondary motion in a duct requires an anisotropic turbulence model.

Many attempts have been made to calculate the flow in a non-circular straight duct by using algebraic models or Reynolds stress models. The algebraic models can be obtained from the Reynolds stress models by neglecting the convection and diffusion terms. Most computations were carried out by using algebraic turbulence models (Launder and Ying 1973; Gessner and Emery 1981; Gosman and Rapley 1980; Naot and Rodi 1982; Demuren and Rodi 1984). Although the algebraic models can give reasonable overall predictions of secondary motion by tuning the model parameters, the models themselves do not correctly reflect the real physical processes (Demuren and Rodi 1984). Among the few applications of the Reynolds stress models to flow in a non-circular duct, wall functions were used to satisfy the boundary conditions (Naot et al. 1974; Reece 1976; Launder and Li 1994). The correct modeling of near-wall turbulence is crucial to the reproduction of the secondary flow in wall-bounded duct flow. Therefore, square duct flow provides a severe case to test the correctness of turbulent modeling of the wall effects. In addition, since the flow is bounded by multiple walls and has two inhomogeneous directions, it is also an ideal case to show the advantages of the wall-independent NNWRS model.

5.3.2 *Cases studied*   The high-Reynolds-number case ($Re_b = 250,000$) investigated by Gessener's group in the laboratory and the low-Reynolds-number case ($Re_b = 10,320$) studied by Huser and Biringen (1993) using DNS are selected to test our turbulence models for square duct flow. Through the continuous effort of Gessener's group, fairly complete experimental data are

available for three-dimensional turbulent flow in a square duct at $\text{Re}_b = 250,000$. These data include mean velocities in streamwise and transverse directions, wall shear stress, and the turbulent stresses along both wall and corner bisector at streamwise locations $x / D_h = 8$, 40 and 84. At location $x / D_h = 84$, the flow is fully developed (Gessener and Emery 1981). These reported data can be found in Gessener et al. (1979, 1991, 1993) and Gessner and Emery (1981). Hereafter this high-Reynolds-number case is referred to as Gessner and Emery's (1981) case. In Huser and Biringen's (1993) case, the flow is fully developed, and detailed DNS data are available. These two cases together will demonstrate the advantages of wall-indepent NNWRS model for flows with multiple walls and should complement the turbulence model validations over a wide range of Reynolds numbers for flow in developing region as well as in fully developed state.

5.3.3 Numerical procedure and boundary conditions   The coordinate system and computational domain for a quarter of the square duct are shown in Fig. 5.10. Three-dimensional parabolic marching scheme of Patankar and Spalding (1972) is adopted to solve the governing equations. This numerical scheme assumes that the streamwise mean velocity is determined by the averaged pressure in the plane perpendicular to the streamwise axis, and iterations are therefore carried out in the transverse plane. At fixed streamwise location (x), the discretization procedure is similar to that described in Section 4 for swirling flow, and a line-by-line iterative scheme is used to solve the tridiagonal matrix in alternating directions. SIMPLEC algorithm (modified from SIMPLE) is adopted to link the pressure field with the velocity field. Fig. 5.11 shows the grid distribution of 91×91 in the lower left quadrant of the duct in the (y, z)-plane. The grid points are clustered near the walls and 91×91 is found to be fine enough for the cases studied. The marching step size increases progressively from $0.004\, D_h$ at the entrance ($x = 0$) to $0.04\, D_h$ at downstream location $x / D_h = 100$.

The inlet ($x = 0$) conditions determine the development of the flow in the square duct because the governing equations are of parabolic-type. At the inlet, the mean flow in the core region is assumed to be uniform with turbulence intensity $I = 0.35\%$. Near the walls the flow field is obtained from the flat-plate boundary layer theory with relative boundary layer thickness

$\delta / a = 0.02$ on the duct midplane ($y = a$), where δ is the boundary layer thickness and a is the length of the wall bisector (see Fig. 5.10). The secondary velocities V and W, and turbulent shear stress $\overline{vw}$ are set to zero at the inlet. All the variables are specified such that their iso-contours are parallel to the duct walls and have a square shape to give symmetric distributions about the corner bisector. No outlet conditions are needed for this parabolic problem. Symmetry conditions are used at the wall bisectors ($y = a$, $z = a$), namely

$$\frac{\partial(U,\ W,\ \overline{uu},\ \overline{vv},\ \overline{ww},\ \overline{uw},\ \varepsilon)}{\partial y} = 0 \ , \text{and} \ V = \overline{uv} = \overline{vw} = 0 \ , \text{at} \ y = a \ , \tag{5-7a}$$

$$\frac{\partial(U,\ V,\ \overline{uu},\ \overline{vv},\ \overline{ww},\ \overline{uv},\ \varepsilon)}{\partial z} = 0 \ , \text{and} \ W = \overline{uw} = \overline{vw} = 0 \ , \text{at} \ z = a \ , \tag{5-7b}$$

and no-slip boundary conditions require all the variables be zero at the walls ($y = a$, $z = a$) except for the dissipation rate, which is specified as

$$\varepsilon = 2\upsilon\left(\frac{\partial\sqrt{k}}{\partial y}\right)_w^2 \ , \text{at} \ y = 0 \ , \tag{5-8a}$$

$$\varepsilon = 2\upsilon\left(\frac{\partial\sqrt{k}}{\partial z}\right)_w^2 \ , \text{at} \ z = 0 \ . \tag{5-8b}$$

5.3.4 Results and discussion   The model-data comparisons are presented first for the case of Huser and Biringen (1993) for fully developed flow at low Reynolds number and then for the case of Gessner and Emery (1981) for developing flow at high Reynolds number. Model predictions for the low Reynolds number case show that the flow at x / D_h = 84 already reaches the fully developed state since no more change is observed further downstream. Therefore, the model results at x / D_h = 84 are used to compare with the DNS data given by Huser and Biringen (1993) for the fully developed flow.

Fig. 5.12 displays the secondary flow velocity vectors predicted by the NNWRS model, revealing two streamwise, counter-rotating, and symmetric (with respect to corner bisector) vortices in the corner. The flow on the transverse plane moves towards the corner along the corner bisector ($y = z$), and by virtue of mass continuity, it moves away from the corner along the walls

($y = 0$ and $z = 0$) and towards the center of the duct along the wall bisectors ($y = a$ and $z = a$). This predicted flow pattern is very similar to that shown in Huser and Biringen (1993), with the centers of the vortices shifted slightly away from the corner. The vortex centers in Fig. 5.12 are located at ($y \approx 0.25a$, $z \approx 0.55a$) and ($y \approx 0.55a$, $z \approx 0.25a$), whereas their counterparts predicted by the DNS are located at ($y \approx 0.2a$, $z \approx 0.4a$) and ($y \approx 0.4a$, $z \approx 0.2a$)

Fig. 5.13 shows the isotachs (lines of constant streamwise mean velocity in (y, z)-plane) of U / U_c (U_c is the mean velocity at the centerline of the duct) predicted by the NNWRS model. The isotachs are bent toward the corner with a milder curvature near the corner bisector compared with those isotachs shown in Huser and Biringen (1993); the predicted isotachs close to the walls are also flatter. Similar secondary flow pattern predicted by the NWRS model is observed (not shown).

The comparison between the predicted normalized wall shear stress $\tau_w / \overline{\tau}_w$ ($\overline{\tau}_w$ is the average value of τ_w over the walls) and the DNS data along one wall is shown in Fig. 5.14. The $\tau_w / \overline{\tau}_w$ given by the NWRS model is much overpredicted near the corner, but agrees reasonably well with the DNS data away from the corner. On the other hand, the $\tau_w / \overline{\tau}_w$ predicted by the NNWRS model follows the DNS data quite well from the corner to the location of the first peak in the DNS data; further away from the corner, the NNWRS model slightly overpredicts the wall shear stress. The predicted mean streamwise velocity profiles U along the wall bisector ($y = a$) are plotted in Fig. 5.15 and compared with the DNS data. Both models give very good predictions of the streamwise mean velocity U.

In Fig. 5.16, the predicted secondary velocity V along the wall and corner bisector are compared with the DNS data. Both models overestimate V along the wall bisector except in the region near the center of the duct (Fig. 5.17a); the results given by the NNWRS model are closer to the data compared with those predicted by the NWRS model. Along the corner bisector (Fig. 5.17b), although the NNWRS model follows the data near the corner and the center quite well, it predicts a secondary velocity profile with a much smaller peak. On the other hand, the NWRS model predicts a secondary velocity profile with a similar shape as shown by the DNS data, but the

199

peak is overpredicted by the NWRS model and its location is shifted toward the corner. The distributions of normal stress difference $(\overline{w^2} - \overline{v^2})$ along the wall bisector are shown in Fig. 5.17. Compared with the DNS data, the NNWRS model gives a very good prediction of the normal stress difference, whereas the NWRS model much overestimates the difference near the walls.

Fig. 5.18 shows the development of streamwise vortices in the lower left quadrant of the duct predicted by the NNWRS model for the high-Reynolds-number ($\mathrm{Re}_b = 250{,}000$) case. The comparisons of secondary flow patterns at locations $x/D_h = 8$, 40 and 84 indicate that the streamwise vortices in the developing flow are initially generated near the corner; as flow develops along the straight duct, they move away from the corner and spread out in the cross section until the flow becomes fully developed. At $x/D_h = 84$, the NNWRS model predicts the vortex centers are located at ($y \approx 0.25a$, $z \approx 0.60a$) and ($y \approx 0.60a$, $z \approx 0.25a$), which are further away from the corner compared with those predicted by the same model for the low-Reynolds-number flow (cf. Fig. 5.18c with Fig. 5.12). Fig. 5.19 plots the predicted and measured isotachs of the streamwise mean velocity U normalized by U_c. The model predictions at $x/D_h = 8$ (Fig. 5.19a), showing that the isotachs are bent toward the corner and are flat along the walls, are in very good agreement with the data. At $x/D_h = 40$ and 84, the predicted isotach contours are less distorted compared with the measured ones (Fig. 5.19b and 5.19c).

The distributions of normalized wall shear stress $\tau_w / \overline{\tau}_w$ at three streamwise locations $x/D_h = 8$, 40, and 84 are shown in Fig. 5.20. Unlike the low-Reynolds-number case, the NWRS and NNWRS models give almost the same predictions of wall shear stress at all three locations for the high-Reynolds-number case (cf. Fig. 5.20 with Fig. 5.14). The predictions agree well with the measurements at $x/D_h = 84$, although they are slightly overpredicted near the wall bisector. The rather flat predicted wall shear stress profiles result from the almost parallel distribution of isotach contours near the wall predicted by the models (Fig. 5.19).

The variation of predicted centerline mean velocity in the streamwise direction is plotted in Fig. 5.21 and compared with the measurements. According to the experimental data, the mean velocity along the centerline first increases to the peak value, and then decreases and levels off to

an asymptotic value in the fully developed region. Both model results agree very well with the data in the developing region. In the shear interaction region near $x / D_h = 40$, the NWRS model gives better predictions of U_c than the NNWRS model does. The NNWRS model predicts a shorter developing region and a lower peak value of U_c. As flow approaches to the fully developed state, the centerline velocity is also predicted well by the NWRS model, whereas underpredicted by the NNWRS model slightly. Fig. 5.22 shows the comparisons between the predicted and measured streamwise mean velocity U normalized by the bulk mean velocity U_b along the wall and corner bisector at locations $x / D_h = 8, 40$ and 84. The predictions given by both models are identical and in very good agreement with the data along both wall and corner bisector at all three locations.

Comparisons between predicted and measured secondary flow velocity profiles along the wall and corner bisector at the same locations are shown in Fig. 5.23. Unlike the low-Reynolds-number case, both models give almost identical predictions of the secondary mean velocity for the high-Reynolds-number case (cf. Fig. 5.23 with Fig. 5.16). The secondary mean velocity is underpredicted by the models along the wall bisector at $x / D_h = 40$ and 84. Along the corner bisector, the model-data agreement is good at $x / D_h = 40$, but both models still underestimate V at $x / D_h = 84$. The underestimation of V in the fully developed region is also observed when the secondary flow velocity is normalized by the local friction velocity u_τ, instead of the bulk velocity U_b (Fig. 5.24).

The comparisons between predicted and measured turbulent stress and kinetic energy distributions along the wall and corner bisector at three streamwise locations are shown in Figs. 5.25-5.29. The NNWRS model predicts slightly higher turbulent stresses and kinetic energy than the NWRS model. Predicted turbulent stresses and kinetic energy along the wall bisector are in pretty good agreement with the experimental data. Along the corner bisector, the predictions of turbulent stresses and kinetic energy are generally overestimated. At $x / D_h = 84$, data and model comparisons are also made for the normal stress difference $(\overline{w^2} - \overline{v^2})$ at locations $z / a = 0.1, 0.6$ and 1.0. Difference in the predictions given by the NWRS and NNWRS models is quite large in the inner layer, but diminishes away from the wall ($y = 0$). Compared with experimental data of

201

Eppich (1982), the normal stress difference is underestimated by the models in the near-wall region.

5.4 Concluding Remarks

In this section, the wall-independent NNWRS model has been applied to two turbulent flows with complex geometry: two-dimensional flow over a backward-facing step and three-dimensional flow in a straight square duct. The performance of the NNWRS model is shown to be as good as the wall-dependent NWRS model. The predictions of mean and turbulence flow fields in backward-facing step flow agree well with the DNS and experimental data. The NNWRS model is able to reproduce complex flow phenomena induced by the presence of the step, such as flow recirculation, reattachment, and boundary-layer redevelopment to fully developed state. The comparison of skin friction coefficient predicted by the two models indicates that the overshooting of the skin friction coefficient after the reattachment point prevalent in those near-wall Reynolds models using wall normals (including the NWRS model) is not caused by the wall normals adopted in the models. Further investigation is needed to find out the root cause for this overshooting behavior in Reynolds stress modeling. The NNWRS model is also shown to be able to capture the secondary motion induced by turbulence for low- and high-Reynolds-number flow in a square duct. It predicts that the vortex centers are closer to the corner in the low-Reynolds-number flow than in high-Reynolds number flow, which agrees with the finding of Huser and Biringen (1993). In high-Reynolds-number flow, both models give about the same predictions of the secondary flow velocity, whereas in low-Reynolds-number flow, the NWRS model predicts stronger secondary flow velocity along the wall and corner bisector compared with the NNWRS model. The larger difference between the model predictions for low-Reynolds-number flow seems to support the findings of Gavrilakis (1992) that viscous effects are more important in a low-Reynolds-number square duct flow.
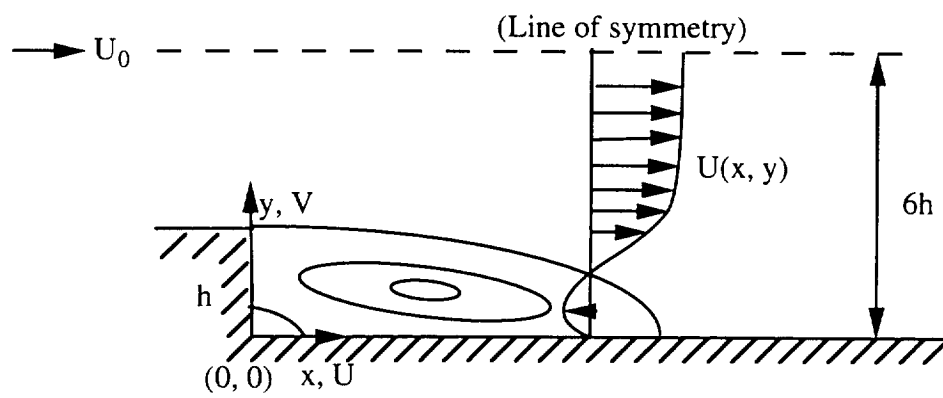
Fig. 5.1 Sketch of plane backward-facing step flow and coordinate system.
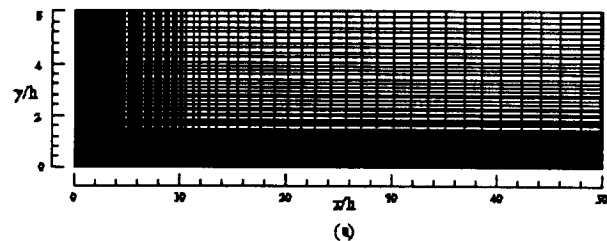
Fig. 5.2 Computational domain with grid distribution 91x81 in the streamwise and transverse directions.
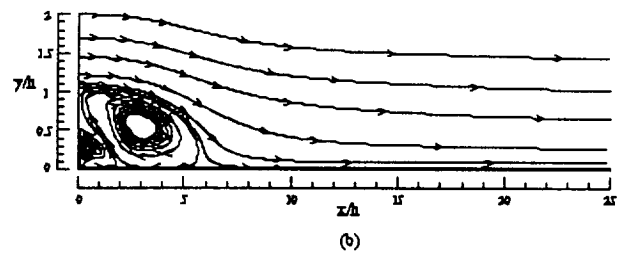
Fig. 5.3 Flow pattern of plane backward-facing step flow predicted by the NNWBS model.
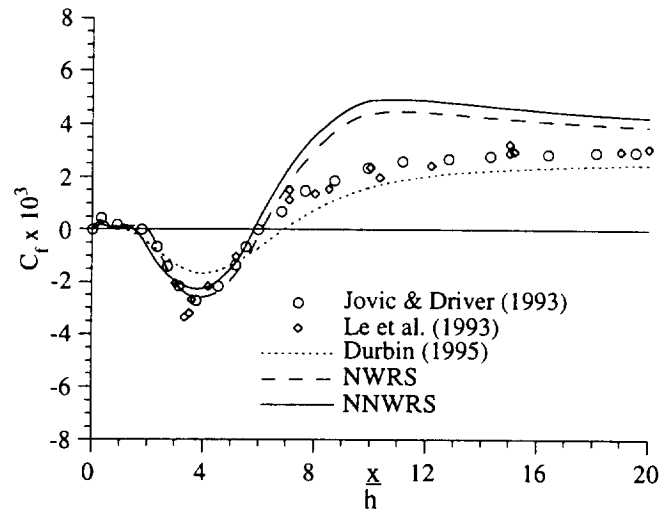
Fig. 5.4 Comparison between predicted and measured skin friction coefficient.
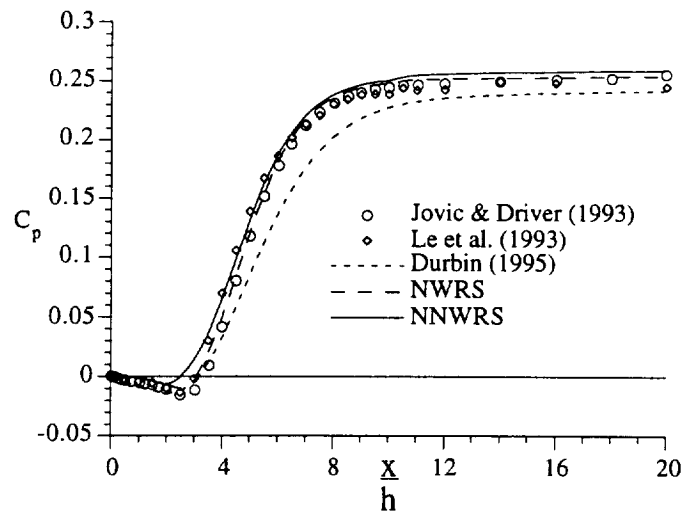
Fig. 5.5 Comparison between predicted and measured wall pressure coefficient.

205

(a)

(b)

206
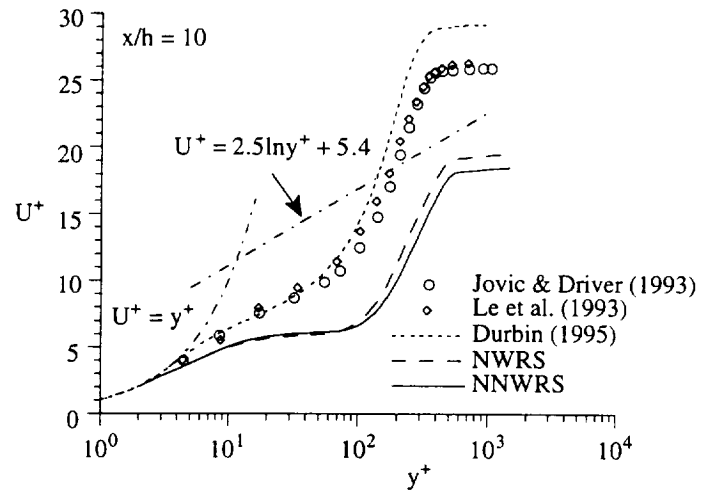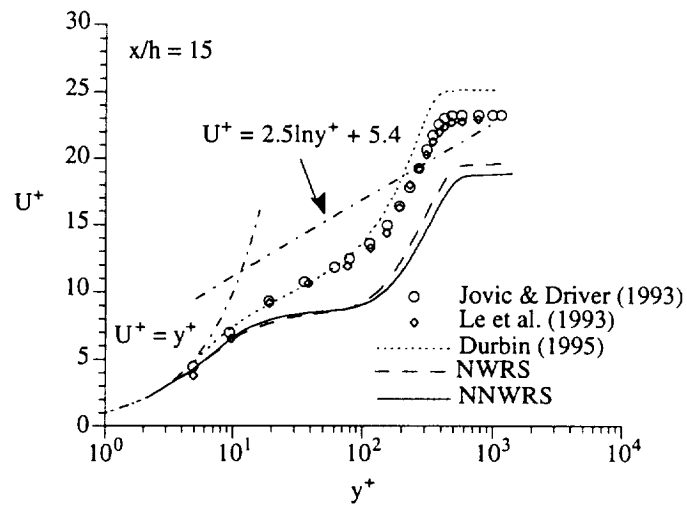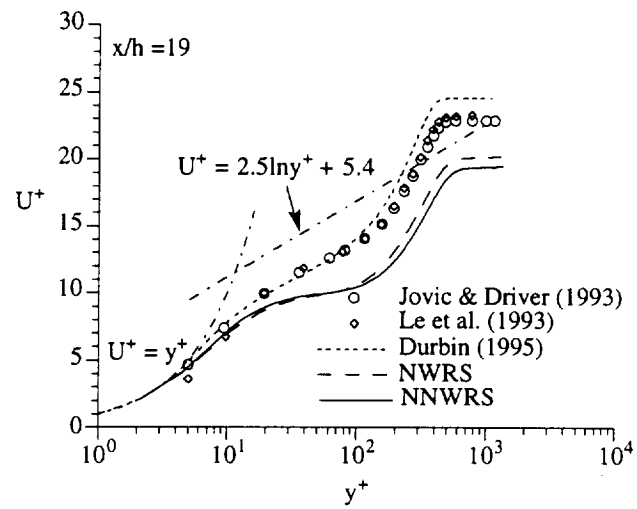
(c)

Fig. 5.6 Comparison between predicted and measured mean velocity profiles U^+ in wall coordinate y^+ at different downstream locations after the the reattachment point: (a) $x / h = 10$, (b) $x / h = 15$, and (c) $x / h = 19$.
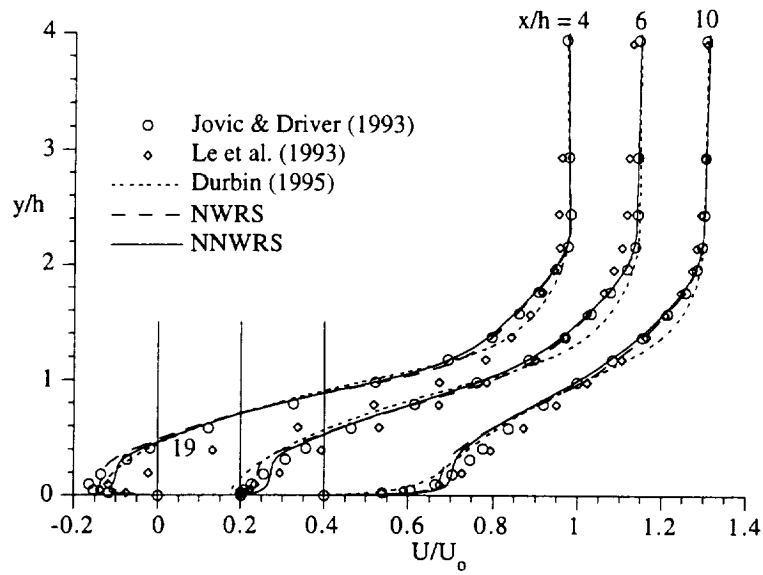
Fig. 5.7 Comparison between predicted and measured mean velocity profiles in global coordinate at different locations.
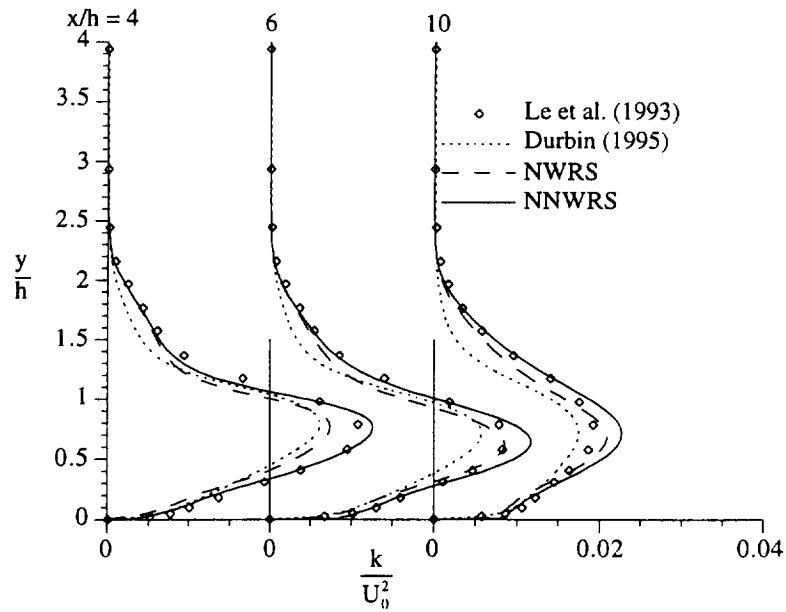
Fig. 5.8 Comparison between predicted and measured turbulent kinetic energy at different locations.
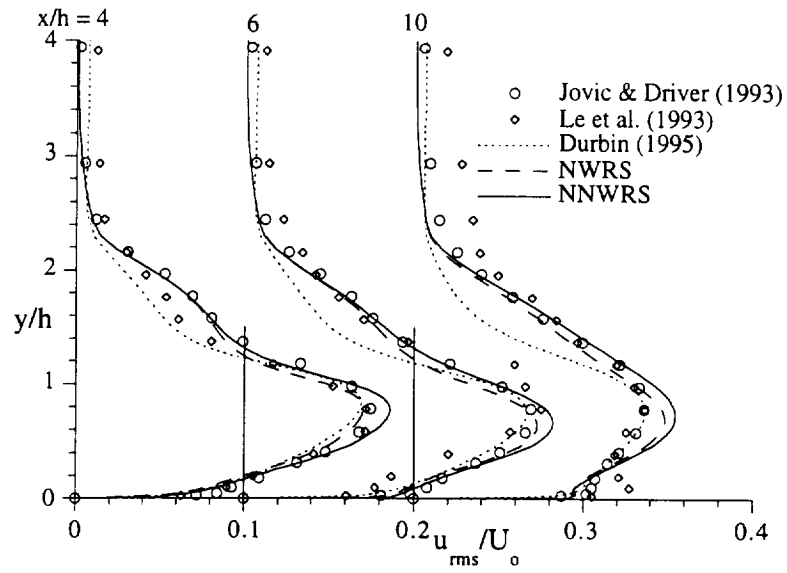
(a)
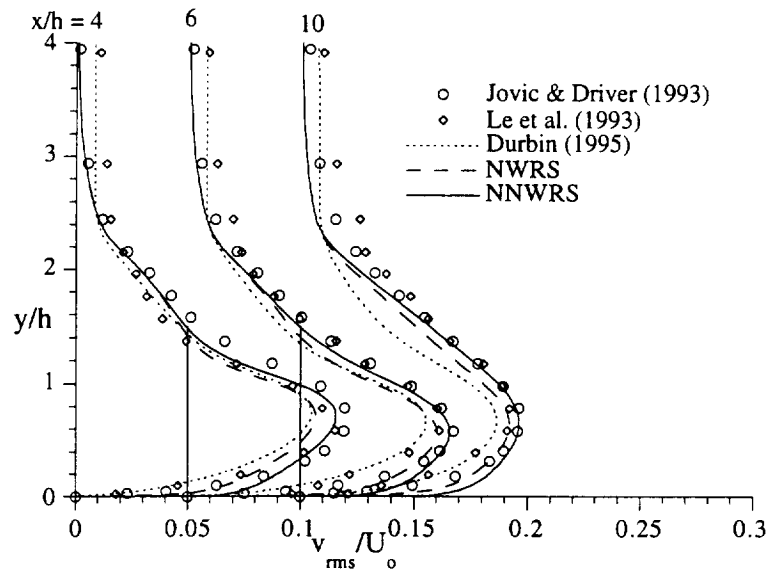
(b)
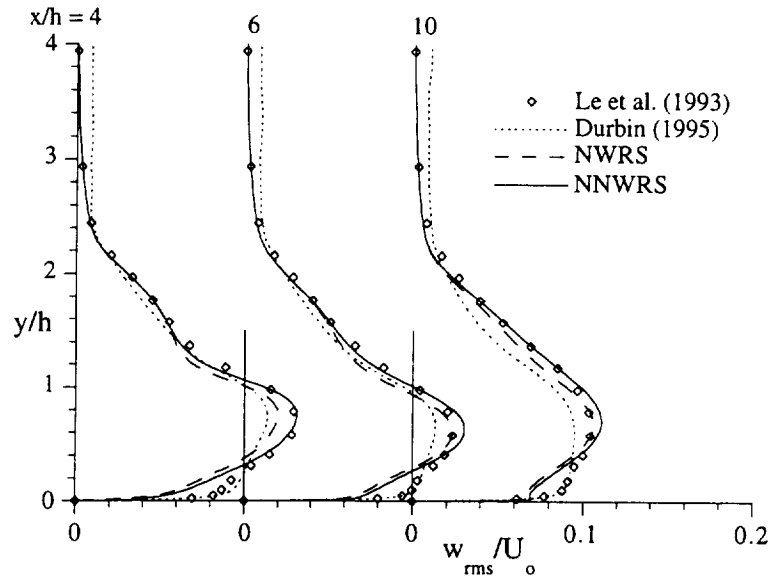
(c)
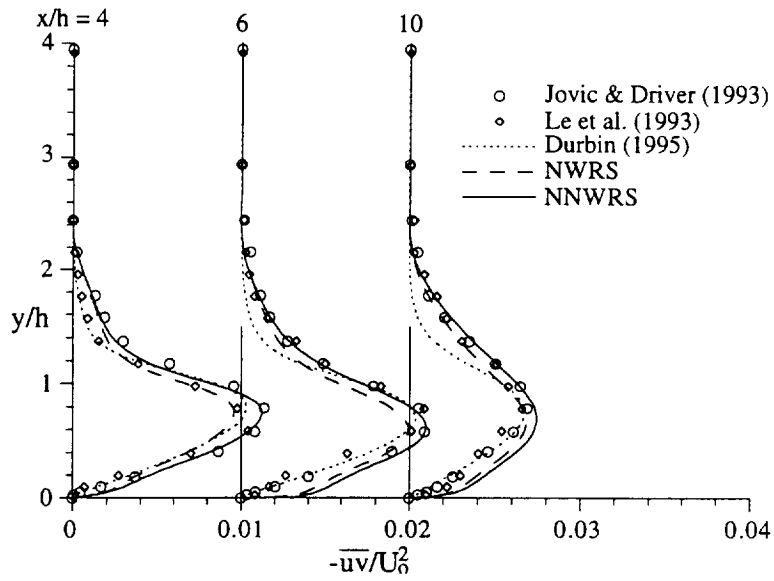
(d)

Fig. 5.9 Comparison between predicted and measured turbulent stresses at different locations: (a) u_{rms}, (b) v_{rms}, (c) w_{rms}, and (d) $-\overline{uv}$.
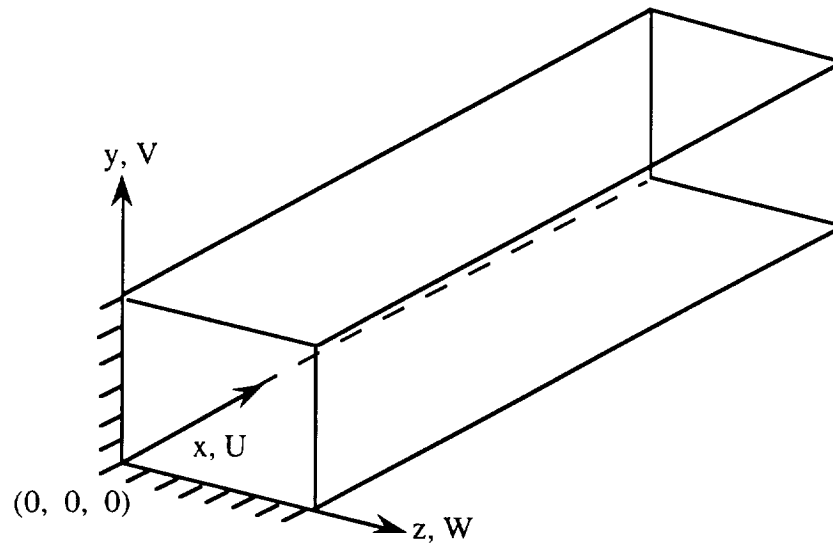
(a)
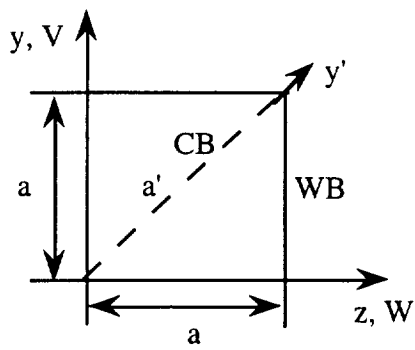
(b)

Fig. 5.10 Sketch of computational domain for straight square duct: (a) overview, and (b) on transverse plane.
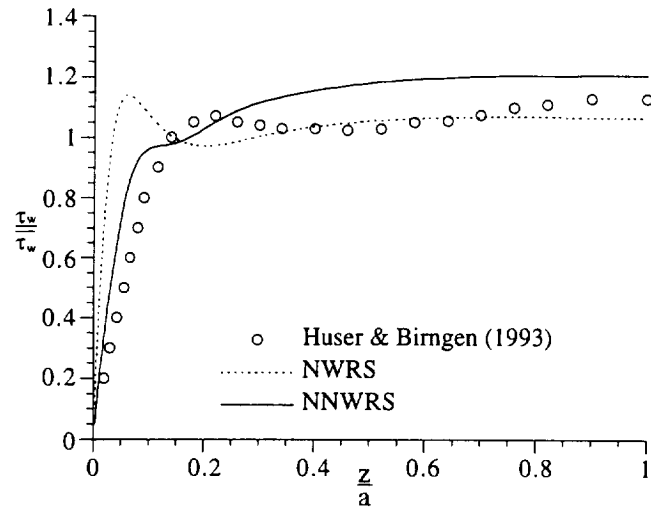
Fig. 5.14 Comparison between predicted and DNS wall shear stress for fully developed square duct flow at $Re = 10,320$.
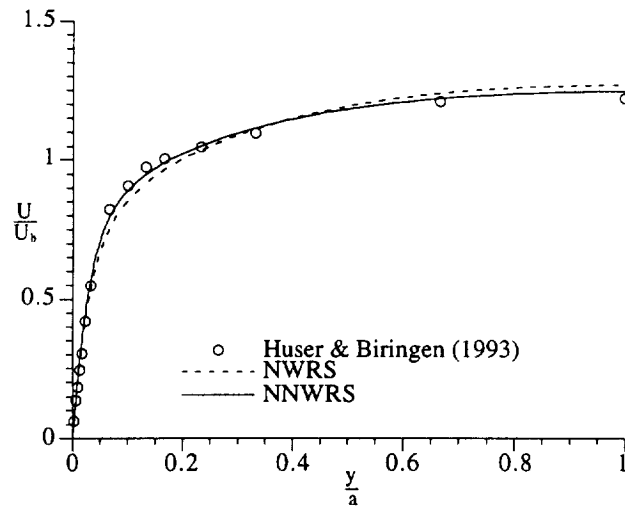
Fig. 5.15 Comparison between predicted and DNS axial mean velocity along wall bisector for for fully developed square duct flow at $Re = 10,320$.

212
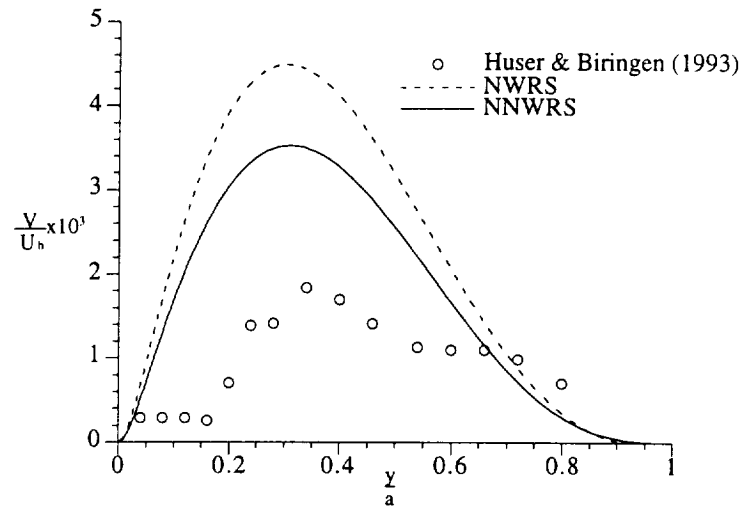
(a)
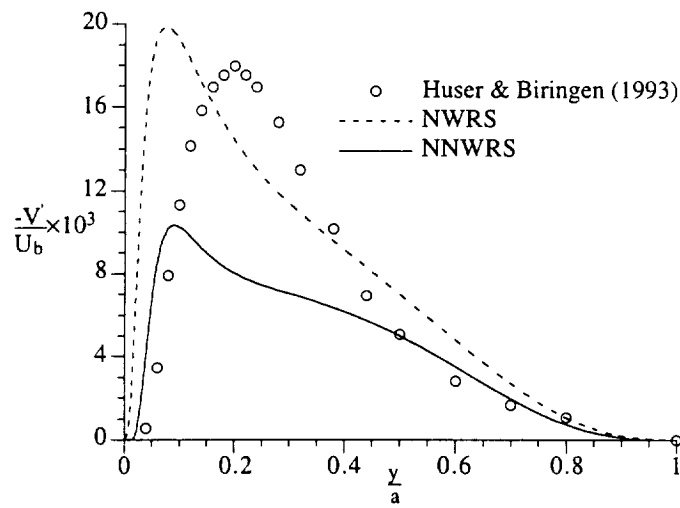
(b)

Fig. 5.16 Comparison between predicted and DNS secondary flow velocity along: (a) wall bisector, and (b) corner bisector for fully developed square duct flow at Re = 10,320.

213
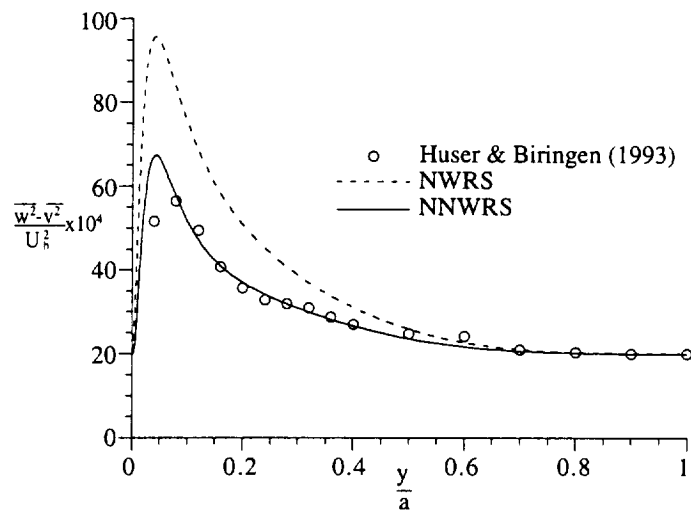
Fig. 5.17 Comparison between predicted and DNS normal stress difference along wall bisector for for fully developed square duct flow at $Re = 10,320$.
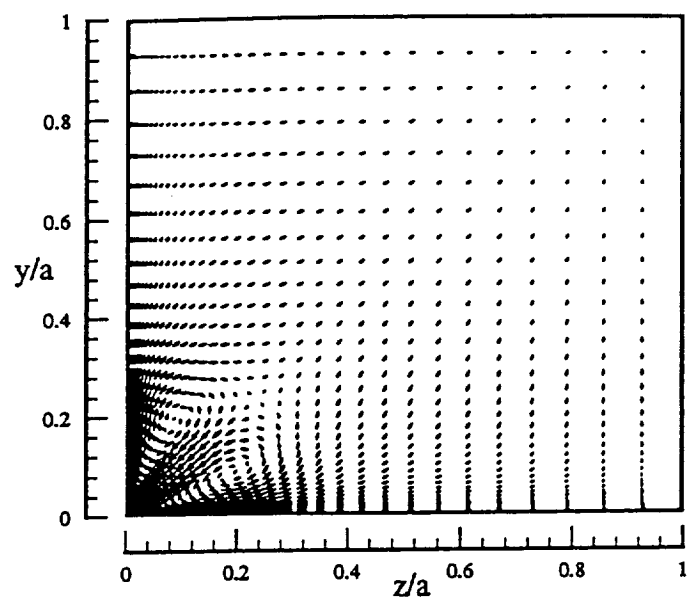
(a)
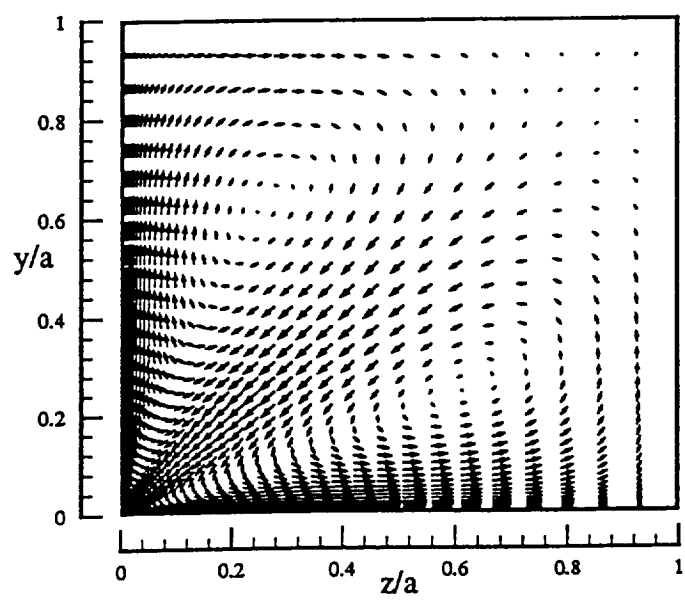
(b)
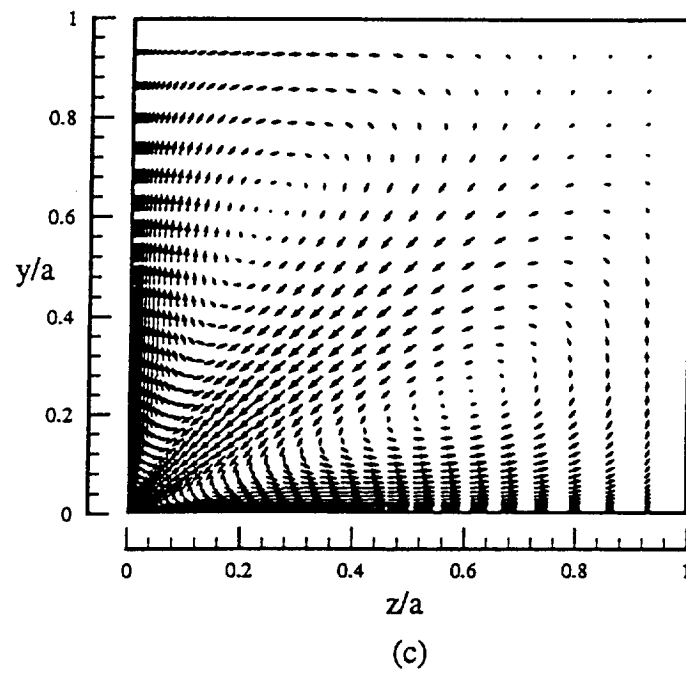
Fig. 5.18 Predicted secondary flow by the NNWRS model at:
(a) $x/D_h = 8$, (b) $x/D_h = 40$ and (c) $x/D_h = 84$.

(a)

(b)
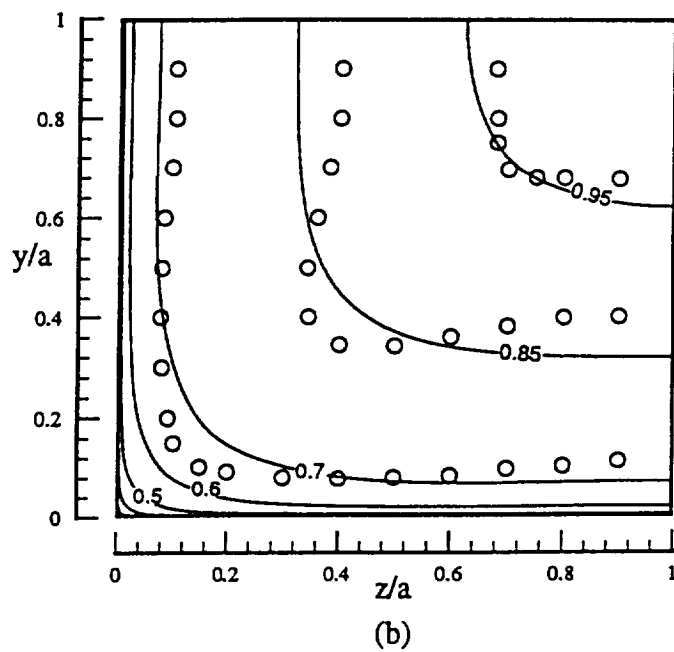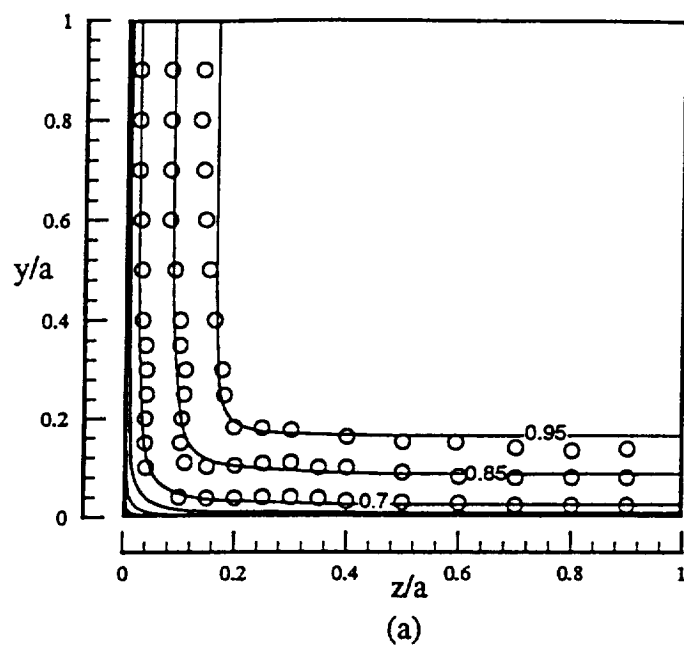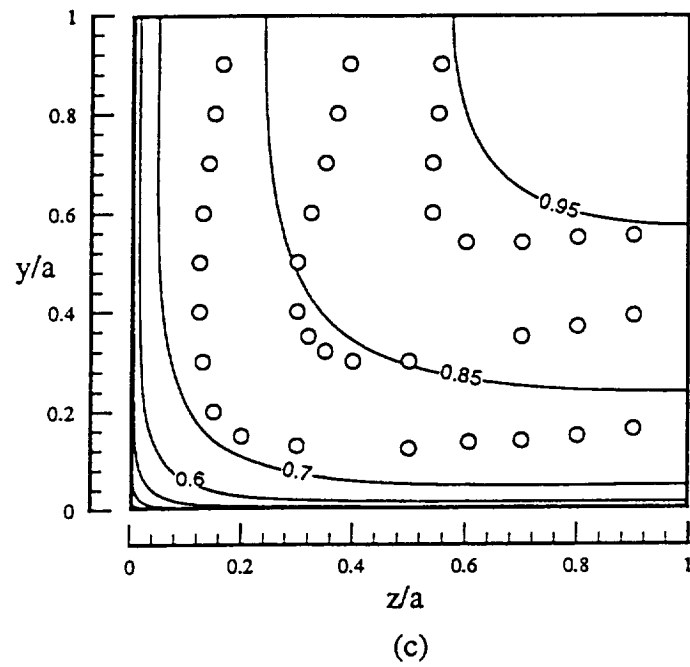
Fig. 5.19 Predicted isotachs by the NNWRS model at:
(a) $x/D_h = 8$, (b) $x/D_h = 40$ and (c) $x/D_h = 84$.
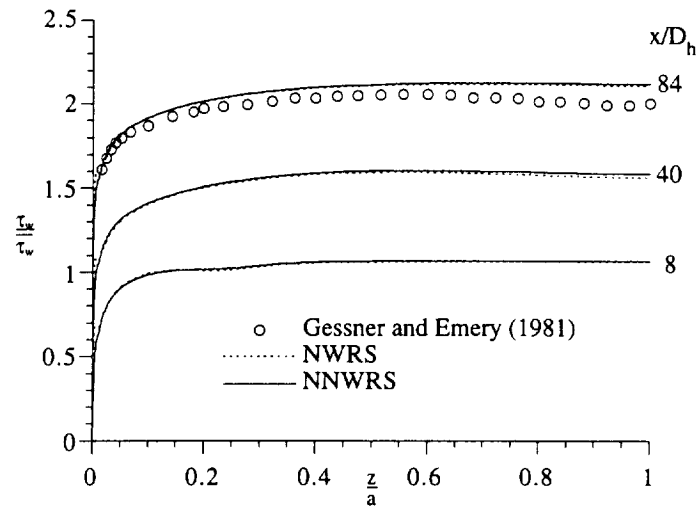
Fig. 5.20 Comparison between predicted and measured wall shear stress for developing square duct flow at $Re = 250,000$.
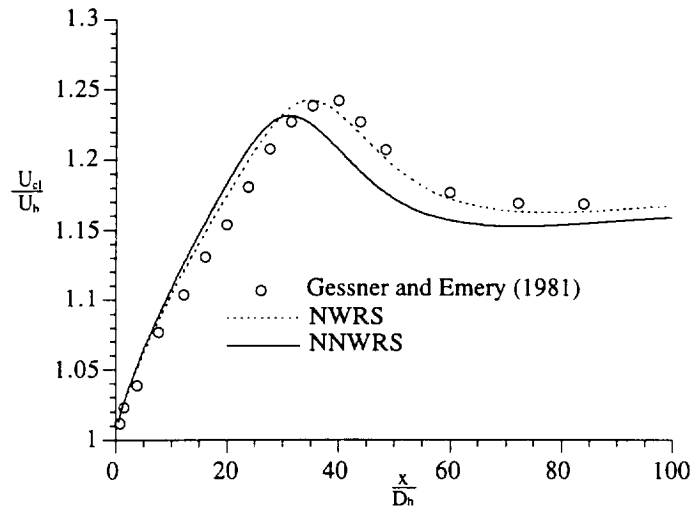
Fig. 5.21 Comparison between predicted and measured axial centerline velocity for developing square duct flow at $Re = 250,000$.

219
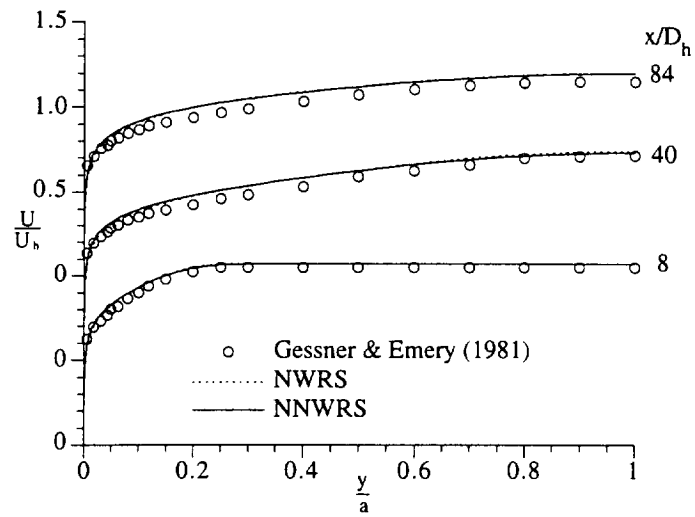
(a)
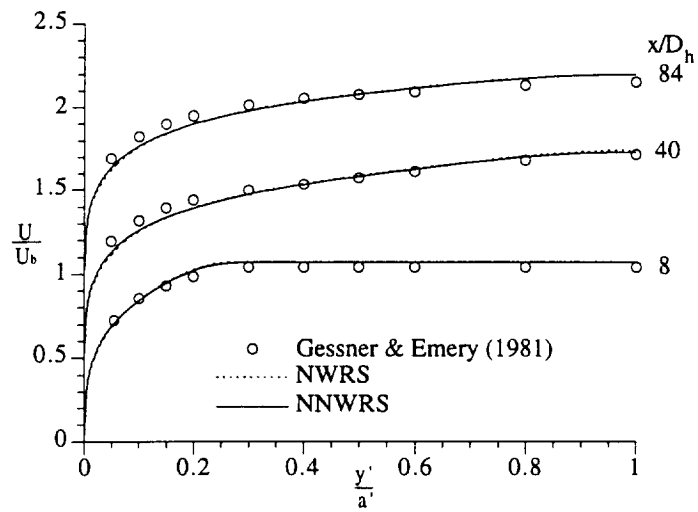
(b)

Fig. 5.22 Comparison between predicted and measured axial mean velocity along: (a) wall bisector, and (b) corner bisector for developing square duct flow at Re = 250,000.

220
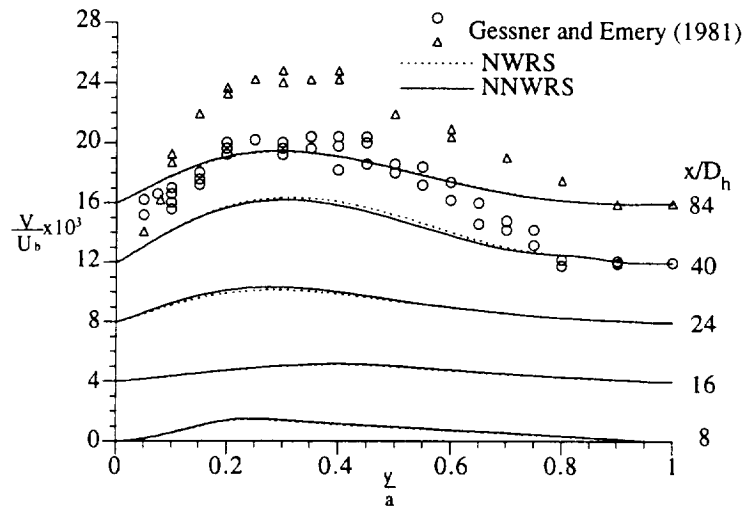
(a)
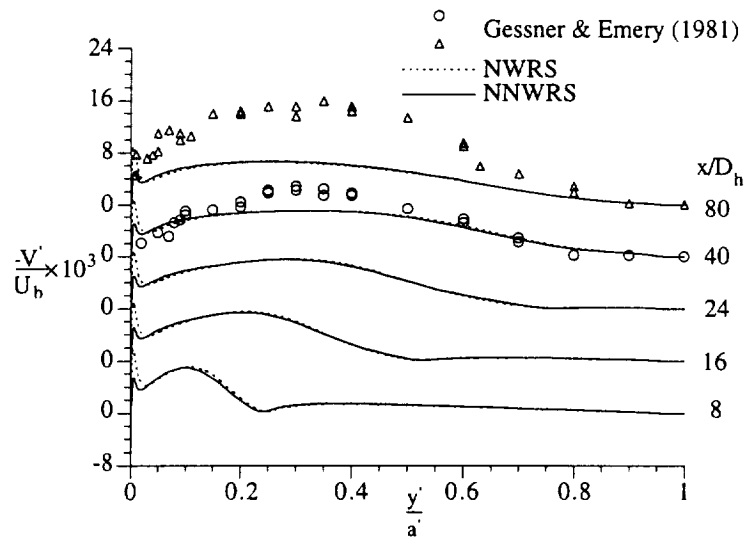
(b)

Fig. 5.23 Comparison between predicted and measured secondary flow velocity along: (a) wall bisector, and (b) corner bisector for developing square duct flow at Re = 250,000.
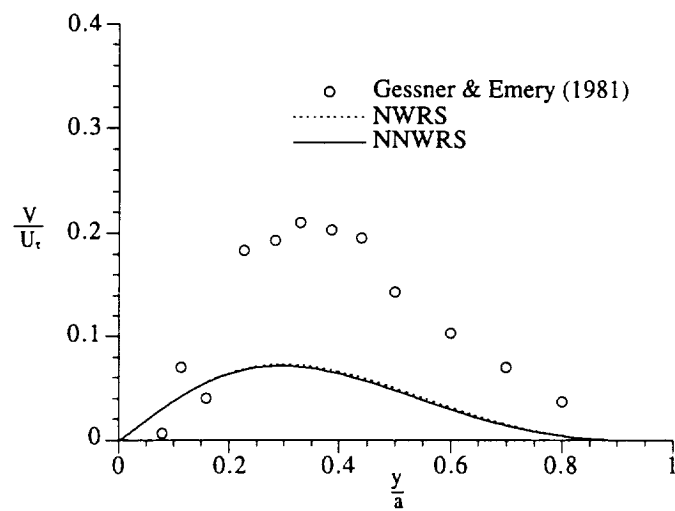
Fig. 5.24 Comparison between predicted and measured secondary flow normalized by local friction velocity along wall bisector for developing square duct flow at Re = 250,000.
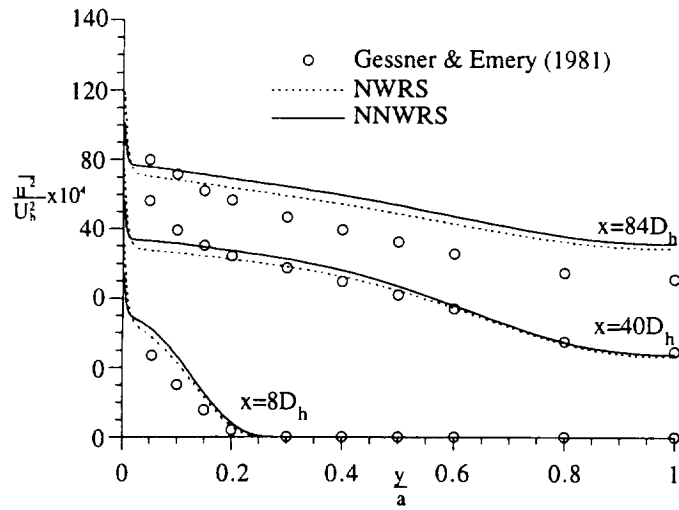
(a)
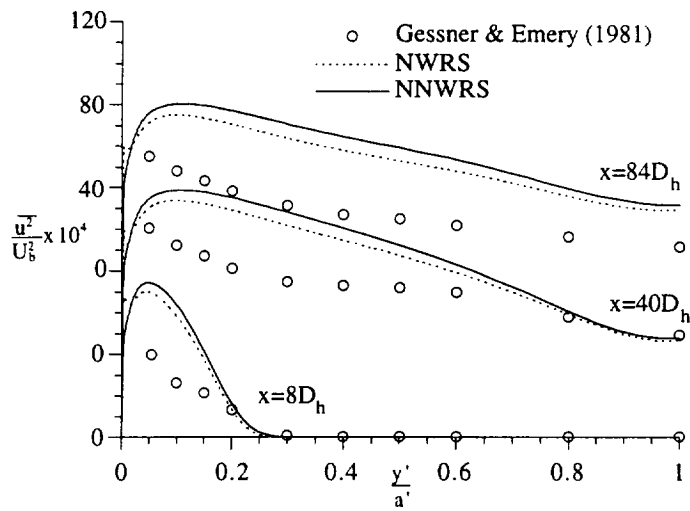
(b)

Fig. 5.25 Comparison between predicted and measured normal stress in axial direction along: (a) wall bisector, and (b) corner bisector for developing square duct flow at Re = 250,000.

40

Gessner & Emery (1981)

.... NWRS

———— NNWRS

20

$\dfrac{\overline{v^2}}{U_b^2} \times 10^4$

0

x=84D$_h$

0

x=40D$_h$

x=8D$_h$

0

0   0.2   0.4 $\dfrac{y}{a}$ 0.6   0.8   1

(a)

40

20

$\dfrac{\overline{v^2}}{U_b^2} \times 10^4$

0

x=84D$_h$

0

x=40D$_h$

0

Gessner & Emery (1981)

.... NWRS

x=8D$_h$ ———— NNWRS

0

0   0.2   0.4 $\dfrac{y'}{a'}$ 0.6   0.8   1
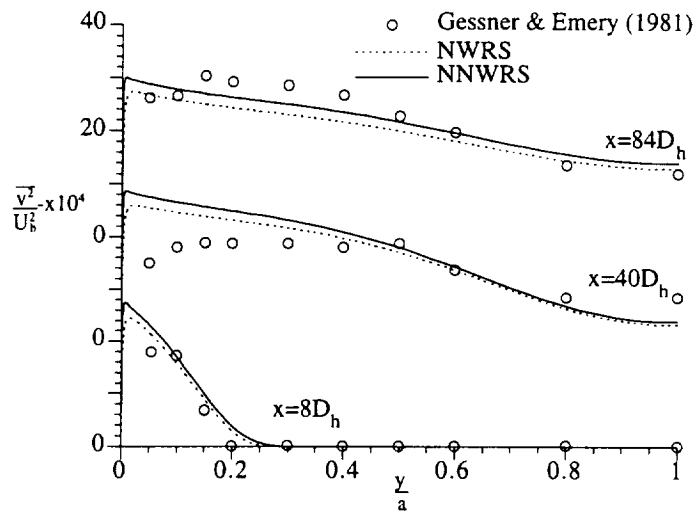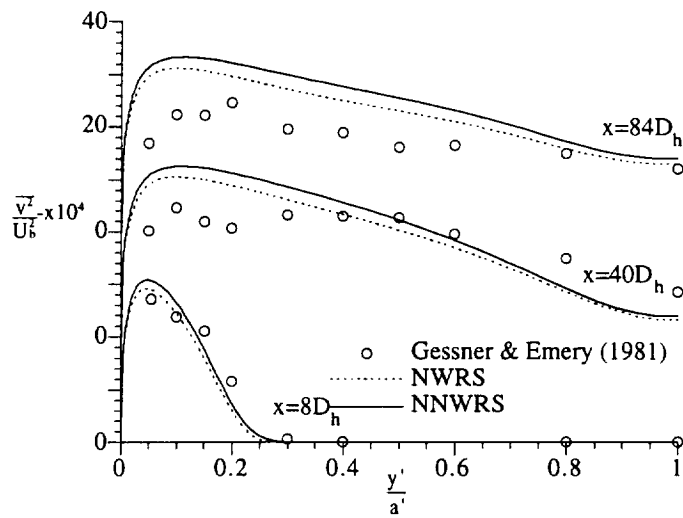
(b)

Fig. 5.26 Comparison between predicted and measured normal stress in vertical direction along: (a) wall bisector, and (b) corner bisector for developing square duct flow at Re = 250,000.

224
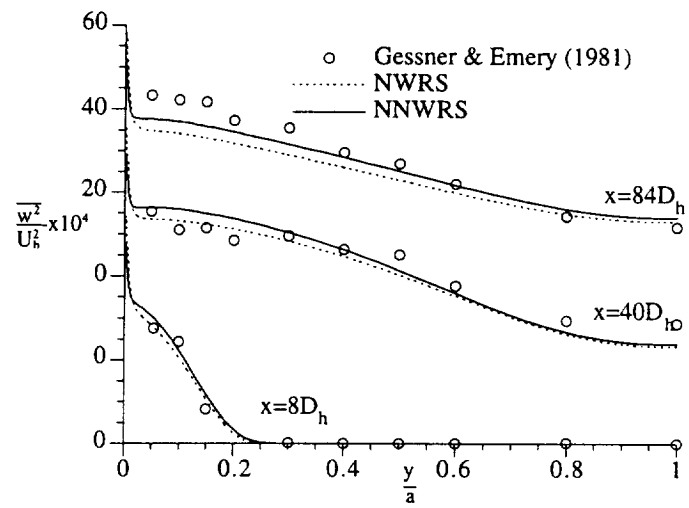
Fig. 5.27 Comparison between predicted and measured normal stress in transverse direction along wall bisector for developing square duct flow at Re = 250,000.
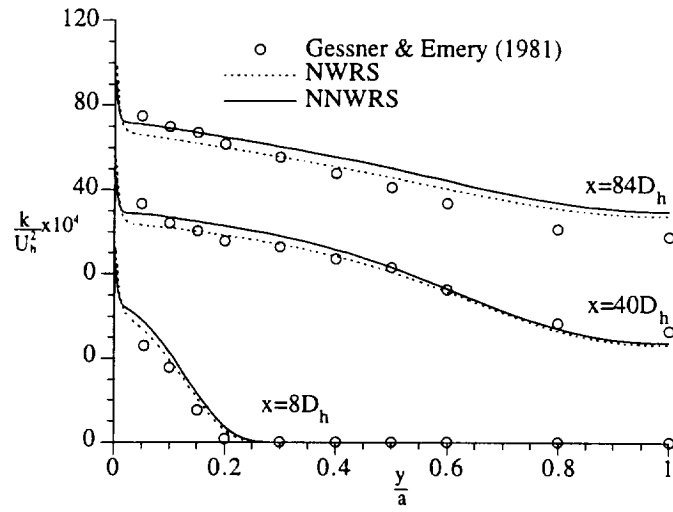
(a)
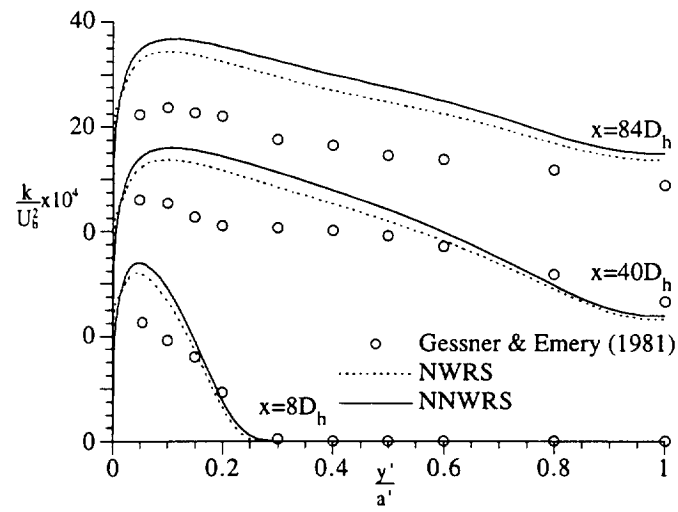
(b)

Fig. 5.28 Comparison between predicted and measured turbulent kinetic energy along: (a) wall bisector, and (b) corner bisector for developing square duct flow at Re = 250,000.
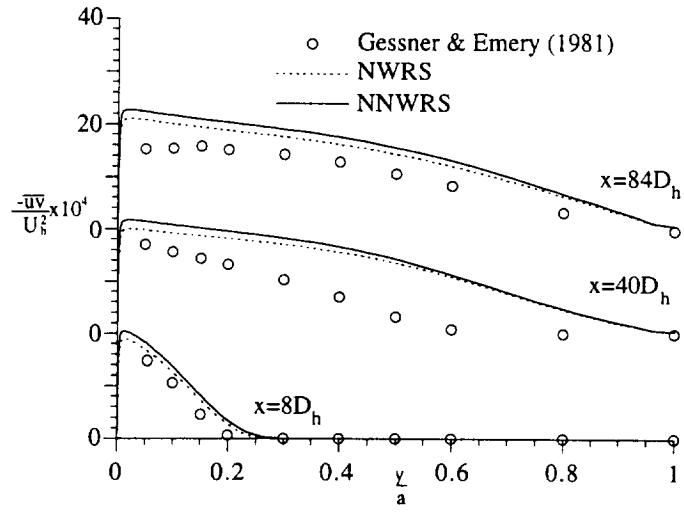
(a)
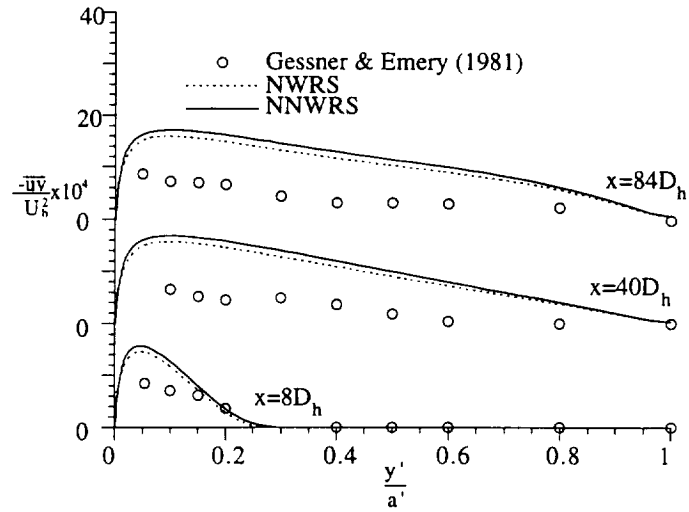
(b)

Fig. 5.29 Comparison between predicted and measured turbulent shear stress along: (a) wall bisector, and (b) corner bisector for developing square duct flow at Re = 250,000.

227
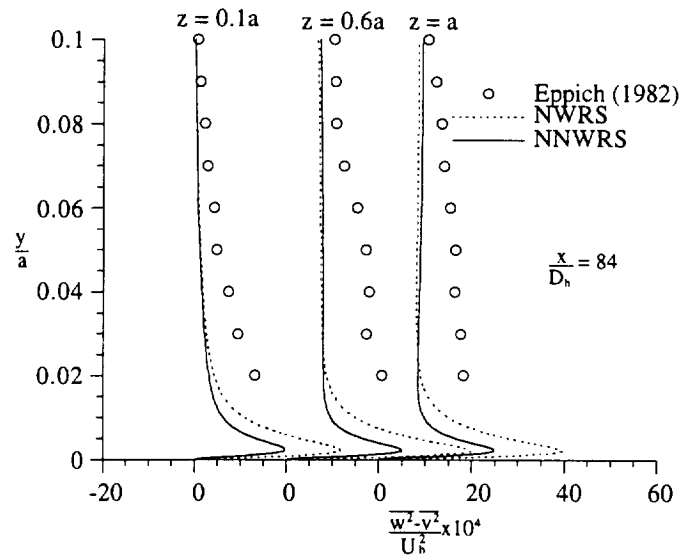
Fig. 5.30 Comparison between predicted and measured normal stress difference at three axial locations for developing square duct flow at $Re = 250,000$.

228

6. CONCLUSIONS

In this study, a new near-wall Reynolds stress model (NNWRS) without wall normals is developed based on the pressure-strain model of Speziale et al. (1991). With the aid of near-wall asymptotic analysis and the results of direct numerical simulation, wall-independent near-wall modifications are incorporated into the expression for the pressure-strain correlation, into the relation for the dissipation rate tensor, and into the modeled dissipation rate equation. A damping function is introduced to ensure that the near-wall modifications will not affect the flow field in the region far away from the walls. The asymptotically correct NNWRS model is the first near-wall Reynolds stress model without wall normals. For comparison, the formulation of the recent near-wall Reynolds stress model (NWRS) with wall normals developed by So et al. (1994a) is also presented. According to the asymptotic analysis, the NNWRS model gives more accurate predictions of those Reynolds stress components uncorrelated with the wall normal direction than the NWRS model, whereas the NWRS model gives more accurate predictions of those components correlated with the wall normal direction. With no wall-dependent variables used in the model and only one damping function, the NNWRS model is more general and flexible for turbulent wall-bounded flows than the wall-dependent NWRS model, which requires two damping functions for different Reynolds number range.

The new model is applied to a wide variety of flows to verify its applicability. These flows range from relatively simple flows, such as fully developed channel/pipe flow, Couette flow, and boundary-layer flow with zero pressure gradient, to complex flows with swirl and rotation, such as swirling pipe flow, axially rotating pipe flow, and channel flow with spanwise rotation. The advantages of using the new proposed model for flows with complex geometry are demonstrated by flow over a backward-facing step and flow in a square duct. The performance of the model in different type of flows is summarized as follows:

(1)   The NNWRS model predicts reasonably well the mean and turbulent flow fields of simple internal and external flows over a wide range of Reynolds numbers. The model is able to

capture the log-law region with a correct von Karman constant. Reynolds number effects on the mean flow and second-order statistics are reproduced well by the model. The main deficiency in the model is that it predicts less degree of turbulence anisotropy in the near-wall region compared with the NWRS model.

(2) In flows with swirl and rotation, the flow complexity is caused by the streamline curvature, centrifugal force, and Coriolis force. The performance of the NNWRS model seems to depend on the relative importance of these factors. In swirling pipe flow, the NNWRS model gives reasonable predictions for flow in no reverse flow region, whereas the model predicts a much smaller reverse flow region than that observed in the experiment. In developing flow along a pipe rotating about its axis, the NNWRS model is able to capture the flow pattern subject to both destabilizing effect resulting from the mean circumferential shear strain and stabilizing effect due to the centrifugal force. In the fully developed channel flow with spanwise rotation, at low rotation rate, the model predictions agree with the data. But, as the rotation rate increases, the model underestimates the Coriolis effect. The NWRS model behaves similarly as the NNWRS model in these flows.

(3) The advantages of using the NNWRS model for flows with complex geometry become more evident when it is applied to two-dimensional flow over a backward-facing step and three-dimensional flow in a straight square duct. The overall performance of the NNWRS model is found to be as good as the wall-dependent NWRS model. The model predictions of mean and turbulence flow fields in backward-facing step flow agree well with the experimental and DNS data. The NNWRS model is able to reproduce complex flow phenomena induced by the presence of the step, such as flow recirculation, reattachment, and boundary-layer redevelopment to a fully developed state. The comparison between the predictions given by the two models indicates that the overshooting of skin friction coefficient prevalent in near-wall Reynolds stress models is not caused by the use of wall normals. The NNWRS model is also able to capture the secondary motion induced by turbulence in low- and high-Reynolds-number square duct flow. The difference in the model predictions of low- and

high-Reynolds-number square duct flow seems to agree with the DNS findings by Gavrilakis (1992) and Huser and Biringen (1993).

Overall, the predictions given by the NNWRS model agree reasonably well with available data from experiments, direct numerical simulation, or large eddy simulation for a wide range of Reynolds numbers, swirl numbers, and rotation numbers. Various complicated flow phenomena are essentially captured by the model. Moreover, the model performance is very close to that of the wall-dependent NWRS model. With further refinement, the wall-independent NNWRS model is expected to replace existing wall-dependent near-wall Reynolds stress models for wall-bounded turbulent flows soon. Modifications of the formulation of the near-wall corrections so that the NNWRS model can give more accurate predictions of those Reynolds stress components correlated with the wall normal direction are expected to improve the performance of the model significantly, which will be pursued in the near future.

REFERENCES

Algifri, A. H., Bhardwaj, R. K. and Rao, Y. V. N., 1987, "Prediction of the Decay Process in Turbulent Swirl Flow," *Proc. Instn. Mech. Engrs.* Vol. 201, pp. 279-283.

Backshall, R. G. and Landis, F., 1969, "The Boundary-Layer Velocity Distribution in Turbulent Swirling Pipe flow," *J. Basic Engineering*, Vol. 91, pp. 728-733.

Baker, D. W., 1967, "Decay of Swirling, Turbulent Flow of Incompressible Fluids in Long Pipes," *Dissertation*, University of Maryland.

Bandyopadhyay, P. R., and Gad-el-Hak, M., 1994, "Reynolds Number Effects in Wall-Bounded Turbulent Flows," *NUWC-NPT Technical Report* 10296, Naval Undersea Warfare Center Division, Newport, Rhode Island.

Brundreit, E. and Baines, W. D., 1964, "The Production and Diffusion of Vorticity in a Square Duct," *Journal of Fluid Mechanics*, Vol. 19, pp. 375-394.

Choi, K. S. and Lumley, J. L., 1984, "Return to Isotropy of Homogenous Turbulence Revisited," *Turbulence and Chaotic Phenomena in Fluids* (Editor: T. Tatsumi), North Holland, pp. 267-272.

Cho, J. R., Craft, T. J., Launder, B. E. and Suga, K., 1995, "Development of Turbulence Models for Transition Prediction," *ERCOFTAC Bulletin*, No. 24, pp. 26-30.

Craft, T. J. and Launder, B. E., 1991, "Computation of Impinging Flows Using Second-Moment Closures," *Eighth Symposium on Turbulent Shear Flows*, Technical University of Munich, Germany, Paper No. 8-5.

Daly, B. J. and Harlow, F. H., 1970, "Transport Equations in Turbulence," *Physics of Fluids* Vol.13, pp. 2634-2649.

Demuren, A. O., 1990, "Calculation of Turbulence-Driven Secondary Motion in Ducts with Arbitrary Cross-Section," *AIAA Paper* 90-0245.

Demuren, A. O., and Rodi, W., 1984, "Calculation of Turbulence Driven Secondary Motions in Non-Circular Ducts," *Journal of Fluid Mechanics*, Vol. 140, pp. 189-222.

Durbin, P. A., 1993, "A Reynolds Stress Model for Near-Wall Turbulence," *Journal of Fluid Mechanics*, Vol. 249, pp. 465-498.

Durbin, P. A., 1995, Private communication.

Durst, F., Jovanovic, J., and Sender, J., 1993, "Detailed Measurements of the Near Wall Region of Turbulent Pipe Flows," *Proceedings of the 9th Symposium on Turbulent Shear Flows*, Kyoto, Japan, Paper No. 2.2.

Einstein, H. and Li, H., 1958, "Secondary Currents in Straight Channels," *Trans. Am. Geophys. Union*, Vol. 39, pp. 1085-1088.

El Telbany, M. M. M., and Reynolds, A. J., 1981, "Turbulence in Plane Channel Flow," *Journal of Fluid Mechanics*, Vol. 100, pp. 1-29.

Eppich, H. M., 1982, "An Experimental Investigation of the Turbulence Structure in the Inner Region of a Three-Dimensional Streamwise Corner Flow," *MS Thesis*, Mechanical Engineering Department, University of Washington.

Fu, S., Huang, P. G. and Launder, B. E. and Leschziner, M. A., 1988, "A Comparison of Algebraic and DIfferential Second-Moment Closures for Axisymmetric Turbulent Shear Flows with and without Swirl," *J. Fluids Engineering*, Vol. 110, pp. 216-221.

Gavrilakis, S., 1992, "Numerical Simulation of Low-Reynolds-Number Turbulent Flow Through a Straight Square Duct," *Journal of Fluid Mechanics*, Vol. 244, pp. 101-129.

Gessner, F. B., 1973, "The Origin of Secondary Flow in Turbulent Flow along a Corner," *Journal of Fluid Mechanics*, Vol. 58, pp. 1-25.

Gessner, F. B., Po, J. K., and Emery, A. F., 1979, "Measurements of Developing Turbulent Flow in a Square Duct," in Durst et al. (eds.),*Turbulent Shear Flows I*, pp. 119-136.

Gessner, F. B. and Emery, A. F., 1981, "The Numerical Prediction of Developing Turbulent Flow in Rectangular Duct," *Journal of Fluids Engineering*, Vol. 103, pp. 445-455.

Gessner, F. B., Eppich, H. M., and Lund, E. G., 1991, "The Near-Wall Structure of Turbulent Flow Along a Streamwise Corner," *Proceedings of the Eigth Symposium on Turbulent Shear Flows*, Technical University of Munich.

Gessner, F. B., Eppich, H. M., and Lund, E. G., 1993, "Reynolds Number Effects on the Near-Wall Structure of Turbulent Flow Along a Streamwise Corner," in So et al. (eds.), *Near-Wall Turbulent Flows*, pp. 965-975.

Gosman, A. D., and Ideriah, F. J. K., 1976, "TEACH-T: A General Computer Program for Two-Dimensional, Turbulent, Recirculating Flows," Mechanical Engineering Department, Imperial College, London.

Hanjalic, K. and Launder, B. E., 1972, "A Reynolds Stress Model of Turbulence and its Application to Thin Shear Flows," *Journal of Fluid Mechanics*, Vol. 52, pp. 609-638.

Hanjalic, K. and Launder, B. E., 1976, "Contribution Towards a Reynolds-Stress Closure for Low-Reynolds-Number Turbulence," *Journal of Fluid Mechanics*, Vol. 74, pp. 593-610.

Hogg, S. and Leschziner, M. A., 1989, "Computation of Hghly Swirling Confined Flow with a Reynolds Stress Turbulence Model," *AIAA Journal*, Vol. 27, pp. 57-63.

Huser, A., and Biringen, S., 1993, "Direct Numerical Simulation of Turbulent Flow in a Square Duct," *Journal of Fluid Mechanics*, Vol. 257, pp. 65-95.

Ito, S., Ogawa, K. and Kuroda, C., 1980, "Turbulent Swirling Flow in a Circular Pipe," *J. Chemical Engineering of Japan*, Vol. 13, pp. 6-10.

Johnston, J. P., Halleen, R. M. and Lezius, D. K., 1972, "Effects of Spanwise Rotation on the Structure of Two-Dimensional Fully Developed Turbulent Channel Flow," *Journal of Fluid Mechanics*, Vol. 56, pp. 533-557.

Jones, W. P. and Pascau, A., 1989, "Calculation of Confined Swirling Flows with a Second Moment Closure," *J. Fluids Eng.* Vol. 111, pp. 248-255.

Jovic, S. and Driver, D., 1994, "Backward-Facing Step Measurements at Low Reynolds-number, Re = 5,100," *NASA* TM 108807.

Karlsson, R. I., and Johansson, T. G., 1988, "LDV Measurements of Higher Order Moments of Velocity Fluctuations in a Turbulent Boundary Layer," in Durao et al. (eds.), *Laser Anemometry in Fluid Mechanics*, Ladoan - Instituto Superior Tecnico, Portugal, pp. 273-289.

Kebede, W., Launder, B. E., and Younis, B. A., 1984, "Large Amplitude Periodic Pipe Flow: A Second Moment Closure Study," *Proceedings of 5th Symposium on Turbulent Shear Flows*, Ithaca, NY, Paper No. 16.

Kikuyama, K., Murakami, M., and Nishibori, K., 1983, "Development of Three-Dimensional Turbulent Boundary-Layer in an Axially Rotating Pipe," *Journal of Fluids Engineering*, Vol. 105, pp. 154-160.

233

Kim, J., Moin, P. and Moser, R. D., 1987, "Turbulence Statistics in Fully Developed Channel Flow at Low Reynolds Number," *Journal of Fluid Mechanics* , Vol. 177, pp. 133-186.

Kim , J., 1983, "The Effect of Rotation on Turbulence Structure," *Proc. 4th Symp. on Turbulent Shear Flows*, Karsruhe, pp. 6.14-6.19.

Kim, J., 1989, "On the Structure of Pressure Fluctuations in Simulated Turbulent Channel Flow," *Journal of Fluid Mechanics* **205**, 421-451.

Kim, J., 1991, Private communication.

Kito, O.and Kato, T., 1984, "Near Wall Velocity Distribution of Turbulent Swirling Flow in Circular Pipe," *Bull. JSME* , Vol. 27, pp. 1659-1666.

Kitoh, O., 1991, "Experimental Study of Turbulent Swirling Flow in a Straight Pipe," *Journal of Fluid Mechanics* , Vol. 225, pp. 445-479.

Kebede, W., Launder, B. E., and Younis, B. A., 1984, "Large Amplitude Periodic Pipe Flow: A Second Moment Closure Study," *Proceedings of the 5th Symposium on Turbulent Shear Flows*, Paper No. 16.5.

Ko, S. H., and Durbin, P. A., 1994, "Separated Turbulent Flows Computed with a Near-Wall Reynolds Stress Model," *ASME* FED-Vol. 196, pp. 83-91.

Kolmogorov, , A. N., 1941, "The Local Structure of Turbulence in an Incompressible Viscous Fluid for Very Large Reynolds Numbers," *Comptes Rendus Academy of Science, U.S.S.R*, Vol. 30, pp. 301-305 (Translation, Turbulence, Classic Papers on Statistical Theory (edited by S. K. Friendlander and L. Topper), Interscience, 1961.

Kreith, F. and Sonju, O. K., 1965, "The Decay of a Turbulent Swirl in a Pipe," *Journal of Fluid Mechanics* , Vol. 22, pp. 257-271.

Kristoffersen, R., Bech, K. H., and Andersson, H. I., 1993, "Numerical Study of Turbulent Plane Couette Flow at Low Reynolds Number," *Applied Scientific Research* , Vol. 51, 337-343.

Kristoffersen, R. and Andersson, H. I., 1993, "Direct Simulations of Low-Reynolds-Number Turbulent Flow in a Rotating Channel," J. Fluid Mechanics, Vol. 256, pp. 163-197.

Lai, Y. G. and So, R. M. C., 1990, "On Near-Wall Turbulent Flow Modeling," *Journal of Fluid Mechanics* , Vol. 221, pp. 641-673.

Laufer, J., 1954, "The Structure of Turbulence in Fully-Developed Pipe Flow," *NACA* Report No. 1174.

Launder, B. E., and Ying, W. M., 1972, "Secondary Flows in Ducts of Square Cross-Section," *Journal of Fluid Mechanics* Vol. 54, pp. 289.

Launder, B. E., and Ying, W. M., 1973, "Prediction of Flow and Heat Transfer in Ducts of Square Cross-Section,"*Proceedings of Institute of Mechanical Engineers*, Vol. 187, pp. 455-461.

Launder, B. E., Reece, G. J. and Rodi, W., 1975, "Progress in the Development of Reynolds-stress Turbulence Closure," *Journal of Fluid Mechanics* 68, 537-566.

Launder, B. E. and Reynolds, W. C., 1983, "Asymptotic Near-Wall Stress Dissipation Rates in a Turbulent Flow," *Physics of Fluids* , Vol. 26, pp. 1157-1158.

Launder, B. E., Tselepidakis, D. P. and Younis, B. A., 1987, "A Second-Moment Closure Study of Rotating Channel Flow," *Journal of Fluid Mechanics*, Vol. 183, pp. 63-75.

Launder, B.E., 1989, "Second-Moment Closure: Present ... and Future?" *Int. Journal of Heat and Fluid Flow* , Vol. 10, No. 4, 282-300.

Launder, B. E. and Shima, N., 1989, "Second-Moment Closure for the Near-Wall Sublayer: Development and Application," *AIAA Journal*, Vol. 27, pp. 1319-1325.

Launder, B. E. and Tselepidakis, D. P., 1993, "Progress and Paradoxes in Modeling Near-Wall Turbulence," *Turbulent Shear Flows* 8, pp. 81-96.

Launder, B. E. and Li, S.-P., 1994, "On the Elimination of Wall-Topography Parameters from Second-Moment Closure," *Physics of Fluids*, Vol. 6, pp. 999-1006.

Le, H., Moin, P. and Kim, J., 1993, "Direct Numerical Simulation of Turbulent Flow Over a Backward-Facing Step," *Report* TF-58, Thermosciences Division, Department of Mechanical Engineering, Stanford University.

Lee, M. J., and Kim, J., 1991, "The Structure of Turbulence in a Simulated Plane Couette Flow," *Proceedings of the 8th Turbulent Shear Flows,* Technical University of Munich, Munich, Paper No. 5.3.

Lien, F. S., and Leschziner, M. A. 1994, "Assessment of Turbulence Transport Models Including Non-Linear RNG Eddy-Viscosity Formulation and Second-Moment Closure for Flow Over a Backward-Facing Step," *Computers Fluids*, Vol. 23, pp. 983-1004.

Lilley, D. G., 1976, "Primitive Pressure-Velocity Code for the Computation of Strongly Swirling Flows," AIAA Journal, Vol. 14, pp. 749-756.

Lilley, D. G. and Chigier, N. A., 1971, "Nonisotropic Turbulent Stress Distribution in Swirling Flows from Mean Value Distributions," *Int. J. Heat Mass Transfer*, Vol. 14, pp. 573-585.

Lumley, J. L., 1978, "Computational Modelling of Turbulent Flows," *Advanced Appllied Mech.anics*, Vol. 18, pp. 123.

Lund, E. G., 1977, " Mean Flow and Turbulence Characteristics in the Near Corner Region of a Square Duct," *MS Thesis*, Mechanical Engineering Department, University of Washington.

Mansour, N. M., Kim, J. & Moin, P., 1988, "Reynolds-Stress and Dissipation-Rate Budgets in a Turbulent Channel Flow," *Journal of Fluid Mechanics*, Vol. 192, pp. 15-44.

Melling, A. and Whitelaw, J. H., 1976, "Turbulent Flow in a Rectangular Duct," *Journal of Fluid Mechanics* Vol.78, pp. 289-315.

Mellor, G. L., and Gibson, D. M., 1966, "Equilibrium Turbulent Boundary Layers," *Journal of Fluid Mechanics*, Vol. 24, pp. 225-253.

Mellor, G. L. and Herring, H. J., 1973, "A Survey of the Mean Turbulent Field Closure Models," *AIAA Journal*, Vol. 11, pp. 590 - 599.

Millikan, C. B., 1939, "A Critical Discussion of Turbulent Flow in Channels and Circular Pipes," *Proceedings of the Fifth International Congress on Applied Mechanics*, Wiley, New York, pp. 386-392.

Miyake, Y. and Kajishima, T., 1986, "Numerical Simulation of the Effects of Coriolis Force on the Structure of Turbulence," *Bull. JSME*, Vol. 256, No. 29, pp. 3347-3351.

Murakami, M. and Kikuyama, K., 1980, "Turbulent Flow in Axially Rotating Pipes," *J. of Fluids Engineering*, Vol. 102, No.1, pp. 97-103.

Murakami, M. , Kito, O., Katayama, Y. and Iida, Y., 1976, "An Experimental Study of Swirling Flow in Pipes," *Bull. JSME*, Vol. 19, pp. 118-126.

Nakabayashi, K. and Kitoh, O., 1996, "Low Reynolds Number Fully Developed Two-Dimensional Turbulent Channel Flow with System Rotation," *Journal of Fluid Mechanics*, Vol. 315, pp. 1-29.

235

Naot, D., Shavit, H. and Wolfshtein, M., 1974, "Numerical Calculation of Reynolds Stresses in a Square Duct with Secondary Flow," Warme- and Stoffubertrayung, Vol. 7, pp. 151-161.

Padmanabhan, M. and Janek, C. R., 1980, "Swirling Flow and its Effcet on Wall Pressure Dropwithin Pipes. Vortex Flows: *ASME* Meeting 1980 (Ed. W. L. Swift, P. S. Barna & C. Dalton), pp. 65-75.

Parchen, R., Steenbergen, W. and Voskamp, J., 1993, "A Study of Swirling Flows in Long Straight Pipes," *Engineering Turbulence Modeling and Experiments* (edited by W. Rodi and F. Martelli), Elsevier Science Publishers, Amsterdam, pp. 207-216.

Patankar, S. V., and Spalding, D. B., 1972, "A Calculation Procedure for Heat, Mass and Momentum Transfer in 3D Parabolic Flows, " *International Journal of Heat and Mass Transfer*, Vol. 15, pp. 1787-1806.

Patankar, S. V., 1980, *Numerical Heat Transfer and Fluid Flow*, McGraw-Hill, New York.

Po, J. K., 1975, "Developing Turbulent Flow in the Entrance Region of a Square Duct," *MS Thesis*, Mechanical Engineering Department, University of Washington.

Prandtl, L., "Uber Die Ausgebildete Turbulenz," Verh. 2nd Int. Kong. Fur Tech. Mech., Zurich. [Trans. NACA Tech. Memo 435, pp. 62-75.]

Prud'homme, M. and Elghobashi, S., 1983, "Prediction of Wall-Bounded Turbulent Flows with an Improved Version of a Reynolds Stress Model," *Proceedings of the 4th Symposium on Turbulent Shear Flows*, Germany, Paper No. 1.2.

Purtell, L. P., Klebanoff, P. S., and Buckley, F. T., 1981, "Turbulent Boundary Layer at Low Reynolds Number," *Physics of Fluids*, Vol. 24, pp. 802-811.

Schildknecht, M., Miller, J. A., and Meier, G. E. A., 1979, "The Influence of Suction on the Structure of Turbulence in Fully-Developed Pipe Flow," *Journal of Fluid Mechanics*, Vol. 90, pp. 67-107.

Seno, Y. and Nagata, T, 1972, "Swirl Flow in through a Long Straight Pipe (4th report), Preprint of Annual Meeting of JSME No. 710-3, pp. 149. (In Japanese).

Shih, T.-H. and Lumley, J. L., 1985, "Modeling of Pressure Correlation Terms in Reynolds Stress and Scalar Flux Equations," Rep. FDA-85-3, Sibley School of Mechanical and Aerospace Engineering, Cornell University, Ithaca, NY.

Shih, T.-H., and Mansour, N. N., 1990, "Modeling of Near-Wall Turbulence," *Engineering Turbulence Modeling and Experiments* (Editors: Rodi, W. and Ganic, E. N.), Elsevier Science Publishing Co., Inc., Amsterdam, The Netherlands, pp. 13- 19.

Shima, N., 1988, "A Reynolds-Stress Model for Near-Wall and Low-Reynolds-Number Regions," *Journal of Fluids Engineering,* Vol. 110, March, 38-44.

Shima, N., 1993, "Predcition of Turbulent Boundary Layers with a Second-Moment Closure: Part II-Effects of Streamline Curvature and Spanwise Rotation," *Journal of Fluids Engineering*, Vol. 115, pp. 64-69.

Shima, N., 1995, "Modeling of Asymptotic Near-Wall Behavior of the Reynolds Stress Dissipation," *Tenth Symposium on Turbulent Shear Flows.* 1, Paper No. 2-13, The Pennsylvania State University, University Park, PA, August 14-16.

Shir, C. C., 1973, "A Preliminary Numerical Study of Atmospheric Turbulent Flows in the Idealized Planetary Boundary Layer," *Journal of Atmospheric Sciences* **30**, 1327-1339.

Sloan, D. G., Smith, P. J. and Smoot, L. D., 1986, "Modeling of Swirling in Turbulent Flow Systems," *Prog. Energy Combust. Sci.*, Vol. 12, pp. 163-250.

So, R. M. C. and Yoo, G. J., 1987, "Low-Reynolds-Number Modeling of Turbulent Flows with and without Wall Tranpiration," *AIAA Journal*, Vol. 25, pp. 1556-1564.

So, R. M. C., Lai, Y. G., Hwang, B. C., and Yoo, G. J., 1988, "Low-Reynolds-Number Modeling of Flows over a Backward-Facing Step," *Journal of Applied Mathematics and Physics (ZAMP)* , Vol. 39, pp. 13-27.

So, R. M. C., Aksoy, H., Sommer, T. P. and Yuan, S. P., 1994, "Development of a Near-Wall Reynolds-Stress Closure Based on the SSG Model for the Pressure Strain," *NASA Contractor Report* 4618.

So, R. M. C., Aksoy, H., Sommer, T. P., and Yuan, S. P., 1996, "Modeling Reynolds Number Effects in Wall-Bounded Flows," *Journal of Fluids Engineering*, Vol. 118, pp. 260-267.

So, R. M. C., Sarkar, A., Gerodimos, G. and Zhang, J., 1997, "A Dissipation Rate Equation for Low-Reynolds-Number and Near-Wall Turbulence," *Journal of Theoretical and Computational Fluid Dynamics* , Vol. 9 (to appear).

Spalart, P. R., 1988, "Direct Simulation of a Turbulent Boundary Layer up to $Re_\theta = 1410$," *Journal of Fluid Mechanics*, Vol. 187, pp. 61-98.

Speziale, C. G., Sarkar, S. and Gatski, T. B., 1991, "Modeling the Pressure-Strain Correlation of Turbulence: An Invariant Dynamical Systems Approach," *Journal of Fluid Mechanics* , Vol. 227, pp. 245-272.

Speziale, C. G., Abid, R. and Anderson, E. C., 1992, "A Critical Evaluation of Two-Equation Models for Near-Wall Turbulence," *AIAA Journal* , Vol. 30, pp. 324-331.

Sreenivasan, K. R., 1983, "A Unified View of the Origin and Morphology of the Turbulent Boundary Layer Structure," *Turbulence Management and Relaminarization* (eds., H. W. Liepmann and R. Narasimha), Springer-Verlag, pp. 37-61.

Tselepidakis, D. P., 1991, "Development and Application of a New Second-Moment Closure for Turbulent Flow Near Walls," *Ph.D. Thesis*, University of Manchester.

Van Driest, E. R., 1956, "On Turbulent Flow Near a Wall," *Journal of Aeronautical Sciences* , Vol. 23, pp. 1007-1011, 1036.

Wei, T., and Willmarth, W. W., 1989, "Reynolds-Number Effects on the Structure of a Turbulent Channel Flow," *Journal of Fluid Mechanics* , Vol. 204, pp. 57-95.

Weske, D. R. and Sturov, G. Y., 1974, "Experimental Study of Turbulent Swirled Flows in a Cylindrical Tube," *Fluid Mechanics -Soviet Research* , Vol. 3, pp. 77-82.

White, A., 1964, "Flow of a Fluid in Axially Rotating Pipe," *J. of Mechanical Engineering Science*, Vol. 6, No.1, pp. 47-54.

Wilcox, D. C., 1993, *Turbulence Modeling for CFD*, DCW Industries, Inc., La Canada, California.

Yajnik, K. S. and Subbaiah, M. V., 1973, "Experiments on Swirling Turbulent Flows. Part I: Similarity in Swirling Flows," *Journal of Fluid Mechanics* , Vol. 60, pp. 665-687.

Yoo, G. J., So, R. M. C. and Hwang, B. C., 1983, "Calculation of Developing Turbulent Flows in a Rotating Pipe," *J. Turbomachinery*, Vol. 113, pp. 34-41.

APPENDIX A

The Equations for the High-Reynolds-Number Models

Speziale et al.'s (1991) high-Reynolds-number pressure-strain correlation formula was published in the following form

$$\Pi_{ij} = -(C_1\varepsilon + C_1^*\tilde{P})b_{ij} + C_2\varepsilon\left(b_{ik}b_{kj} - \frac{1}{3}\Pi\delta_{ij}\right) + (C_3 - C_3^*\Pi^{1/2})kS_{ij}$$
$$+ C_4k\left(b_{ik}S_{jk} + b_{ik}S_{jk} - \frac{2}{3}b_{mn}S_{mn}\delta_{ij}\right) + C_5k(b_{ik}W_{jk} + b_{jk}W_{ik}).$$

(A-1)

The mean vorticity W_{ij} is defined as

$$W_{ij} = \omega_{ij} + e_{mji}\Omega_m \quad,$$

(A-2)

where ω_{ij} is the anti-symmetric mean velocity gradient tensor, e_{mji} is the permutation tensor and Ω_m is the rotation rate vector of the non-inertial frame relative to an inertial frame. The definitions of the other terms in (A-1) are

$$b_{ij} = \frac{1}{2k}(\overline{u_iu_j} - \frac{2}{3}k\delta_{ij}) \quad,$$

(A-3a)

$$\Pi = b_{mn}b_{mn} \quad,$$

(A-3b)

$$S_{ij} = \frac{1}{2}(\frac{\partial U_i}{\partial x_j} + \frac{\partial U_j}{\partial x_i}) \quad,$$

(A-3c)

$$P_{ij} = -\left[\overline{u_iu_k}\frac{\partial U_j}{\partial x_k} + \overline{u_ju_k}\frac{\partial U_i}{\partial x_k}\right],$$

(A-3d)

$$\tilde{P} = 2P_{ii} \quad,$$

(A-3e)

$$\omega_{ij} = \frac{1}{2}(\frac{\partial U_i}{\partial x_j} - \frac{\partial U_j}{\partial x_i}) \quad,$$

(A-3f)

and the coefficients are $C_1 = 3.4$, $C_2 = 4.2$, $C_3 = 0.8$, $C_4 = 1.25$, $C_5 = 0.4$, $C_1^* = 1.8$, $C_3^* = 1.3$.

Comparing (A-1) with the LRR model, which can be written as,

$$\Pi_{ij}^{LRR} = -C_1 \varepsilon b_{ij} - \alpha_1(P_{ij} - \frac{2}{3}\tilde{P}\delta_{ij}) - \beta_1(D_{ij} - \frac{2}{3}\tilde{P}\delta_{ij}) - 2\gamma_1 k S_{ij} \quad , \tag{A-4}$$

it can be noted that the first two terms in (A-1) are the return part and its nonlinear modification, respectively. The mean vorticity caused by rotation is separated from the anti-symmetric mean velocity gradient tensor and excluded from the transformation. Therefore, the terms need to be transformed are

$$\Pi_{ij}^{SSG} = (C_3 - C_3^* \Pi^{1/2}) k S_{ij} + C_4 k \left(b_{ik} S_{jk} + b_{ik} S_{jk} - \frac{2}{3} b_{mn} S_{mn} \delta_{ij} \right)$$
$$+ C_5 k (b_{ik} \omega_{jk} + b_{jk} \omega_{ik}) . \tag{A-5}$$

The SSG model (A-1) was developed for plane homogenous turbulence by Speziale et al. (1991). Under this assumption the symmetric and anti-symmetric tensors $\hat{S}_{ij}$ and $\hat{\omega}_{ij}$ can be written as

$$\hat{S}_{ij} = \begin{pmatrix} 0 & S & 0 \\ S & 0 & 0 \\ 0 & 0 & 0 \end{pmatrix}; \; \hat{\omega}_{ij} = \begin{pmatrix} 0 & \omega & 0 \\ -\omega & 0 & 0 \\ 0 & 0 & 0 \end{pmatrix} \quad , \tag{A-6}$$

and the anisotropy tensor is of the form

$$\hat{b}_{ij} = \begin{pmatrix} b_{11} & b_{12} & 0 \\ b_{12} & b_{22} & 0 \\ 0 & 0 & b_{33} \end{pmatrix} . \tag{A-7}$$

Accordingly,

$$\Pi_{ij}^{SSG} = (C_3 - C_3^* \Pi^{1/2}) k \begin{pmatrix} 0 & S & 0 \\ S & 0 & 0 \\ 0 & 0 & 0 \end{pmatrix} + C_4 k \begin{pmatrix} \frac{2}{3} b_{12} S & (b_{11} + b_{22}) S & 0 \\ (b_{11} + b_{22}) S & \frac{2}{3} b_{12} S & 0 \\ 0 & 0 & -\frac{4}{3} b_{12} S \end{pmatrix}$$

$$+ C_5 k \begin{pmatrix} 2 b_{12} \omega & (b_{22} - b_{11}) \omega & 0 \\ (b_{22} - b_{11}) \omega & -2 b_{12} \omega & 0 \\ 0 & 0 & 0 \end{pmatrix} ,$$

or

$$\Pi_{ij}^{SSG} = \begin{pmatrix} C_{11} & C_{12} & 0 \\ C_{12} & C_{22} & 0 \\ 0 & 0 & C_{33} \end{pmatrix} \quad , \tag{A-8}$$

where

$$C_{11} = \left(\frac{2}{3}C_4 + 2C_5 \right) b_{12} kS \quad , \tag{A-9a}$$

$$C_{12} = \left[\left(C_3 - C_3^* \Pi^{1/2} \right) + C_4 (b_{11} + b_{22}) + C_5 (b_{22} - b_{11}) \right] kS \quad , \tag{A-9b}$$

$$C_{22} = \left(\frac{2}{3}C_4 - 2C_5 \right) b_{12} kS \quad , \tag{A-9c}$$

$$C_{33} = -\frac{4}{3} C_4 b_{12} kS \quad , \tag{A-9d}$$

To determine the coefficients in the final form (A-9), consider a thin shear layer flow where

$$S = \omega = \frac{1}{2} \frac{\partial U}{\partial y} \quad . \tag{A-10}$$

On substitution of (A-10) and the anisotropy tensor definition (A-3a), (A-9) becomes

$$C_{11} = \frac{1}{2} \left(\frac{1}{3}C_4 + C_5 \right) \overline{uv} \frac{\partial U}{\partial y} \quad , \tag{A-11a}$$

$$C_{12} = \left(\frac{C_4}{12} - \frac{C_5}{4} + \frac{C_3 - C_3^* \Pi^{1/2}}{4} \right) \overline{u^2} \frac{\partial U}{\partial y} + \left(\frac{C_4}{12} + \frac{C_5}{4} + \frac{C_3 - C_3^* \Pi^{1/2}}{4} \right) \overline{v^2} \frac{\partial U}{\partial y}$$
$$+ \left(-\frac{C_4}{6} + \frac{C_3 - C_3^* \Pi^{1/2}}{4} \right) \overline{w^2} \frac{\partial U}{\partial y} \quad , \tag{A-11b}$$

$$C_{22} = \frac{1}{2} \left(\frac{1}{3}C_4 - C_5 \right) \overline{uv} \frac{\partial U}{\partial y} \quad , \tag{A-11c}$$

$$C_{33} = -\frac{1}{3} C_4 \overline{uv} \frac{\partial U}{\partial y} \quad . \tag{A-11d}$$

Similarly, last three terms in (A-4) can be written in the form

240

$$\Pi_{ij}^{SSG} = -\alpha_1 \begin{pmatrix} -\dfrac{4}{3}\overline{uv}\dfrac{\partial U}{\partial y} & -\overline{v^2}\dfrac{\partial U}{\partial y} & 0 \\[2ex] -\overline{v^2}\dfrac{\partial U}{\partial y} & \dfrac{2}{3}\overline{uv}\dfrac{\partial U}{\partial y} & 0 \\[2ex] 0 & 0 & \dfrac{2}{3}\overline{uv}\dfrac{\partial U}{\partial y} \end{pmatrix} - \beta_1 \begin{pmatrix} \dfrac{2}{3}\overline{uv}\dfrac{\partial U}{\partial y} & -\overline{u^2}\dfrac{\partial U}{\partial y} & 0 \\[2ex] -\overline{u^2}\dfrac{\partial U}{\partial y} & -\dfrac{4}{3}\overline{uv}\dfrac{\partial U}{\partial y} & 0 \\[2ex] 0 & 0 & \dfrac{2}{3}\overline{uv}\dfrac{\partial U}{\partial y} \end{pmatrix}$$

$$-\gamma_1 \begin{pmatrix} 0 & k\dfrac{\partial U}{\partial y} & 0 \\[2ex] k\dfrac{\partial U}{\partial y} & 0 & 0 \\[2ex] 0 & 0 & 0 \end{pmatrix},$$

or

$$\Pi_{ij}^{SSG} = \begin{pmatrix} C_{11}' & C_{12}' & 0 \\ C_{12}' & C_{22}' & 0 \\ 0 & 0 & C_{33}' \end{pmatrix}, \tag{A-12}$$

where

$$C_{11}' = (2\alpha_1 - \beta_1)\dfrac{2}{3}\overline{uv}\dfrac{\partial U}{\partial y}, \tag{A-13a}$$

$$C_{12}' = \left[\left(\beta_1 - \dfrac{\gamma_1}{2} \right)\overline{u^2} + \left(\alpha_1 - \dfrac{\gamma_1}{2} \right)\overline{v^2} - \dfrac{\gamma_1}{2}\overline{w^2} \right]\dfrac{\partial U}{\partial y}, \tag{A-13b}$$

$$C_{22}' = \dfrac{2}{3}(2\beta_1 - \alpha_1)\overline{uv}\dfrac{\partial U}{\partial y}, \tag{A-13c}$$

$$C_{33}' = -\dfrac{2}{3}(\alpha_1 + \beta_1)\overline{uv}\dfrac{\partial U}{\partial y}. \tag{A-13d}$$

By comparing (A-11) with (A-13), the following equations are obtained

$$\dfrac{2}{3}(2\alpha_1 - \beta_1) = \dfrac{1}{2}\left(\dfrac{1}{3}C_4 + C_5 \right), \tag{A-14a}$$

$$\dfrac{2}{3}(2\beta_1 - \alpha_1) = \dfrac{1}{2}\left(\dfrac{1}{3}C_4 - C_5 \right), \tag{A-14b}$$

$$\frac{2}{3}(\alpha_1 + \beta_1) = \frac{1}{3}C_4 \quad , \tag{A-14c}$$

$$\alpha_1 - \frac{\gamma_1}{2} = \frac{C_4}{12} + \frac{C_5}{4} + \frac{1}{4}\left(C_3 - C_3^*\Pi^{1/2}\right) \quad , \tag{A-14d}$$

$$\beta_1 - \frac{\gamma_1}{2} = \frac{C_4}{12} - \frac{C_5}{4} + \frac{1}{4}\left(C_3 - C_3^*\Pi^{1/2}\right) \quad , \tag{A-14e}$$

$$-\frac{\gamma_1}{2} = -\frac{C_4}{6} + \frac{1}{4}\left(C_3 - C_3^*\Pi^{1/2}\right) \quad , \tag{A-14f}$$

Only three of the above equations are independent and undetermined coefficients, α_1, β_1, and γ_1, are solved from them, which are

$$\alpha_1 = \frac{C_4 + C_5}{4} \quad ; \quad \beta_1 = \frac{C_4 - C_5}{4} \quad ; \quad \gamma_1 = \frac{C_4}{3} - \frac{1}{2}\left(C_3 - C_3^*\Pi^{1/2}\right) . \tag{A-15}$$

Substituting $C_3 = 0.8$, $C_4 = 1.25$, $C_5 = 0.4$, $C_3^* = 1.3$ into (A-15), we have

$$\alpha_1 = 0.4125 \quad ; \quad \beta_1 = 0.2125 \quad \text{and} \quad \gamma_1 = 0.01667 + \frac{C_3^*}{2}\Pi^{1/2} \quad . \tag{A-16}$$

Therefore, the transformed SSG model is

$$\Pi_{ij}^{SSG} = -(C_1\varepsilon + C_1^*\tilde{P})b_{ij} + C_2\varepsilon(b_{ik}b_{kj} - \frac{1}{3}\Pi\delta_{ij}) + C_5\Omega_m(b_{ik}e_{mkj} + b_{jk}e_{mki})k$$

$$- \alpha_1(P_{ij} - \frac{2}{3}\tilde{P}\delta_{ij}) - \beta_1(D_{ij} - \frac{2}{3}\tilde{P}\delta_{ij}) - 2(\gamma_1 + \frac{C_3^*}{2}\Pi^{1/2})kS_{ij} \tag{A-17}$$

with $\alpha_1 = 0.4125$; $\beta_1 = 0.2125$ and $\gamma_1 = 0.01667$ and $C_1 = 3.4$, $C_2 = 4.2$, $C_5 = 0.4$, $C_1^* = 1.8$.

APPENDIX B

SUMMARY OF MODEL EQUATIONS

B.1 NNWRS Model

The Reynolds-stress transport equation for the NNWRS model can be written as

$$U_k \frac{\partial \overline{u_i u_j}}{\partial x_k} = \frac{\partial}{\partial x_k}\left(v \frac{\partial \overline{u_i u_j}}{\partial x_k}\right) + D_{ij}^T + [-\overline{u_i u_k}\frac{\partial U_j}{\partial x_k} - \overline{u_j u_k}\frac{\partial U_i}{\partial x_k}]$$
$$- 2\Omega_k(\overline{u_j u_m}e_{ikm} + \overline{u_i u_m}e_{jkm}) + \Pi_{ij} - \varepsilon_{ij} \ . \tag{B-1}$$

where the modeled terms are

$$D_{ij}^T = \frac{\partial}{\partial x_k}\left[C_s \frac{k}{\varepsilon}\left(\overline{u_i u_l}\frac{\partial \overline{u_j u_k}}{\partial x_l} + \overline{u_j u_l}\frac{\partial \overline{u_k u_i}}{\partial x_l} + \overline{u_k u_l}\frac{\partial \overline{u_i u_j}}{\partial x_l}\right)\right] \ , \tag{B-2}$$

$$\Pi_{ij} = -(C_1\varepsilon + C_1^*\tilde{P})b_{ij} + C_2\varepsilon(b_{ik}b_{kj} - \frac{1}{3}\Pi\delta_{ij}) + C_5\Omega_m(b_{ik}e_{mkj} + b_{jk}e_{mki})k$$
$$- \alpha_1(P_{ij} - \frac{2}{3}\tilde{P}\delta_{ij}) - \beta_1(D_{ij} - \frac{2}{3}\tilde{P}\delta_{ij}) - 2(\gamma_1 + \frac{C_3^*}{2}\Pi^{1/2})kS_{ij}$$
$$+ f_{w,1}\Pi_{ij}^w \ . \tag{B-3a}$$

$$\Pi_{ij}^w = (C_1\varepsilon + C_1^*\tilde{P})b_{ij} - C_2\varepsilon(b_{ik}b_{kj} - \frac{1}{3}\Pi\delta_{ij}) + \alpha^*(P_{ij} - \frac{2}{3}\tilde{P}\delta_{ij}) + 2\gamma^*kS_{ij} \ , \tag{B-3b}$$

$$\varepsilon_{ij} = \frac{2}{3}\delta_{ij}\varepsilon(1 - f_{w,1}) + f_{w,1}\varepsilon_{ij}^w + \varepsilon_{ij}^* \ , \tag{B-4a}$$

$$\varepsilon_{ij}^w = \frac{\varepsilon}{k}\overline{u_i u_j} \ , \tag{B-4b}$$

$$\varepsilon_{ij}^* = \frac{1}{2}\left[\frac{\partial}{\partial x_k}(v \frac{\partial \overline{u_i u_j}}{\partial x_k}) - \frac{\overline{u_i u_j}}{k}\frac{\partial}{\partial x_k}(v \frac{\partial k}{\partial x_k})\right] \ , \tag{B-4c}$$

The dissipation rate equation is given by

$$U_k \frac{\partial \varepsilon}{\partial x_k} = \frac{\partial}{\partial x_k}\left(v \frac{\partial \varepsilon}{\partial x_k}\right) + \frac{\partial}{\partial x_j}(C_\varepsilon \frac{k}{\varepsilon}\overline{u_i u_j}\frac{\partial \varepsilon}{\partial x_i}) + C_{\varepsilon 1}\frac{\varepsilon}{k}\tilde{P} - C_{\varepsilon 2}f_\varepsilon \frac{\varepsilon^2}{k}$$
$$+ C_{\varepsilon 3}v\frac{\varepsilon}{k}\left(\frac{\partial \sqrt{k}}{\partial x_k}\right)^2 \ . \tag{B-5}$$

B.2 NWRS Model

The Reynolds-stress transport equation for the NWRS model can be written as

$$U_k \frac{\partial \overline{u_i u_j}}{\partial x_k} = \frac{\partial}{\partial x_k}\left(\upsilon \frac{\partial \overline{u_i u_j}}{\partial x_k}\right) + D_{ij}^T + [-\overline{u_i u_k}\frac{\partial U_j}{\partial x_k} - \overline{u_j u_k}\frac{\partial U_i}{\partial x_k}]$$
$$- 2\Omega_k (\overline{u_j u_m}e_{ikm} + \overline{u_i u_m}e_{jkm})k + \Pi_{ij} - \varepsilon_{ij} .$$

(B-6)

The modeled terms are given by

$$D_{ij}^T = \frac{\partial}{\partial x_k}\left[C_s \frac{k}{\varepsilon}\left(\overline{u_i u_l}\frac{\partial \overline{u_j u_k}}{\partial x_l} + \overline{u_j u_l}\frac{\partial \overline{u_k u_i}}{\partial x_l} + \overline{u_k u_l}\frac{\partial \overline{u_i u_j}}{\partial x_l}\right)\right] .$$

(B-7)

$$\Pi_{ij} = -(C_1\varepsilon + C_1^* \tilde{P})b_{ij} + C_2\varepsilon(b_{ik}b_{kj} - \frac{1}{3}\Pi\delta_{ij}) + C_5\Omega_m(b_{ik}e_{mkj} + b_{jk}e_{mki})k$$
$$- \alpha_1(P_{ij} - \frac{2}{3}\tilde{P}\delta_{ij}) - \beta_1(D_{ij} - \frac{2}{3}\tilde{P}\delta_{ij}) - 2(\gamma_1 + \frac{C_3^*}{2}\Pi^{1/2})kS_{ij}$$
$$+ f_{w,1}\Pi_{ij}^w + \Pi_{ij}^p .$$

(B-8a)

where

$$\Pi_{ij}^w = (C_1\varepsilon + C_1^* \tilde{P})b_{ij} - C_2\varepsilon(b_{ik}b_{kj} - \frac{1}{3}\Pi\delta_{ij}) + \alpha^*(P_{ij} - \frac{2}{3}\tilde{P}\delta_{ij}) + 2\gamma^*kS_{ij} ,$$

(B-8b)

$$\Pi_{ij}^p = -\frac{1}{3}\left[\frac{\partial}{\partial x_l}\left(\upsilon\frac{\partial \overline{u_i u_k}}{\partial x_l}\right)n_k n_j + \frac{\partial}{\partial x_l}\left(\upsilon\frac{\partial \overline{u_j u_k}}{\partial x_l}\right)n_k n_i\right] + \frac{1}{3}\frac{\partial}{\partial x_m}\left(\upsilon\frac{\partial \overline{u_k u_l}}{\partial x_m}\right)n_k n_i n_i n_j ,$$

(B-8c)

$$\varepsilon_{ij} = \frac{2}{3}\delta_{ij}\varepsilon(1 - f_{w,1}) + f_{w,1}\varepsilon_{ij}^w ,$$

(B-9a)

$$\varepsilon_{ij}^w = \frac{\varepsilon}{k}\frac{\overline{u_i u_j} + \overline{u_i u_k}n_k n_j + \overline{u_j u_k}n_k n_i + n_i n_j \overline{u_k u_l}n_k n_l}{1 + 3\overline{u_k u_l}n_k n_l / 2k} .$$

(B-9b)

The dissipation rate equation is given by

$$U_k \frac{\partial \varepsilon}{\partial x_k} = \frac{\partial}{\partial x_k}\left(\upsilon\frac{\partial \varepsilon}{\partial x_k}\right) + \frac{\partial}{\partial x_j}(C_\varepsilon \frac{k}{\varepsilon}\overline{u_i u_j}\frac{\partial \varepsilon}{\partial x_i}) + C_{\varepsilon 1}\frac{\varepsilon}{k}\tilde{P} - C_{\varepsilon 2}\frac{\varepsilon\tilde{\varepsilon}}{k} + \zeta ,$$

(B-10a)

where

244

$$\zeta = f_{w,2}\left(-L\frac{\varepsilon}{k}\tilde{P} + M\frac{\bar{\varepsilon}^2}{k} - N\frac{\varepsilon\tilde{\varepsilon}}{k}\right),$$ (B-10b)

$$\bar{\varepsilon} = \varepsilon - 2\upsilon k / y^2 \quad,$$ (B-10c)

$$\tilde{\varepsilon} = \varepsilon - 2\upsilon\left(\partial\sqrt{k} / \partial y\right)^2 \quad,$$ (B-10d)

Other tensors and vectors appearing in the NWRS and NNWRS models are given by

$$P_{ij} = -\left[\overline{u_i u_k}\frac{\partial U_j}{\partial x_k} + \overline{u_j u_k}\frac{\partial U_i}{\partial x_k}\right],$$ (B-11a)

$$\tilde{P} = 2P_{ii} \quad,$$ (B-11b)

$$b_{ij} = \frac{1}{2k}(\overline{u_i u_j} - \frac{2}{3}k\delta_{ij}) \quad,$$ (B-11c)

$$\Pi = b_{mn}b_{mn} \quad,$$ (b-11d)

$$S_{ij} = \frac{1}{2}(\frac{\partial U_i}{\partial x_j} + \frac{\partial U_j}{\partial x_i}) \quad,$$ (B-11e)

$$D_{ij} = -\left[\overline{u_i u_k}\frac{\partial U_k}{\partial x_j} + \overline{u_j u_k}\frac{\partial U_k}{\partial x_i}\right] \quad,$$ (B-11f)

$$\bar{n} = (0, 1, 0) \quad,$$ (B-11h)

$$e_{ijk} = \begin{cases} 0, & \textit{if any two of i, j, k are the same} \\ 1, & \textit{if ijk is an even permutation of 123} \\ -1, & \textit{if ijk is an odd permutation of 123} \end{cases} \quad.$$ (B-11i)

B.3 Model Constants and Damping Functions

The model constants and damping functions are listed in the table below.

Constants/Functions	NNWRS	NWRS
C_1	3.4	3.4
C_2	4.2	4.2
C_1^*	1.8	1.8
C_3^*	1.3	1.3
α_1	0.4125	0.4125
β_1	0.2125	0.2125
γ_1	0.01667	0.01667
α^*	-0.32	-0.29
γ^*	0.072	0.065
C_s	0.11	0.11
$C_{\varepsilon 1}$	1.5	1.5
$C_{\varepsilon 2}$	1.9	1.83
$C_{\varepsilon 3}$	2.95	
C_5	0.4	0.4
C_ε	0.12	0.12
L		2.25
M		0.5
N		0.57
f_ε	$1-(2/9)e^{-\left(Re_t/6\right)^2}$	
f_{w1}	$e^{-\left(Re_t/150\right)^2}$	$e^{-\left(A\,Re_t/60\right)^3}, \; e^{-\left(Re_t/200\right)^2}$
f_{w2}		$e^{-\left(Re_t/40\right)^2}$

where

$$\mathrm{Re}_t = \frac{k^2}{\upsilon \varepsilon} \quad , \tag{B-12}$$

$$A = 1 - (9/2)(b_{ij}b_{ij} - 2b_{ij}b_{jk}b_{ki}) \quad . \tag{B-13}$$

APPENDIX C

SUMMARY OF GOVERNING EQUATIONS

C.1 Fully-Developed Channel Flows

C.1.1 Mean flow equation

$$0 = \frac{\partial^2 U^+}{\partial y^{+2}} - \frac{\partial \overline{uv}^+}{\partial y^+} + \frac{1}{Re_\tau} \quad . \tag{C-1}$$

C.1.2 NNWRS modeled equations

$$0 = \frac{\partial}{\partial y^+}\left(\left(1 + C_s \frac{k^+}{\varepsilon^+}\overline{v^2}^+\right)\frac{\partial \overline{u^2}^+}{\partial y^+} + 2C_s \frac{k^+}{\varepsilon^+}\overline{uv}^+ \frac{\partial \overline{uv}^+}{\partial y^+}\right) - 2\overline{uv}^+ \frac{\partial U^+}{\partial y^+}$$

$$-C_1 \varepsilon^+ (1 - f_{w1})b_{11} + \left\{\frac{4}{3}(\alpha_1 - f_{w1}\alpha^*) - \frac{2}{3}\beta_1 + C_1^*(1 - f_{w1})b_{11}\right\}\overline{uv}^+ \frac{\partial U^+}{\partial y^+}$$

$$+C_2 \varepsilon^+ (1 - f_{w1})\left(b_{11}^2 + b_{12}^2 - \frac{1}{3}\Pi\right) - \frac{2}{3}(1 - f_{w1})\varepsilon^+ - f_{w1}\frac{\varepsilon^+}{k^+}\overline{u^2}^+$$

$$-\frac{1}{2}\left[\frac{\partial}{\partial y^+}\left(\frac{\partial \overline{u^2}^+}{\partial y^+}\right) - \frac{\overline{u^2}^+}{k^+}\frac{\partial}{\partial y^+}\left(\frac{\partial k^+}{\partial y^+}\right)\right] \quad , \tag{C-2}$$

$$0 = \frac{\partial}{\partial y^+}\left(\left(1 + 3C_s \frac{k^+}{\varepsilon^+}\overline{v^2}^+\right)\frac{\partial \overline{v^2}^+}{\partial y^+}\right) - C_1 \varepsilon^+ (1 - f_{w1})b_{22}$$

$$-\left\{\frac{2}{3}(\alpha_1 - f_{w1}\alpha^*) - \frac{4}{3}\beta_1 - C_1^*(1 - f_{w1})b_{22}\right\}\overline{uv}^+ \frac{\partial U^+}{\partial y^+}$$

$$+C_2 \varepsilon^+ (1 - f_{w1})\left(b_{22}^2 + b_{12}^2 - \frac{1}{3}\Pi\right) - \frac{2}{3}(1 - f_{w1})\varepsilon^+ - f_{w1}\frac{\varepsilon^+}{k^+}\overline{v^2}^+$$

$$-\frac{1}{2}\left[\frac{\partial}{\partial y^+}\left(\frac{\partial \overline{v^2}^+}{\partial y^+}\right) - \frac{\overline{v^2}^+}{k^+}\frac{\partial}{\partial y^+}\left(\frac{\partial k^+}{\partial y^+}\right)\right] \quad , \tag{C-3}$$

248

$$0 = \frac{\partial}{\partial y^+}\left[\left(1 + C_s \frac{k^+}{\varepsilon^+}\overline{v^2}^+\right)\frac{\partial \overline{w^2}^+}{\partial y^+}\right] - C_1 \varepsilon^+ (1 - f_{w1}) b_{33}$$

$$-\left\{\frac{2}{3}(\alpha_1 - f_{w1}\alpha^*) + \frac{2}{3}\beta_1 - C_1^*(1-f_{w1})b_{33}\right\}\overline{uv}^+ \frac{\partial U^+}{\partial y^+}$$

$$+C_2 \varepsilon^+ (1-f_{w1})\left(b_{33}^2 - \frac{1}{3}\Pi\right) - \frac{2}{3}(1-f_{w1})\varepsilon^+ - f_{w1}\frac{\varepsilon^+}{k^+}\overline{w^2}^+$$

$$-\frac{1}{2}\left[\frac{\partial}{\partial y^+}\left(\frac{\partial \overline{w^2}^+}{\partial y^+}\right) - \frac{\overline{w^2}^+}{k^+}\frac{\partial}{\partial y^+}\left(\frac{\partial k^+}{\partial y^+}\right)\right] \quad , \tag{C-4}$$

$$0 = \frac{\partial}{\partial y^+}\left[\left(1 + 2C_s\frac{k^+}{\varepsilon^+}\overline{v^2}^+\right)\frac{\partial \overline{uv}^+}{\partial y^+} + C_s\frac{k^+}{\varepsilon^+}\overline{uv}^+\frac{\partial \overline{v^2}^+}{\partial y^+}\right] - \overline{v^2}^+\frac{\partial U^+}{\partial y^+}$$

$$-C_1 \varepsilon^+(1-f_{w1})b_{12} + (\alpha_1 - f_{w1}\alpha^*)\overline{v^2}^+\frac{\partial U^+}{\partial y^+} + \beta_1 \overline{u^2}^+\frac{\partial U^+}{\partial y^+}$$

$$+C_1^*(1-f_{w1})b_{12}\overline{uv}^+\frac{\partial U^+}{\partial y^+} - \left(\gamma_1 - f_{w1}\gamma^* + \frac{C_3^*}{2}\Pi^{1/2}\right)k^+\frac{\partial U^+}{\partial y^+}$$

$$+C_2\varepsilon^+(1-f_{w1})(b_{11}b_{12}+b_{12}b_{22}) - f_{w1}\frac{\varepsilon^+}{k^+}\overline{uv}^+$$

$$-\frac{1}{2}\left[\frac{\partial}{\partial y^+}\left(\frac{\partial \overline{uv}^+}{\partial y^+}\right) - \frac{\overline{uv}^+}{k^+}\frac{\partial}{\partial y^+}\left(\frac{\partial k^+}{\partial y^+}\right)\right] \quad , \tag{C-5}$$

$$0 = \frac{\partial}{\partial y^+}\left[\left(1 + C_\varepsilon\frac{k^+}{\varepsilon^+}\overline{v^2}\right)\frac{\partial \varepsilon^+}{\partial y^+}\right] - C_{\varepsilon 1}\frac{\varepsilon^+}{k^+}\overline{uv}^+\frac{\partial U^+}{\partial y^+} - C_{\varepsilon 2}\frac{\varepsilon^+}{k^+}\tilde{P}^+$$

$$+C_{\varepsilon 3}\frac{\varepsilon^+}{k^+}\left(\frac{\partial \sqrt{k^+}}{\partial y^+}\right)^2 \quad . \tag{C-6}$$

C.1.3 NWRS modeled equations

$$0 = \frac{\partial}{\partial y^+}\left(\left(1 + C_s \frac{k^+}{\varepsilon^+}\overline{v^2}^+\right)\frac{\partial \overline{u^2}^+}{\partial y^+} + 2C_s \frac{k^+}{\varepsilon^+}\overline{uv}^+ \frac{\partial \overline{uv}^+}{\partial y^+}\right) - 2\overline{uv}^+ \frac{\partial U^+}{\partial y^+}$$

$$-C_1 \varepsilon^+ \left(1 - f_{w1}\right)b_{11} + \left\{\frac{4}{3}\left(\alpha_1 - f_{w1}\alpha^*\right) - \frac{2}{3}\beta_1 + C_1^*\left(1 - f_{w1}\right)b_{11}\right\}\overline{uv}^+ \frac{\partial U^+}{\partial y^+}$$

$$+C_2 \varepsilon^+ \left(1 - f_{w1}\right)\left(b_{11}^{\;2} + b_{12}^{\;2} - \frac{1}{3}\Pi\right)$$

$$-f_{w1} \frac{\overline{u^2}^+}{k^+ + 3\overline{v^2}^+/2}\varepsilon^+ - \frac{2}{3}\left(1 - f_{w1}\right)\varepsilon^+ \quad , \tag{C-7}$$

$$0 = \frac{\partial}{\partial y^+}\left(\left(\frac{2}{3} + 3C_s \frac{k^+}{\varepsilon^+}\overline{v^2}^+\right)\frac{\partial \overline{v^2}^+}{\partial y^+}\right) - C_1 \varepsilon^+ \left(1 - f_{w1}\right)b_{22}$$

$$-\left\{\frac{2}{3}\left(\alpha_1 - f_{w1}\alpha^*\right) - \frac{4}{3}\beta_1 - C_1^*\left(1 - f_{w1}\right)b_{22}\right\}\overline{uv}^+ \frac{\partial U^+}{\partial y^+}$$

$$+C_2 \varepsilon^+ \left(1 - f_{w1}\right)\left(b_{22}^{\;2} + b_{12}^{\;2} - \frac{1}{3}\Pi\right)$$

$$-4f_{w1} \frac{\overline{v^2}^+}{k^+ + 3\overline{v^2}^+/2}\varepsilon^+ - \frac{2}{3}\left(1 - f_{w1}\right)\varepsilon^+ \quad , \tag{C-8}$$

$$0 = \frac{\partial}{\partial y^+}\left(\left(1 + C_s \frac{k^+}{\varepsilon^+}\overline{v^2}^+\right)\frac{\partial \overline{w^2}^+}{\partial y^+}\right) - C_1 \varepsilon^+ \left(1 - f_{w1}\right)b_{33}$$

$$-\left\{\frac{2}{3}\left(\alpha_1 - f_{w1}\alpha^*\right) + \frac{2}{3}\beta_1 - C_1^*\left(1 - f_{w1}\right)b_{33}\right\}\overline{uv}^+ \frac{\partial U^+}{\partial y^+}$$

$$+C_2 \varepsilon^+ \left(1 - f_{w1}\right)\left(b_{33}^{\;2} - \frac{1}{3}\Pi\right)$$

$$-f_{w1} \frac{\overline{w^2}^+}{k^+ + 3\overline{v^2}^+/2}\varepsilon^+ - \frac{2}{3}\left(1 - f_{w1}\right)\varepsilon^+ \quad , \tag{C-9}$$

$$0 = \frac{\partial}{\partial y^+}\left[\left(\frac{2}{3} + 2C_s \frac{k^+}{\varepsilon^+}\overline{v^2}^+\right)\frac{\partial \overline{uv}^+}{\partial y^+} + C_s \frac{k^+}{\varepsilon^+}\overline{uv}^+ \frac{\partial \overline{v^2}^+}{\partial y^+}\right] - \overline{v^2}^+ \frac{\partial U^+}{\partial y^+}$$

$$- C_1 \varepsilon^+ (1 - f_{w1})b_{12} + (\alpha_1 - f_{w1}\alpha^*)\overline{v^2}^+ \frac{\partial U^+}{\partial y^+} + \beta_1 \overline{u^2}^+ \frac{\partial U^+}{\partial y^+}$$

$$+ C_1^* (1 - f_{w1})b_{12}\overline{uv}^+ \frac{\partial U^+}{\partial y^+} - \left(\gamma_1 - f_{w1}\gamma^* + \frac{C_3^*}{2}\Pi^{1/2}\right)k^+ \frac{\partial U^+}{\partial y^+}$$

$$+ C_2 \varepsilon^+ (1 - f_{w1})(b_{11}b_{12} + b_{12}b_{22}) - 2f_{w1}\frac{\overline{uv}^+}{k^+ + 3\overline{v^2}^+ / 2}\varepsilon^+ \quad , \tag{C-10}$$

$$0 = \frac{\partial}{\partial y^+}\left[\left(1 + C_\varepsilon \frac{k^+}{\varepsilon^+}\overline{v^2}\right)\frac{\partial \varepsilon^+}{\partial y^+}\right] - C_{\varepsilon 1}\frac{\varepsilon^+}{k^+}\overline{uv}^+ \frac{\partial U^+}{\partial y^+} - C_{\varepsilon 2}\frac{\tilde{\varepsilon}^+ \varepsilon^+}{k^+}$$

$$+ f_{w2}\left(L\frac{\varepsilon^+}{k^+}\overline{uv}^+ \frac{\partial U^+}{\partial y^+} + M\frac{\bar{\varepsilon}^2}{k^+} - N\frac{\tilde{\varepsilon}^+ \varepsilon^+}{k^+}\right) \quad . \tag{C-11}$$

C.1.4 Boundary conditions

At $y^+ = 0$ (wall)

$$U^+ = 0, \ k^+ = 0, \ \overline{u^2}^+ = 0, \ \overline{v^2}^+ = 0, \ \overline{w^2}^+ = 0, \ \overline{uv}^+ = 0$$

$$\varepsilon^+ = 2\left(\frac{\partial \sqrt{k}}{\partial y^+}\right)^2 \quad . \tag{C-12}$$

At $y^+ = Re_\tau$ (centerline)

$$\frac{\partial U^+}{\partial y^+} = 0, \ \frac{\partial k^+}{\partial y^+} = 0, \ \frac{\partial \overline{u^2}^+}{\partial y^+} = 0, \ \frac{\partial \overline{v^2}^+}{\partial y^+} = 0, \ \frac{\partial \overline{w^2}^+}{\partial y^+} = 0, \ \overline{uv}^+ = 0$$

$$\frac{\partial \varepsilon^+}{\partial y^+} = 0 \quad . \tag{C-13}$$

251

C.2 Fully-Developed Pipe Flow

C.2.1 Mean flow equation

$$0 = \frac{1}{r^+}\frac{\partial}{\partial r^+}\left(r^+ \frac{\partial U^+}{\partial r^+}\right) - \frac{1}{r^+}\frac{\partial}{\partial r^+}\left(r^+ \overline{uv}^+\right) + \frac{2}{Re_\tau} \qquad .$$

(C-14)

C.2.2 NNWRS modeled equations

$$0 = \frac{1}{r^+}\frac{\partial}{\partial r^+}\left[r^+\left(1 + C_S \frac{k^+}{\varepsilon^+}\overline{v^2}^+\right)\frac{\partial \overline{u^2}^+}{\partial r^+} + 2r^+ C_S \frac{k^+}{\varepsilon^+}\overline{uv}^+ \frac{\partial \overline{uv}^+}{\partial r^+}\right] - 2\overline{uv}^+ \frac{\partial U^+}{\partial r^+}$$

$$- C_I \varepsilon^+ (1 - f_{wI})b_{11} + \left\{ \frac{4}{3}(\alpha_I - f_{wI}\alpha^*) - \frac{2}{3}\beta_I + C_I^*(1 - f_{wI})b_{11}\right\}\overline{uv}^+ \frac{\partial U^+}{\partial r^+}$$

$$+ C_2 \varepsilon^+ (1 - f_{wI})\left(b_{11}^2 + b_{12}^2 - \frac{1}{3}\Pi\right) - \frac{2}{3}(1 - f_{wI})\varepsilon^+ - f_{wI}\frac{\varepsilon^+}{k^+}\overline{u^2}^+$$

$$- \frac{1}{2}\left[\frac{1}{r^+}\frac{\partial}{\partial r^+}\left(r^+ \frac{\partial \overline{u^2}^+}{\partial r^+}\right) - \frac{\overline{u^2}^+}{k^+}\frac{1}{r^+}\frac{\partial}{\partial r^+}\left(r^+ \frac{\partial k^+}{\partial r^+}\right)\right] \quad ,$$

(C-15)

$$0 = \frac{1}{r^+}\frac{\partial}{\partial r^+}\left[r^+\left(1 + 3C_S \frac{k^+}{\varepsilon^+}\overline{v^2}^+\right)\frac{\partial \overline{v^2}^+}{\partial r^+}\right] - \frac{2}{r^{+2}}\left(\overline{v^2}^+ - \overline{w^2}^+\right) + \frac{2}{3}\frac{2\overline{v^2}^+}{r^{+2}}$$

$$- \frac{2}{r^+}C_S \frac{k^+}{\varepsilon^+}\overline{v^2}^+ \frac{\partial \overline{w^2}^+}{\partial r^+} - \frac{4}{r^{+2}}C_S \frac{k^+}{\varepsilon^+}\overline{w^2}^+ \left(\overline{v^2}^+ - \overline{w^2}^+\right)$$

$$- C_I \varepsilon^+ (1 - f_{wI})b_{22} - \left\{ \frac{2}{3}(\alpha_I - f_{wI}\alpha^*) - \frac{4}{3}\beta_I - C_I^*(1 - f_{wI})b_{22}\right\}\overline{uv}^+ \frac{\partial U^+}{\partial r^+}$$

$$+ C_2 \varepsilon^+ (1 - f_{wI})\left(b_{22}^2 + b_{12}^2 - \frac{1}{3}\Pi\right) - \frac{2}{3}(1 - f_{wI})\varepsilon^+ - f_{wI}\frac{\varepsilon^+}{k^+}\overline{v^2}^+$$

$$- \frac{1}{2}\left[\frac{1}{r^+}\frac{\partial}{\partial r^+}\left(r^+ \frac{\partial \overline{v^2}^+}{\partial r^+}\right) - \frac{\overline{v^2}^+}{k^+}\frac{1}{r^+}\frac{\partial}{\partial r^+}\left(r^+ \frac{\partial k^+}{\partial r^+}\right)\right] \quad ,$$

(C-16)

252

$$0 = \frac{1}{r^+}\frac{\partial}{\partial r^+}\left(r^+\left(1 + C_s\frac{k^+}{\varepsilon^+}\overline{v^2}^+\right)\frac{\partial \overline{w^2}^+}{\partial r^+}\right) + \frac{2}{r^{+2}}\left(\overline{v^2}^+ - \overline{w^2}^+\right) - \frac{2}{3}\frac{\overline{v^2}^+}{r^{+2}}$$

$$+\frac{2}{r^+}C_s\frac{k^+}{\varepsilon^+}\overline{v^2}^+\frac{\partial \overline{w^2}^+}{\partial r^+} + \frac{4}{r^{+2}}C_s\frac{k^+}{\varepsilon^+}\overline{w^2}^+\left(\overline{v^2}^+ - \overline{w^2}^+\right) + \frac{2}{r^+}\frac{\partial}{\partial r^+}\left(C_s\frac{k^+}{\varepsilon^+}\overline{w^2}^+\left(\overline{v^2}^+ - \overline{w^2}^+\right)\right)$$

$$-C_1\varepsilon^+(1 - f_{w1})b_{33}^+ - \left\{\frac{2}{3}\left(\alpha_1 - f_{w1}\alpha^*\right) + \frac{2}{3}\beta_1 - C_1^*(1 - f_{w1})b_{33}\right\}\overline{uv}^+\frac{\partial U^+}{\partial r^+}$$

$$+C_2\varepsilon^+(1 - f_{w1})\left(b_{33}{}^2 - \frac{1}{3}\Pi\right) - \frac{2}{3}(1 - f_{w1})\varepsilon^+ - f_{w1}\frac{\varepsilon^+}{k^+}\overline{w^2}^+$$

$$-\frac{1}{2}\left[\frac{1}{r^+}\frac{\partial}{\partial r^+}\left(r^+\frac{\partial \overline{w^2}^+}{\partial r^+}\right) - \frac{\overline{w^2}^+}{k^+}\frac{1}{r^+}\frac{\partial}{\partial r^+}\left(r^+\frac{\partial k^+}{\partial r^+}\right)\right] \quad , \tag{C-17}$$

$$0 = \frac{1}{r^+}\frac{\partial}{\partial r^+}\left(r^+\left(1 + 2C_s\frac{k^+}{\varepsilon^+}\overline{v^2}^+\right)\frac{\partial \overline{uv}^+}{\partial r^+} + r^+C_s\frac{k^+}{\varepsilon^+}\overline{uv}^+\frac{\partial \overline{v^2}^+}{\partial r^+}\right) - \frac{2}{3}\frac{\overline{uv}^+}{r^{+2}}$$

$$-\frac{1}{r^+}C_s\frac{k^+}{\varepsilon^+}\overline{uv}^+\frac{\partial \overline{w^2}^+}{\partial r^+} - \frac{2}{r^{+2}}C_s\frac{k^+}{\varepsilon^+}\overline{uv}^+\overline{w^2}^+ - \overline{v^2}^+\frac{\partial U^+}{\partial r^+} - C_1\varepsilon^+(1 - f_{w1})b_{12}$$

$$+\left(\alpha_1 - f_{w1}\alpha^*\right)\overline{v^2}^+\frac{\partial U^+}{\partial r^+} + \beta_1\overline{u^2}^+\frac{\partial U^+}{\partial r^+} + C_1^*(1 - f_{w1})b_{12}\overline{uv}^+\frac{\partial U^+}{\partial r^+}$$

$$-\left(\gamma_1 - f_{w1}\gamma^* + \frac{C_3^*}{2}\Pi^{1/2}\right)k^+\frac{\partial U^+}{\partial y^+} + C_2\varepsilon^+(1 - f_{w1})(b_{11}b_{12} + b_{12}b_{22})$$

$$-f_{w,1}\frac{\varepsilon^+}{k^+}\overline{uv}^+ - \frac{1}{2}\left[\frac{1}{r^+}\frac{\partial}{\partial r^+}\left(r^+\frac{\partial \overline{uv}^+}{\partial r^+}\right) - \frac{\overline{uv}^+}{k^+}\frac{1}{r^+}\frac{\partial}{\partial r^+}\left(r^+\frac{\partial k^+}{\partial r^+}\right)\right] \quad , \tag{C-18}$$

$$0 = \frac{1}{r^+}\frac{\partial}{\partial r^+}\left(r^+\left(1 + C_\varepsilon\frac{k^+}{\varepsilon^+}\overline{v^2}\right)\frac{\partial \varepsilon^+}{\partial r^+}\right) - C_{\varepsilon 1}\frac{\varepsilon^+}{k^+}\overline{uv}^+\frac{\partial U^+}{\partial r^+} - C_{\varepsilon 2}\frac{\varepsilon^+}{k^+}\tilde{P}^+$$

$$+C_{\varepsilon 3}\frac{\varepsilon^+}{k^+}\left(\frac{\partial \sqrt{k^+}}{\partial r^+}\right)^2 \tag{C-19}$$

253

C.2.3 NWRS modeled equations

$$0 = \frac{1}{r^+} \frac{\partial}{\partial r^+} \left(r^+ \left(1 + C_s \frac{k^+}{\varepsilon^+} \overline{v^2}^+ \right) \frac{\partial \overline{u^2}^+}{\partial r^+} + 2 r^+ C_s \frac{k^+}{\varepsilon^+} \overline{uv}^+ \frac{\partial \overline{uv}^+}{\partial r^+} \right) - 2 \overline{uv}^+ \frac{\partial U^+}{\partial r^+}$$

$$- C_1 \varepsilon^+ (1 - f_{w1}) b_{11} + \left\{ \frac{4}{3} (\alpha_1 - f_{w1} \alpha^*) - \frac{2}{3} \beta_1 + C_1^* (1 - f_{w1}) b_{11} \right\} \overline{uv}^+ \frac{\partial U^+}{\partial r^+}$$

$$+ C_2 \varepsilon^+ (1 - f_{w1}) \left(b_{11}^{\ 2} + b_{12}^{\ 2} - \frac{1}{3} \Pi \right)$$

$$- f_{w1} \overline{u^2}^+ \frac{\varepsilon^+}{k^+ + 3 \overline{v^2}^+ / 2} - \frac{2}{3} (1 - f_{w1}) \varepsilon^+ \quad , \tag{C-20}$$

$$0 = \frac{1}{r^+} \frac{\partial}{\partial r^+} \left(\left(\frac{2}{3} + 3 C_s \frac{k^+}{\varepsilon^+} \overline{v^2}^+ \right) \frac{\partial \overline{v^2}^+}{\partial r^+} \right) - \frac{2}{r^{+2}} \left(\overline{v^2}^+ - \overline{w^2}^+ \right) + \frac{2}{3} \frac{2 \overline{v^2}^+}{r^{+2}}$$

$$- \frac{2}{r^+} C_s \frac{k^+}{\varepsilon^+} \overline{v^2}^+ \frac{\partial \overline{w^2}^+}{\partial r^+} - \frac{4}{r^{+2}} C_s \frac{k^+}{\varepsilon^+} \overline{w^2}^+ \left(\overline{v^2}^+ - \overline{w^2}^+ \right)$$

$$- C_1 \varepsilon^+ (1 - f_{w1}) b_{22} - \left\{ \frac{2}{3} (\alpha_1 - f_{w1} \alpha^*) - \frac{4}{3} \beta_1 - C_1^* (1 - f_{w1}) b_{22} \right\} \overline{uv}^+ \frac{\partial U^+}{\partial r^+}$$

$$+ C_2 \varepsilon^+ (1 - f_{w1}) \left(b_{22}^{\ 2} + b_{12}^{\ 2} - \frac{1}{3} \Pi \right)$$

$$- 4 f_{w1} \overline{v^2}^+ \frac{\varepsilon^+}{k^+ + 3 \overline{v^2}^+ / 2} - \frac{2}{3} (1 - f_{w1}) \varepsilon^+ \quad , \tag{C-21}$$

$$0 = \frac{1}{r^+} \frac{\partial}{\partial r^+} \left(r^+ \left(1 + C_s \frac{k^+}{\varepsilon^+} \overline{v^2}^+ \right) \frac{\partial \overline{w^2}^+}{\partial r^+} \right) + \frac{2}{r^{+2}} \left(\overline{v^2}^+ - \overline{w^2}^+ \right) - \frac{2}{3} \frac{\overline{v^2}^+}{r^{+2}}$$

$$+ \frac{2}{r^+} C_s \frac{k^+}{\varepsilon^+} \overline{v^2}^+ \frac{\partial \overline{w^2}^+}{\partial r^+} + \frac{4}{r^{+2}} C_s \frac{k^+}{\varepsilon^+} \overline{w^2}^+ \left(\overline{v^2}^+ - \overline{w^2}^+ \right) + \frac{2}{r^+} \frac{\partial}{\partial r^+} \left(C_s \frac{k^+}{\varepsilon^+} \overline{w^2}^+ \left(\overline{v^2}^+ - \overline{w^2}^+ \right) \right)$$

$$- C_1 \varepsilon^+ (1 - f_{w1}) b_{33}^+ - \left\{ \frac{2}{3} (\alpha_1 - f_{w1} \alpha^*) + \frac{2}{3} \beta_1 - C_1^* (1 - f_{w1}) b_{33} \right\} \overline{uv}^+ \frac{\partial U^+}{\partial r^+}$$

<div style="text-align:center">254</div>

$$+C_2\,\varepsilon^+\left(1-f_{w1}\right)\left(b_{33}^2-\frac{1}{3}\Pi\right)$$

$$-f_{w1}\overline{w^2}^+\frac{\varepsilon^+}{k^++3\overline{v^2}^+/2}-\frac{2}{3}\left(1-f_{w1}\right)\varepsilon^+\quad,\qquad\text{(C-22)}$$

$$0=\frac{1}{r^+}\frac{\partial}{\partial r^+}\left(r^+\left(\frac{2}{3}+2C_S\frac{k^+}{\varepsilon^+}\overline{v^2}^+\right)\frac{\partial\overline{uv}^+}{\partial r^+}+r^+C_S\frac{k^+}{\varepsilon^+}\overline{uv}^+\frac{\partial\overline{v^2}^+}{\partial r^+}\right)-\frac{2}{3}\frac{\overline{uv}^+}{r^{+2}}$$

$$-\frac{1}{r^+}C_S\frac{k^+}{\varepsilon^+}\overline{uv}^+\frac{\partial\overline{w^2}^+}{\partial r^+}-\frac{2}{r^{+2}}C_S\frac{k^+}{\varepsilon^+}\overline{uv}^+\overline{w^2}^+-\overline{v^2}^+\frac{\partial U^+}{\partial r^+}-C_1\varepsilon^+\left(1-f_{w1}\right)b_{12}$$

$$+\left(\alpha_1-f_{w1}\alpha^*\right)\overline{v^2}^+\frac{\partial U^+}{\partial r^+}+\beta_1\overline{u^2}^+\frac{\partial U^+}{\partial r^+}+C_1^*\left(1-f_{w1}\right)b_{12}\overline{uv}^+\frac{\partial U^+}{\partial r^+}$$

$$-\left(\gamma_1-f_{w1}\gamma^*+\frac{C_3^*}{2}\Pi^{1/2}\right)k^+\frac{\partial U^+}{\partial y^+}+C_2\varepsilon^+\left(1-f_{w1}\right)\left(b_{11}b_{12}+b_{12}b_{22}\right)$$

$$-2f_{w1}\overline{uv}^+\frac{\varepsilon^+}{k^++3\overline{v^2}^+/2}\quad,\qquad\text{(C-23)}$$

$$0=\frac{1}{r^+}\frac{\partial}{\partial r^+}\left(r^+\left(1+C_\varepsilon\frac{k^+}{\varepsilon^+}\overline{v^2}\right)\frac{\partial\varepsilon^+}{\partial r^+}\right)-C_{\varepsilon 1}\frac{\varepsilon^+}{k^+}\overline{uv}^+\frac{\partial U^+}{\partial r^+}-C_{\varepsilon 2}\frac{\tilde{\varepsilon}^+\varepsilon^+}{k^+}$$

$$+f_{w2}\left(L\frac{\varepsilon^+}{k^+}\overline{uv}^+\frac{\partial U^+}{\partial r^+}+M\frac{\tilde{\varepsilon}^2}{k^+}-N\frac{\tilde{\varepsilon}^+\varepsilon^+}{k^+}\right)\quad.\qquad\text{(C-24)}$$

C.2.4 Boundary conditions

At $r^+=Re_\tau$ (wall)

$$U^+=0,\;\;k^+=0,\;\overline{u^2}^+=0,\;\overline{v^2}^+=0,\;\overline{w^2}^+=0,\;\overline{uv}^+=0,$$

$$\varepsilon^+=2\left(\frac{\partial\sqrt{k}}{\partial\left(Re_\tau-r^+\right)}\right)^2\quad.\qquad\text{(C-25)}$$

At $r^+=0$ (centerline)

$$\frac{\partial U^+}{\partial r^+}=0,\ \frac{\partial k^+}{\partial r^+}=0,\ \frac{\partial \overline{u^2}^+}{\partial r^+}=0,\ \frac{\partial \overline{v^2}^+}{\partial r^+}=0,\ \frac{\partial \overline{w^2}^+}{\partial r^+}=0,\ \overline{uv}^+=0,$$

$$\frac{\partial \varepsilon^+}{\partial r^+}=0 \qquad . \tag{C-26}$$

C.3 Fully-Developed Couette Flow

C.3.1 Mean flow equation

$$0 = \frac{\partial^2 U^+}{\partial y^{+2}} - \frac{\partial \overline{uv}^+}{\partial y^+} \quad .$$

(C-27)

C.3.2 NNWRS modeled equations

The equations are the same as those given for the fully-developed channel flow.

C.3.3 NWRS modeled equations

The equations are the same as those given for the fully-developed channel flow.

C.3.4 Boundary conditions

At $y^+ = 0$ (fixed wall)

$$U^+ = 0, \ k^+ = 0, \ \overline{u^2}^+ = 0, \ \overline{v^2}^+ = 0, \ \overline{w^2}^+ = 0, \ \overline{uv}^+ = 0$$

$$\varepsilon^+ = 2\left(\frac{\partial \sqrt{k}}{\partial y^+}\right)^2 \quad .$$

(C-28)

At $y^+ = 2\,\mathrm{Re}_\tau$ (moving wall)

$$U^+ = U^+_{specified}, \ k^+ = 0, \ \overline{u^2}^+ = 0, \ \overline{v^2}^+ = 0, \ \overline{w^2}^+ = 0, \ \overline{uv}^+ = 0$$

$$\varepsilon^+ = 2\left(\frac{\partial \sqrt{k}}{\partial y^+}\right)^2 \quad .$$

(C-29)

257

C.4 Incompressible Boundary-Layer Flow

C.4.1 Mean flow equations

$$\frac{\partial U}{\partial x} + \frac{\partial V}{\partial y} = 0 \quad , \tag{C-30a}$$

$$U\frac{\partial U}{\partial x} + V\frac{\partial U}{\partial y} = -\frac{\partial P}{\partial y} + \frac{\partial}{\partial y}\left\{ v\frac{\partial U}{\partial y} \right\} - \frac{\partial \overline{uv}}{\partial y} \quad . \tag{C-30b}$$

C.4.2 NNWRS modeled equations

$$U\frac{\partial \overline{u^2}}{\partial x} + V\frac{\partial \overline{u^2}}{\partial y} = \frac{\partial}{\partial y}\left(\left(v + C_S\frac{k}{\varepsilon}\overline{v^2} \right)\frac{\partial \overline{u^2}}{\partial y} + 2C_S\frac{k}{\varepsilon}\overline{uv}\frac{\partial \overline{uv}}{\partial y} \right) - 2\overline{uv}\frac{\partial U}{\partial y}$$

$$-C_1\varepsilon(1-f_{w1})b_{11} + \left\{ \frac{4}{3}\left(\alpha_1 - f_{w1}\alpha^* \right) - \frac{2}{3}\beta_1 + C_1^*(1-f_{w1})b_{11} \right\}\overline{uv}\frac{\partial U}{\partial y}$$

$$+C_2\varepsilon(1-f_{w1})\left(b_{11}{}^2 + b_{12}{}^2 - \frac{1}{3}\Pi \right) - \frac{2}{3}(1-f_{w1})\varepsilon - f_{w1}\frac{\varepsilon}{k}\overline{u^2}$$

$$-\frac{1}{2}\left[\frac{\partial}{\partial y}\left(v\frac{\partial \overline{u^2}}{\partial y} \right) - \frac{\overline{u^2}}{k}\frac{\partial}{\partial y}\left(v\frac{\partial k}{\partial y} \right) \right] \quad , \tag{C-31}$$

$$U\frac{\partial \overline{v^2}}{\partial x} + V\frac{\partial \overline{v^2}}{\partial y} = \frac{\partial}{\partial y}\left(\left(v + 3C_S\frac{k}{\varepsilon}\overline{v^2} \right)\frac{\partial \overline{v^2}}{\partial y} \right) - C_1\varepsilon(1-f_{w1})b_{22}$$

$$-\left\{ \frac{2}{3}\left(\alpha_1 - f_{w1}\alpha^* \right) - \frac{4}{3}\beta_1 - C_1^*(1-f_{w1})b_{22} \right\}\overline{uv}\frac{\partial U}{\partial y}$$

$$+C_2\varepsilon(1-f_{w1})\left(b_{22}{}^2 + b_{12}{}^2 - \frac{1}{3}\Pi \right) - \frac{2}{3}(1-f_{w1})\varepsilon - f_{w1}\frac{\varepsilon}{k}\overline{v^2}$$

$$-\frac{1}{2}\left[\frac{\partial}{\partial y}\left(v\frac{\partial \overline{v^2}}{\partial y} \right) - \frac{\overline{v^2}}{k}\frac{\partial}{\partial y}\left(v\frac{\partial k}{\partial y} \right) \right] \quad , \tag{C-32}$$

$$U\frac{\partial \overline{w^2}}{\partial x} + V\frac{\partial \overline{w^2}}{\partial y} = \frac{\partial}{\partial y}\left(\left(v + C_S\frac{k}{\varepsilon}\overline{v^2} \right)\frac{\partial \overline{w^2}}{\partial y} \right) - C_1\varepsilon(1-f_{w1})b_{33}$$

$$-\left\{\frac{2}{3}\left(\alpha_1 - f_{w1}\alpha^*\right) + \frac{2}{3}\beta_1 - C_1^*(1-f_{w1})b_{33}\right\}\overline{uv}\frac{\partial U}{\partial y}$$

$$+C_2\,\varepsilon\left(1 - f_{w1}\right)\left(b_{33}^2 - \frac{1}{3}\Pi\right) - \frac{2}{3}\left(1 - f_{w1}\right)\varepsilon - f_{w1}\frac{\varepsilon}{k}\overline{w^2}$$

$$-\frac{1}{2}\left[\frac{\partial}{\partial y}\left(v\frac{\partial\overline{w^2}}{\partial y}\right) - \frac{\overline{w^2}}{k}\frac{\partial}{\partial y}\left(v\frac{\partial k}{\partial y}\right)\right] \quad , \tag{C-33}$$

$$U\frac{\partial\overline{uv}}{\partial x} + V\frac{\partial\overline{uv}}{\partial y} = \frac{\partial}{\partial y}\left(\left(v + 2C_S\frac{k}{\varepsilon}\overline{v^2}\right)\frac{\partial\overline{uv}}{\partial y} + C_S\frac{k}{\varepsilon}\overline{uv}\frac{\partial\overline{v^2}}{\partial y}\right)$$

$$-\overline{v^2}\frac{\partial U}{\partial y} - C_1\,\varepsilon(1 - f_{w1})b_{12} + \left(\alpha_1 - f_{w1}\alpha^*\right)\overline{v^2}\frac{\partial U}{\partial y} + \beta_1\overline{u^2}\frac{\partial U}{\partial y}$$

$$+C_1^*(1 - f_{w1})b_{12}\overline{uv}\frac{\partial U}{\partial y} - \left(\gamma_1 - f_{w1}\gamma^* + \frac{C_3^*}{2}\Pi^{1/2}\right)k\frac{\partial U}{\partial y}$$

$$+C_2\,\varepsilon(1 - f_{w1})(b_{11}\,b_{12} + b_{12}\,b_{22}) - f_{w1}\frac{\varepsilon}{k}\overline{uv}$$

$$-\frac{1}{2}\left[\frac{\partial}{\partial y}\left(v\frac{\partial\overline{uv}}{\partial y}\right) - \frac{\overline{uv}}{k}\frac{\partial}{\partial y}\left(v\frac{\partial k}{\partial y}\right)\right] \quad , \tag{C-34}$$

$$U\frac{\partial\varepsilon}{\partial x} + V\frac{\partial\varepsilon}{\partial y} = \frac{\partial}{\partial y}\left(\left(v + C_\varepsilon\frac{k}{\varepsilon}\overline{v^2}\right)\frac{\partial\varepsilon}{\partial y}\right) - C_{\varepsilon1}\frac{\varepsilon}{k}\overline{uv}\frac{\partial U}{\partial y} - C_{\varepsilon2}\frac{\varepsilon}{k}\tilde{P}$$

$$+ C_{\varepsilon3}v\frac{\varepsilon}{k}\left(\frac{\partial\sqrt{k}}{\partial y}\right)^2 \tag{C-35}$$

C.4.3 NWRS modeled equations

$$U\frac{\partial\overline{u^2}}{\partial x} + V\frac{\partial\overline{u^2}}{\partial y} = \frac{\partial}{\partial y}\left(\left(v + C_S\frac{k}{\varepsilon}\overline{v^2}\right)\frac{\partial\overline{u^2}}{\partial y} + 2C_S\frac{k}{\varepsilon}\overline{uv}\frac{\partial\overline{uv}}{\partial y}\right) - 2\overline{uv}\frac{\partial U}{\partial y}$$

$$-C_1\,\varepsilon(1 - f_{w1})b_{11} + \left\{\frac{4}{3}\left(\alpha_1 - f_{w1}\alpha^*\right) - \frac{2}{3}\beta_1 + C_1^*(1 - f_{w1})b_{11}\right\}\overline{uv}\frac{\partial U}{\partial y}$$

$$+C_2\varepsilon(1 - f_{w,1})(b_{11}^2 + b_{12}^2 - \frac{1}{3}\Pi)$$

259

$$-f_{w1}\frac{\overline{u^2}}{k+3\overline{v^2}/2}\varepsilon-\frac{2}{3}\left(1-f_{w1}\right)\varepsilon\quad,\tag{C-36}$$

$$U\frac{\partial\overline{v^2}}{\partial x}+V\frac{\partial\overline{v^2}}{\partial y}=\frac{\partial}{\partial y}\left(\left(\frac{2}{3}\upsilon+3C_S\frac{k}{\varepsilon}\overline{v^2}\right)\frac{\partial\overline{v^2}}{\partial y}\right)-C_1\varepsilon\left(1-f_{w1}\right)b_{22}$$

$$-\left\{\frac{2}{3}\left(\alpha_1-f_{w1}\alpha^*\right)-\frac{4}{3}\beta_1-C_1^*(1-f_{w1})b_{22}\right\}\overline{uv}\frac{\partial U}{\partial y}$$

$$+C_2\varepsilon(1-f_{w,1})(b_{22}^2+b_{12}^2-\frac{1}{3}\Pi)$$

$$-4f_{w1}\frac{\overline{v^2}}{k+3\overline{v^2}/2}\varepsilon-\frac{2}{3}\left(1-f_{w1}\right)\varepsilon\quad,\tag{C-37}$$

$$U\frac{\partial\overline{w^2}}{\partial x}+V\frac{\partial\overline{w^2}}{\partial y}=\frac{\partial}{\partial y}\left(\left(\upsilon+C_S\frac{k}{\varepsilon}\overline{v^2}\right)\frac{\partial\overline{w^2}}{\partial y}\right)-C_1(1-f_{w1})b_{33}$$

$$-\left\{\frac{2}{3}\left(\alpha_1-f_{w1}\alpha^*\right)+\frac{2}{3}\beta_1-C_1^*(1-f_{w1})b_{33}\right\}\overline{uv}\frac{\partial U}{\partial y}$$

$$+C_2\varepsilon(1-f_{w1})(b_{33}^2-\frac{1}{3}\Pi)$$

$$-f_{w1}\frac{\overline{w^2}}{k+3\overline{v^2}/2}\varepsilon-\frac{2}{3}\left(1-f_{w1}\right)\varepsilon\quad,\tag{C-38}$$

$$U\frac{\partial\overline{uv}}{\partial x}+V\frac{\partial\overline{uv}}{\partial y}=\frac{\partial}{\partial y}\left(\left(\frac{2}{3}\upsilon+2C_S\frac{k}{\varepsilon}\overline{v^2}\right)\frac{\partial\overline{uv}}{\partial y}+C_S\frac{k}{\varepsilon}\overline{uv}\frac{\partial\overline{v^2}}{\partial y}\right)$$

$$-\overline{v^2}\frac{\partial U}{\partial y}-C_1\varepsilon(1-f_{w1})b_{12}+\left(\alpha_1-f_{w1}\alpha^*\right)\overline{v^2}\frac{\partial U}{\partial y}+\beta_1\overline{u^2}\frac{\partial U}{\partial y}$$

$$+C_1^*(1-f_{w1})b_{12}\overline{uv}\frac{\partial U}{\partial y}-\left(\gamma_1-f_{w1}\gamma^*+\frac{C_3^*}{2}\Pi^{1/2}\right)k\frac{\partial U}{\partial y}$$

$$+C_2\varepsilon(1-f_{w1})(b_{11}b_{12}+b_{12}b_{22})-2f_{w1}\frac{\overline{uv}}{k+3\overline{v^2}/2}\varepsilon\quad,\tag{C-39}$$

$$U\frac{\partial \varepsilon}{\partial x}+V\frac{\partial \varepsilon}{\partial y}=\frac{\partial}{\partial y}\left(\left(\upsilon+C_\varepsilon\frac{k}{\varepsilon}\overline{v^2}\right)\frac{\partial \varepsilon}{\partial y}\right)-C_{\varepsilon 1}\frac{\varepsilon}{k}\overline{uv}\frac{\partial U}{\partial y}$$

$$-C_{\varepsilon 2}\frac{\tilde{\varepsilon}\varepsilon}{k}+f_{w2}\left(L\frac{\varepsilon}{k}\overline{uv}\frac{\partial U}{\partial y}+M\frac{\bar{\varepsilon}^2}{k}-N\frac{\tilde{\varepsilon}\varepsilon}{k}\right) \quad . \tag{C-40}$$

261

C.5 Levy-Lees Transformation for Boundary-Layer Flows

The body-oriented physical coordinates (x,y) and transformed coordinates (ξ,η) are related by,

$$d\xi = \bar{\rho}_e \tilde{u}_e \bar{\mu}_e r_o^{2j} dx \quad \text{and} \quad d\eta = \frac{\bar{\rho}\tilde{u}_e(r_o+y)^j dy}{\sqrt{2\xi}} \quad , \tag{C-41}$$

where r_o is the body radius, e stands for the freestream value and $j=0,1$ for plane and axisymmetric flow, respectively. Equivalent to these expressions are the following:

$$\xi(x) = \int_0^x \bar{\rho}_e \tilde{u}_e \bar{\mu}_e r_o^{2j} dx \quad \text{and} \quad \eta(x,y) = \frac{\bar{\rho}_e \tilde{u}_e r_o^j}{\sqrt{2\xi}} \int_0^\eta \left(\frac{\bar{\rho}}{\bar{\rho}_e}\right) t^j dy \quad , \tag{C-42}$$

where $t = r/r_o$ is the transverse curvature. By using the chain-rule of calculus we can relate the derivatives of the two coordinate systems:

$$\left(\frac{\partial}{\partial x}\right)_y = \bar{\rho}_e \tilde{u}_e \bar{\mu}_e r_o^{2j}\left(\frac{\partial}{\partial \xi}\right)_\eta + \left(\frac{\partial \eta}{\partial x}\right)_y \left(\frac{\partial}{\partial \eta}\right)_\xi \quad , \tag{C-43a}$$

$$\left(\frac{\partial}{\partial y}\right)_x = \frac{\bar{\rho}_e \tilde{u}_e r_o^j t^j}{\sqrt{2\xi}}\left(\frac{\bar{\rho}}{\bar{\rho}_e}\right)\left(\frac{\partial}{\partial \eta}\right)_\xi \quad . \tag{C-43b}$$

The dependent variables are transformed according to the following relations:

$$F(\xi,\eta) = \frac{\tilde{u}}{\tilde{u}_e} \quad , \qquad V(\xi,\eta) = \frac{2\xi}{\bar{\rho}_e \tilde{u}_e \bar{\mu}_e r_o^{2j}}\left[F\left(\frac{\partial \eta}{\partial s}\right) + \frac{\rho \tilde{v} r_o^j t^j}{2\xi}\right] \quad ,$$

$$K(\xi,\eta) = \frac{k}{\tilde{u}_e^2} \quad , \qquad \hat{W}(\xi,\eta) = \frac{2\xi\omega}{\tilde{u}_e^2} \quad , \qquad \hat{\mathcal{E}}(\xi,\eta) = \frac{2\xi\tilde{\varepsilon}}{\tilde{u}_e^4} \quad , \tag{C-44}$$

where the expression for V is extracted from the continuity equation assuming a stream-function exists. The equations governing the mean flow after the transformation are then given by,

$$2\bar{\xi}\frac{\partial F}{\partial \bar{\xi}} + \frac{\partial V}{\partial \eta} + F = 0 \quad , \tag{C-45}$$

$$2\bar{\xi}F\frac{\partial F}{\partial \bar{\xi}} + V\frac{\partial F}{\partial \eta} - \frac{\partial}{\partial \eta}\left[t^{2j}L(1+\bar{\mu}_T)\frac{\partial F}{\partial \eta}\right] + \bar{\beta}(F^2 - \Theta - 1) = 0 \quad . \tag{C-46}$$

For the $k - \varepsilon$ model the equations are transformed to,

$$2\bar{\xi}F\frac{\partial K}{\partial \bar{\xi}} + V\frac{\partial K}{\partial \eta} - \frac{\partial}{\partial \eta}\left[t^{2j}L\left(1+\frac{\bar{\mu}_T}{\sigma_k}\right)\frac{\partial K}{\partial \eta}\right] + 2\bar{\beta}FK - t^{2j}L\bar{\mu}_T\left(\frac{\partial F}{\partial \eta}\right)^2$$

$$+\frac{(\mathcal{E}+\mathcal{E}_w)}{\hat{\rho}_e\hat{\mu}_e\hat{r}_o^{2j}} = 0 \quad , \tag{C-47}$$

$$2\bar{\xi}F\frac{\partial \mathcal{E}}{\partial \bar{\xi}} + V\frac{\partial \mathcal{E}}{\partial \eta} - \frac{\partial}{\partial \eta}\left[t^{2j}L\left(1+\frac{\bar{\mu}_T}{\sigma_\varepsilon}\right)\frac{\partial \mathcal{E}}{\partial \eta}\right] + 2(2\bar{\beta}-1)F\mathcal{E}$$

$$-C_{\varepsilon 1}f_1\frac{\mathcal{E}}{K}t^{2j}L\bar{\mu}_T\left(\frac{\partial F}{\partial \eta}\right)^2 + \frac{C_{\varepsilon 2}f_2}{\hat{\rho}_e\hat{\mu}_e\hat{r}_o^{2j}}\frac{\mathcal{E}^2}{K} - \Sigma = 0 \quad , \tag{C-48}$$

where,

$$\mathcal{E}_\omega = \frac{A\,2\bar{\xi}}{U_\infty^3\hat{u}_e^4}\varepsilon_w, \quad \bar{\mu}_T = C_\mu f_\mu\frac{2\bar{\xi}\hat{\rho}_e}{\hat{\mu}_e\varphi^2}\frac{K^2}{L(1+\Theta)^2\mathcal{E}}, \quad \Sigma = \frac{A^2}{U_\infty^4}\frac{(2\bar{\xi})^2}{\hat{\rho}_e\hat{u}_e^6\hat{\mu}_e\hat{r}_o^{2j}}E \quad . \tag{C-49}$$

The dimensionless parameters introduced are given by,

$$\bar{\xi} = \frac{\xi}{\rho_\infty U_\infty \mu_r A^{2j+1}} \quad , \qquad \hat{u}_e = \frac{\tilde{u}_e}{U_\infty} \quad , \qquad \hat{\rho}_e = \frac{\bar{\rho}_e}{\rho_\infty} \quad , \tag{C-50a}$$

$$\hat{r}_o = \frac{r_o}{A} \quad , \qquad \hat{\mu}_e = \frac{\mu_e}{\mu_r} \quad , \qquad \varphi = \sqrt{\frac{\mu_r}{\rho_\infty U_\infty A}} \quad , \tag{C-50b}$$

$$W = \frac{\hat{W}}{\rho_\infty\mu_r A^{2j}} \quad , \qquad \mathcal{E} = \frac{\hat{\mathcal{E}}}{\rho_\infty\mu_r A^{2j}} \quad . \tag{C-50c}$$

The quantities,

$$\Theta = \frac{\tilde{T}-\tilde{T}_e}{\tilde{T}_e} \quad , \qquad L \equiv \frac{\bar{\rho}}{\bar{\rho}_e}\frac{\mu}{\mu_e} \quad \text{and} \quad \bar{\beta} \equiv \frac{2\xi}{\tilde{u}_e}\frac{d\tilde{u}_e}{d\xi} \quad , \tag{C-51}$$

are the dimensionless temperature, density/viscosity and pressure gradient terms, respectively. The first two terms are introduced from the transformation and are zero and one, respectively, for isothermal, incompressible flows. The last term in (C-51) vanishes for flows with zero pressure gradient. The parameter A is a reference length and is set to 1 with no loss in generality. Similar transformations are also applied to the modeled transport equations of the near-wall Reynolds-stress models.

263